REFLECTARRAY ANTENNAS

Analysis, Design, Fabrication, and Measurement

Jafar Shaker • Mohammad Reza Chaharmir • Jonathan Ethier

Reflectarray Antennas

Analysis, Design, Fabrication, and Measurement

For a listing of recent titles in the
Artech House Antennas and Propagation Series,
turn to the back of this book.

Reflectarray Antennas

Analysis, Design, Fabrication, and Measurement

Jafar Shaker
Mohammad Reza Chaharmir
Jonathan Ethier

ARTECH
HOUSE
BOSTON | LONDON
artechhouse.com

Library of Congress Cataloging-in-Publication Data
A catalog record for this book is available from the U.S. Library of Congress.

British Library Cataloguing in Publication Data
A catalog record for this book is available from the British Library.

ISBN-13: 978-1-60807-499-0

Cover design by Vicki Kane

10 9 8 7 6 5 4 3 2 1

To our wives

Contents

CHAPTER 1

Introduction

1.1 General Background

The first step in presenting a scientific or technical subject is providing clear and distinct definitions and "reflectarrays" are not an exception to this general rule. "Reflectarray antenna" refers to the class of radiating structures that are comprised of an array of radiating elements, reradiating the energy that is impinged on them from one or more radiating feeds that are located in free space. The whole diversity and variety in the world of reflectarray stems from the variety of constituent elements used, the way they are set into a lattice, and the method of feeding the structure.

Reflectarray technology is a hybrid of conventional reflector and phased array technologies [1, 2]. Constituent elements of the reflectarray that are set into a regular lattice mimic the function of phased array radiating elements and the free space acts as the transmission medium between the elements and the signal source (feed). The fact that the reflectarray, in its most general form, collimates the plane wave that impinges on its surface into the feed constitutes the affinity between the conventional parabolic reflector and reflectarray. Generally, adjustment of the geometrical features of constituent elements of reflectarray is utilized to realize desired aperture field distribution [3, 4]. Contrary to conventional microstrip phased arrays that employ printed transmission lines and henceforth suffer from excessive loss at higher frequencies [5], reflectarrays use the free space medium to transmit the electrical signal from the feed to the elements and thus avoid degradation in the gain performance as a result of loss in the feeding system.

Open waveguide structures are among the radiators that have a long record of implementation both as an isolated or array of radiator(s). Therefore, open waveguide turned out to be a natural choice for initial introduction and realization of a reflectarray that was comprised of 426 lattice of open-waveguides fed by a horn antenna [6]. Complexity of the fabrication process of waveguide structures, especially when their operating frequency band is high, hindered further development of waveguide-based reflectarray. Subsequent developments and advances in lithographic technology was an impetus to reflectarray research and raised its profile as a viable and appealing high gain antenna with versatile and flexible features as will be described throughout this book. Amenability of reflectarray technology to

etching and lithographic techniques is an important advantage for reflectarrays as it permits adoption of new developments in fabrication technology to further enhance the functionality and performance of reflectarrays. For instance, microelectromechanical system (MEMS) technology was utilized to realize reconfigurable reflectarray [7], amplifiers were embedded in a cell to enhance power handling of reflectarray at higher frequencies [8], or laser induced plasma was exploited in realization of beam switched reflectarray [9]. A more exhaustive presentation of various reflectarray structures with added functionalities that demonstrate exploitation of emerging fabrication techniques will be given in the coming chapters.

1.2 Why Reflectarrays?

Geometrical rules are the basis of the first-order synthesis and analysis algorithms in the case of conventional parabolic reflectors. Physical optics and Geometrical Theory of Diffraction (GTD) are used to increase accuracy in the design and analysis [10]. It is important to note that the laws of geometry are neutral to the operating frequency and polarization of the incoming wave. In other words, the surface of a conventional solid parabolic reflector does not distinguish different frequency bands or polarizations of the incoming signal and treats them the same to the first order of approximation. Therefore, a conventional parabolic reflector is capable of operating at a given frequency band and polarization as long as the feed accommodates that same frequency band and polarization. However, constituent printed elements of a reflectarray that are located on its surface impart a given phase onto the incoming wave that depends on frequency, polarization, and angle of incidence of the incoming wave. Therefore, a judicious design of the constituent elements of reflectarray leads to a unique aperture field distribution for each of its operating bands and polarizations. This fundamental difference between the underlying operating principles of conventional reflector and reflectarray brings about a whole range of flexibility and versatility in operation of reflectarray that is not readily available in the case of conventional reflectors as will be pointed in the coming sections.

A reflectarray is shown in Figure 1.1 that is comprised of printed dipoles. Lithographic technology is a low-cost and mature technology that can be used for fabrication of printed reflectarrays. As noted above, the reflected phase response of the elements depends on their geometrical features. A different class of elements with a given phase response to polarization and/or frequency that is different from the polarization and/or operating frequency of the first set of elements, can be embedded within the lattice of the first set of elements to achieve collimation for this second set of elements [1]. It is obvious that the coupling between the two sets must be accounted for in the design process [11]. Having embedded two sets of elements within the reflectarray lattice, two different focal points can be achieved and only one focal point is dedicated to each combination of frequency band and state of polarization. Figure 1.2 shows the case of a reflectarray with two focal points, each dedicated to a given linear polarization. Two sets of dipoles are shown on the reflectarray with different orientations. Each set collimates the incoming field with horizontal or vertical into a separate dedicated feed. The possibility of achieving a dedicated focal point for each given frequency and/or polarization is not readily

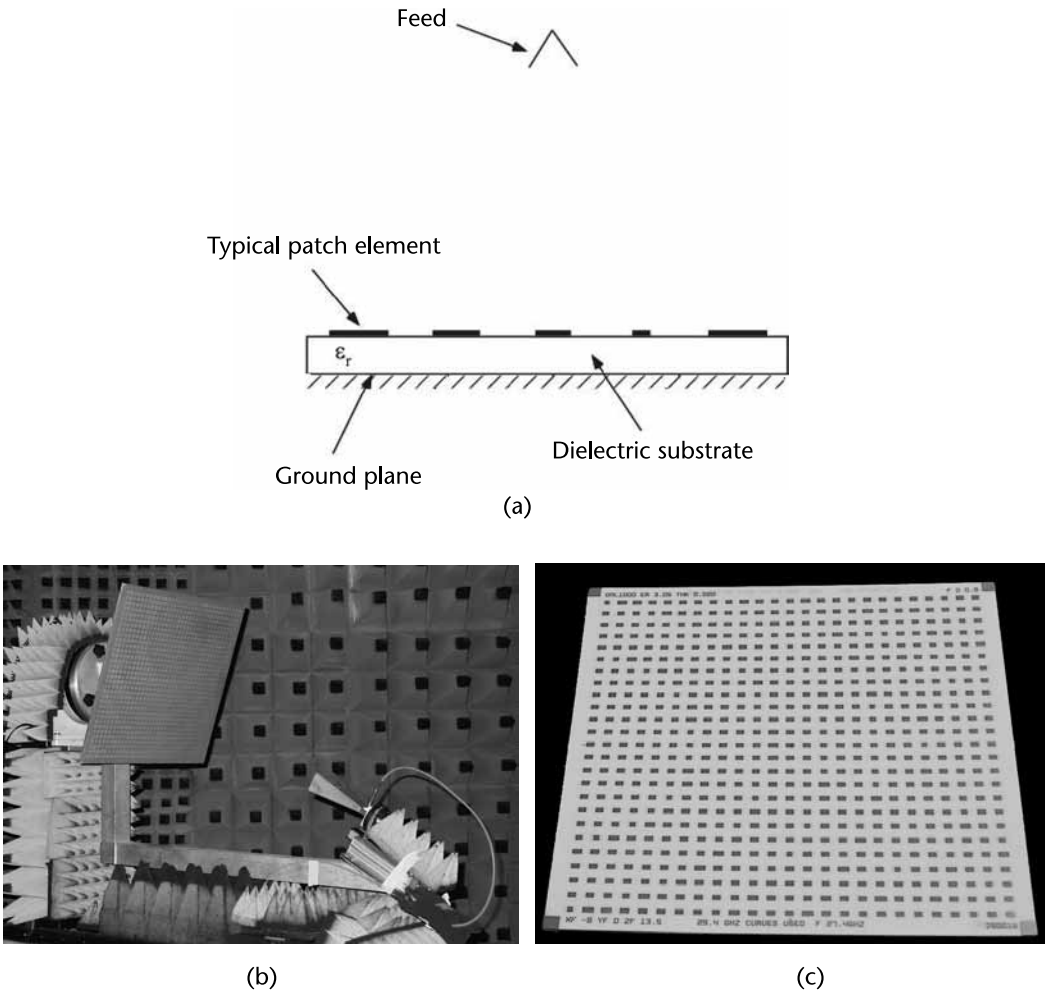

Figure 1.1 (a) Constituent components of a reflectarray. (b) Reflectarray structure with printed dipole as the cell element. (c) Reflectarray structure in the far-field antenna chamber.

available in the case of conventional solid reflectors, whereas reflectarray structure is inherently amenable to multifoci operation for multibands [12]. This can result in major simplification of the feed system as will be pointed out in Chapter 4.

One of the challenges in high gain antenna technology is design of antennas that are portable and easily deployable in extreme and adverse environmental conditions. Reflectarrays are superior in terms of portability as a result of its flat shape. Transportation and deployment of large conventional reflectors can pose challenges in using such antennas in extreme field conditions. However, multipanel rendition of flat reflectors offers an effective response to portability and deployability factors.

Radar cross section (RCS) and volume specifications of antennas can be an important factor in a particular application. The flat nature of reflectarrays is better suited to the fulfillment of volume requirements. Reduced volume of the antenna is generally tantamount to lower RCS. However, more involved reflectarray designs can be implemented to disperse selected frequency bands in order to further reduce RCS at given bands.

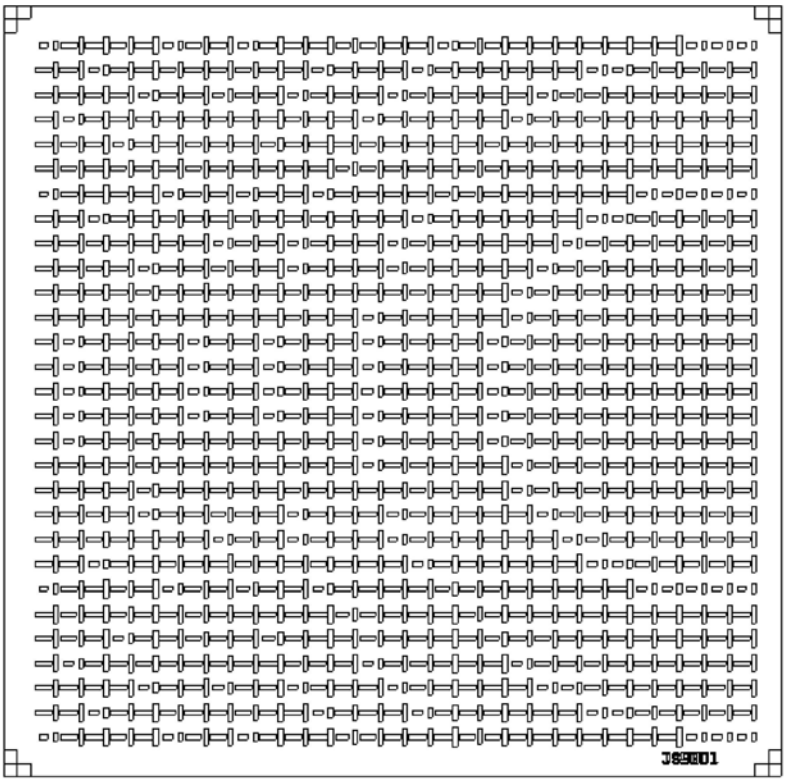

Figure 1.2 Local multipoint communication system (LMCS) reflectarray that is designed for two focal points, each dedicated to a given linear polarization.

Severing the ties with Euclidean geometry in the operation of reflectarray allows for straightforward design and fabrication of conformal reflectarray antennas [13]. This does not necessarily require a complicated feed design as opposed to conventional reflectors. The same feed structure can be used and the feed complexity can be relegated to the adjustment of the cell elements that can be addressed easily by appropriate lithographic technology. In closing, in the light of the aforementioned arguments, the opening question of this section (why reflectarrays?) should be transformed into an exploratory one: Why not reflectarrays?

1.3 The Structure of the Book

The present text is meant to serve as a complete exposition of design, analysis, fabrication, test, and operation of reflectarray antennas. An emphasis has been laid on the presentation of underlying physical principles of such radiating structures. Chapter 2 is devoted to description of general design guidelines in which a direct comparison with conventional reflector antenna is provided, focusing on conventional efficiency figures of reflectors [14]. Important design parameters in the synthesis of reflectarrays composed of patch or printed dipole elements will be

described and the effect of such parameters as substrate thickness and permittivity on the performance of reflectarrays will be presented [15].

As noted above, the choice of cell element has an important impact on the type of application and level of performance that is realizable in a reflectarray. Chapter 3 focuses on different types of cell elements, their special features, and considerations that might make one type of cell element superior to another for a given set of specifications that addresses a particular application. Conventional resonant cell elements such as single patch [15], stacked patch [16], slotted patch [17], and different variations of loop elements [18] will be studied in this chapter. Also, the novel and emerging subwavelength coupled resonant (SCR) [19] elements and fragmented elements will be presented in this same chapter.

Chapter 4 deals with different types of reflectarrays. Depending of the types of elements used as the expanded constituent elements, the range of functionalities of reflectarrays can be expended [1]. Different types of elements can be combined and/or novel aperture field distributions can be realized. Examples are multifeed, multiband/multipolarization reflectarrays, beam shaping, and power combining.

The basis of most synthesis methods in the design of reflectarrays is calculation of scattering from an infinite periodic structure that is illuminated by a plane wave. Knowledge of the phase of scattered field (direct reflection component) versus the size of geometrical features of the cell elements is utilized to realize the desired phase transformation [15]. Smooth variation of the cell elements across the reflectarray surface justifies application of infinite periodicity assumption. Method of moment (MoM) is among the most versatile and conceptually rich numerical methods that have been used in the calculation of scattering from infinite periodic structures illuminated by plane wave [20, 21]. MoM is briefly described in Chapter 5 in the context of its application to the design of reflectarrays. Physical insights obtained from the application of the method are presented. Characteristic mode (CM) [22] is another promising numerical method that has recently been applied in the design of reflectarrays comprised of fragmented elements. These methods are suited to the analysis of cell elements that are rather complicated. New developments in commercial software [23] as far as related to the analysis and design of reflectarrays have been presented in this same chapter. It is demonstrated that intelligent application of the commercial software can lead to important insight and understanding of reflectarray performance, such as bandwidth, the origin of undesired radiation components such as cross-polarization, and feed image.

Limited operational bandwidth has been a major shortcoming of reflectarrays as compared to conventional solid reflectors. In the case of a solid reflector, the bandwidth is limited by the bandwidth of the feed structure, whereas the nature of elements and the size of the structure (its geometric size and focal/distance (F/D)) limit the operating bandwidth of the reflectarray. Chapter 6 is devoted to the presentation of extensive research on broadening bandwidth of reflectarray structures [16, 23].

Extension of the range of application of reflectarrays calls for utilization of low-cost substrates. However, low-cost substrates are generally lossy and special techniques that are subject of Chapter 7 should be developed to prevent degradation of the performance as a result of lossy substrate. Subwavelength coupled resonant (SCR) cell elements will be shown to be quite promising in mitigation of loss [24, 25].

Various other antenna structures have emerged as a result of research on reflectarray and among these are transmitarrays and subreflectarrays, which will be presented in Chapter 8. A transmitarray [26] emulates conventional lens through implementation of consecutive periodic structures to manipulate the phase front of the outgoing beam that emanates from a feed structure. The design procedure is more involved as compared to reflectarray because both phase and amplitude of transmission should be optimized to achieve desired performance. Subreflectarray [27, 28] mimics the function of a solid subreflector. Analytic formulas are obtained for the design and simulation and experimental results will be shown to verify the validity of the design equations. Subreflectarrays have also been used for the phase correction on the main reflector, which suffers from fabrication error or mechanical loading [28].

As was pointed out above, reflectarrays are inherently well suited to integration of electronics that can be used for reconfigurability. The subject of Chapter 9 is presentation of extensive research that has been carried out in this field [7, 29–31]. Also, several novel mechanical techniques will be presented for switched beam and beam-steering applications [32]. These mechanical techniques do not necessarily lead to degradation of radiation pattern of the steered or switched beam that is in contrast to deterioration of performance in the case of solid reflectors when the beam is steered through mechanical means such as movement of the feed. Reflectarrays can benefit highly from new developments in the material science in the context of materials with electrical properties (refractive index, conductivity, permeability, and so on) sensitive to light, voltage, and temperature. A detailed presentation of the implementation of photo-induced reflectarray on high resistivity silicon is given to elucidate the importance of emerging materials in the context of reflectarray research [9, 33].

The fundamental building block of a reflectarray is its cell element and particular care should be exercised in the fabrication process to maintain fine features of the cell elements. The smaller the cell element, the smaller the feature size and thus the tighter the fabrication tolerance required. The effect of etching tolerance on the performance of reflectarrays will be presented in Chapter 10. Also, the application of novel techniques such as inkjet printing in the fabrication of reflectarrays will be presented. The technique is promising for the fabrication of reflectarrays that employ SCR elements and operate at higher bands (Ka-band and above). A detailed study will be presented on the elements that are more prone to fabrication tolerance, which has an impact on the selection of appropriate cell element for a given application.

Chapter 11 includes concluding remarks on the future directions of reflectarray research and also potential applications of the technology in face of the emergence of new fabrication techniques to accommodate both passive and active elements.

References

[1] Shaker, J., et al., "Reflectarray Research in Communications Research Centre Canada," *IEEE Antenna and Propagation Magazine*, Vol. 50, No. 4, August 2008, pp. 31–52.

[2] Huang, J., and J. A. Encinar, *Reflectarray Antennas*, New York: Wiley-Interscience, 2008.

[3] Chaharmir, M. R., et al., "Design of a Wideband Single Layer Subreflectarray for Space Applications," *Proceedings of European Conference of Antennas and Propagation*, Barcelona, Spain, April 12–16, 2010.

[4] Pozar, D. M., S. D. Targonski, and R. Polkus, "A Shaped-Beam Microstrip Patch Reflectarray Antenna," *IEEE Transactions on Antennas and Propagation*, Vol. 47, No. 7, 1999, pp. 1167–1173.

[5] Mailloux, R. J., *Phased Array Antenna Handbook*, 2nd ed., Norwood, MA: Artech House, 2005.

[6] Berry, D., R. Malech, and W. Kennedy, "The Reflectarray Antenna," *IEEE Transactions on Antennas and Propagation*, Vol. 11, No. 6, 1963, pp. 645–651.

[7] Legay, H., et al., "A Steerable Reflectarray Antenna with MEMs Controls," *IEEE International Symposium on Phased Array Systems and Technology*, October 14–17, 2003, pp. 494–499.

[8] Robinson, A. W., and M. E. Bialkowski, "An X-Band Active Microstrip Reflectarray," *Proceedings of Asia-Pacific Microwave Conference*, 1997, pp. 925–928.

[9] Chaharmir, M. R., J. Shaker, M. Cuhaci, "Novel Photonically-Controlled Reflectarray Antenna," *IEEE Transactions on Antennas and Propagation*, Vol. 54, No. 4, April 2006, pp. 1134–1141.

[10] Love, A., "Reflector Antennas," *IEEE Press Selected Reprint Series,* NY: John Wiley & Sons, 1978.

[11] Chaharmir, R., J. Shaker, and M. Cuhaci, "Development of Dual Band Circularly Polarized Reflectarray," *IEE Proceedings Microwaves, Antennas, and Propagation*, Vol. 153, No. 1, February 6, 2006, pp. 49–54.

[12] Shaker, J., and M. Cuhaci, "Multi-Band, Multi-Polarization Reflector-Reflectarray Antenna with Simplified Feed System and Mutually Independent Radiation Patterns," *IEE Proceedings on Microwaves, Antennas, and Propagation*, Vol. 152, No. 2, April 2005, pp. 97–101.

[13] Huang, J., "Capabilities of Printed Reflectarray Antennas," *IEEE International Symposium on Phased Array Systems and Technologies*, 1996, pp. 131–134.

[14] Collin, R. E., *Antennas and Radiowave Propagation*, New York: McGraw-Hill, 1985.

[15] Pozar, D. M., S. D. Targonski, H. D. Syrigos, "Design of Millimeter Wave Microstrip Reflectarrays," *IEEE Transactions on Antennas and Propagation*, Vol. 45, No. 2, February 1997, pp. 287–296.

[16] Encinar, J. A., and J. A. Zornoza, "Broadband Design of Three-Layer Printed Reflectarrays," *IEEE Transactions on Antennas and Propagation*, Vol. 51, No. 7, July 2003, pp. 1662–1664.

[17] Chaharmir, M. R., J. Shaker, and A. Sebak, "Reflectarray with Variable Slots on the Ground Plane," *IEE Proceedings of Microwaves, Antennas and Propagations*, Vol. 150, No. 6, July 2003, pp. 436–439.

[18] Chaharmir, M. R., and J. Shaker, "Broadband Reflectarray with Combination of Cross and Rectangle Loop Elements," *Electronics Letters*, Vol. 44, No. 11, 2008, pp. 658–659.

[19] Ethier, J., M. R. Chaharmir, and J. Shaker, "Reflectarray Design Comprised of Sub-Wavelength Coupled-Resonant Square Loop Elements," *Electronics Letters*, Vol. 47, No. 22, 2011, pp. 1215–1217.

[20] Munk, B., *Frequency Selective Surfaces: Theory and Design*, New York: John Wiley & Sons, 2000.

[21] Harrington, R. F., *Field Computation by Moment Methods*, New York: IEEE Press, 2000.

[22] Harrington, R. F., and J. R. Mautz, Theory of Characteristic Modes for Conducting Bodies," *IEEE Transactions on Antennas and Propagation*, Vol. 19, No. 5, September 1971, pp. 622–628.

[23] Chaharmir, M. R., et al., "Design of Broadband, Single Layer Dual-Band Large Reflectarray Using Multi-Open Loop Elements," *IEEE Transactions on Antennas and Propagation*, Vol. 58, No. 9, September 2010, pp. 2875–2883.

[24] Rajagopalan, H., and Y. Rahmat-Samii, "On Reflection Characteristics of a Reflectarray Element with Low-Loss and High-Loss Substrates," *IEEE Antenna and Propagation Magazine*, Vol. 52, No. 4, 2010, pp. 73–89.

[25] Ethier, J., M. R. Chaharmir, and J. Shaker, "Novel Approach for Low-Loss Reflectarray Designs," *Proceedings of IEEE Antenna and Propagation Symposium*, 2011, pp. 373–376.

[26] Ryan, C., M. R. Chaharmir, and J. Shaker, "A Wideband Transmitarray Using Dual-Resonant Double Square Rings," *IEEE Transactions on Antennas and Propagation*, Vol. 58, No. 5, May 2010, pp. 1486–1493.

[27] Almajali, E., et al., "Experimental Validation of Design Expressions for Sub-Reflectarrays," *Proceedings of 14th International Symposium on Antenna Technology and Applied Electromagnetics and the American Electromagnetics Conference (ANTEM-AMREM)*, Ottawa, Ontario, Canada, 2010.

[28] Xu, S., Y. Rahmat-Samii, and W. A. Imberiale, "Subreflectarrays for Reflector Surface Distortion Compensation," *IEEE Transactions on Antennas and Propagation*, Vol. 57, No. 2, February 2009, pp. 364–371.

[29] Cabria, L., et al., "An Active Reflectarray with Beam-Steering Capabilities," *18th Conference on Applied Electromagnetics and Communications*, 2005.

[30] Robinson, A. W., and M. Bialkowski, "An X-Band Active Microstrip Reflectarray," *Proceedings of Asia-Pacific Microwave Conference*, Vol. 3, 1993, pp. 925–928.

[31] Hum, S., and M. Okoniewski, "Realizing an Electronically Tunable Reflectarray Using Varactor Diode-Tuned Elements," *IEEE Microwave and Wireless Components Letters*, Vol. 15, No. 6, June 2005, pp. 422–424.

[32] Chaharmir, M. R., et al., "Novel Mechanically Controlled Reflectarray Antenna for Beam Switching and Beam Shaping in Millimeter Wave Applications," *Electronics Letters*, Vol. 39, No. 7, 2003, pp. 591–592.

[33] Chaharmir, M. R., et al., "Application of Waveguide Technology for the Characterization of Photoconductivity of Poly(9-vinylcarbozole) for Millimeter-Wave Applications," *Proceedings of ANTEM 2005*, Saint-Malo, France, June 2005, pp. 232–233.

CHAPTER 2

Fundamentals of Reflectarray and General Design Guidelines

General design equations of a reflectarray antenna that imitates the operation of a conventional parabolic antenna will be given in Section 2.1. The flexibility of reflectarray antennas has rendered them as suitable candidates in a wide range of applications as will be described in subsequent chapters. Therefore, performance criteria and benchmarks are needed to assess the efficiency of the reflectarray and fulfillment of design specifications. Resemblance between reflectarrays and conventional reflectors justifies tailoring the efficiency figures that are used in evaluation of the latter to gauge the performance of the former. In the meantime, particular attention should be devoted to the modification of the conventional aperture efficiency figures of conventional reflectors to capture unique features of reflectarrays, which is the topic of Section 2.2.

Microstrip patches were widely used as the cell element at the initial stages of printed reflectarray research and development. The patch cell element is highlighted in Section 2.3 to present some general trends in the performance of the cell elements of reflectarrays such as the effect of thickness and permittivity of the substrate material. Similar trends exist for the more complicated cell elements. This should lay the foundation for the discussion of more complicated cell elements that will follow in Chapter 3.

2.1 General Design Equations

Reflectarray antennas are comprised of a quasi-periodic set of cell elements often set in a regular lattice to emulate a given phase front transformation. In its most basic form, the antenna carries out spherical to planar phase front transformation which is akin to the function of its conventional counterpart, namely, the center-fed parabolic reflector. The side view of a reflectarray antenna is shown in Figure 2.1 which is comprised of printed elements on a substrate of thickness h and relative permittivity ε_r. The structure is illuminated by a horn antenna located at the focal point F. Patch dimensions are adjusted to realize an equiphase aperture field distribution that is tantamount to broadside radiation from the reflectarray. To achieve this objective, the patch element located at A (see Figure 2.1) of the reflectarray

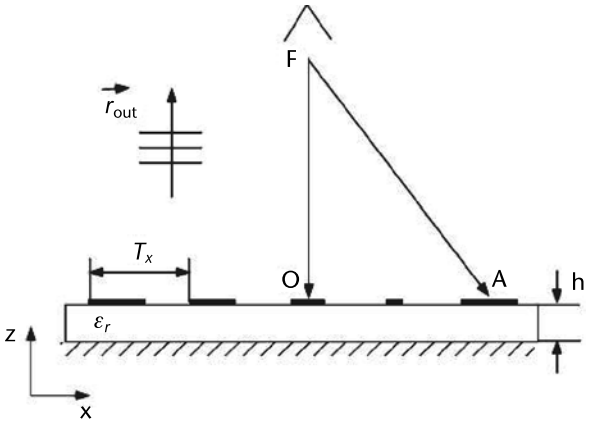

Figure 2.1 Side view of a center-fed reflectarray with broadside beam.

ought to impart the following phase to the incoming spherical field that originates from the focal point:

$$k_0 (FA - FO) - \phi_A = 2n\pi \tag{2.1}$$

where n is an integer, k_0 is the free space wavenumber, and ϕ_A is the scattered phase generated by the patch located at point A. Fulfillment of (2.1) forces a phase difference of $2n\pi$ between any given patch on the reflectarray and the patch located at O, which is the center of reflectarray. The phase generated by the patch is limited between 0° and 360°. Therefore, the integer n is used to keep ϕ_A within this bound. The regions of the reflectarray, where ϕ_A jumps between 0° and 360°, are called transition regions.

The same procedure can be followed to obtain the required phase contribution of each given patch to realize a scanned beam reflectarray shown in Figure 2.2. The direction of the outgoing beam is represented as r_{out}. The following relationship gives the amount of phase to be imparted by the patch located at point A of reflectarray to maintain the scanned beam:

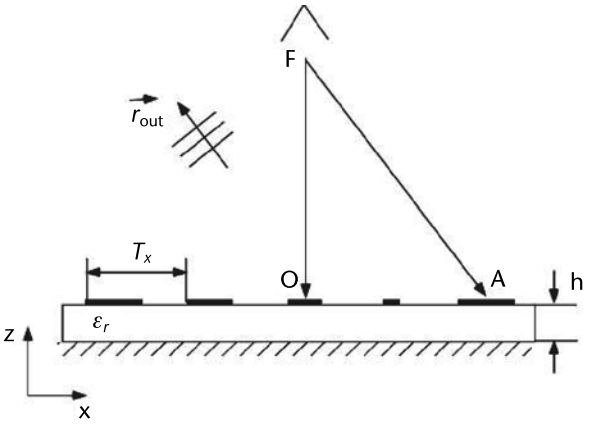

Figure 2.2 Side view of scanned beam center-fed reflectarray

$$k_0\left(FA - F\vec{O}\cdot\hat{r}_{out}\right) - \phi_A = 2n\pi \tag{2.2}$$

Scanned-beam, center-fed reflectarray is a construct that does not have an equivalent in the case of conventional center-fed "parabolic reflector." Offset reflectors have been devised in the past to achieve scanned-beam operation at the expense of less mechanical robustness compared to centre-fed reflectors and higher cross-polarization. This is an illustration of the one of the many flexibilities offered by reflectarrays.

A reflectarray can be used to emulate phase transformations carried out by a shaped reflector. Figure 2.3 shows a known shaped reflector and its equivalent reflectarray. The function of the reflectarray is to realize the same aperture phase distribution as the shaped reflector. To this end, it is attempted to find the required phase shift on the patch located at point *B* by examination of the ray that emanates from the feed phase center *F* and lands on *B* after reflection from point *A* on the shaped reflector. Note that point *B* is at the center of a given cell location on the reflectarray. The required phase to be imparted by the patch to realize the same phase distribution as the shaped reflector on aperture of reflectarray is given as:

$$k_0\left(FA + AB - FB\right) - \phi_{patch} = 2n\pi \tag{2.3}$$

One common factor between these three equations is the presence of free-space wavenumber, k_0, that corresponds to the design frequency of the reflectarray and constrains the desired phase shift to be valid for optimum performance at a given design frequency. Therefore, deviation from the design frequency leads to a different value for the required phase that might not be fulfilled once the element dimensions have been chosen for optimum performance at the design frequency. This leads to loss of gain because of the emergence of phase error on the radiating

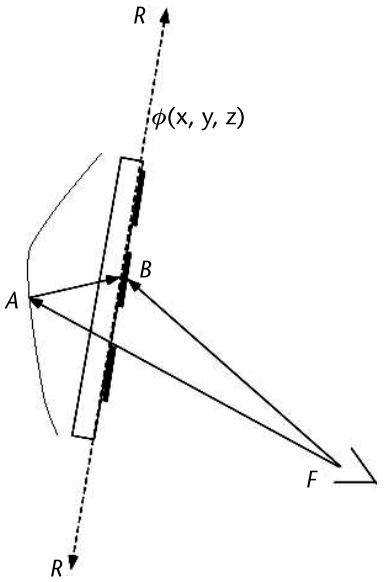

Figure 2.3 Shaped reflector and its equivalent reflectarray counterpart.

aperture of the reflectarray. Techniques will be presented in Chapter 6 to broaden the reflectarray gain bandwidth.

So far, we have restricted ourselves to derivation of the phase value required at each patch and have not discussed methods to realize this phase. Figure 2.4 shows an infinite two-dimensional periodic structure composed of microstrip patches that is illuminated by a normally incident plane wave. A typical plot of the phase of the reflected wave versus the length of the patch is also shown in Figure 2.4. Lattice dimensions along the x-axis and y-axis (T_x and T_y) are selected to be less than free-space half wavelength ($\lambda_0/2$) to prevent the emergence of grating lobes. As will be discussed in more detail in Chapter 5, the propagating reflected wave is composed of direct reflection from the grounded dielectric substrate and patches. The presence of the ground plane does not allow scattering into the lower half-plane, which implies unity amplitude of the reflected wave in upper half plane for lossless dielectric substrate and perfect electric conductor (PEC) patches. However, the phase of the reflected wave can be adjusted by changing the length of the patch. Noting the gradual variation of the desired phase on the surface of the reflectarray, the infinite periodic structure approximation can be used to synthesize the length of the patch based on the desired phase at a given location. In other words, each locality of the reflectarray is assumed to be an infinite two-dimensional periodic structure

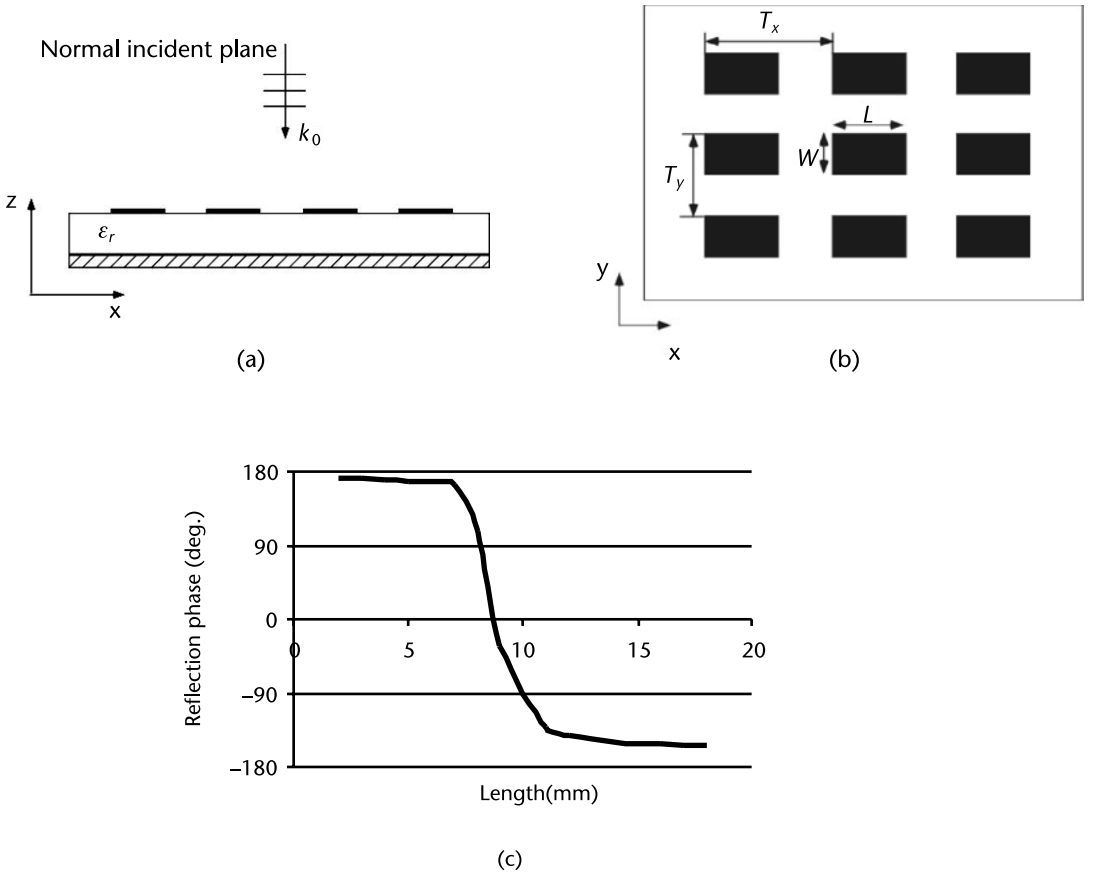

Figure 2.4 Two-dimensional array of square patches: (a) side view, (b) top view, and (c) typical phase-length design curve that is used in the design of a reflectarray.

that is illuminated by a plane wave whose direction of propagation is along the ray that connects the feed and that given locality. Then the phase of the reflected wave is calculated for this infinite periodic structure using numerical methods that will be presented in Chapter 5. Therefore, the required patch phase as outlined in (2.1) to (2.4) can be obtained by changing patch dimensions according the phase-length plot of Figure 2.4(c). The same two-dimensional infinite periodic structure assumption can be used for other types of cell elements. Figure 2.5 shows a number of conventional cell elements that have been used in reflectarray structure and the geometrical feature that is to be adjusted in order to realize the required phase shift.

2.2 Aperture Efficiency of Reflectarray and Comparison with Conventional Parabolic Reflector

Aperture efficiency of a conventional reflector has been decomposed into a number of efficiency figures to isolate the factors that cause deviation from ideal performance [1]. The most common factors that degrade the performance are listed as: feed illumination taper, feed illumination spillover, aperture phase error, cross-polarization effects, feed blockage, dielectric and conductor loss, and feed mismatch. The definitions used in [1] are applied in this section to present a mathematical expression for each of these degrading factors and provide a qualitative comparison of the performance of reflectarrays with conventional parabolic reflector in terms of each of these factors.

2.2.1 Illumination Efficiency

Illumination efficiency is a measure of the uniformity of the feed illumination of the reflectarray. It is well known that as the illumination tapers toward the rim of the reflectarray or reflector, the sidelobe level tends to decrease and the main beam broadens. The mathematical expression for illumination efficiency is given as follows:

$$\eta_t = \frac{1}{\pi a^2} \frac{\left[\int_0^{2\pi}\int_0^{a} \left|E_y(\rho,\phi)\right| \rho d\rho d\phi\right]^2}{\int_0^{2\pi}\int_0^{a} \left|E_y(\rho,\phi)\right|^2 \rho d\rho d\phi} \tag{2.4}$$

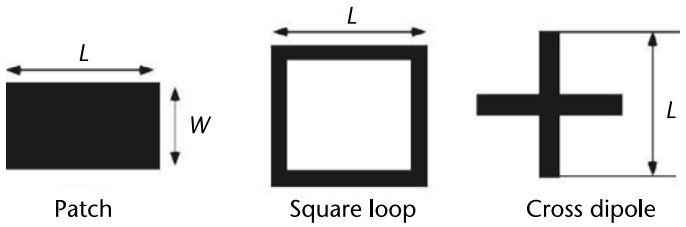

Figure 2.5 Several conventional cell elements that have been used in reflectarray antennas.

where it is assumed that the desired aperture field is *y*-polarized and the aperture is of circular shape with radius *a*. In the case of conventional reflector, the feed illumination taper is solely determined by the feed pattern but in the case of reflectarray, the illumination also depends on the radiation pattern of the constituent elements of the reflectarray. The broadside radiation pattern of the cell element necessarily leads to reduction of intercepted power by the element when it is illuminated by rays from the feed that are away from the broadside direction of that given element. Therefore, the illumination taper of the feed is further accentuated by the element pattern. The element pattern makes an impact for $F/D < 0.5$ when the illumination angle of feed for the edge elements of the reflectarray is increased. This relatively larger taper entails marginally lower illumination efficiency in the case of reflectarray and also lower sidelobe levels.

2.2.2 Spillover Efficiency

This efficiency figure represents the amount of power that is not intercepted by the reflectarray and it is calculated using the following expression:

$$\eta_s = \frac{\int_0^{2\pi}\int_0^{\psi/2} \left|g(\theta,\phi)\right| d\theta\, d\phi}{\int_0^{2\pi}\int_0^{\pi} \left|g(\theta,\phi)\right| d\theta\, d\phi} \tag{2.5}$$

where ψ is the subtended angle of reflectarray or reflector aperture defined in Figure 2.6 and $g(\theta, \phi)$ is the feed radiation pattern. It can be seen that for the same D and F/D ratio, the subtended angle of the parabolic reflector is slightly larger than that of the reflectarray. The difference between the subtended angles of parabolic reflector and its equivalent reflectarray increases as F/D shrinks and puts parabolic reflector at an advantage in terms of spillover efficiency as compared to its reflectarray equivalent.

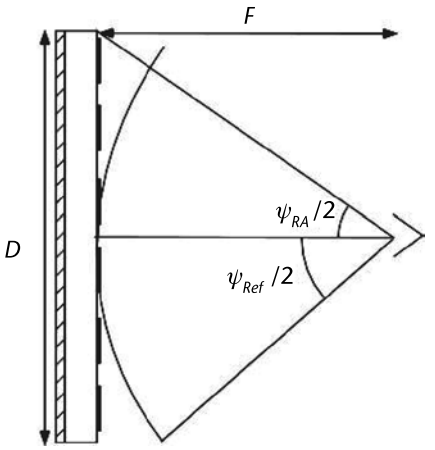

Figure 2.6 Side views of a center-fed parabolic reflector and its equivalent reflectarray. The two structures have the same diameter and F/D ratio.

Assuming that the feed pattern is of $\cos^n(\theta)$ form, one can derive the following expression for spillover efficiency [2]:

$$\eta_s = 1 - \cos^{n+1}\left(\psi_{RA}/2\right) \tag{2.6}$$

where ψ_{RA} is the subtended angle of the reflectarray that is shown in Figure 2.6. A similar expression has been derived for illumination efficiency of the reflectarray illuminated by $\cos^n(\theta)$ feed structure [2]:

$$\eta_t = \frac{2n}{\tan^2\left(\psi_{RA}/2\right)} \frac{\left(1-\cos^{n/2-1}\left(\psi_{RA}/2\right)\right)^2}{\left(\frac{n}{2}-1\right)^2\left(1-\cos^n\left(\psi_{RA}/2\right)\right)} \tag{2.7}$$

The illumination efficiency is the product of spillover and taper efficiencies. The reflectarray illumination efficiency is plotted in Figure 2.7 for different values of n for the feed pattern of $\cos^n(\theta)$. As it is the case for conventional reflector, it can be seen for a given feed pattern, there is an optimum subtended angle for which the illumination efficiency is maximized. This optimum subtended angle can be translated into an optimum *F/D* ratio.

2.2.3 Polarization Efficiency

This efficiency term represents the polarization purity of the antenna radiation and is calculated according to the following relation:

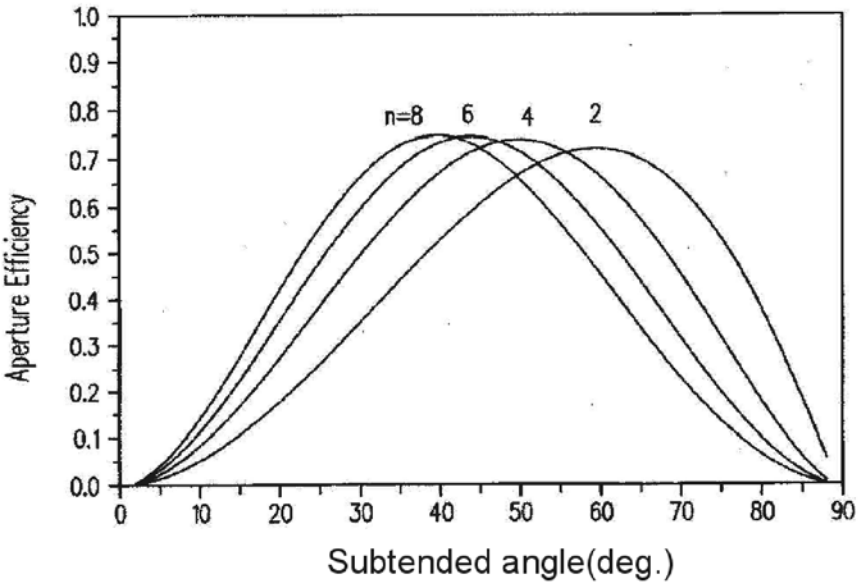

Figure 2.7 Aperture efficiency of the reflectarray for different feed patterns. (© 1997 IEEE. *From:* [3]. Reprinted with permission.)

$$\eta_x = \frac{1}{\pi a^2} \frac{\left[\int_0^{2\pi}\int_0^{a} \left|E_y(\rho,\phi)\rho d\rho d\phi\right|\right]^2}{\int_0^{2\pi}\int_0^{a}\left(\left|E_x(\rho,\phi)\right|^2 + \left|E_y(\rho,\phi)\right|^2\right)\rho d\rho d\phi} \tag{2.8}$$

The above expression is a measure of the power that is coupled into the cross-polarization component of the antenna radiation. Normally, a feed with poor cross-polarization performance leads to low η_x in the case of center-fed parabolic reflector because its surface is indifferent the sense of linear polarization and it collimates both co- and cross-polarization components. However, the elements of a reflectarray can be selected on the basis of low cross-polarization radiation (such as printed dipole), which leads to diffraction and scattering of cross-polarization component of the feed radiation. Hence, one can expect superior cross-polarization performance with a feed of moderate cross-polarization performance in the case of center-fed broadside reflectarray as compared to it conventional reflector counterpart. The same statement holds for the case of offset-fed reflectors that are plagued by relatively high cross-polarization for observation angles off the main beam. The equivalent offset-fed reflectarray can attain better cross-polarization as compared to its equivalent conventional reflector, as a result of the polarization selectivity of its constituent elements.

2.2.4 Phase Efficiency

Deviation from uniform phase on the radiating aperture of the antenna leads to degradation in antenna gain. The measure of phase uniformity is defined as follows:

$$\eta_p = \frac{1}{\pi a^2} \frac{\left|\int_0^{2\pi}\int_0^{a} E_y(\rho,\phi)\rho d\rho d\phi\right|^2}{\int_0^{2\pi}\int_0^{a}\left|E_y(\rho,\phi)\right|^2 \rho d\rho d\phi} \tag{2.9}$$

The uniformity of the aperture field distribution of a reflectarray can be disrupted by three factors. The first stems from using infinite periodic structure assumption at the design stage of the reflectarray. It should be noted that gradual variation of the geometrical features of the constituent elements of reflectarray throughout its aperture is a deviation from infinite periodic structure assumption at the design stage. Therefore, the actual phase that is realized on the reflectarray can be different from the desired phase. Departure from desired phase values is more intense in the transition regions where there is a phase jump from 0 to 2π, which is manifested in abrupt changes of element dimensions in such regions. Noting that the phase transformation is carried out in a quantized fashion, a quantization error might occur for lattice size in excess of $\lambda/2$. However, the quantization error is less than 0.1 dB if the lattice size is in the order of a half-wavelength and reduces rapidly as the lattice size shrinks. Therefore, one can see the importance of maintaining small lattice size in achieving uniform phase because the quantization error

is reduced significantly and also the assumption of infinite periodic structure becomes more relevant. The second source of nonuniform phase is fabrication error. The etching technology that is used for the fabrication of the reflectarray should be capable of exact realization of design dimensions. Any error in fabrication leads to deviation from desired phase. Surface roughness in the case of conventional solid reflectors acts similarly in degrading phase efficiency. It is usually difficult to maintain roughness tolerance for large reflectors that operate in *Ka*- and higher frequency bands, whereas the required fabrication tolerance for reflectarrays in such bands is well within the realm of conventional lithographic techniques. The last factor that can adversely impact the phase uniformity of aperture field distribution is deviation of the radiated phase front of the feed from spherical phase front and also movement of the feed phase centre throughout the operating band of the reflectarray. This issue can either be addressed by careful selection of the feed or dispersion engineering of the elements reflected phase to compensate for the movement of the phase center of the feed.

2.2.5 Blockage Efficiency

The feed assembly blocks the aperture radiation and hence degrades the performance by reducing the gain and also increasing the cross-polarization. Calculation of the following expression gives a measure of the adverse effect of blockage on the antenna performance:

$$\eta_b = \frac{1}{\pi a^2} \frac{\left| \int_0^{2\pi} \int_0^{b} E_y(\rho,\phi)\, \rho d\rho d\phi \right|^2}{\int_0^{2\pi} \int_0^{a} \left| E_y(\rho,\phi) \right|^2 \rho d\rho d\phi} \tag{2.10}$$

where b is the radius of the feed region. Feed blockage is inevitable in the case of centre-fed parabolic reflectors. The larger the feed assembly is, the lower is the blockage efficiency. However, a center-fed reflectarray can be designed to avoid the blockage completely by setting the direction of the outgoing beam appropriately. Implementing this measure, higher blockage efficiency is quite practical in the case of center-fed reflectarrays. Additionally, feed return loss can be significantly improved in the case of center-fed reflectarray by setting the outgoing beam at an off-boresight direction to avoid the feed assembly region.

2.2.6 Dielectric and Conductor Loss

Conductor loss and substrate loss are among the other factors that can reduce the efficiency of the reflectarray. These two loss factors lead to less than unity reflection coefficient for the reflectarray. Methods will be presented in Chapter 7 of this book to mitigate the losses of reflectarray structures etched on lossy substrate. This particular loss factor can be quantified using the following expression:

$$\eta_l = \frac{\sum_{n=1}^{N} \left| \Gamma_n \right|^2}{N} \tag{2.11}$$

where Γ_n is reflection from the nth cell element and summation has been carried out over the total N cells.

Some of these efficiency figures were estimated in [3] for a typical reflectarray structure. Dielectric and conductor losses were underlined in the case discussed for two 6-inch reflectarrays that were designed to operate at 28.0 GHz. One of the reflectarrays was etched on 0.020-inch Duroid material with $\varepsilon_r = 2.2$ of loss tangent 0.0028 and the other was etched on 0.010-inch Taconic TLE substrate of $\varepsilon_r = 2.95$ and loss tangent 0.0074. Both reflectarrays were center-fed with the same feed and the subtended angle was set to 72°. This translated to –7-dB edge taper at the rim of the reflectarray. The reflectarrays were designed to scan the main beam to 25 to mitigate the feed blockage. Figure 2.8 shows a view of the reflectarray. Calculated efficiency figures for these two reflectarrays are tabulated in Table 2.1.

In summary, using figures of merit that are used in the case of conventional reflector to assess its performance and efficiency leads to meaningful measures in the case of reflectarray. However, one should be attentive of the differences of reflectarrays and reflectors when using these criteria to assess the performance of the former.

2.3 Simplest Reflectarray Cell Element: Microstrip Patch

The salient feature of a reflectarray is that it is composed of a quasi-periodic lattice of elements etched on substrate. Therefore, any new insight or technological advancement in the fields of periodic structures and printed microstrip patches can potentially benefit the performance of reflectarrays. Microstrip patch and printed dipole are among the most widely studied radiating printed elements. Therefore,

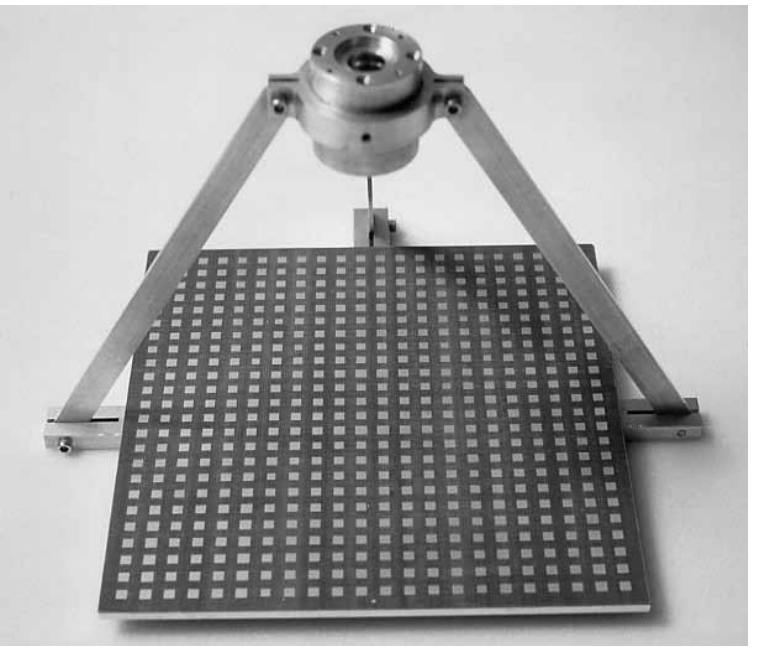

Figure 2.8 Photograph of a 6-inch reflectarray with an operating frequency of 28 GHz. (© 1997 IEEE. *From:* [3]. Reprinted with permission.)

Table 2.1 Loss Budget for the Two Six-Inch Reflectarrays

	0.010" Taconic	*0.020" Duroid*
Maximum Directivity	33.7 dB	34.1 dB
cos θ Loss	–0.4 dB	–0.4 dB
Spillover Loss	–0.7 dB	–0.7 dB
Taper Loss	–0.7 dB	–0.7 dB
Dielectric Loss	–1.8 dB	–0.2 dB
Copper Loss	–0.2 dB	–0.1 dB
Design Phase Error Loss	–1.5 dB	–0.7 dB
Calculated Gain	28.4 dB	31.3 dB
Measured Gain	28.7 dB	31.0 dB
Aperture Efficiency	35%	54%

Source: [3].

their use was prevalent at the early phase of reflectarray research and development [4, 5]. This section is devoted to presentation of microstrip patch as a cell of a reflectarray and description of related trade-offs and trends. It is an overture to a more detailed description of different types of cell elements that will be presented in Chapter 3.

2.3.1 Phase Versus Length Curves

A microstrip patch is a resonant type radiator [6] and the nature of its resonance is a function of its geometrical parameters and also the thickness and permittivity of the supporting substrate. However, frequency selective surfaces (FSS) composed of microstrip patches have been studied extensively in the past [7]. General trends that govern a reflectarray antenna that employs microstrip patch as its cell element can be deduced from the prior knowledge and research on microstrip patch antennas and also FSS structures comprised of such elements.

Referring to Figure 2.4, which depicts side and top views of a two-dimensional lattice of microstrip patches etched on lossless dielectric substrate, it is well known that in the absence of the ground plane, the resulting FSS operates as a reflective structure at resonance that represents series resonance [7]. The effect of the ground plane on a thin substrate can be approximated to the first order as an inductive loading of the series resonance circuit that shifts down the series resonance frequency of FSS while imposing unity reflection throughout the band. The approximate equivalent circuit of the structure is shown in Figure 2.9. Changing the size of the patch shifts the resonant frequency of the FSS without the ground plane. The phase variation of the reflected wave versus the length of the patch is plotted in Figure 2.10 for the FSS with a ground plane. It is seen that the phase shift swings approximately between –160° and 180° and it crosses 0° in between which represents the resonance of the grounded FSS structure. The slope of the phase curve while it crosses 0° is a representative of the bandwidth. The more gradual slope corresponds to the wider bandwidth of the element. A demonstration of this statement will be given in Chapter 3 when microstrip and printed dipole cell elements are discussed in more detail.

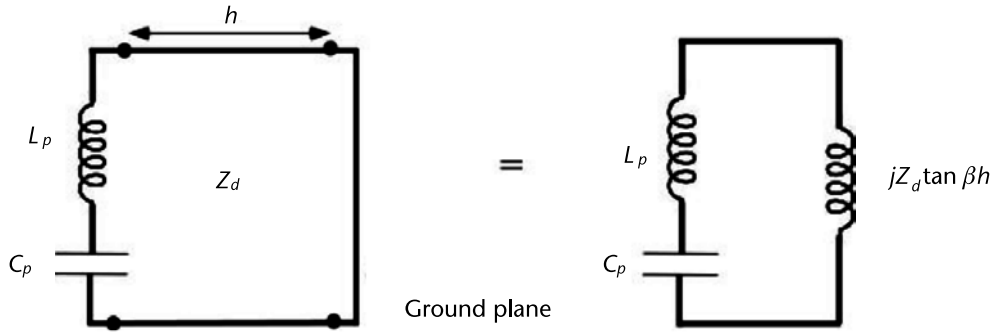

Figure 2.9 Equivalent circuit of two-dimensional lattice patches on ground plane and supported by a substrate of height *h*.

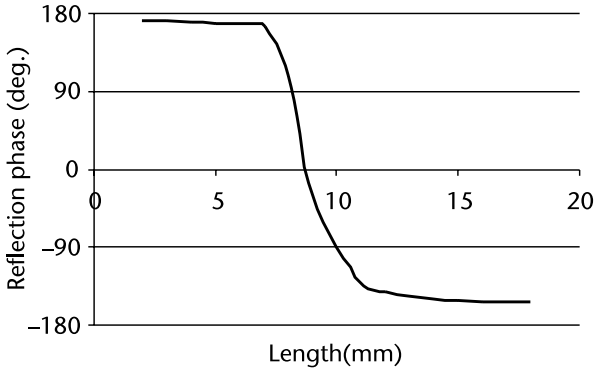

Figure 2.10 Phase-length characteristic for the reflectarray patch cell element at f = 7.5 GHz (see Figure 2.4 for notations): Tx = Ty = 20.0 mm, L = W = 10.0 mm, $\varepsilon_r = 3.0$, and h = 2.0 mm.

Figure 2.11 gives the phasor diagram of scattering from the FSS with ground for a better understanding of the physical phenomenon. It is to be noted scattering is composed of scattering from the grounded substrate and the periodic structure that is etched on the substrate. The scattering from the grounded substrate is unity, whereas scattering from the periodic structure can exceed unity and phasor addition of these two scattering components amounts to unity. In other words, the addition of the two amounts to unity magnitude reflection coefficient and phase ϕ.

2.3.2 General Trends for Phase-Length Characteristics of the Patch

The effects of structural parameters such as dielectric constant of the substrate, substrate height, substrate loss, and angle of incidence of the incoming plane wave on phase-length characteristic of the reflectarray cell element are discussed in this section. These trends are generally valid for other types of cell elements.

Increasing the substrate permittivity generally leads to lower resonant frequency for an FSS structure [8]. This general trend when applied to the case of reflectarray cell element translates into the shift of the phase-length characteristics towards shorter patches as shown in Figure 2.12. It is also quite insightful to draw conclusions from the point of view of the operation of the cell element at the element

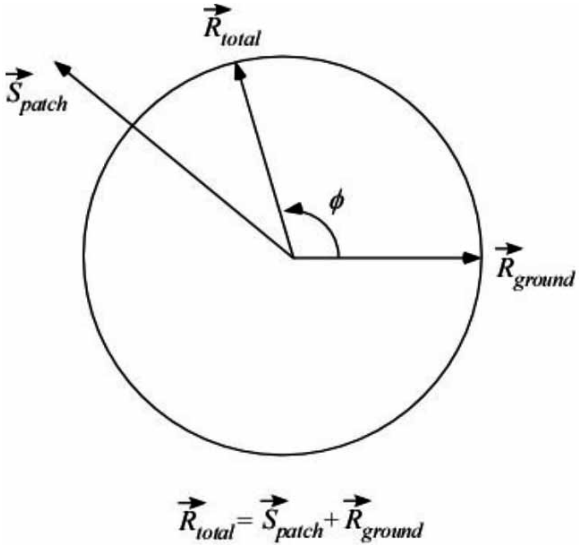

Figure 2.11 Phasor diagram of the constituent components of the reflection from the grounded periodic structure.

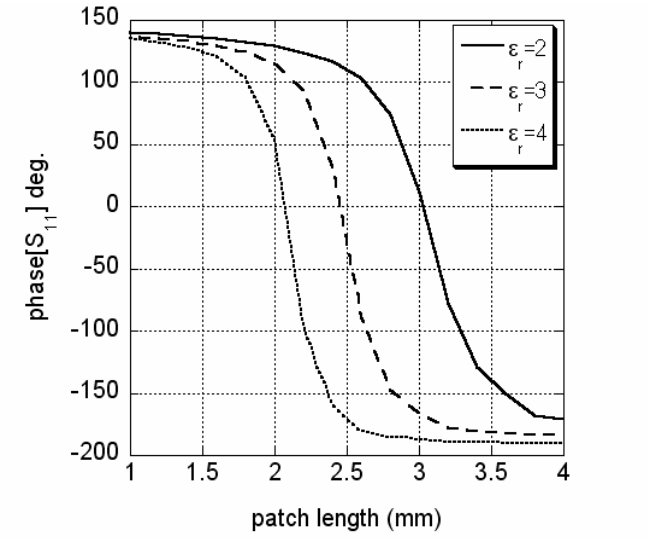

Figure 2.12 Phase-length curve for a periodic structure composed of patches illuminated by normally incident plane wave for different substrate permittivities. The lattice size is Tx = Ty = 5.4 mm, patch width = 3.5 mm, f = 30.0 GHz. (© 2011 John Wiley & Sons. *From:* [9]. Reprinted with permission.)

level, namely, microstrip patch. It is known that increasing the substrate permittivity increases the reactive power which drives up the quality factor Q and reduces the bandwidth of a microstrip patch element [2, 6]. Application of this observation to the case of the patch as the cell element of a reflectarray leads to the conclusion that the phase-length slope increases as the substrate permittivity increases which is actually the trend that is observed in Figure 2.12. Generally, the width of the phase transition region represents the width of the resonance. Therefore, more gradual slope represents a wider transition and also wider element bandwidth.

The effect of the substrate height on the phase-length characteristic of the patch cell element is shown in Figure 2.13, which demonstrates reduction of the realizable phase range as the substrate height is increased. The reduced phase range leads to phase error on the reflectarray because the whole 360° phase range is required to realize the correct phase transformation. Therefore, reduced phase range leads to lower phase efficiency.

Dielectric substrates are inherently lossy and this is another factor in the degradation of the performance of a reflectarray. The electrical current on the element reaches its maximum when the element is resonant for the length that is at the center of phase-length curve. Maximum current flow on the elements leads to maximum loss at resonant conditions. This conclusion can be drawn from Figure 2.14, which shows the return loss as a function for dielectric loss. Having established a relationship between resonance and loss, one can conclude that the more intense the resonance, the higher the loss. Therefore, any factor that enhances the resonance such as: decreasing patch width, decreasing substrate height, and increasing substrate permittivity can lead to narrower, more intense resonance and thus higher loss. The impact of thickness of the lossy substrate on the return loss performance is also shown in Figure 2.14. It is to be noted that ΔL represents deviation from resonant length and the peak of the loss occurs when this deviation vanishes. The above statements hold for moderate amounts of loss in dielectric substrates and some of the above trends might reverse for excessive loss as pointed out in [10]. Methods to mitigate the impact of lossy substrates on reflectarray performance will be studied in detail in Chapter 7.

As will be discussed in Chapter 5, the analysis of the reflectarray is based on the assumption that it is locally periodic or quasiperiodic. In other words, each region of the reflectarray is assumed to be an infinite periodic structure that is illuminated by a plane wave propagating along the line that connects the feed to the center

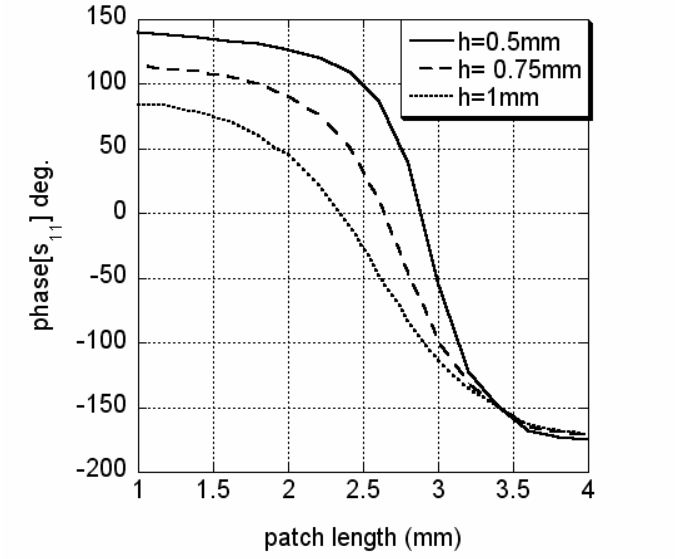

Figure 2.13 Phase-length curve for a periodic structure composed of patches illuminated by normally incident plane wave for different substrate heights. The lattice size is Tx = Ty = 5.4 mm, patch width = 3.5 mm, ε_r = 2.2, and f = 30.0 GHz. (© 2011 John Wiley & Sons. *From:* [9]. Reprinted with permission.)

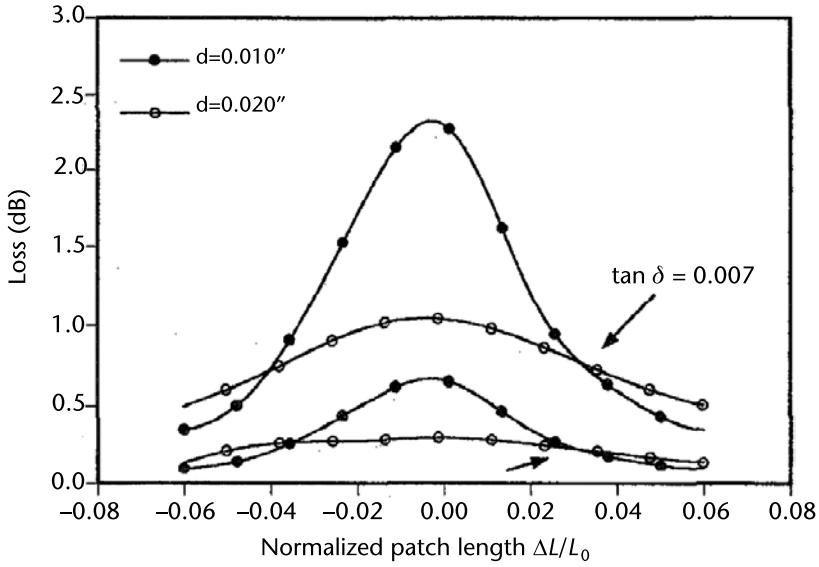

Figure 2.14 Return loss for an array of microstrip patches versus patch size: Tx = Ty = 0.536 cm, L = W = 0.296 cm, $\varepsilon_r = 2.95$, h = 0.20 inch, and f = 28.0 GHz. (© 1997 IEEE. *From:* [3]. Reprinted with permission.)

of that same region with same polarization as the feed. For a center-fed reflectarray that is shown in Figure 2.6, it is evident that as the subtended angle decreases (smaller *F/D* ratio), the incident angle of the plane wave for the peripheral regions of reflectarray deviates further from normal incidence. Therefore, it is important to account for the angular sensitivity of the phase response of the element for reflectarray with small *F/D* ratio (typically $F/D < 0.5$). Angular sensitivity of a typical patch cell element is shown in Figure 2.15, which shows a noticeable deviation from normal incidence as the angle of incidence exceeds $\theta_0 = 20°$.

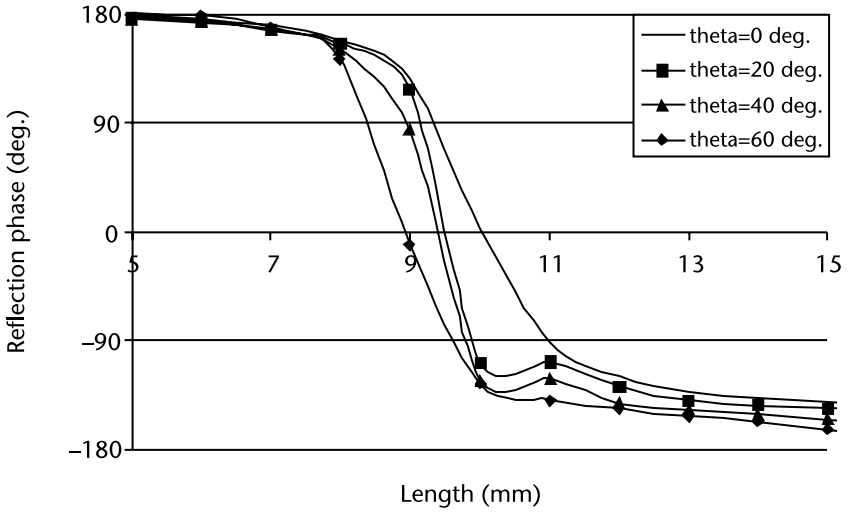

Figure 2.15 Reflection phase of the reflectarray cell element by plane wave of different angles of incidence and polarized parallel to the length of the element. Design parameters are as follows: Tx = Ty = 20.0 mm, W = 10.0 mm, $\varepsilon_r = 3.0$, h = 2.0 mm, and f = 7.5 GHz.

References

[1] Collin, R. E., *Antennas and Radiowave Propagation*, New York: McGraw-Hill, 1985.

[2] Balanis, C., *Antenna Theory: Analysis and Design*, New York: John Wiley & Sons, 1997.

[3] Pozar, D. M., S. D. Targonski, and H. D. Syrigos, "Design of Millimetre Waves Microstrip Reflectarrays," *IEEE Transactions on Antennas and Propagation*, Vol. 45, No. 2, 1997, pp. 287–296.

[4] Gonzalez, D. G., G. E. Pollon, and J. F. Walker, "Microwave Phasing Structures for Electromagnetically Emulating Reflective Surfaces and Focusing Elements of Selected Geometry," U.S. Patent 4905014, 1990.

[5] Javor, R. D., X. Wu, and K. Chang, "Design and Performance of a Microstrip Reflectarray Antenna," *IEEE Transactions on Antennas and Propagation*, Vol. 43, No. 9, September 1995, pp. 932–939.

[6] James, J. R., and P. S. Hall, *Handbook of Microstrip Antennas*, London, U.K.: Peter Peregrinus, 1989.

[7] Shaker, J., and L. Shafai, "Reflection Properties of Conducting Rectangular Elements Printed on a Dielectric Slab," *Canadian Journal of Physics*, Vol. 72, 1994, pp. 299–310.

[8] Munk, B., *Frequency Selective Surfaces: Theory and Design*, New York: John Wiley & Sons, 2000.

[9] Guta, D., and Y. M. M. Antar, (eds.), *Microstrip and Printed Antennas: New Trends, Techniques, and Applications*, New York: John Wiley & Sons, 2011.

[10] Rajagopalan, H., and Y. Rahmat-Samii, "On Reflection Characteristics of a Reflectarray Element with Low-Loss and High-Loss Substrates," *IEEE Antennas and Propagation Magazine*, Vol. 52, No. 4, August 2010, pp. 73–89.

CHAPTER 3

Different Types of Cell Elements for Reflectarrays

As noted previously, a reflectarray is a quasi-periodic assembly of elements that operates in an array environment to achieve a given phase transformation. These elements can be printed elements or volumetric types such as patches [1, 2] or dielectric resonators [3], respectively. The advantage of printed elements is their simplicity in terms of fabrication process. However, the quasi-periodic nature of a reflectarray establishes its similarity to a frequency selective surface (FSS). Therefore, advancements in the fields of FSSs and printed antenna elements can directly benefit reflectarray technology. A large class of reflectarray cell elements has been inspired by earlier developments in these two fields.

Different types of cell elements have been devised to respond to different sets of requirements in the fabrication and operation of a reflectarray, such as mechanical robustness, fabrication accuracy, bandwidth, polarization, and so on. The mechanism through which a periodic arrangement of cell elements imparts phase onto an incident plane wave has been adopted in this chapter as a means of systematic investigation and study of reflectarray cell elements. Different types of resonant cell elements will be addressed. Subsequently, elements that use loading effect as a means of shifting the phase of plane wave excitation will be presented. Emerging subwavelength cell elements are also included.

3.1 Resonant Cell Elements

An FSS structure composed of patches was briefly studied in Section 2.3 and it was pointed out that by covering the back of the FSS with PEC, its series resonance can be used to impart a phase shift of nearly 360° to an incoming plane wave. Printed patches are one of the many types of resonant radiators that can be used to realize reflectarrays. Among these are stacked patches, different types of loop elements (square loop, cross loop, multiloop), and different combinations of slot and patch that will be presented in this chapter.

3.1.1 Patch Element

The magnitude of the reflection coefficient of FSS without ground plane and the reflection phase of the same structure in the presence of the ground plane at the back of the substrate are shown in Figure 3.1. Both structures are illuminated by normally incident plane wave and it is obvious that the magnitude of the reflection for the FSS with ground plane is unity (assuming lossless materials). It is interesting to note that the phase of the FSS with ground plane goes through a 360° cycle and the reflection coefficient of the FSS without ground plane goes through series resonance. Using this simple physical observation, it is sufficient to judiciously adjust the size of the cell element and the height of dielectric substrate to impart a given phase shift to the reflection from the reflectarray cell element. The effect of the ground plane can be captured by a parallel inductive element that lowers that resonant frequency of the FSS. Figure 3.2 shows the phase versus length plot for the reflectarray cell element (FSS with ground plane in the back) at $f = 7.5$ GHz. The slope of the phase-length plot corresponds to the bandwidth of the FSS without ground plane, as will be shown in Chapter 6.

The same line of reasoning can be followed to make further conclusions about the trends that govern phase-length characteristics of the reflectarray cell element from the knowledge of its FSS counterpart. For instance, it is well known [4] that the bandwidth of FSS composed of printed patches is reduced as the patch width is reduced, which is shown in Figure 3.3. The phase response of the reflectarray cell element, which is actually FSS with PEC backing, is shown in Figure 3.4 for different widths of the cell element. The phase response of the structure for different widths is the same throughout the band apart from the frequency band within the dotted enclosure, which is labeled as the resonant region. It is evident that,

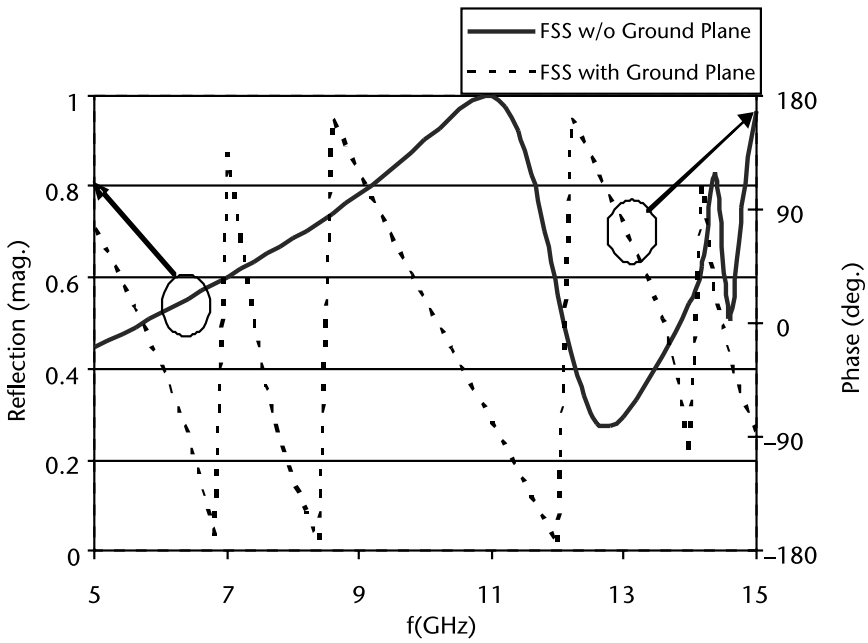

Figure 3.1 FSS structure with and without ground plane illuminated by normal incidence plane wave. Design parameters of the two periodic structures are as follows (see Figure 2.4 for notations): $Tx = Ty = 20.0$ mm, $L = W = 10.0$ mm, $\varepsilon_r = 3.0$, and $h = 2.0$ mm.

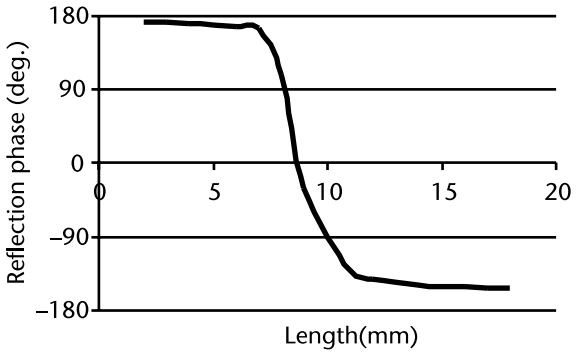

Figure 3.2 Phase-length characteristic for the reflectarray patch cell element at f = 7.5 GHz (see Figure 2.4 for notations): $Tx = Ty = 20.0$ mm, $L = W = 10.0$ mm, $\varepsilon_r = 3.0$, and $h = 2.0$ mm.

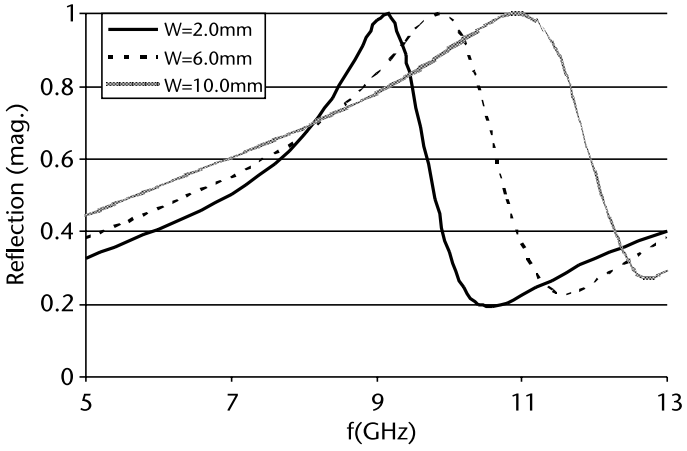

Figure 3.3 Reflection from FSS structures without ground plane illuminated by normal incidence plane wave polarized parallel to the length of the element for different widths of the cell element. Design parameters of the structure are as follows (see Figure 2.4 for notations): $Tx = Ty = 20.0$ mm, $L = 10.0$ mm, $\varepsilon_r = 3.0$, and $h = 2.0$ mm.

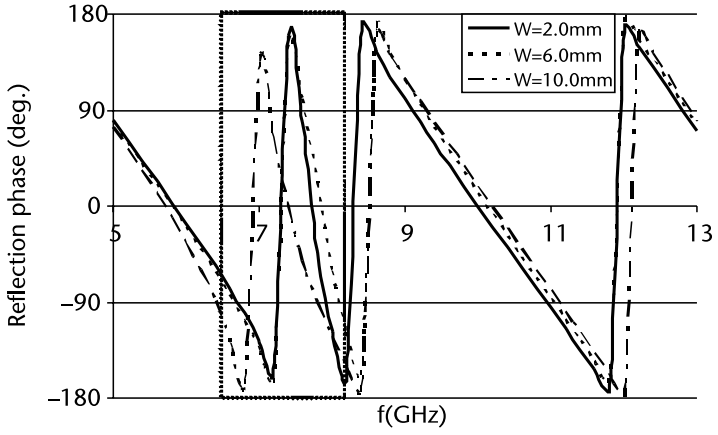

Figure 3.4 Reflection phase response of FSS structures with ground plane illuminated by normal incidence plane wave polarized parallel to the length of the element for different widths of the cell element. Design parameters of the structure are as follows (see Figure 2.4 for notations): $Tx = Ty = 20.0$ mm, $L = 10.0$ mm, $\varepsilon_r = 3.0$, and $h = 2.0$m. The region shown by the dotted rectangle corresponds to the resonance band of the structure.

within this resonant band, the periodic structure contributes significantly to the phase response and the slope of phase-frequency plot is increased as the width of the element is decreased, which is an indication of the reduced bandwidth of the cell element.

Having obtained the phase response of a given patch element across the frequency band, it is anticipated that variation of the patch length while the operating frequency is held constant leads to a variation of the phase of reflection from the periodic structure because changing the patch length changes its resonant condition. Typical phase-length characteristics for microstrip patch as reflectarray cell element are shown in Figure 3.5 for different widths of the patch element. Again, it is observed that shrinking the patch width leads to a steeper slope for the phase-length plot, which is an indication of narrower element bandwidth.

The reduction of the patch width leads to a steeper phase characteristic, which implies increased tolerance in terms of fabrication efficiency. Fabrication error is amplified by the high slope of the phase-length curve. Printed dipoles are generally narrowband, which is synonymous to a steeper phase curve. However, such elements are highly selective of the polarization of the incoming wave. To improve their operating bandwidth while preserving their polarization selectivity, dipole elements can be set into the Gangbuster configuration that has already been widely used in the context of FSS [5]. Figure 3.6 shows a Gangbuster structure along with its phase-length curve [6]. It is anticipated that the bandwidth of the element can be further enhanced by increasing the order of the Gangbuster structure.

3.1.2 Multiresonant Patch Cell Elements

Stacking two patches that are of slightly different sizes is a known technique to broaden the bandwidth of microstrip patch antenna [7]. However, it should be noted that structure is more complex in terms of fabrication as compared to a single-layer microstrip patch. Wider bandwidth is the result of coupled resonance of two patches with isolated resonances in close proximity of each other. Figure 3.7 shows a two-layer reflectarray that employs stacked patch as its cell element [8, 9]. This particular cell element has clearly been inspired by the development

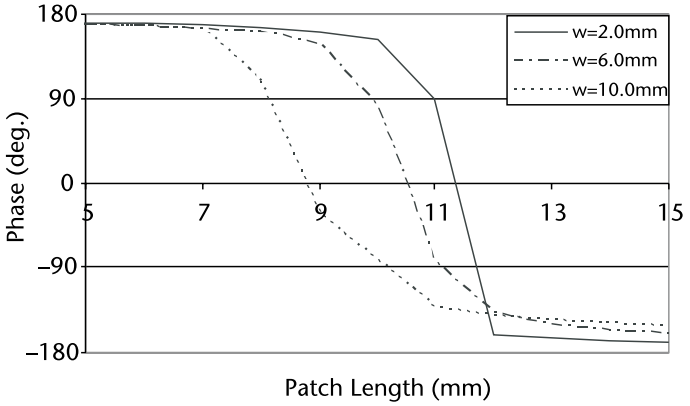

Figure 3.5 Reflection phase of the reflectarray cell element with different widths when illuminated by normally incident plane wave polarized parallel to the length of the element. Design parameters are as follows: $Tx = Ty = 20.0$ mm, $L = 10.0$ mm, ε_r=3.0, $h = 2.0$ mm, and $f = 7.5$ GHz.

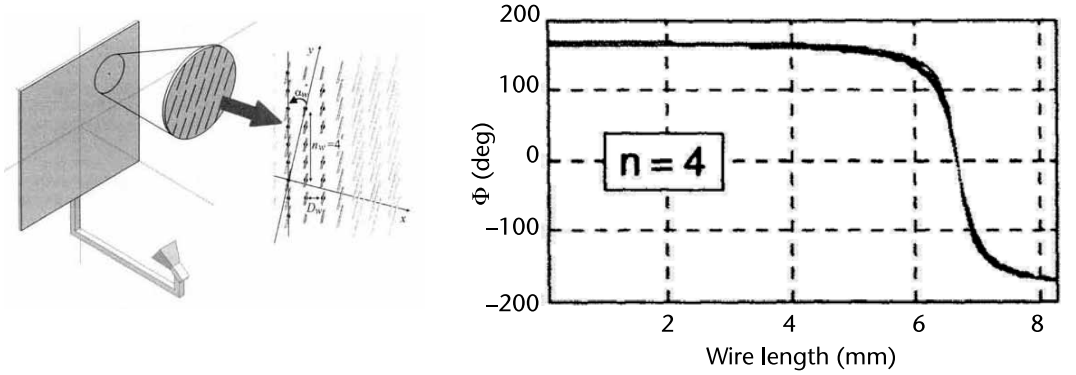

Figure 3.6 Reflectarray composed of Gangbuster cell elements along with the phase-length curve of the cell element. (© 2005 IEEE. *From:* [6].)

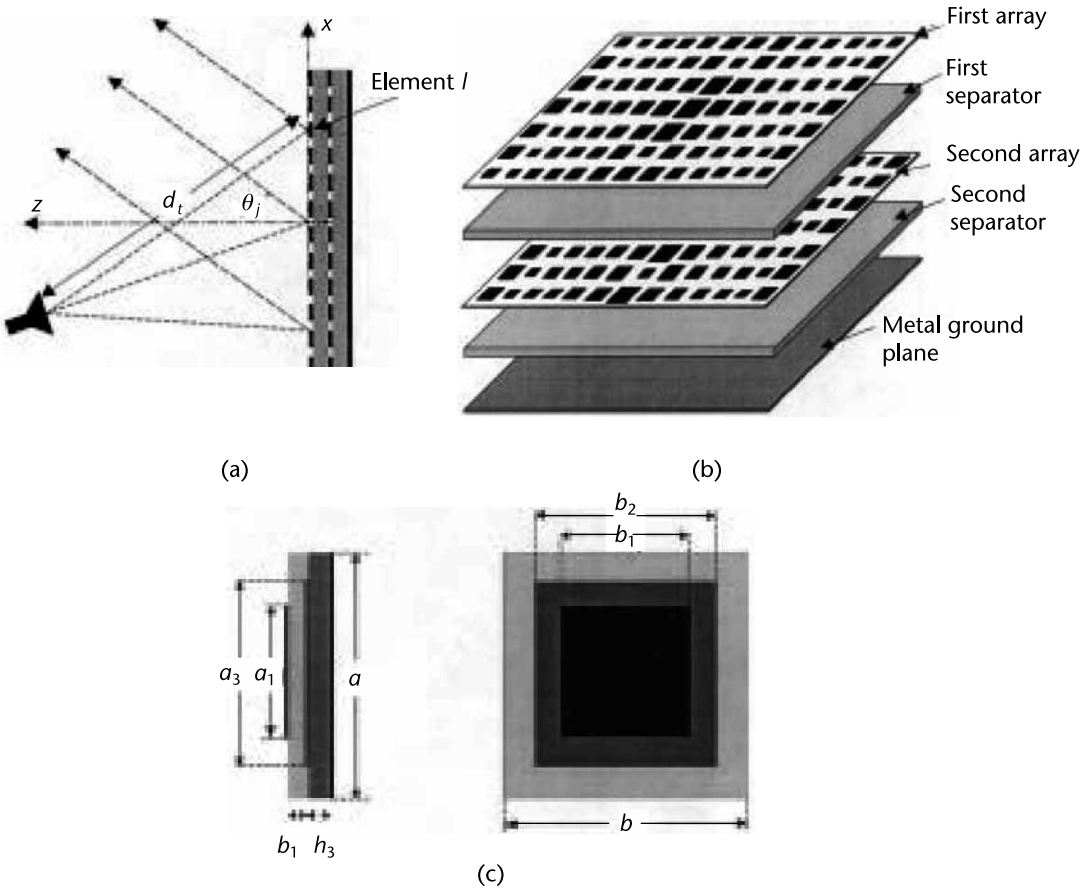

Figure 3.7 Two-layer reflectarray using patches of variable size: (a) reflectarray illuminated by a feed, (b) multilayer structure, and (c) periodic cell. (© 2001 IEEE. *From:* [8].)

of wideband microstrip radiators and attempts to exploit this same feature of the isolated radiator to broaden the operating band of the reflectarray. The variation of the size of the cell element was used to achieve the required phase shift for reflected wave from the reflectarray as shown in Figure 3.8. The phase characteristic of the

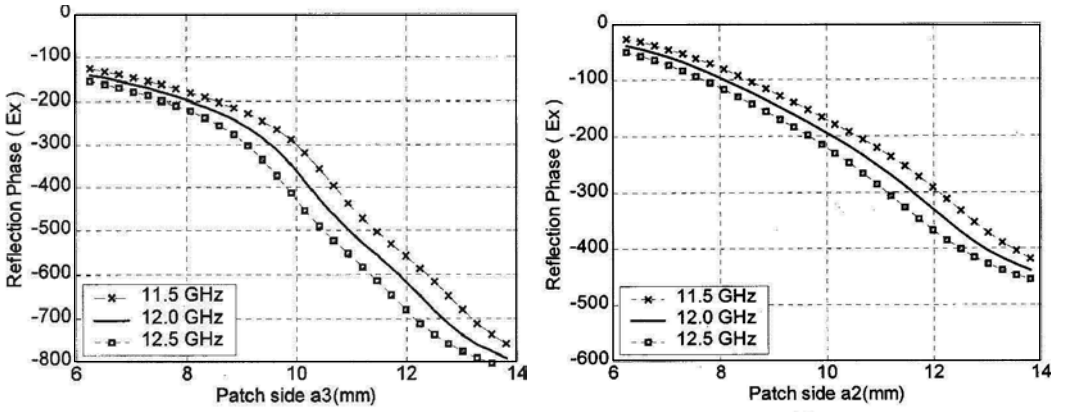

Figure 3.8 Phase and reflection coefficient at normal incidence for a multilayer periodic structure defined in Figure 3.7(c) for two-layer versus patch side of the array closer to the ground plane ($a_1 = b_1$, $a_2 = b_2$, $a = b = 14$ mm, $\varepsilon_r = 1.05$): (a) two-layer arrays ($a_1 = 0.7a_2$) and (b) three-layer arrays ($a_1 = 0.7a_2$, $a_2 = 0.9a_3$). (© 2001 IEEE. *From:* [8].)

three-layer cell element is also shown in the same figure. It is to be noted that the size of patch elements of a given cell were varied simultaneously and the relative size of the patches on the layers (whether a two- or three-layer cell element) was held constant. As will be seen in the case of multiresonant loop elements, this is only one of the strategies in the toolbox of the designer to achieve a wideband cell element. For instance, instead of selecting relative size of the patches as constant, one can enforce the actual difference between the patch sizes ($a_1 - a_2$) to be a constant parameter of design. It is evident from Figure 3.8 that coupled resonance of the stacked patch cell element has resulted in a smoother and also more gradual phase-length characteristic. Changing the ratio of the stacked patch elements results in the variation of the slope of phase-length characteristics, which will be discussed in Chapter 6, and has been used to mitigate frequency dispersion to realize wideband large reflectarray structures.

Multiresonance behavior can also be obtained by embedding a secondary resonant element such as a slot or multiplicity of slots within the patch radiator [10]. This same technique has been used in the context of reflectarray cell element to broaden the element bandwidth and at the same time use the freedom of controlling the resonant frequencies to mitigate frequency dispersion [11, 12]. One possibility for embedding the slot(s) within the patch is shown in Figure 3.9.

It should be noted that the first resonance of the patch (slot) is capacitive (inductive), which dictates the substrate thickness accordingly to cancel the reactive part of the impedance and obtain resonance. Therefore, one of the two resonators becomes active depending on the height of the substrate. Phase-slot length characteristics for different heights of the substrate are shown in Figure 3.10 which confirms patch only resonance for inductive PEC backed substrate [$h = 1.0$ mm of Figure 3.10(a)] and slot only resonance for capacitive backed substrate [$h = 7.0$ mm of Figure 3.10(c)]. However, both patch and slot are resonant for a substrate thickness between these two extremes [$h = 3.175$ mm of Figure 3.10(b)], which leads to a more gradual phase-slot length characteristic. The full 360° phase span can be obtained by using the patch size as a parameter.

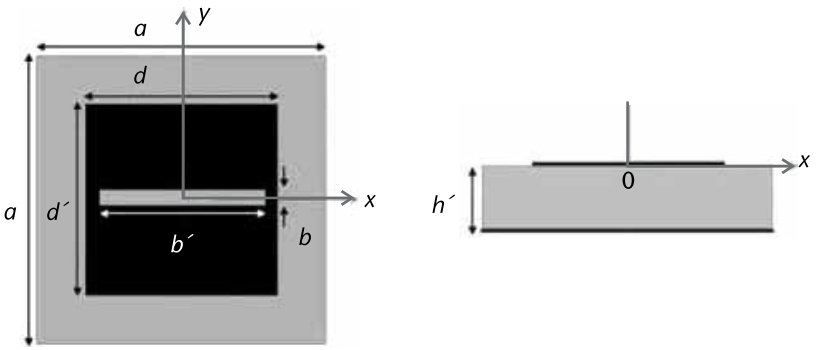

Figure 3.9 Structure geometries for a simple patch structure loaded with a slot a= 16.8 mm with central frequency of 12.5 GHz. (© 2005 John Wiley & Sons. *From:* [11].)

3.2 Loop Elements

It is well understood in the FSS research that cell element should be as small as possible to avoid excitation of higher-order modes and also achieve broadband response and stable performance as the incident angle of the incoming plane varies [5]. Loop element meets this requirement in the sense that for the same size of the loop and microstrip patch, the resonant frequency of the loop is lower. Resonance of the loop is dictated by the size of its periphery, whereas resonant dimension of the patch is its length, hence follows the possibility of a denser lattice for an FSS comprised of loop. The small resonant size of the element serves the twofold objective of the exclusion of the higher-order modes and enhancement of the validity of the commonly used infinite periodic structure approximation that is used in the design of a reflectarray. A smaller reflectarray cell element is also superior in capturing sharp and abrupt phase reversals on the reflectarray, as will be pointed out later.

To demonstrate the trends that govern the phase-length behavior of loop structures, a comparison has been made in Figure 3.11 between phase characteristics of infinite periodic structures composed of single-loop cell and double-loop cell elements, respectively. As can be seen, the presence of two loops leads to two resonances which are represented as two transition regions in the phase-length characteristics of this particular element. The presence of two transition regions increases the attainable phase range as compared to the single ring case. The higher slope of the phase-length curve in the second transition region of the two-loop cell element points to the simultaneous resonance of both loops for this range of element dimensions. It is demonstrated in Figure 3.12 that the attainable phase range can be increased for a double-ring cell element in comparison to a solid patch. Another parameter that can be utilized to adjust phase versus length slope is the spacing between the two rings, as shown in Figure 3.11.

The cross-loop cell element shown in Figure 3.13 is a variation of the loop cell element that has been the subject of intense study for broadband reflectarray operation [14, 15]. Phase versus outer dimension of the cross loop structure is shown in Figure 3.14, which confirms the possibility of achieving a very smooth phase characteristic by adjusting the separation between the two loops.

Embedding additional loops within a larger loop gives rise to a higher number of resonances and transition regions. Figure 3.15 presents a comparison between

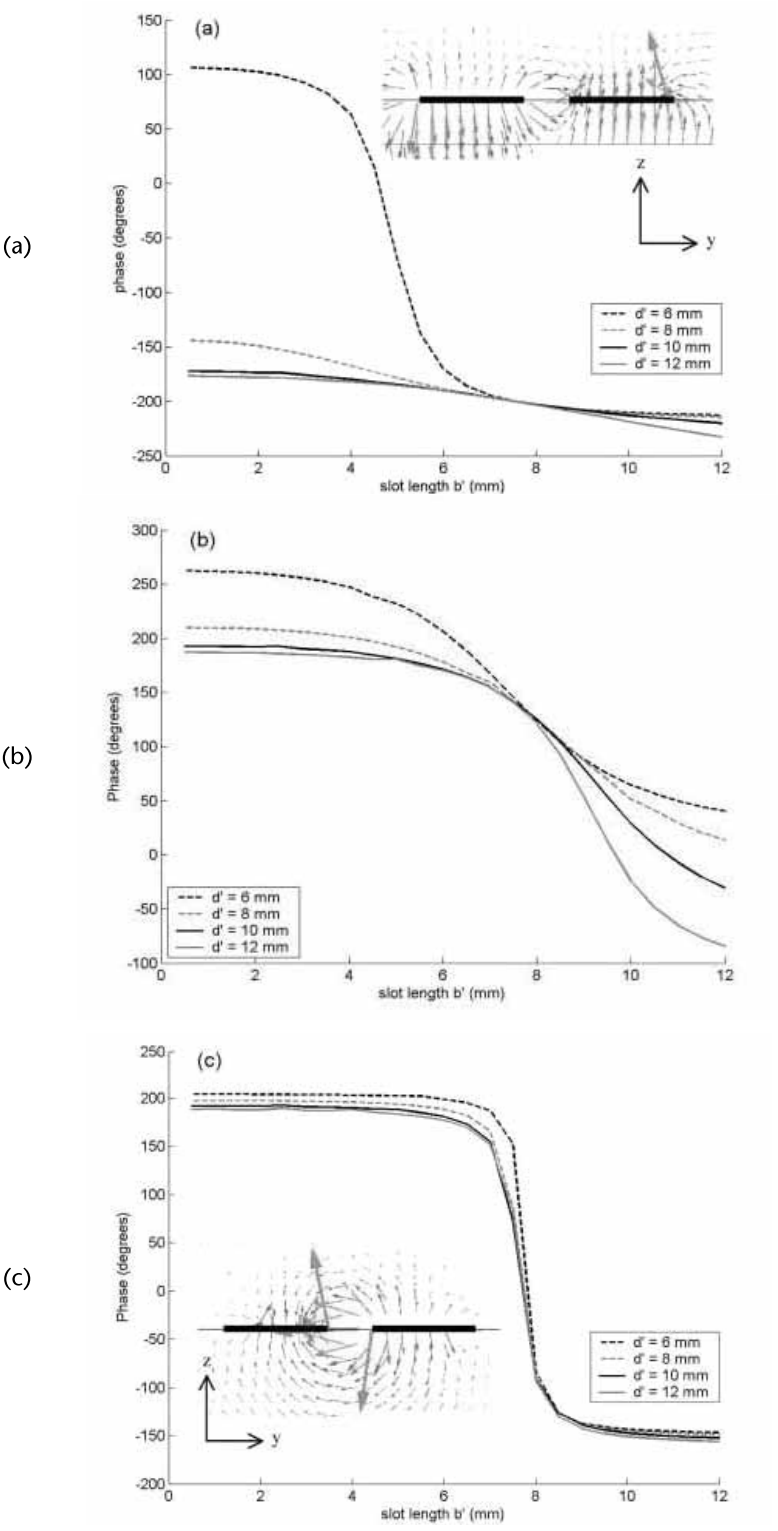

Figure 3.10 Phase variations versus slot length and electrical-field vector cartography (z–y plane) for different patch widths (d''): (a) $h = 1$ mm, thin substrate: patch mode; (b) $h = 3.175$ mm, intermediate substrate: hybrid mode; and (c) $h = 7$ mm, thick substrate: slot mode. (© 2005 John Wiley & Sons. *From:* [11].)

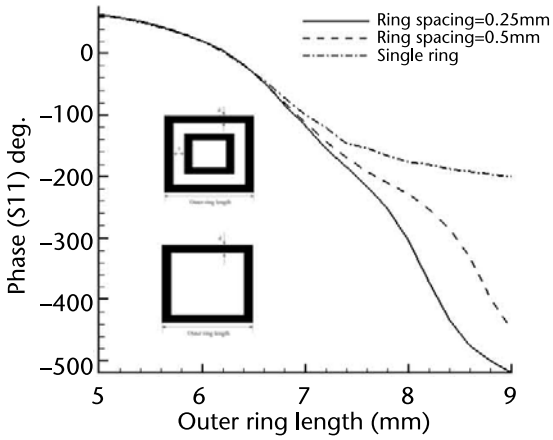

Figure 3.11 Phase-length plots for single and double square loops: $Tx = Ty = 12.0$ mm, $d = 0.5$ mm, substrate permittivity = 2.17, substrate thickness = 0.125 inch, and $f = 12.5$ GHz. (© 2009 IEEE. *From:* [13].)

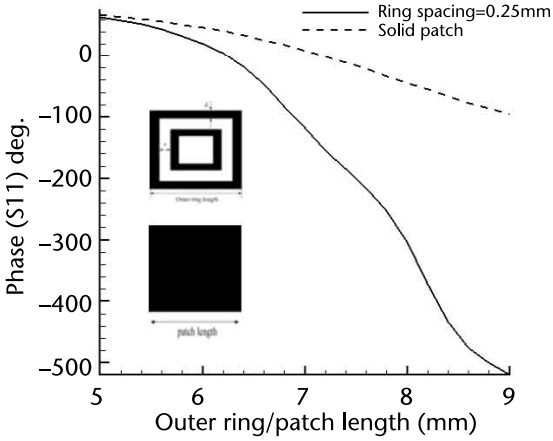

Figure 3.12 Phase-length plots for double square loop and solid square patch: $Tx = Ty = 12.0$ mm, $d = 0.25$ mm, substrate permittivity = 2.17, substrate thickness = 0.125 inch, and $f = 12.5$ GHz. (© 2009 IEEE. *From:* [13].)

phase length of multiloop structures to demonstrate clearly one single resonance for each additional loop. It is important to note that simultaneous resonance of the loops is translated into a higher slope of the phase-length characteristics in such regions. A given phase-length characteristic can be tailored by adjusting the coupling between the loops through judicious selection of separation between them. A combination of different types of loop elements along with adjustment of separation between them was used to attain significantly smoother phase-length characteristics as shown in Figure 3.16. A medium-size prototype reflectarray that was designed using this element attained a 1-dB gain bandwidth of 24% and 60% aperture efficiency [16].

At the border of two neighboring Fresnel zones of a reflectarray, the required phase shift switches from 0° to 360°. This abrupt change of phase gives rise to similar change in the size of the elements that are located in that neighborhood as shown in Figure 3.17. The calculated phase from the Floquet analysis is no longer valid in these regions because the infinite periodicity assumption has been violated.

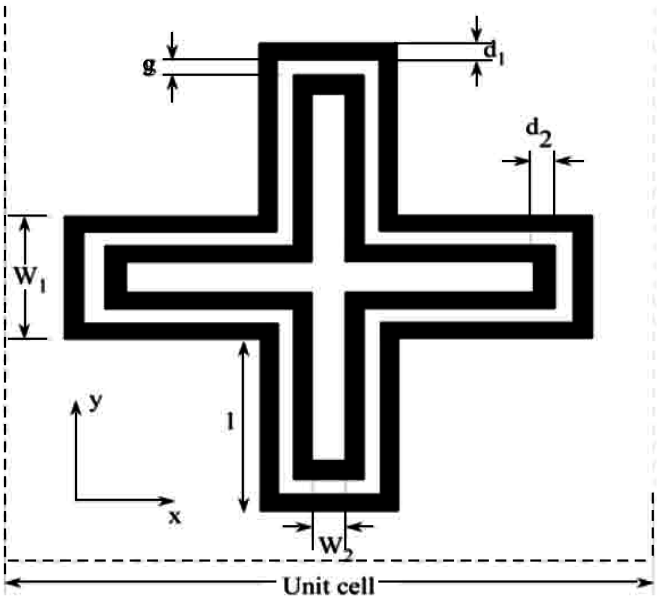

Figure 3.13 Double cross loop cell element: unit cell= 12 mm, $W_1 = 3.4$ mm, $W_2 = 0.4$ mm, $d_1 = d_2 = 0.5$ mm. (© 2009 IEEE. *From:* [13].)

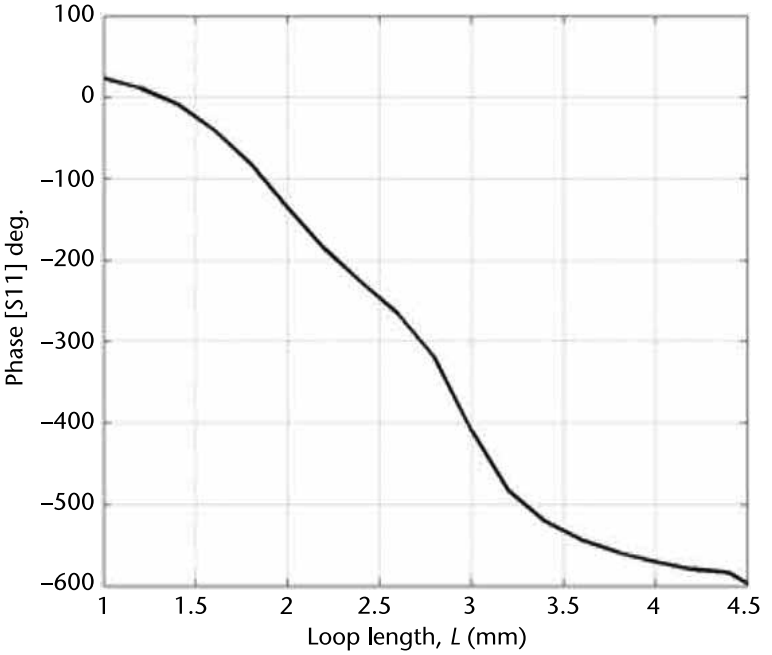

Figure 3.14 Simulated phase versus the length of cross loop arm, $\varepsilon_r = 2.17$, $h = 0.125$ inch, cell size = 12 mm, $W_1 = 3.4$ mm, $W_2 = 0.4$ mm, $d_1 = d_2 = g = 0.5$ mm, and $f = 12.5$ GHz. (© 2009 IEEE. *From:* [13].)

Therefore, special types of elements such as the one shown in Figure 3.18 have been devised to overcome abrupt change of the geometry while maintaining the phase jump [18]. As can be seen, there is a high similarity between the first and

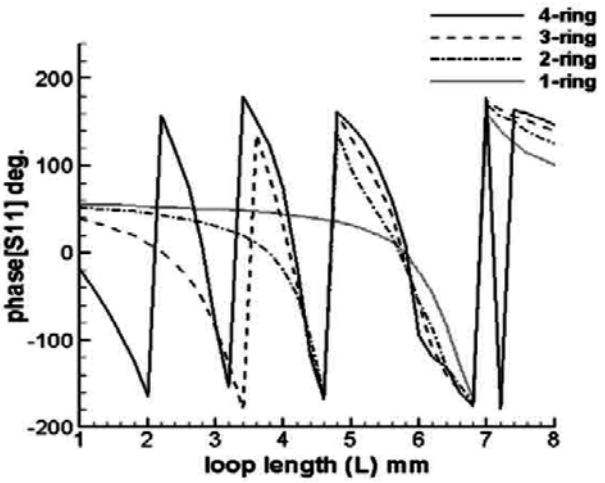

Figure 3.15 Phase-loop size characteristics for cell elements composed of one, two, and three cross loops. (© 2009 IEEE. *From:* [13].)

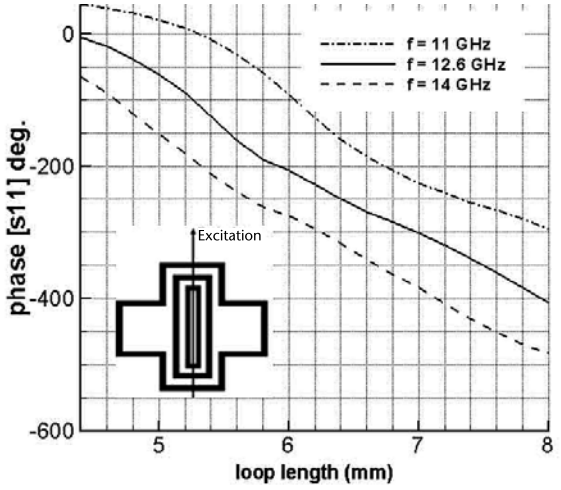

Figure 3.16 Phase-loop size characteristics for cell elements composed one cross loop and two rectangular loops. (© 2009 IEEE. *From:* [13].)

last elements of phoenix cycle which represent 0° and 360° phase shifts. As will be presented later in this chapter, the same objective can be achieved by synthesizing subwavelength elements to optimize similarity between adjacent elements located at border to two Fresnel zones.

3.3 Phase Shift by Loading Resonant Elements

The resonant condition of a system can be altered by loading the system with reactive elements. This has been the guiding principle of the early reflectarray [19]. A cell element of this type is shown in Figure 3.19, which is composed of a resonant

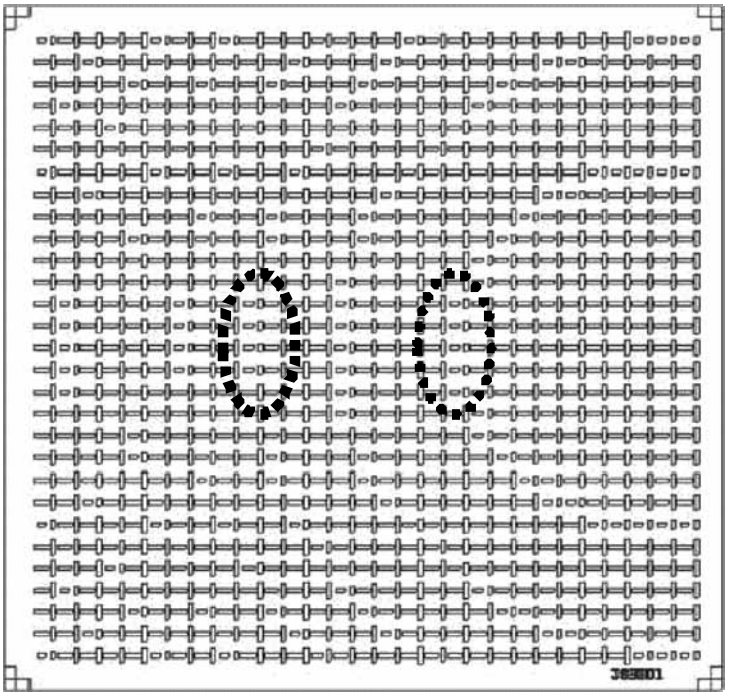

Figure 3.17 Typical reflectarray with dual polarization. Two phase jump regions have been marked to reside inside dotted ellipses superimposed. (© 1999 IEEE. *From:* [17].)

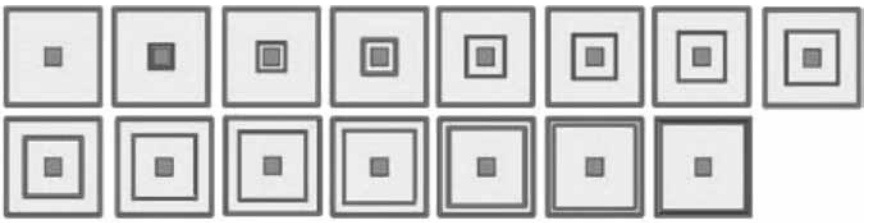

Figure 3.18 A cycle of phoenix element to realize gradual variation of the cell element to attain gradual phase variation. The similarity of the first and last elements that respectively represent 0° and 360° phase variations is noteworthy. (© 2011 IEEE. *From:* [18].)

patch that is loaded by a microstrip line. The incoming plane wave is intercepted by the patch coupled into the line, reflected back from the open circuit, and reradiated by the patch. The phase of the reflected wave is determined by the length of the microstrip line. Different variations of this element type have been reported in the literature. For instance, in a measure to improve cross-polarization performance of the reflectarray, mirror symmetry can be enforced on delay lines as shown in Figure 3.20.

Another loading mechanism is shown in Figure 3.21, which consists of a resonant microstrip patch loaded with a slot in the ground plane [21]. Variation of the slot length alters loading condition and changes the phase of the reflected wave as shown in Figure 3.22.

The addition of a varying microstrip line to the slot-coupled patch with a similar size throughout the reflectarray has led to the element that is shown in Figure

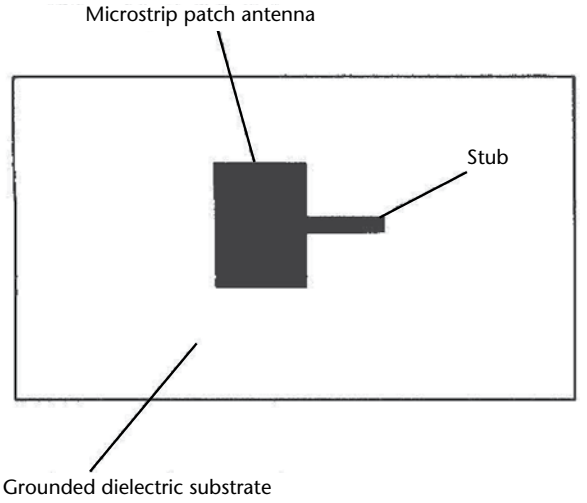

Figure 3.19 Stub-loaded patch cell element. (© 1995 IEEE. *From:* [19].)

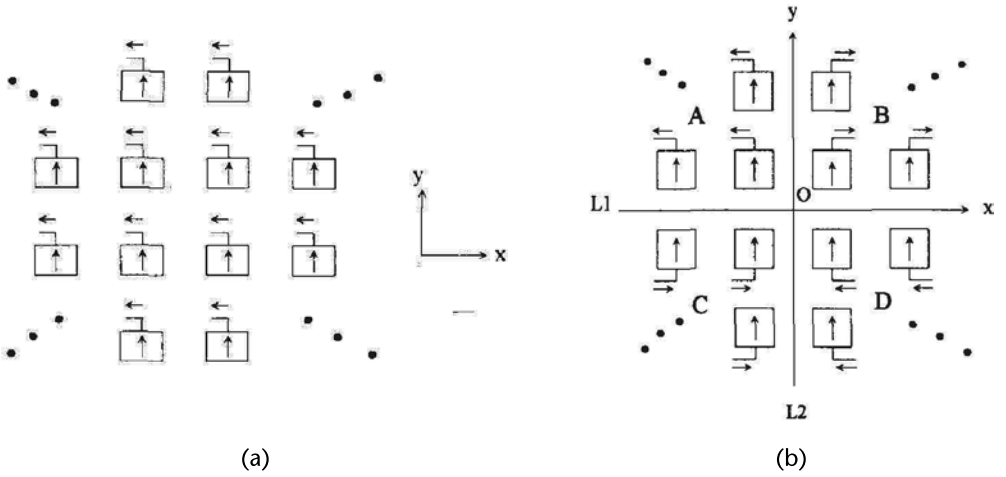

Figure 3.20 (a) Earlier design shows all delay lines bent in the same direction. (b) Proposed design with mirror symmetry to reduce cross-polarization. (© 1995 IEEE. *From:* [20].)

3.23 [22]. Two different implementations of the delay line have been have been introduced in the figure to realize truncated 360° and phase delay in excess of 360° to achieve true time delay and increase the reflectarray bandwidth, as will be discussed in Chapter 6. The phase versus length of delay line characteristics is shown in Figure 3.24 for U-shaped delay line which shows close to $3 \times 360°$ phase shift for the whole range of line length. The geometrical parameters of the cell element are given in the Table 3.1. The occurrence of phase cycles in excess of a single 360° cycle for the reflected phase of the cell element has the effect of delaying the emergence of phase jumps as shown in Figure 3.25, which also provides a comparison between the required phase for reflectarrays composed of elements with one and three cycles of 360°. This can lead to less phase jumps on reflectarray and higher phase efficiency.

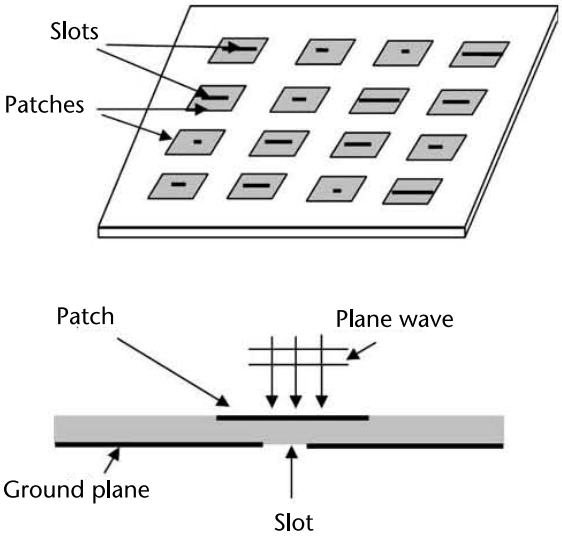

Figure 3.21 Microstrip reflectarray with variable slot loading on the ground plane. (© 2003 IEEE. *From:* [21].)

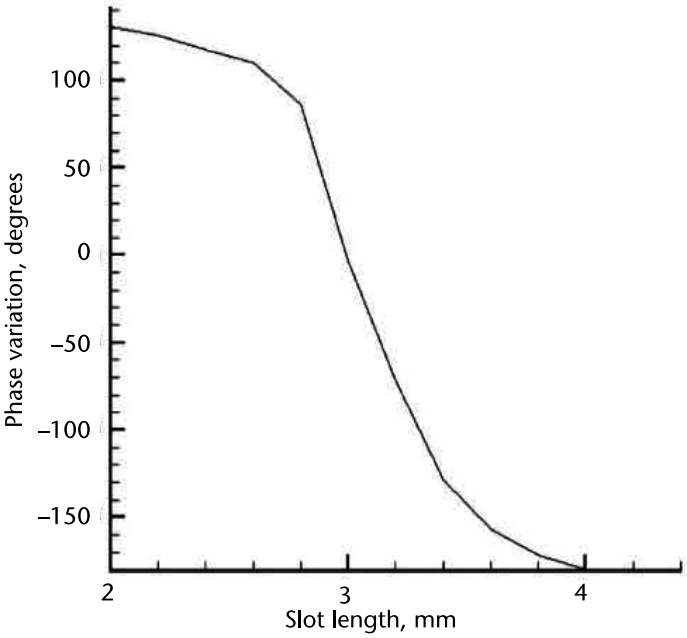

Figure 3.22 Typical phase versus slot length characteristic: substrate permittivity = 3.0, substrate thickness = 0.020 inch, patch dimensions = 3.2 mm × 2.3 mm, and slot width = 0.2 mm.

This same element was later evolved to a cluster of slot coupled patches with delay line loading, which is shown in Figure 3.26. The main advantage of this element, as will be explained in Chapter 9, is that it reduces the number of active elements by a factor of two for electronically steerable reflectarrays because each phase shifter at the end of the delay line can be dedicated to a cluster of two

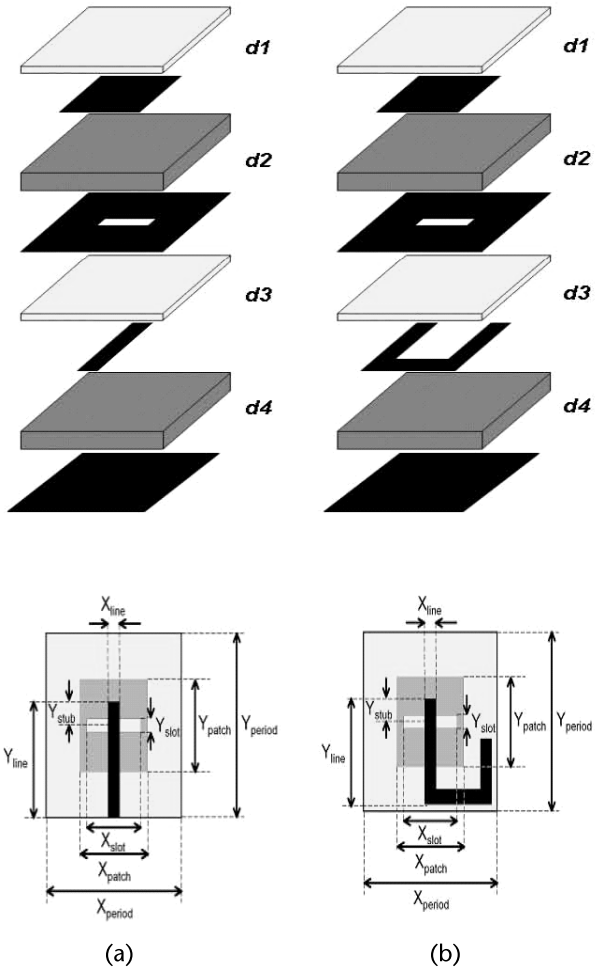

Figure 3.23 Slot coupled patch with delay line: (a) simple line to implement the phase truncated to 360° and (b) U-shaped line used to allow TTD. (© 2007 IEEE. *From:* [22].)

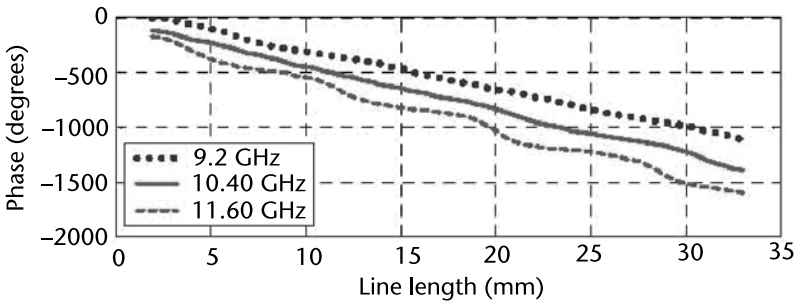

Figure 3.24 Phase of the reflection coefficient of the periodic structure composed of elements shown in Figure 3.24 as a function of the length of delay line. (© 2007 IEEE. *From:* [22].)

elements. This same trend can be further generalized by creating larger clusters as shown in Figure 3.27.

Table 3.1 Radiating Element Data

Layer	*X-dimension (mm)*	*Y-dimension (mm)*	
Period	16.5	16.5	
Patch	9.30	9.30	
Slot	7.00	1.00	
Substrate	*Thickness (mm)*	ε_r	*tan δ*
d1	0.508	3.380	0.0050
d2	2.000	1.067	0.0002
d3	0.508	3.380	0.0050
d4	7.20 (λ/4)	1.067	0.0002

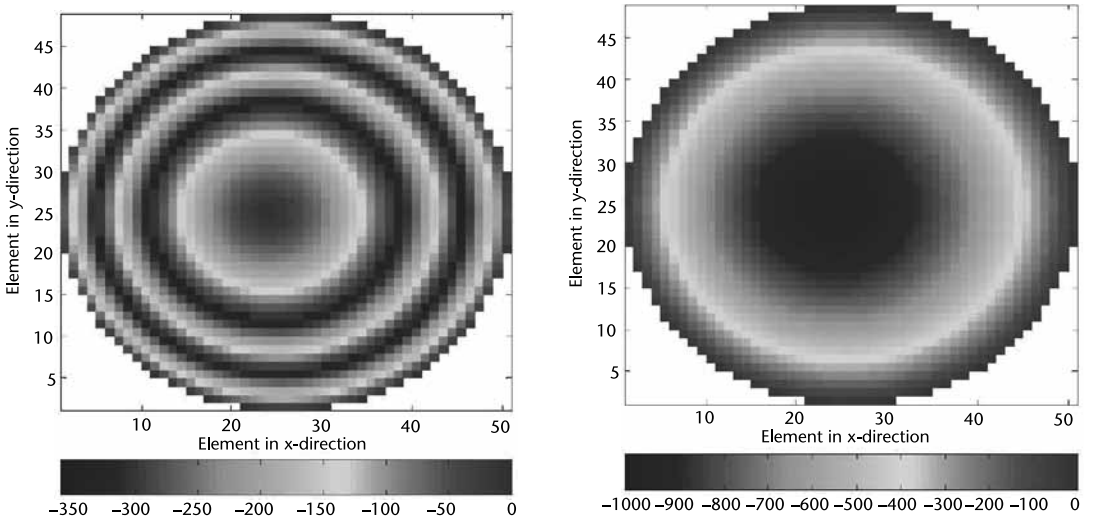

(a) (b)

Figure 3.25 (a) Phase distribution on a reflectarray with elements that accommodate only 360° of phase range. (b) Phase distribution on a reflectarray with elements that accommodate 3 × 360° of phase range. (© 2007 IEEE. *From:* [22].)

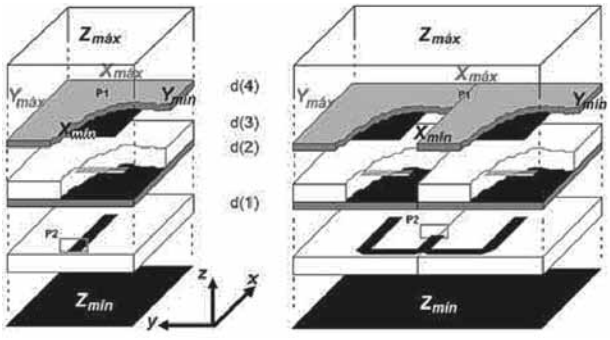

(a) (b)

Figure 3.26 Reflectarray elements based on patches slot-coupled to delay lines. (a) Expanded view of an individual element. (b) Expanded view of a two-element subarray. (© 2011 IEEE. *From:* [23].)

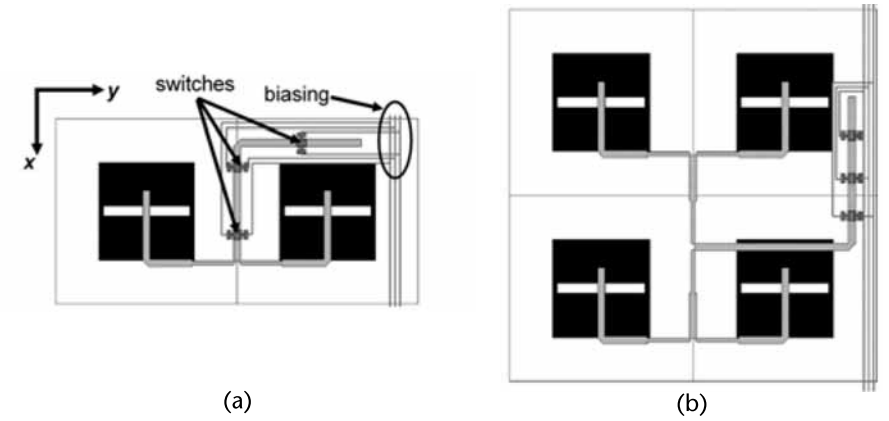

Figure 3.27 Reconfigurable reflectarray cell elements: (a) cluster of two elements and (b) cluster of four elements. (© 2001 IEEE. *From:* [23].)

The list of reflectarray cell elements based on loading mechanism is not limited to what has been presented above and other creative geometries have also been reported in the literature. Figure 3.28 shows an example of such an element which is based on loading a patch of constant size with a variable interdigital capacitor. The variation of the finger size of the capacitor is used to realize close to 1,000° phase shift.

3.4 Volumetric Cell Elements

Resonant radiating elements are by no means restricted to planar structures. Volumetric three-dimensional structures such as dielectric resonators (DRs) [25] and waveguide-fed antennas [26] have been subject of intensive research and development. Therefore, these same resonant radiators can be utilized as cell elements of reflectarrays. The resulting reflectarray structure is at disadvantage from the point of view of fabrication complexity as compared to its counterpart that utilizes planar cell element.

The first reflectarray comprised of DRs was reported in [27], which suggested variation of the length dimension of DR elements to adjust the phase shift. Figure 3.29 shows the cell element along with the fabricated reflectarray. The phase-DR length characteristic is shown in Figure 3.30. Similar to planar resonant elements, other methods of realization of phase shift such as loading has been attempted [28]. A strip with variable length on the top face of an otherwise similar DR throughout the reflectarray was utilized to adjust the phase of the reflected wave [28].

Another type of volumetric cell element that is used in the fabrication of reflectarray is rectangular groove [29]. In this case, the height of the rectangular groove was changed to adjust the phase of the reflected wave. Figure 3.31 shows a view of the cell element and also the reflectarray.

An important shortcoming of reflectarray composed of volumetric cell elements is that it is very difficult to embed multipolarization and/or multiband capabilities within such structures. This has been an important shortcoming on further development of such antennas.

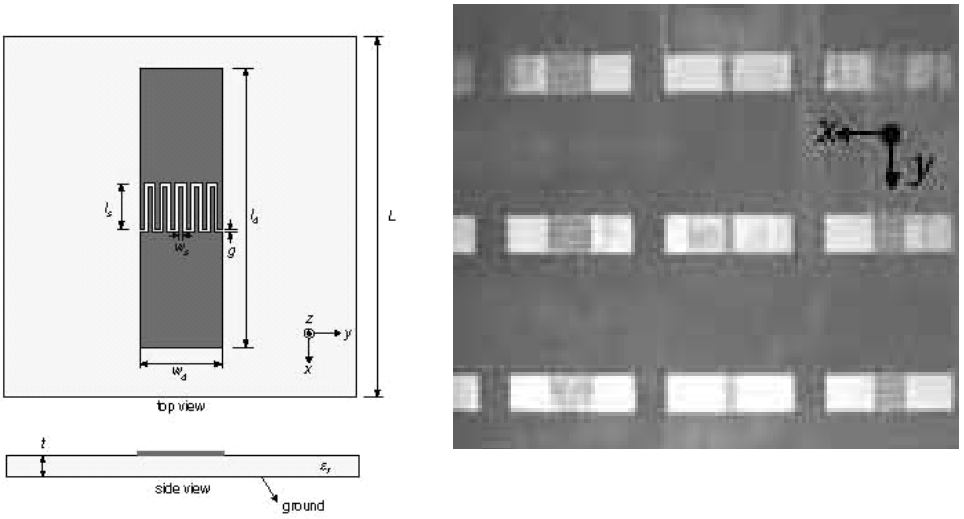

(a) (b)

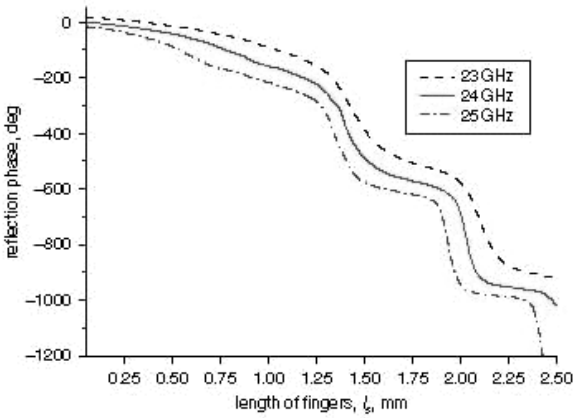

(c)

Figure 3.28 (a) Geometry of the interdigital loading element. (b) Photograph of a region of the reflectarray. (c) Plots of phase shift versus finger size for different frequencies. (© 2011 IET. *From:* [24].)

3.5 Subwavelength, Coupled Resonant Elements

3.5.1 Subwavelength Patches and Loops

The patch element is ubiquitous in antenna engineering in general and finds a comfortable home in reflectarray designs. The patch element placed in a resonant lattice (half-wavelength spacing) can be self-resonant; that is, it can exhibit resonance irrespective of the adjacent elements in the lattice, provided that the ground plane is present and is at an appropriate distance from the patch. This is an expected property because a single patch antenna, fed by probe or microstrip line, can be a resonant antenna. If the patch is electrically small, it can no longer exhibit resonance and hence cannot be used productively in reflectarray designs. However, as additional elements are brought adjacent to the electrically small patch (forming a periodic structure), a coupled resonance can arise. The coupling between

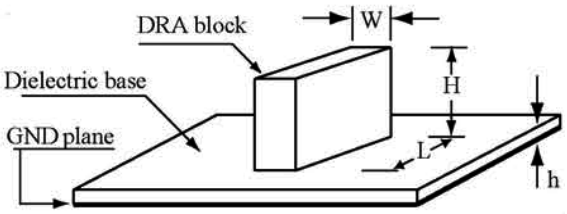

(a)

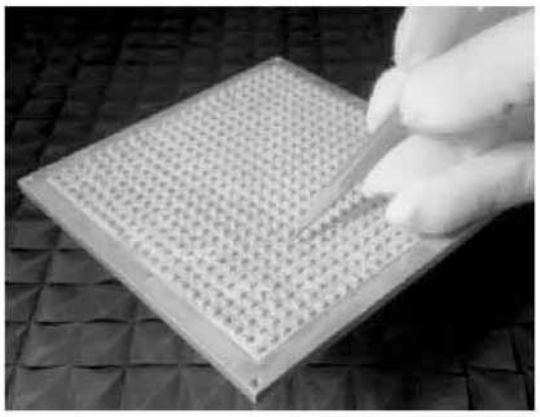

(b)

Figure 3.29 (a) Individual DRA block machined out of continuous substrate, h = 0.020 inch, W = 0.060 inch, H = 0.080 inch, and L is a variable length. (b) DR reflectarray mounted on a metal plate. (© 2000 IEEE. *From:* [27].)

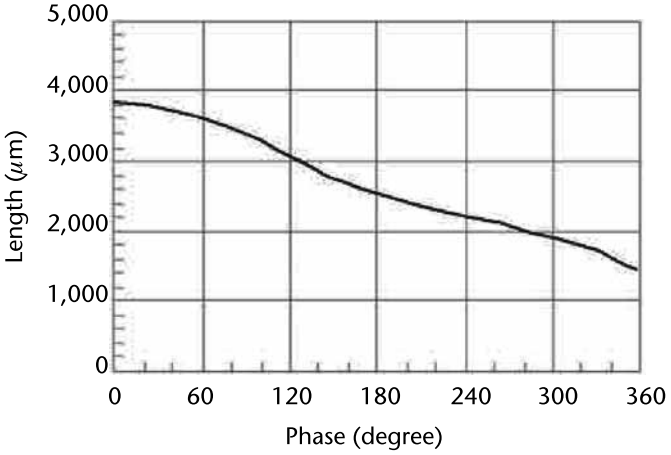

Figure 3.30 DR phase shift versus its length at 30 GHz. (© 2000 IEEE. *From:* [27].)

adjacent elements gives rise to a useful resonance and hence electrically small or subwavelength, coupled resonant elements can indeed be used to great advantage in reflectarray designs. The design approach is indistinguishable from the traditional approach involving resonant elements; the only difference is that the lattice size is less than half-wavelength and thus a greater number of elements are used in any

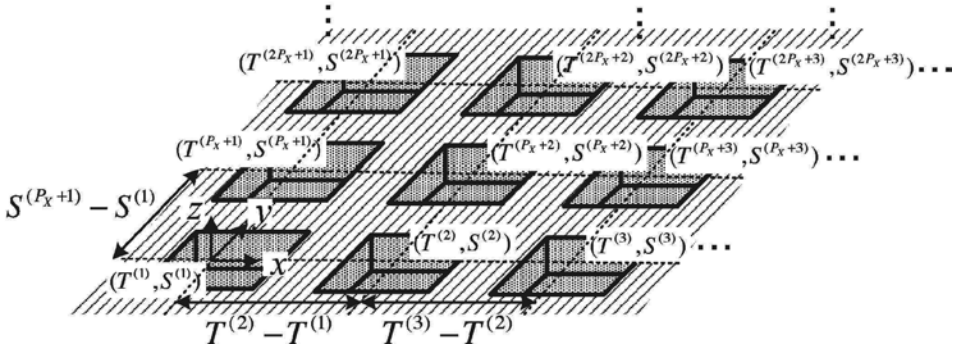

(a)

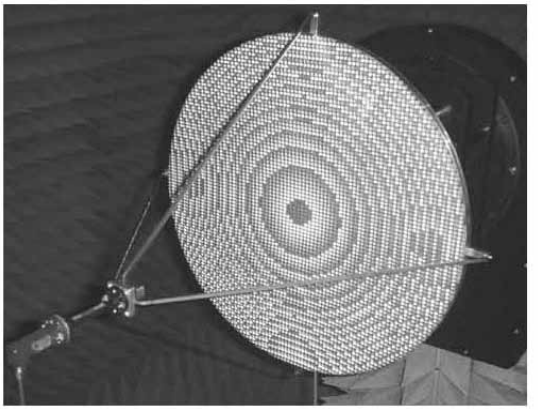

(b)

Figure 3.31 (a) Rectangular groove cell element. (b) Reflectarray composed of rectangular grooves. (© 2011 IEEE. *From:* [29].)

given reflectarray design. Lastly, it should be pointed out that the geometry of any subwavelength element can be utilized as a resonant element (assuming scaling up in size in a larger lattice). The elements discussed in this section are therefore not unique to the subwavelength regime. However, they are shown to operate uniquely well in the subwavelength regime, with the upcoming elements showing a gradual decrease in the overall lattice dimensions in which they reside.

The first suggestion that a subwavelength element can be used in reflectarray designs involved subwavelength patches appeared in [30]. The author used the term "artificial impedance surface" to describe the elements, but the design approach using array theory, aperture discretization, and the conversion of a spherical phase front to a planar phase front remains unchanged. It was however noted that very small feature sizes (small interelement gaps) were required to obtain a full range of reflection phase. Nevertheless, the lattice size can be reduced from the standard $\lambda/2$ lattice to the smaller $\lambda/3$ lattice. The benefit obtained through the lattice size reduction was an immediate improvement in gain-bandwidth performance. A minute amount of gain was lost, mostly due to a reduction in the phase range, but this is deemed an acceptable price to pay for a substantial improvement in bandwidth (from 12% to 22%). An example of the gain-bandwidth curves for resonant and

subwavelength-based reflectarrays is shown in Figure 3.32(a) and an example of a subwavelength reflectarray layout is shown in Figure 3.32(b).

A paper involving the use of polarization-sensitive subwavelength rectangular patches was considered [31] whereby the beneficial wideband behavior was used in a reflectarray that also converted linearly polarized feed radiation into circular polarization.

To further reduce the lattice size, the authors in [32] used a multilayer stack of subwavelength patches. The additional layer improved the phase range for the smaller lattice size of $\lambda/4$, with the benefits of improved bandwidth obtained thereafter. An example of the gain-bandwidth curves for resonant and subwavelength based reflectarrays is shown in Figure 3.33(a) and an example of a subwavelength multilayer reflectarray patch element is shown in Figure 3.33(b).

A study on the properties of subwavelength elements was discussed in [33], with the conclusion that subwavelength elements provide a reduced angular sensitivity over their resonant counterparts, making them ideal candidates for electrically large reflectarray designs. However, the benefit of reduced angular sensitivity is found for any size of reflectarray because the oft-assumed normal incidence is approximate for any sized reflectarray. Examples of the reflection phase curves for resonant and subwavelength patches are shown in Figures 3.34(a) and 3.34(b), respectively, for various angles of incidence.

Further reduction in lattice size was obtained through the use of subwavelength loops [34–37]. The subwavelength loop was shown to provide upwards of 300° phase range for a substantially smaller lattice size of $\lambda/6$. This improved phase range and smaller lattice size was found to be possible using modest etching requirements as opposed to more stringent etching requirements of patches [30–33]. Currently, $\lambda/6$ is the smallest lattice size used in a fabricated reflectarray design (Ku-band). An additional benefit of the smaller lattice is a substantial reduction in dielectric and ohmic losses in the substrate and metal regions, which will be discussed

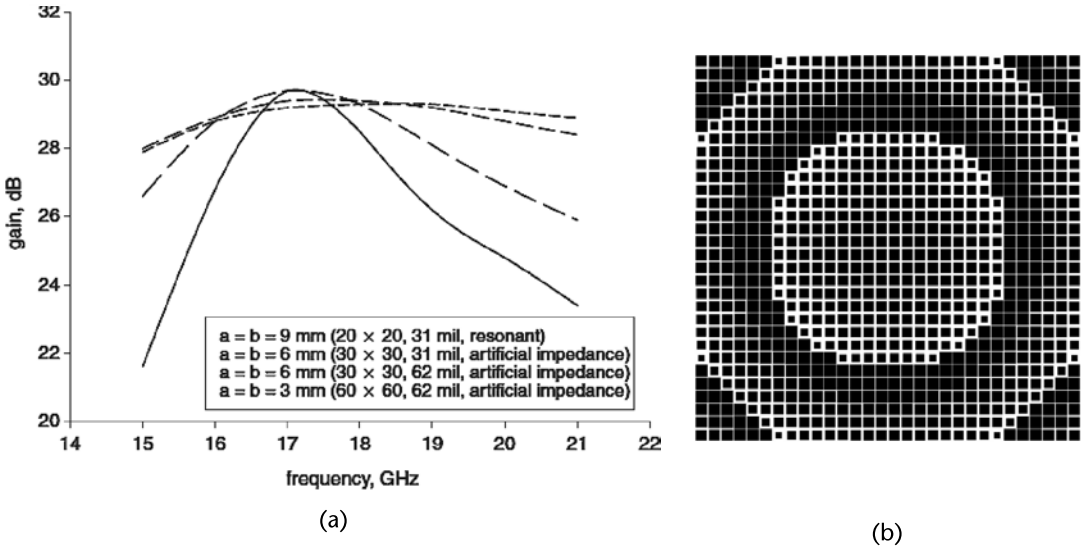

Figure 3.32 Gain bandwidth of various (a) resonant and subwavelength reflectarrays and a (b) subwavelength reflectarray mask layout. (© 2007 IET. *From:* [30].)

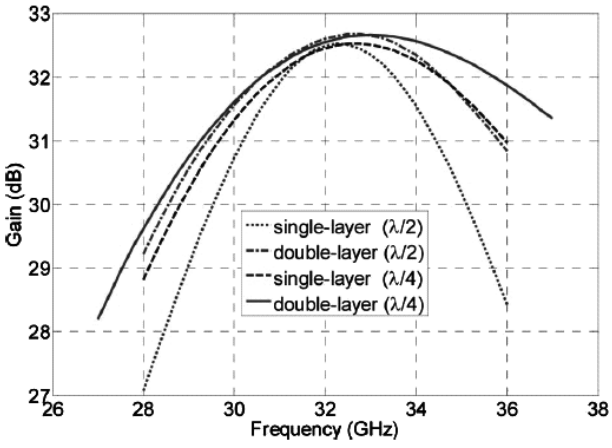

(a)

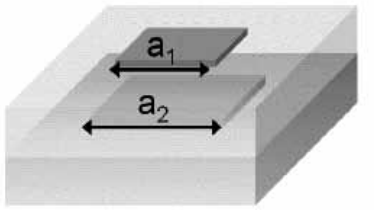

(b)

Figure 3.33 (a) Gain bandwidth of various single- and dual-layer subwavelength reflectarrays and (b) an example of a subwavelength dual-layer reflectarray element configuration. (© 2010 IEEE. *From:* [32].)

at length in Chapter 7. The superior behavior of the loop element over the patch in the subwavelength lattice arises from the additional inductance obtained from the loop structure over that of the patch structure [37]. The additional inductance effectively lowers the resonance frequency and hence a smaller lattice size can be successfully arranged.

Due to the very low-frequency dispersion of the reflection phase of subwavelength loops, the gain-bandwidth of a reflectarray using these elements is wideband. A reflectarray is designed with specifications: center frequency of 12.5 GHz, offset feed of 16°, main beam direct reflection of $F/D = 1.13$, aperture size of 400 mm, lattice size of 4 mm, and Rogers 3003 of 125-mil substrate with the feed horn Q-par QSH17S15S. The resulting fabricated reflectarray is shown in Figure 3.35(a) and the gain versus frequency shown in Figure 3.35(b). The 1-dB gain bandwidth obtained is 19% and the aperture efficiency approximately 60%.

3.5.2 Advanced Subwavelength Elements

3.5.2.1 Dogbone Element

More advanced subwavelength elements can be envisioned beyond that of the patch and loop elements. An element observed in periodic structure research, mostly involving frequency selective surfaces, includes the dogbone element, shown in Figure 3.36(a). By varying the numerous physical parameters, one is able to obtain a

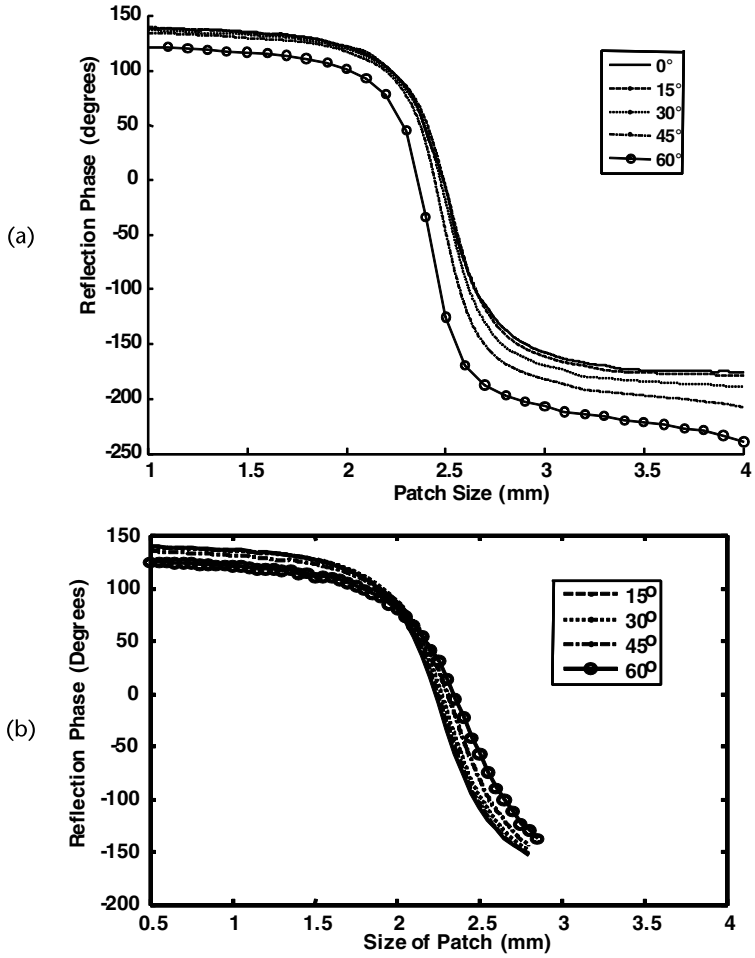

Figure 3.34 Reflection phase angular sensitivity for (a) resonant ($\lambda/2$) patches and (b) subwavelength ($\lambda/3$) patches. (© 2011 IEEE. *From:* [33].)

myriad of possible reflection phases and phase dispersions (variation of phase with respect to frequency). Consider a lattice size of 4 mm, a center frequency of 12.5 GHz, and a 125-mil FR4 substrate (loss tangent of 0.016 and relative permittivity of 4.45). We then vary the dimensions of rectangular patches, rectangular loops, and the newly introduced dogbone element over all possible configurations with parameter variation density on the order of 0.2 mm. The resulting reflection phase versus dispersion is shown in Figure 3.36(b). Note that the patch element offers a limited range of reflection phase (<250°) while the loop element provides in excess of 300°. Additionally, the dogbone element shows a complete 360° phase range but also a much wider range of phase dispersions. As we will discuss in Chapter 6, the ability to select from a host of elements with varying phase dispersions for any given reflection phase is of paramount importance when designing a wideband reflectarray. Thus, the dogbone element represents a superior selection over the patch and loop element if bandwidth is of particular interest. Note that the element is polarization sensitive, which can be undesirable in some applications; a Jerusalem cross can be used in its stead for polarization insensitive applications.

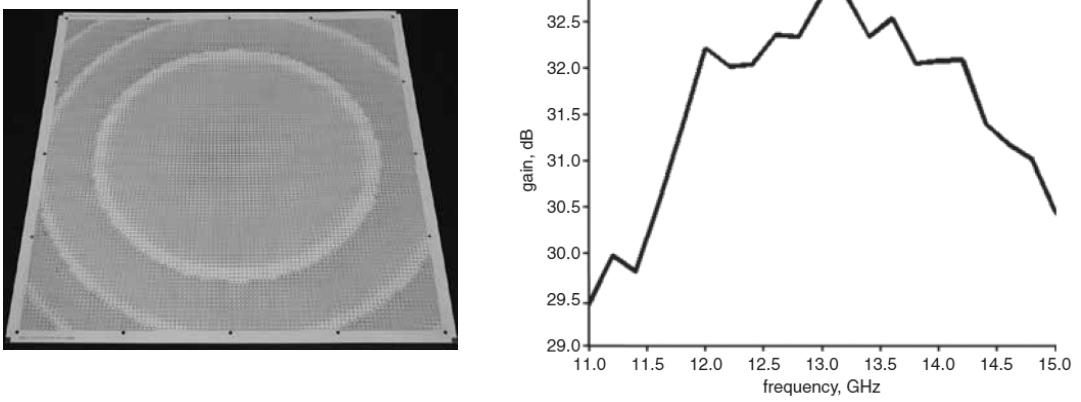

(a) (b)

Figure 3.35 Example of (a) a photograph of subwavelength loop-based reflectarray and (b) gain versus bandwidth. (© 2011 IET. *From:* [37].)

3.5.2.2 Extended Dogbone Element

We now introduce an additional reflectarray element, which we will denote as the extended dogbone element, as shown in Figure 3.37. This element exhibits a very large number of tunable physical parameters. However, it was discovered that by the selection of $d_1 = d_2 = 0.2$ mm and varying L, e_1, and e_2 in tandem, an interesting property arises. Maintaining identical lattice and substrate parameters from the previous basic dogbone example, thus remaining in the electrically small $\lambda/6$ lattice, the double-resonance phenomenon appears, as shown in Figure 3.38. Despite being in the electrically small confines, the element exhibits two resonances: one associated with the cross-element coupling along the edge associated with the length L and a secondary resonance associated with the interelement (self) coupling along the length e_2. The electrically small element provides over 600 of reflection phase variation. It is well established that multiresonant elements can be beneficial in designing wideband elements. An additional unique property of this element is that a moderately sized reflectarray designed using the extended dogbone would exhibit a smooth transition through the first Fresnel zone due to the property of greater than 360° phase range.

3.5.2.3 Rectangular Extended Dogbone Element

Consider again the extended dogbone from the previous discussion. Because this element has greater than 600° of phase range, and a reflectarray requires only 360° (somewhat less with marginal gain drop), we should be able to reduce the size of the element and still design a high-gain reflectarray. The first attempt at cell size reduction maintains the 4-mm lattice dimension horizontally, but reduces the cell size vertically from 4 mm to 1.6 mm (from $\lambda/6$ down to $\lambda/15$). This leads to an incredibly fine aperture sample density along one of the planes, which is fortuitously parallel to the polarization associated with sufficient 350° phase variation. The rectangular element is shown in Figure 3.39. The parameters are set to $d_1 = d_2 = g = 0.2$ mm and

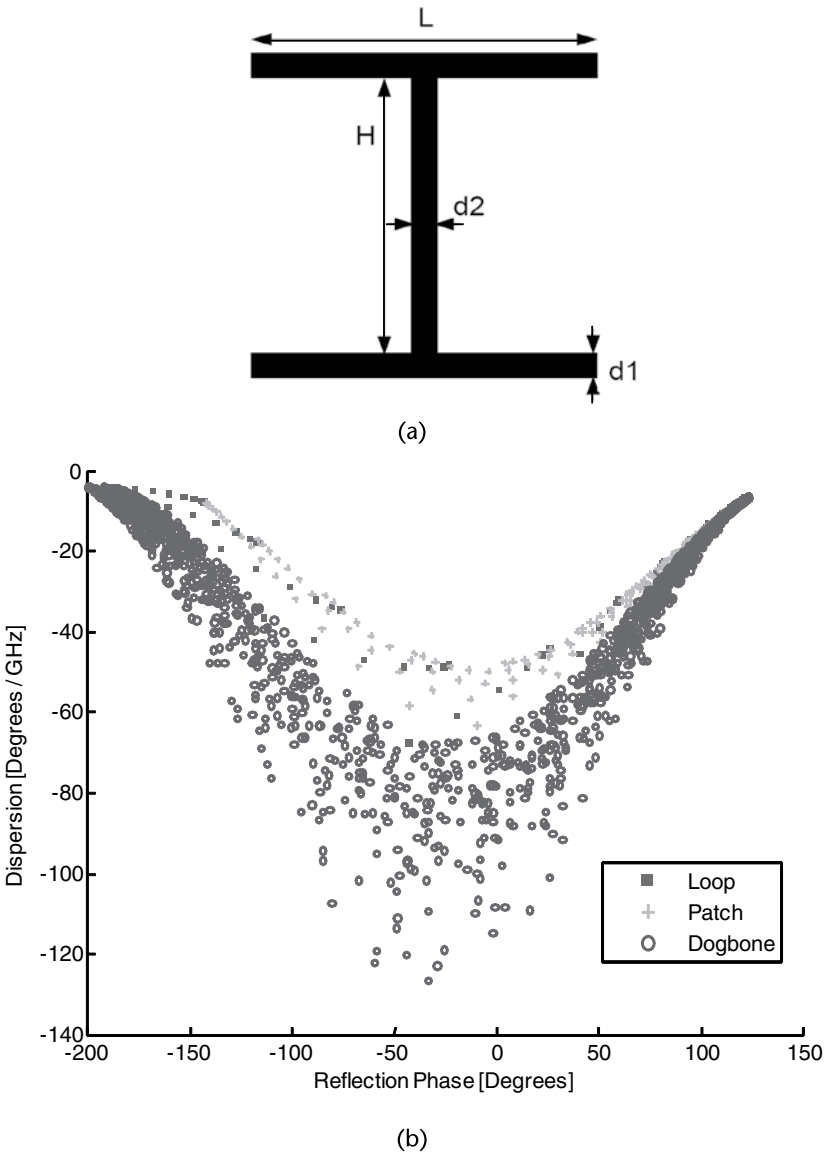

Figure 3.36 Example of a reflectarray: (a) dogbone element and (b) dispersion versus reflection phase for various subwavelength elements.

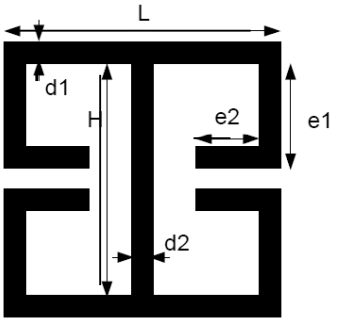

Figure 3.37 Example of an extended dogbone reflectarray element.

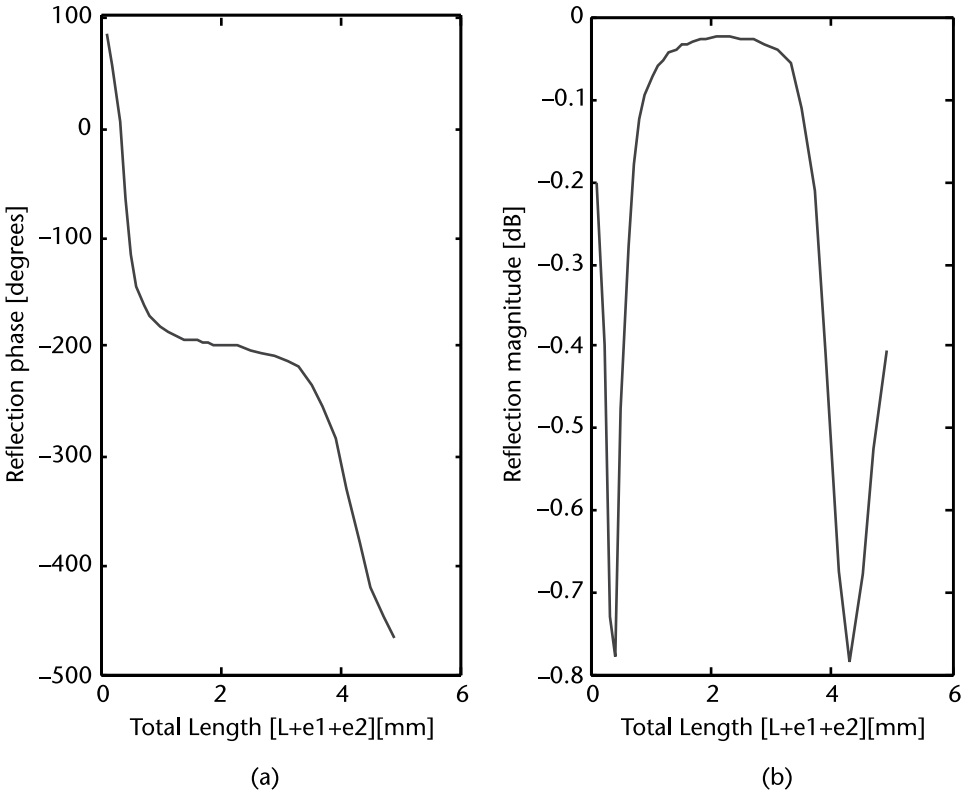

Figure 3.38 Examples of the (a) reflection phase and (b) reflection magnitude of the extended dogbone element.

$H = 1.4$ mm at most. The lengths $L_1 + L_2 + L_3$ are varied in tandem. The reflection phase of this element is shown in Figure 3.40, showing 350° of phase range from a $\lambda/6$ by $\lambda/15$ lattice. Such an element should provide excellent angle of incidence insensitivity in a linear polarized reflectarray, allowing for improved aperture efficiency and lower than typical *F/D* ratios.

3.5.3 Subwavelength Fragmented Elements

The subwavelength fragmented element for reflectarrays was first introduced in [39, 40]. The notion of a fragmented antenna has been used elsewhere (refer to [40] for a thorough review) and finds use in the design of reflectarrays. The fragmented element concept can be described as the discretization (or fragmentation) of the lattice space of a periodic structure and then optimization of the geometry of the element can proceed unimpeded by geometric restrictions. In other words, rather than simply varying the element length or line width, the entire geometry itself is varied amongst many possible shapes. For example, an element that is discretized to have 19×19 fragments (or pixels) has a startling 4.69×10^{108} possible element shapes. Parameter sweeping is obviously not an option; thus, optimization is a necessity. In particular, genetic algorithms are a natural selection as the driving optimizer for fragmented antennas. An example of a fragmented reflectarray element (in unaltered form) is shown in Figure 3.41(a), while an optimized element

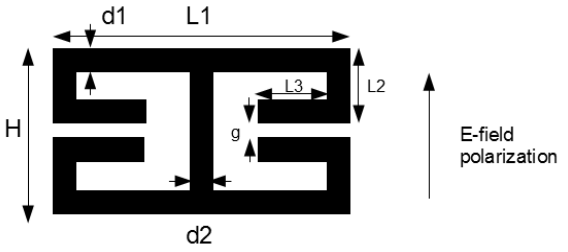

Figure 3.39 Example of a rectangular extended dogbone element, with E-field polarization shown.

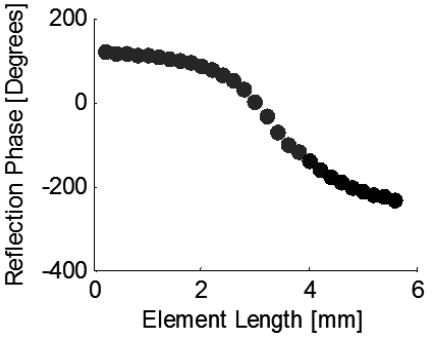

Figure 3.40 Example reflection phase as a function of element length for rectangular extended dogbone element.

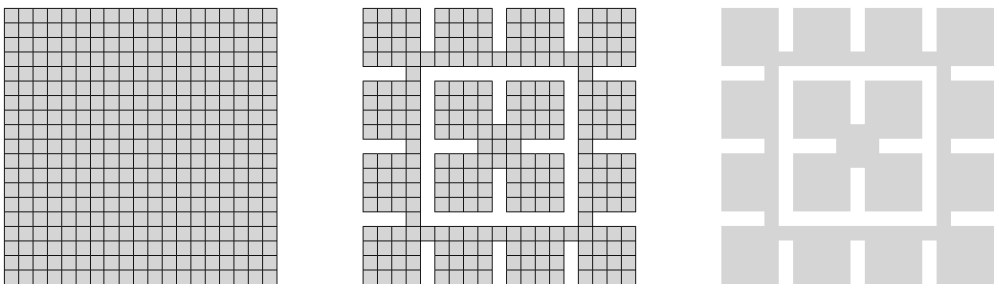

Figure 3.41 Example of fragmented elements: (a) unaltered, (b) optimized, and (c) optimized elements in contiguous etchable format.

is shown in Figure 3.41(b), and lastly the actual etched element shape shown in Figure 3.41(c). As a last point before moving onto practical examples, there are two motivating factors in using subwavelength fragmented elements: (1) we know that subwavelength elements offer distinct electrical performance advantages over resonant elements and (2) due to the smaller physical size of the subwavelength element, the electrically dense mesh discretization implies the expansion functions describe behavior over electrically small regions and hence will provide a more accurate simulation result.

3.5.3.1 Similarity-Optimized Reflectarray Elements

The first application of subwavelength fragmented elements is for the synthesis of very high aperture efficiency reflectarrays. As discussed in Chapter 2, a reflectarray has an upper bound on aperture efficiency given the feed illumination and spillover efficiencies. A reflectarray that exhibits a perfect, error free spherical-to-plane wave conversion will obtain aperture efficiency (gain) that reaches this limit. To achieve this limit, the elements in the reflectarray must provide precisely the required reflection phase. The majority of reflectarrays are designed using periodic structure analysis. Namely, an element is placed in an infinite periodic structure, its physical properties are varied, and the resulting reflection phase values obtained allow one to synthesize the reflectarray surface. When the element is used in practice, it no longer resides in the presumed infinite and uniform periodic structure. It now appears in a finite structure that is potentially very highly nonuniform. The consequence is that the reflection phase is in error in regions where nonuniformity is greatest, that is, significant geometric discontinuities in the reflectarray elements. One method that can be used to mitigate the nonuniformity is known as the surrounded-element technique [41]. Any number of elements in the reflectarray can be simulated in the vicinity of the actual environment within which it resides and the physical properties tuned to obtain the precise reflection phase desired. While effective, it requires a fair amount of computational overhead.

Alternatively, we introduce the concept of similarity-optimized reflectarray elements. The technique can be described simply as the shape optimization of reflectarray elements for both reflection phase and geometric similarity between adjacent elements in the reflectarray. This is accomplished by starting with a particular reflection phase (e.g., 180), optimizing for the phase and proceeding to the next desired reflection phase (e.g., 170°). Upon obtaining the desired phase, the geometric similarity between the current element (170) is maximized with respect to the previous element (180°). Upon conclusion, the two elements now provide a set of desired reflection phases and additionally exhibit a high degree of geometric similarity.

Consider a reflectarray with the following design specifications:

- Frequency of 12.5 GHz;
- Offset feed of 16°;
- Main beam direct reflection of F/D = 1.13;
- Lattice size of 4 mm;
- 4-mm air substrate;
- Feed horn Q-par QSH17S15S.

A collection of elements were optimized for maximum geometric similarity while covering a phase range of 300°. These elements are shown in Figure 3.42. One can observe a smooth geometric progression as the reflection phase decreases from the first element. The consequence is the elements in the reflectarray will exhibit similar smooth variation, thereby reducing the effects of nonuniformity. A photograph of the resulting fabricated reflectarray is shown in Figure 3.43 supporting this claim.

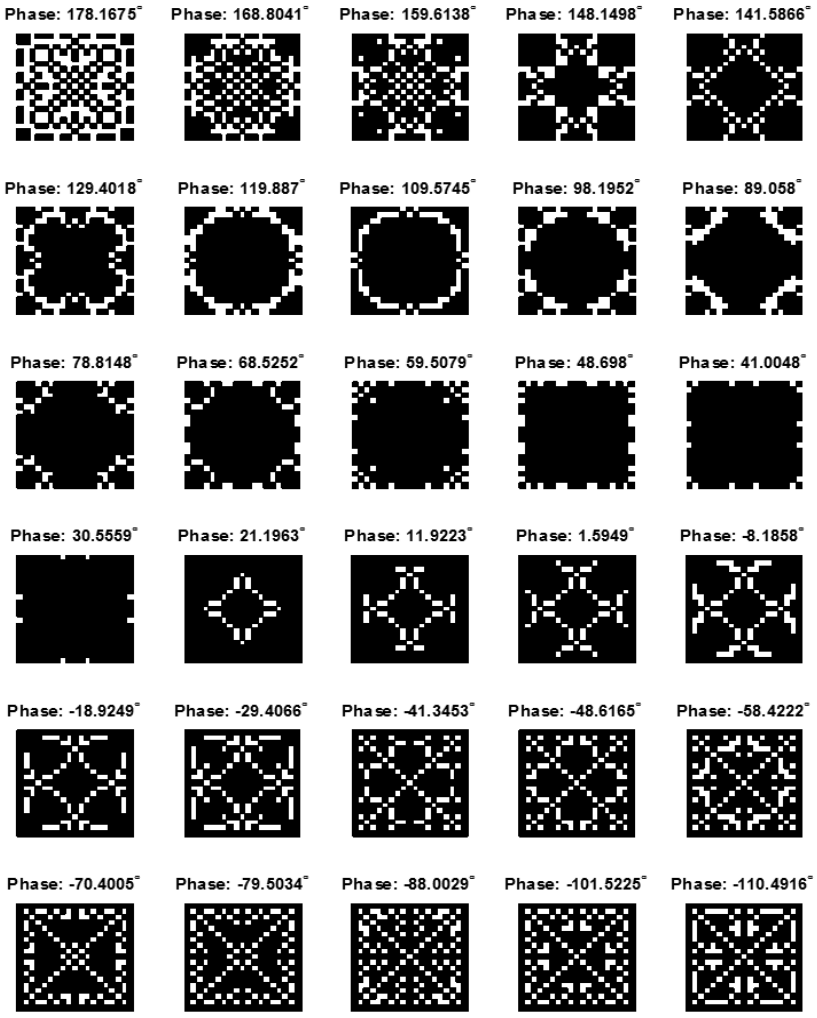

Figure 3.42 Similarity-optimized reflectarray elements.

For the given feed and aperture configuration, the maximum gain permissible is 33.17 dBi. The measured gain of this reflectarray was 33.06 dBi. The measured gain is quite close to the upper bound and thus we conclude that the similarity optimization technique is effective in reducing the reflection phase errors over the aperture of reflectarray antennas.

3.5.3.2 The Mosaic Reflectarray

The mosaic reflectarray is an antenna design that meets both the requirements of a particular set of reflection phases over the surface (e.g., the reflectarrays that we have designed thus far) and simultaneously attempts to synthesize an optical image with its surface patterning. We therefore utilize the fragmented reflectarray elements in a manner that both meets the requirements of reflection phase as well

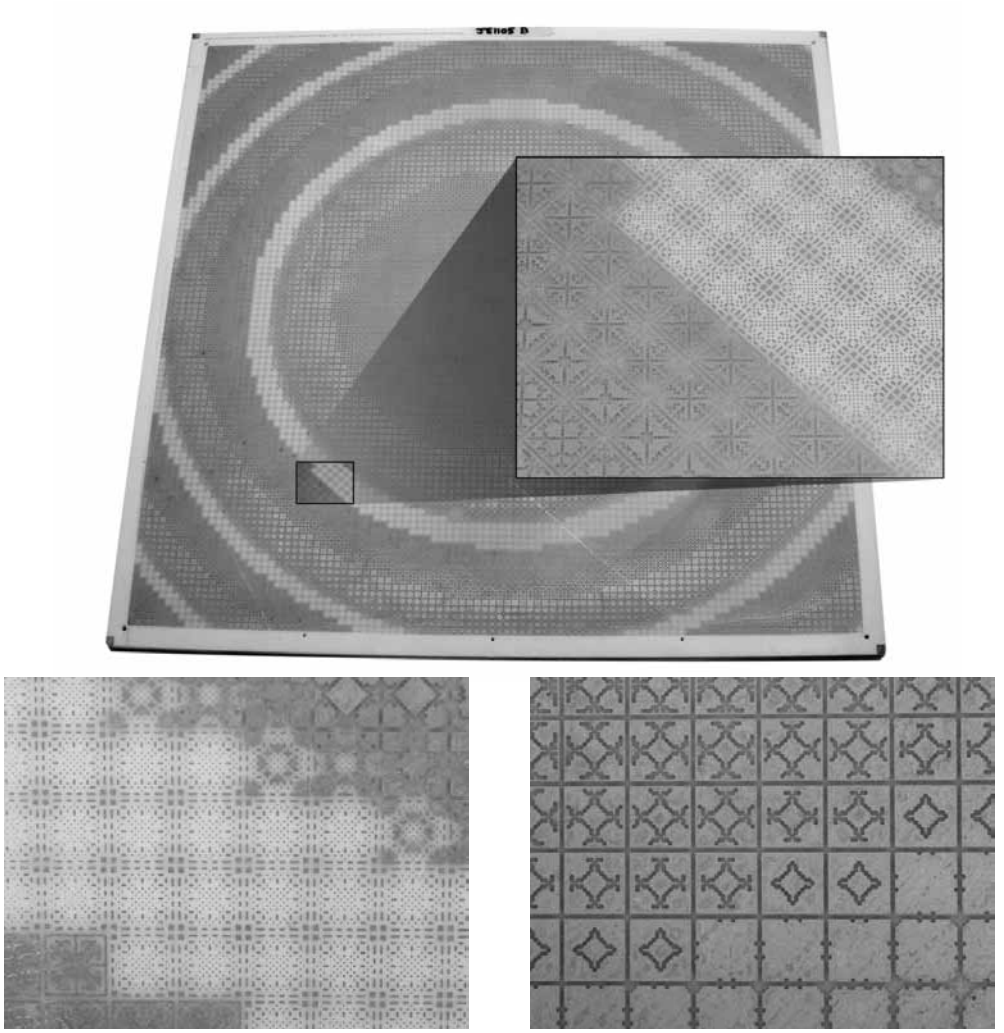

Figure 3.43 Photograph of similarity-optimized reflectarray.

as using the metal density (which can be thought of as an optical property of the element) to simultaneously mimic an optical image, thus forming a mosaic.

A secondary metric is now used to classify a fragmented element: its metal density. This quantity will be defined in a basic fashion, giving no concern to the actual shape and positional dependence of the metal density. It will simply be defined as the ratio of the total number of pixels in a given element divided by the total number of pixels in the starting element shape (a solid patch in all of our examples). The first step in our design process is generating a wide variety of elements with which to design our mosaic reflectarray. The ideal collection of elements would entail groups of elements with reflection phase in, for example, 10° steps (as was done before) only now each reflection phase (effectively an index) has numerous elements associated with it, each with a different shape and optimistically with a variety of different metal densities. As a first optimization approach, we will simply optimize the elements to achieve the desired phase to within 2° error in steps of 10°, which is precisely the same approach used previously. The only difference now is

we demand 128 elements from the optimizer for each index, thereby synthesizing nearly 4,000 fragmented elements. The minimum, average, and maximum metal densities of these elements are shown in Figure 3.44, confirming that we have a wide range of metal densities for each index, where index 1 is 180°, index 2 is 170°, and so on. An example collection of 128 elements is shown in Figure 3.45 for index 15 representing resonant elements (reflection phase of zero).

We now proceed with the design of two mosaic based reflectarrays. The reflectarray design parameters are identical to that of previous section. The desired optical image in both cases is apparent from the photographs of the fabricated reflectarrays shown in Figures 3.46(a) and 3.46(b). The measured far-field pattern at 12.5 GHz is shown in Figure 3.47 for the mosaics in Figures 3.46(a) and 3.46(b), showing measured aperture efficiencies of 50% and 55%, which is quite high considering that the reflectarray collimates at microwave frequencies while simultaneously displaying the optical mosaic.

3.5.4 Array Thinning with Subwavelength Elements

The electromagnetic nature of subwavelength elements can be best described through the interelement coupling between adjacent elements [42]. The individual elements are important, but it is the cross-coupling between elements that give rise to the interesting behavior of these elements. A consequence of the criticality of coupling is that for the single linear polarization excitation of a subwavelength element, only certain elements become relevant for this essential cross-coupling. This phenomenon is described graphically in Figure 3.48(b). The regions of low-intensity coupling imply their presence is unnecessary to generate resonance and thus play a diminished role in generating the required range of reflection phases

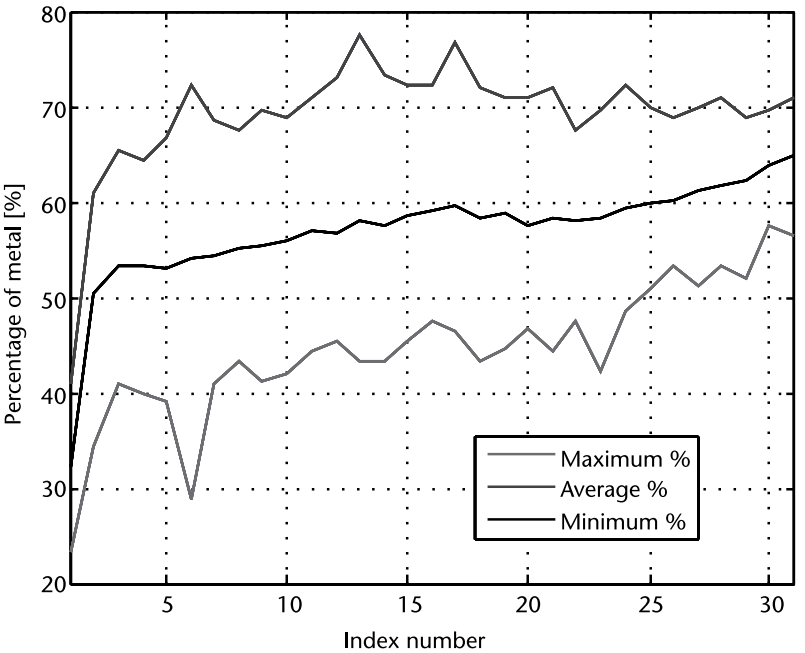

Figure 3.44 Maximum, average, and minimum percentage of metal for each reflection phase index in the generated database of fragmented reflectarray elements.

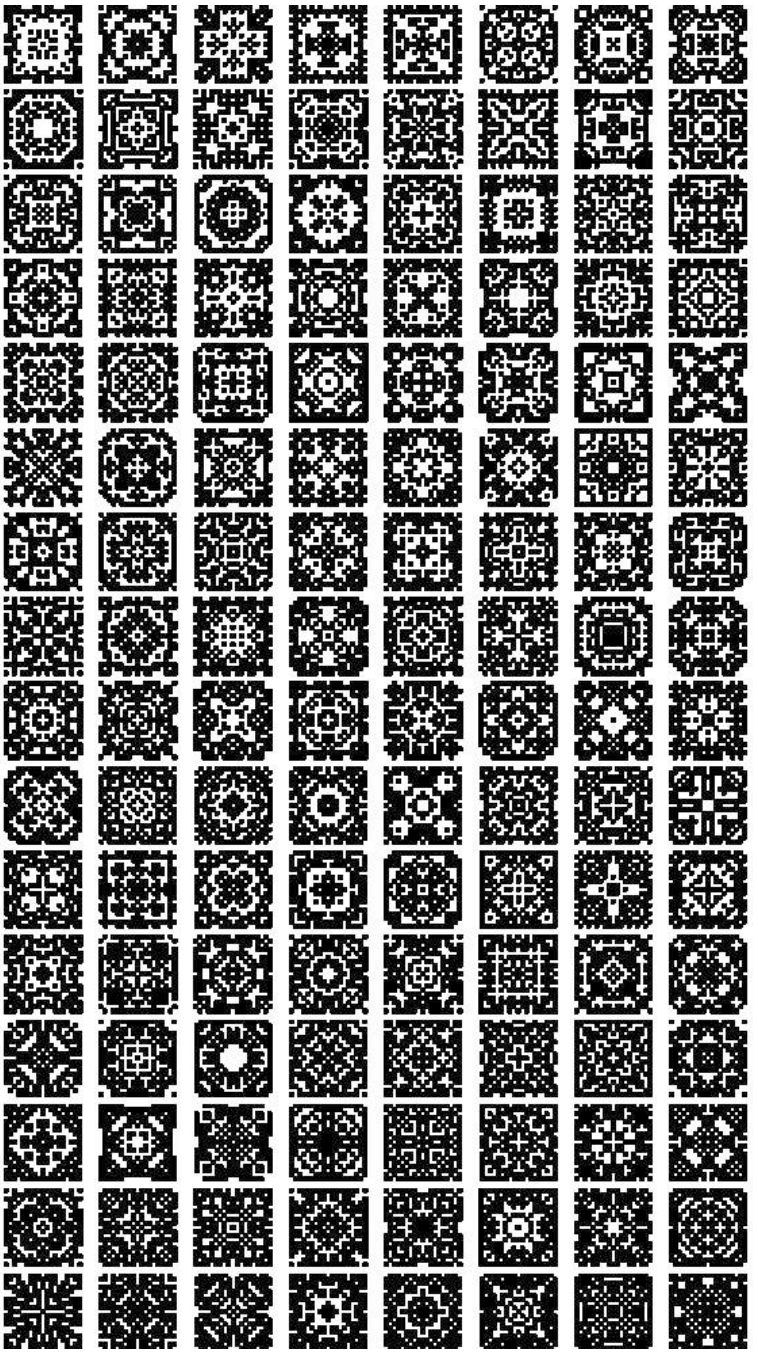

Figure 3.45 Collection of 128 fragmented elements. Note that each element has a reflection phase that is within 2° phase of 0° and yet 128 uniquely shaped elements are shown (metal density varies from 40% to 70%).

for reflectarray operation. The supposition is therefore that the lattice dimension in Figure 3.48(a) can be altered such that the lattice dimension d_x can be dramatically increased in size while d_y remains subwavelength in electrical size (the orientation of electric field polarization is important in this regard). In the Ku-band (12.5 GHz),

(a)

(b)

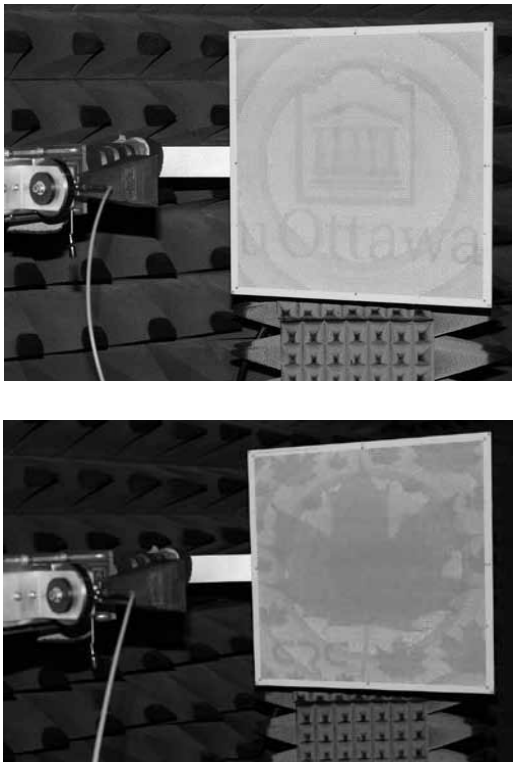

Figure 3.46 (a, b) Fabricated mosaic reflectarrays.

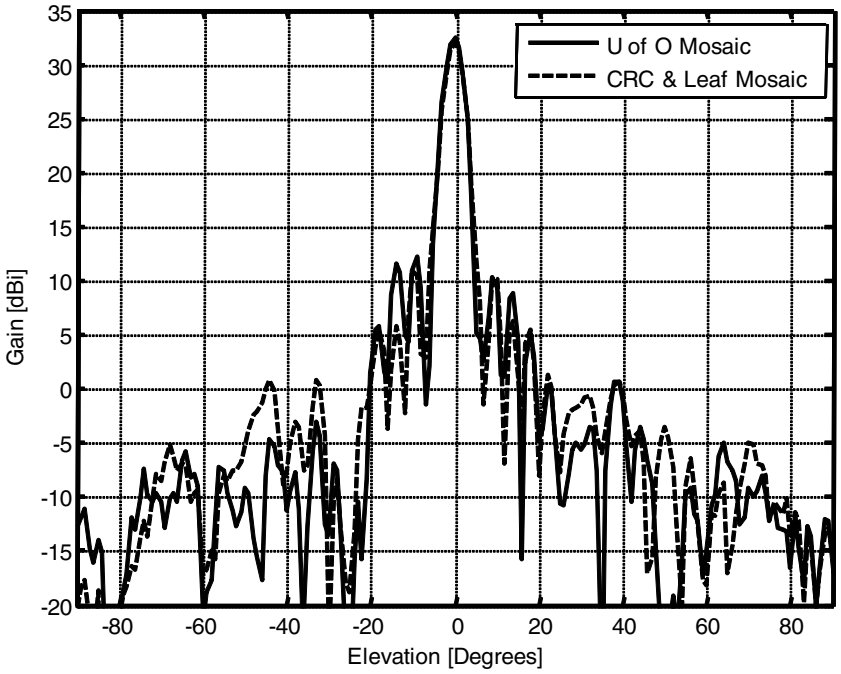

Figure 3.47 Antenna E-plane gain pattern of mosaic fragmented reflectarrays from Figure 4.16(a) and (b).

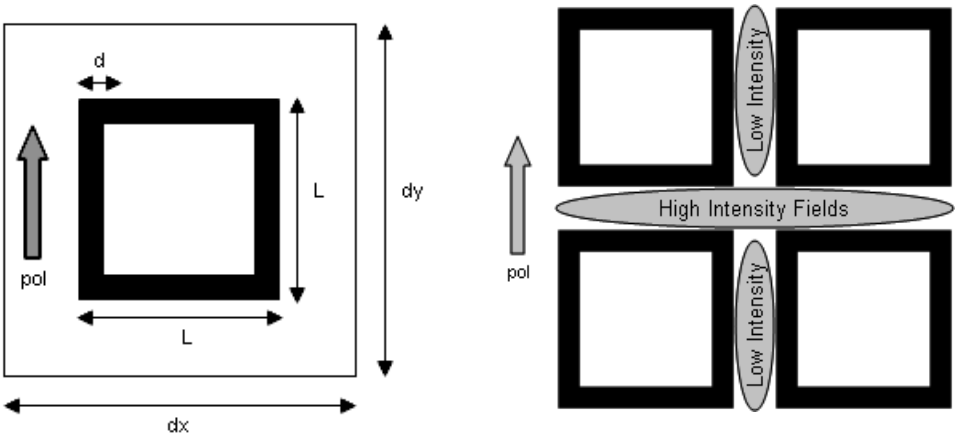

(a) (b)

Figure 3.48 (a, b) Nature of interelement coupling for subwavelength elements under single polarization excitation.

the reflection phase of a loop element (substrate 60 mils, $\varepsilon_r = 3$) is considered with lattice size 4 mm × 4 mm (traditional subwavelength lattice) and 4 mm × 12 mm (a thinned lattice). The thinned lattice experiences no reduction in achievable phase range, although the resonance is sharper, implying a potential reduction in reflectarray bandwidth, as shown in Figure 3.49. Two reflectarrays are fabricated using the same configuration as Section 3.5.1, one using a fully populated configuration of subwavelength loops and the other using the thinned elements described previously. The resulting gain bandwidth of the reflectarrays is shown in Figure 3.50(a), with a photograph of the thinned reflectarray shown in Figure 3.50(b). Around the

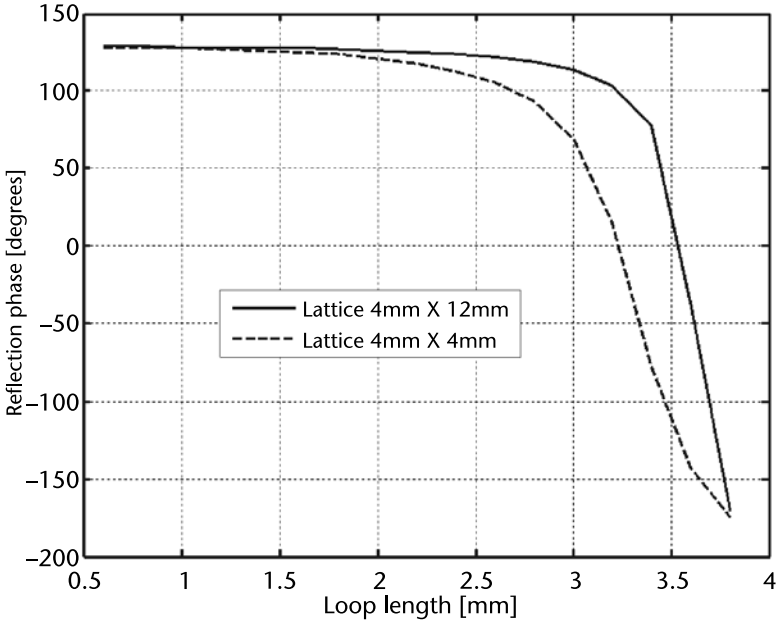

Figure 3.49 Reflection phase of normal and thinned subwavelength element.

(a)

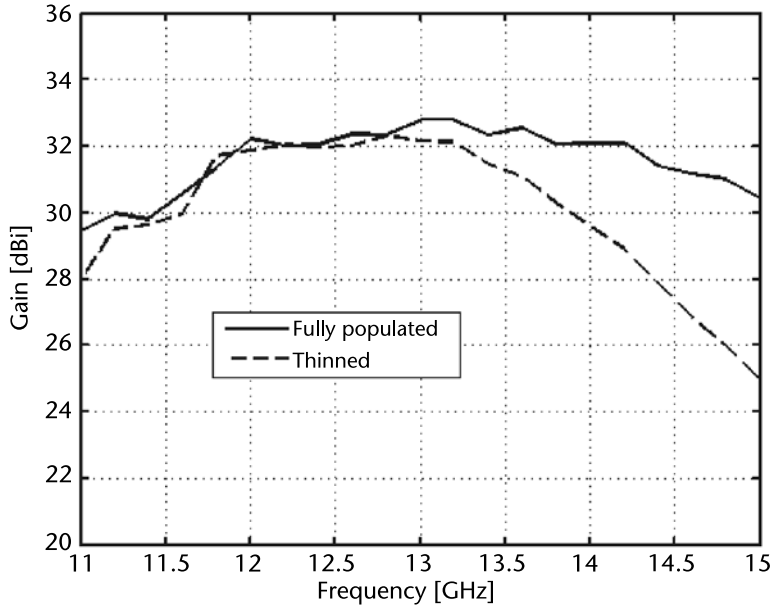

(b)

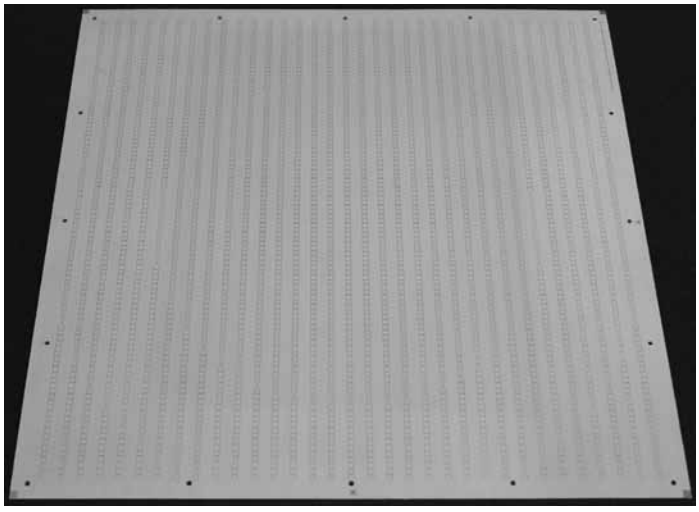

Figure 3.50 Fabricated regular and thinned reflectarrays with (a) gain bandwidth and (b) photograph of fabricated thinned reflectarray.

center frequency of 12.5 GHz, there is marginal difference in gain with the only consequence in using the thinned array being a reduction in 1-dB gain bandwidth from 19% to 15%. The latter obtained bandwidth is ample for many Ku-band applications. The thinned reflectarray has potential uses in reconfigurable reflectarrays since two-thirds of the reflectarray surface is barren.

References

[1] Pozar, D. M., and S. D. Targonski, "Design of Millimeter Wave Microstrip Reflectarrays," *IEEE Transactions on Antennas and Propagations*, Vol. 45, No. 2, 1997, pp. 287–295.

[2] Chaharmir, M. R., et al., "Wideband Reflectarray Research at the Communications Research Centre Canada," *Proceedings of 13th International Symposium on Antenna Technology and Applied Electromagnetics*, 2009.

[3] Keller, M., et al., "A Ka-Band Dielectric Resonator Antenna Reflectarrays," *30th European Microwave Conference*, Paris, France, October 2000, pp. 272–275.

[4] Shaker, J., and L. Shafai, "Reflection Properties of Conducting Rectangular Elements Printed on a Dielectric Slab," *Canadian Journal of Physics*, Vol. 72, 1994, pp. 299–310.

[5] Munk, B., *Frequency Selective Surfaces: Theory and Design*, New York: John Wiley & Sons, 2000.

[6] Mussetta, M., et al., "Optimization of a Gangbuster Reflectarray Antenna," *Proceedings of IEEE International Symposium on Antennas and Propagations*, 2005, pp. 626–629.

[7] James, J. R., and P. S. Hall, (eds.), *Handbook of Microstrip Antennas*, London, U.K.: Peter Peregrinus, 1989, Chapter 6.

[8] Encinar, J. A., "Design of Two-Layer Printed Reflectarrays Using Patches of Variable Size," *IEEE Transactions on Antennas and Propagation*, Vol. 49, No. 10, October 2001, pp. 1403–1410.

[9] Encinar, J. A., and J. A. Zornoza, "Three-Layer Printed Reflectarrays for Contoured Beam Space Applications," *IEEE Transactions on Antennas and Propagation*, Vol. 52, No. 5, May 2004, pp. 1138–1148.

[10] Maci, S., et al., "Dual-Band Slot Loaded Patch Antenna," *IEE Proceedings of Microwaves and Antennas Propagation*, Vol. 142, No. 3, June 1995, pp. 225–232.

[11] Cadorete, D., et al., "A New Reflectarray Cell Using Microstrip Patches Loaded with Slots," *Microwave and Optical Technology Letters*, Vol. 44, No. 3, February 2005, pp. 270–272.

[12] Marnat, L., et al., "Accurate Synthesis of a Dual Linearly Polarized Reflectarray," *Proceedings of Third European Conference on Antennas and Propagation (EUCAP)*, 2009, pp. 2523–2526.

[13] Chaharmir, M. M. R., et al., "Wideband Reflectarray Research at the Communications Research Centre Canada," *Proceedings of ANTEM 2009*, Session TA1, Paper 053.

[14] Chaharmir, M. M. R., J. Shaker, and N. Gagnon, "Novel Broadband Dual-Band Linear Orthogonal Polarization Reflectarray," *Electronics Letters*, Vol. 45, No. 1, January 2009, pp. 13–14.

[15] Chaharmir, M. R., et al., "Design of Broadband, Single Layer Dual-Band Large Reflectarray Using Multi Open Loop Elements," *IEEE Transactions on Antennas and Propagation*, Vol. 58, No. 9, September 2010, pp. 2875–2883.

[16] Chaharmir, M. R., and J. Shaker, "Novel Broadband Reflectarray with Combination of Cross and Rectangle Loop Elements," *Electronics Letters*, Vol. 44, No. 11, May 22, 2008, pp. 658–659.

[17] Shaker, J., and M. Cuhaci, "Planar Reflector for LMCS Applications," *Electronics Letters*, Vol. 35, No. 2, February 1999, pp. 103–104.

[18] Moustafa, L., et al., "The Phoenix Cell: A New Reflectarray Cell with Large Bandwidth and Rebirth Capabilities," *IEEE Antennas and Wireless Propagation Letters*, Vol. 10, 2011, pp. 71–74.

[19] Javor, R. D., X. Wu, and K. Chang, "Design and Performance of a Microstrip Reflectarray Antenna," *IEEE Transactions on Antennas and Propagation*, Vol. 43, No. 9, September 1995, pp. 932–939.

[20] Chang, D., and M. Huang, "Multiple Polarization Microstrip Reflectarray Antenna with High Efficiency and Low Cross-Polarization," *IEEE Transactions on Antennas and Propagation*, Vol. 43, No. 8, August 1995, pp. 829–834.

[21] Chaharmir, M. M. R., et al., "Reflectarray with Variable Slots on Ground Plane," *IEE Proceeding of Microwaves, Antennas and Propagation*, Vol. 150, No. 6, December 2003, pp. 436–439.

[22] Carassco, E., J. Encinar, and M. Barba, "Wideband Reflectarray Antenna Using True-Time Delay Lines," *Proceedings of 2nd European Conference on Antennas and Propagation (EUCAP)*, 2007.

[23] Carassco, E., M. Barba, and J. Encinar, "Design and Validation of Gathered Elements for Steerable-Beam Reflectarrays Based on Patches Aperture-Coupled to Delay Lines," *IEEE Transactions on Antennas and Propagation*, Vol. 59, No. 5, May 2011, pp. 1756–1761.

[24] Li, J., et al., "Reflectarray Element Using Interdigital Gap Loading Structure," *Electronics Letters*, Vol. 47, No. 2, January 2011, pp. 83–85.

[25] Petosa, A., et al., "Recent Advances in Dielectric Resonator Antenna Technology," *IEEE Antennas and Propagation Magazine*, Vol. 40, No. 3, June 1998, pp. 35–48.

[26] Chang, D., and M. Huang, "A Slot Design for Uniform Aperture Field Distribution in Single-Layered Radial Line Slot Antennas," *IEEE Transactions on Antennas and Propagation*, Vol. 39, No. 7, July 1991, pp. 954–959.

[27] Keller, M., et al., "A Ka-Band Dielectric Resonator Antenna Reflectarray," *Proceedings of 30th European Microwave Conference*, 2000.

[28] Jamaluddin, M., et al., "A Dielectric Resonator Antenna (DRA) Reflectarray," *Proceedings of European Microwave Conference*, 2009, pp. 25–28.

[29] Heui, Y., W. Byun, and M. Song, "High Gain Metal-Only Reflectarray Antenna Composed of Multiple Rectangular Grooves," *IEEE Transactions on Antennas and Propagation*, Vol. 59, No. 12, December 2011, pp. 4549–4568.

[30] Pozar, D. M., "Wideband Reflectarrays Using Artificial Impedance Surfaces," *Electronics Letters*, Vol. 43, No. 3, February 1, 2007, pp. 148–149.

[31] Zhao, G., et al., "A Subwavelength Element for Broadband Circularly Polarized Reflectarrays," *IEEE Antennas and Wireless Prop. Letters*, Vol. 9, 2010, pp. 330–333.

[32] Nayeri, P., F. Yang, and A. Z. Elsherbeni, "Broadband Reflectarray Antennas Using Double-Layer Sub-Wavelength Patch Elements," *IEEE Ant. and Wireless Prop. Letters*, Vol. 9, 2010, pp. 1139–1142.

[33] Almajali, E., et al., "Observations on the Performance of Reflectarrays with Reduced Inter-Element Spacings," *IEEE Intl. Symp. on Antennas and Prop. (URSI/APS)*, Spokane, WA, July 3–8, 2011.

[34] Ethier, J., M. R. Chaharmir and J. Shaker, "Novel Approach for Low-Loss Reflectarray Designs," *IEEE International Symposium on Antennas and Propagation (URSI/APS)*, Spokane, WA, July 3–8, 2011.

[35] Chaharmir, M. R., et al., "Novel Low-Cost Reflectarray Designs for Commercial Applications," *33rd ESA Antenna Workshop*, Noordwijk, the Netherlands, October 18–21, 2011.

[36] Ethier, J., M. R. Chaharmir, and J. Shaker, "New Developments in Reflectarray Research at the Communications Research Centre Canada (CRC)," *Proceedings of the 16th International Symposium on Antenna Technology & Applied Electromagnetics (ANTEM 2012)*, Toulouse, France, June 2012.

[37] Ethier, J., M. R. Chaharmir and J. Shaker, "Reflectarray Design Comprised of Sub-Wavelength Coupled-Resonant Square Loop Elements," *Electronics Letters.*, Vol. 47, No. 22, October 2011, pp. 1215–1217.

[38] Marcuvitz, N., *Waveguide Handbook*, New York: McGraw-Hill, 1951.

[39] Ethier, J., et al., "Reflectarray Design Using Similarity-Shaped Fragmented Sub-Wavelength Elements," *Electronics Letters*, Vol. 48, No. 15, July 2012, pp. 900–902.

[40] Ethier, J., "Antenna Shape Synthesis Using Characteristic Mode Concepts," Doctoral Thesis, University of Ottawa, 2012

[41] Milon, M. A., et al., "Surrounded Element Approach for the Simulation Reflectarray Radiating Cells," *IET Microwaves, Antennas & Propagation*, Vol. 1, No. 2, 2007, pp. 289–293.

[42] Ethier, J., M. R. Chaharmir, and J. Shaker, "Reflectarray Thinning Using Sub-Wavelength Coupled-Resonant Elements," *Electronics Letters*, Vol. 48, No. 8, March 2012, pp. 359–360.

CHAPTER 4

Different Types of Reflectarrays

Inherent flexibility in the type of cell elements that can be used in reflectarrays and creative ways of synthesizing the lattice structure to accommodate different types of cell elements on the same substrate give rise to many variations of reflectarrays to address specific operational conditions and specifications. Polarization and/or frequency sensitivity of the cell elements can be exploited to realize multiband/multipolarization reflectarrays with simplified feed apparatus as will be discussed.

While the design of the feed for multiband circularly polarized (CP) conventional reflectors can be a challenging task, a particular cell element is suggested in this chapter to realize a dual-band CP reflectarray with simplified two single-band linearly polarized (LP) feed structures. Folded reflectarrays will be introduced subsequently as a compact alternative for reflectarray structures. Power combining and beam splitting using reflectarrays will also be discussed. There has not been much precedence in using a conventional reflector structure in such applications. Beam shaping by realization of given aperture phase distribution is subsequently presented. Subreflectarray design equations are derived afterwards as a special case of shaped-reflector structure in the sense that the structure transforms a given spherical wave to another spherical wave (whether being used in Cassegrain or Gregorian configuration).

4.1 Multiband Reflectarray

The elements of the reflectarray can be selected based on their band of operation and then set into a periodic lattice configuration either on the same layer [1–3] or on separate layers [4, 5]. Another possibility for the realization of multiband reflectarray structures is to replace the ground plane with an FSS and judiciously cascade reflectarray thus constructed [6–8].

4.1.1 Single-Layer, Dual-Band Reflectarray with Interlaced Elements

Printed microstrip patch and dipole were discussed in detail in Chapter 3 as the cell element of reflectarray. Frequency-sensitive behavior of such cell elements can be exploited to realize multiband, single-layer reflectarrays. Dipole and microstrip patch elements that operate in two different bands can be interlaced onto the same layer of substrate as shown in Figure 4.1. The reflectarray was designed to operate

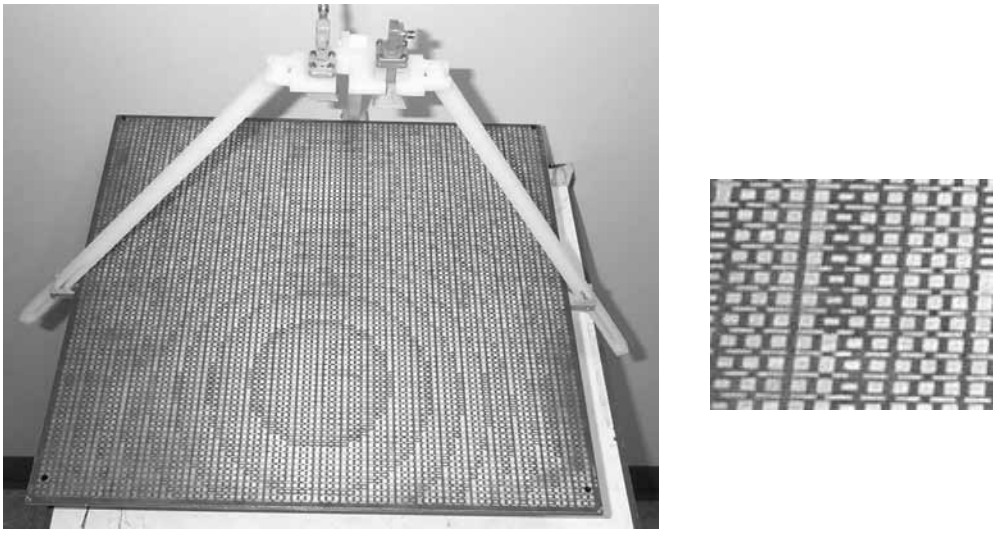

(a) (b)

Figure 4.1 Views of bifocal dual-band reflectarray. The antenna size is 44 cm × 44 cm, F/D is 0.5, and the separation between the feeds is 5.0 cm. (a) Photo of bifocal dual-band reflectarray. (b) Close-up view of the reflectarray lattice. (© 2000 IEEE. *From:* [2]. Reprinted with permission.)

with Rx/Tx bands of the Ka-band corresponding to 20/30 GHz. To satisfy more stringent link budget and bandwidth requirements for the Tx band, wider band microstrip patches were employed as the cell element for that band and thin printed dipoles were utilized as the cell element of the lower 20-GHz band. The polarization of the Tx and Rx bands were orthogonal linear with respect to each other, which simplifies the design and operation of the reflectarray.

The phase-length characteristics of the elements at the upper and lower bands are shown in Figure 4.2. It can be seen the slope of plot for lower-band elements is steeper as compared to the one for higher-band elements. Also, it should be noted that the variable dimensions of the Rx-band and Tx-band elements are orthogonal to each other to accommodate the orthogonal linear polarizations of the two bands. The reader should note that the phase versus length plots of Figure 4.2 have been generated using an in-house software that enforces $e^{-j\omega t}$ time dependence. This reversed hysteresis plots as compared to the general phase plots that were given in the previous chapter.

As shown in Figure 4.1, two pyramidal horns have been used to feed the reflectarray, which simplifies significantly the feed apparatus of the reflectarray as compared to conventional reflectors for which the feeding structure must be a wideband horn in conjunction with an orthomode transducer to separate the two bands from each other. Variation of the gain of the reflectarray is given in Figure 4.3. The typical radiation pattern of the antenna in Tx/Rx bands are shown in Figures 4.4 and 4.5, which show scanned beam in the E-plane for both bands.

The isolation between the upper and lower bands was measured as well and the result is shown in Figure 4.6, which demonstrates better than 45-dB isolation between the two bands. This high level of isolation between the two feeds relaxes the filtering specifications between the two operating bands quite significantly.

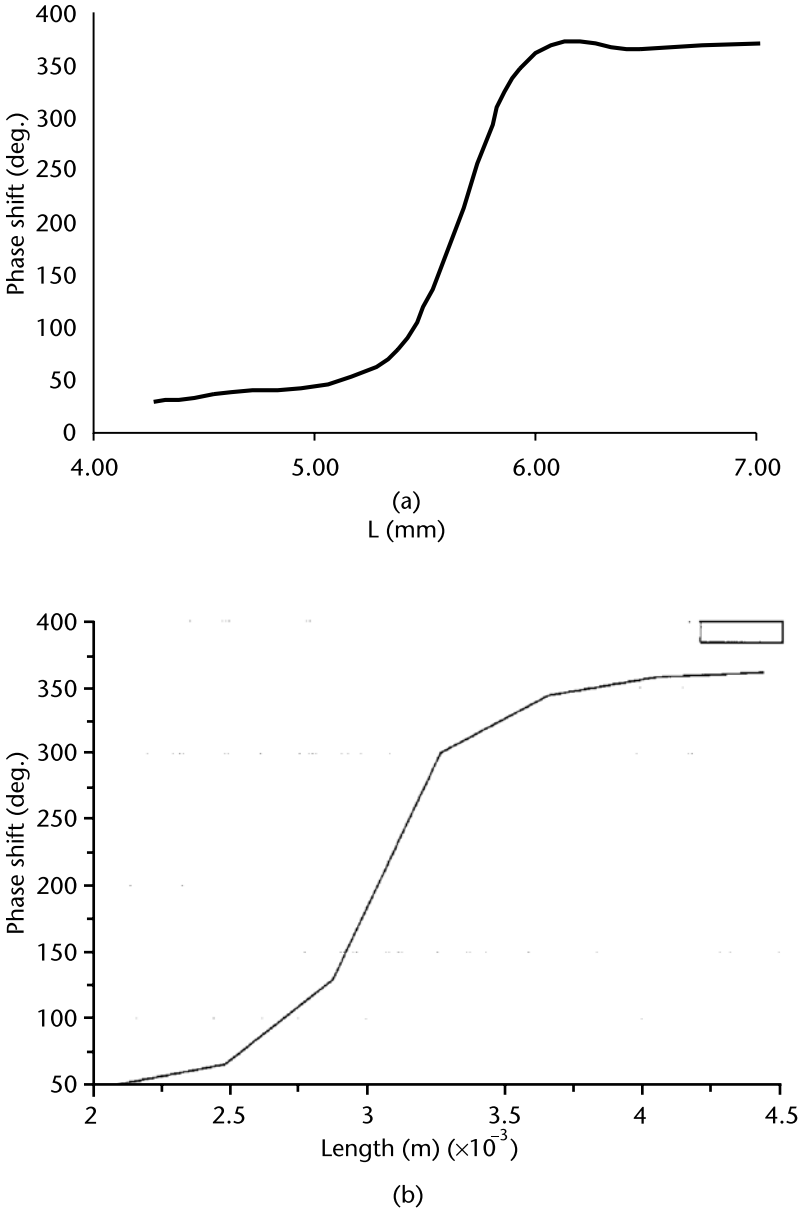

Figure 4.2 Phase shift of the reflected wave versus length for (a) lower-band and (b) upper-band elements. The structure is an infinite periodic structure of patches printed on grounded dielectric substrate of $\varepsilon_r = 2.2$ and substrate thickness = 0.020 inch. The lattice size was set to 0.5 cm × 0.5 cm for both the lower-band and upper-band cell elements and widths of the cell elements were set to 0.7 mm and 0.3 cm for the lower-band and upper-band elements, respectively. (© 2000 IEEE. *From:* [2]. Reprinted with permission.)

The design in Figure 4.1 was the first step of an exploratory study to design a Ka-band Tx/Rx reflectarray with active feeds for both bands. The feed block was composed of a cavity-backed microstrip with an LNA for the Rx band and an array of four patches along with power amplifiers for the Tx band as shown in Figure 4.7. Also shown in the same figure is the whole reflectarray structure along with the active feed block. The reflectarray was designed to divert its main beam to

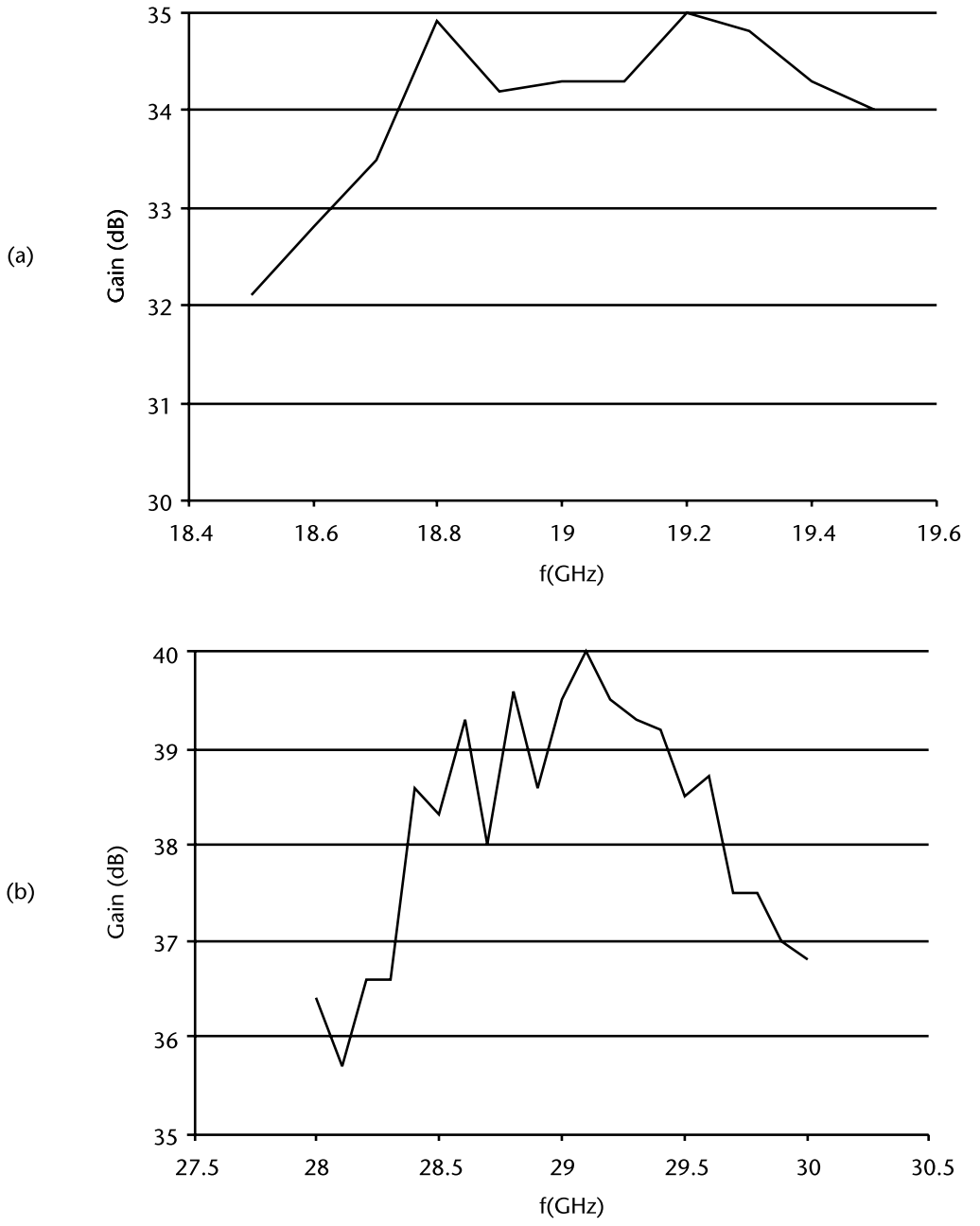

Figure 4.3 Frequency response of the gain of the bifocal dual-band reflectarray: (a) Rx and (b) Tx bands. (© 2000 IEEE. *From:* [2]. Reprinted with permission.)

$\theta = 26°$ to avoid blockage by the feed block and it was used to establish closed link to NASA Advanced Communication Satellite Technology (ACTS). Spatial separation between the Tx and Rx feed blocks reduced the filter requirements at the Rx side significantly. Further isolation between the two can be achieved by increasing their spatial separations.

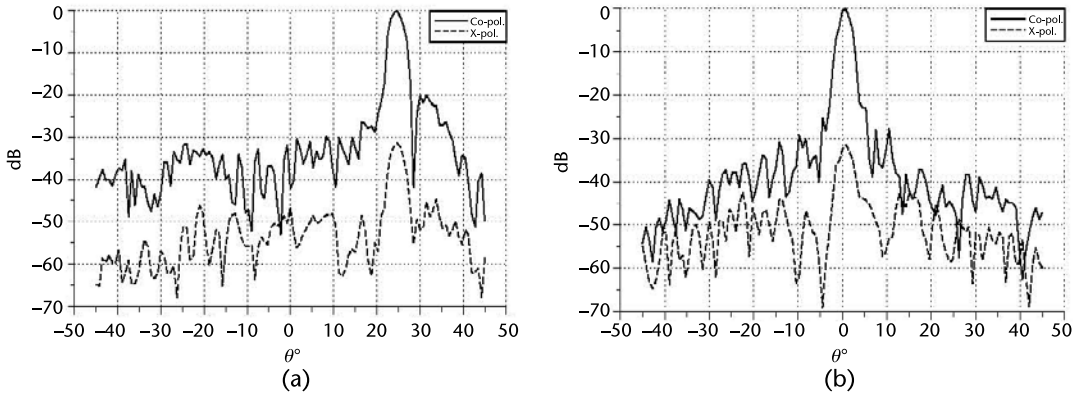

Figure 4.4 Copolarization and cross-polarization radiation patterns of the flat reflector at f = 29.2 GHz: (a) E-plane and (b) H-plane. (© 2000 IEEE. *From:* [2]. Reprinted with permission.)

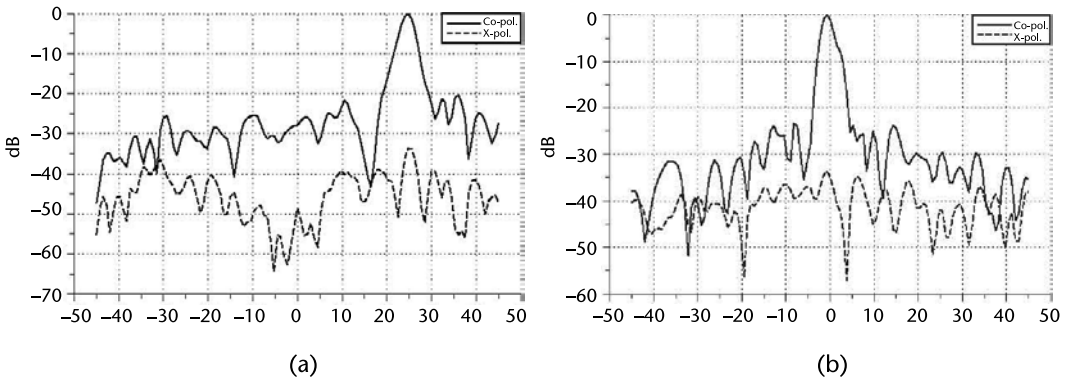

Figure 4.5 Copolarization and cross-polarization radiation patterns of the flat reflector at f = 19.5 GHz: (a) E-plane and (b) H-plane. (© 2000 IEEE. *From:* [2]. Reprinted with permission.)

4.1.2 Dual-Band, Double-Layer Reflectarray with Stacked Elements

Stacked elements can be used rather than single-layer interlaced elements to achieve dual-band reflectarray performance. For the interlaced case, the choice of elements is restricted to geometries that can be embedded within a lattice structure, whereas this restriction is significantly alleviated for stacked elements [5].

The lower-band elements of a reflectarray with stacked elements are located on the top and higher-band elements are located on the bottom. Simulations should be carried out to ensure low cross coupling between the elements of the two bands; otherwise, the design process will become utterly complicated. Figure 4.8 shows a typical dual X/Ka-band reflectarray that was designed in NASA for deep-space telecommunication. Circular rings with gaps were used as the cell element for both bands.

The reflectarray is fed by circular polarized (CP) feed and narrow gaps were implemented within the rings. It has been established that the phase of the reflected CP field can be adjusted by rotating the rings [9]. Specifically, rotation of the ring by angle ψ imparts a phase of 2ψ on the reflected CP wave of the same handedness

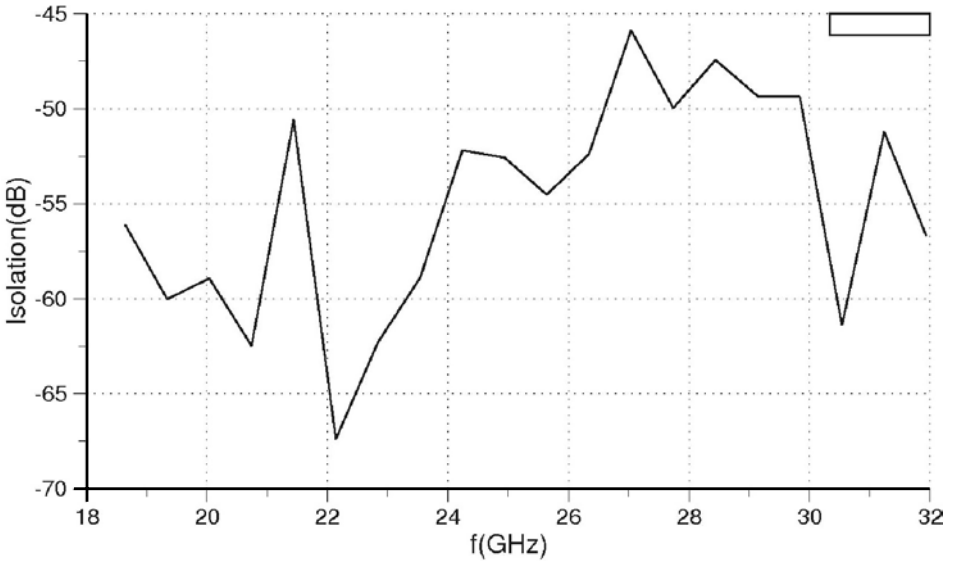

Figure 4.6 Measured isolation between the two feeds of the bifocal dual-band reflectarray shown in Figure 4.1 (© 2000 IEEE. *From:* [2]. Reprinted with permission.)

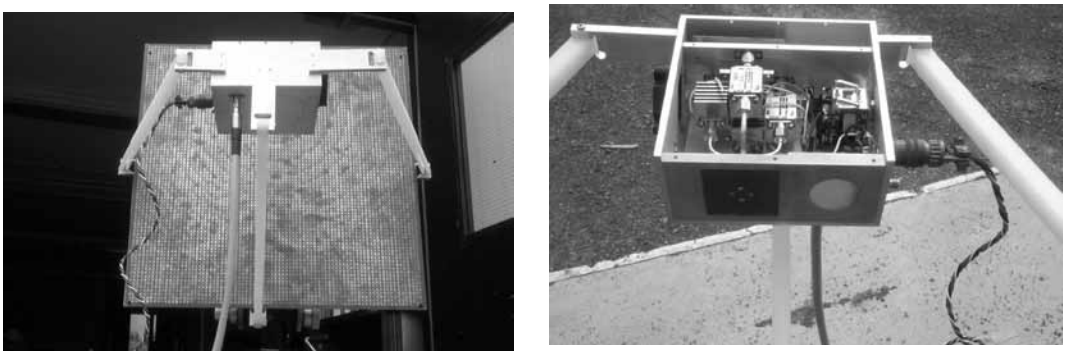

(a) (b)

Figure 4.7 Bifocal dual-band reflectarray fed by an active feed block: (a) close-up view of the active feed block and (b) the whole reflectarray structure. (© 2000 IEEE. *From:* [3]. Reprinted with permission.)

as the incoming CP field. The rings were intentionally made narrow to reduce their cross coupling. Typical radiation patterns of the reflectarray at its two operating bands are shown in Figure 4.9.

Measurement results for radiation patterns with and without X-band elements are shown in Figure 4.9. Relatively similar performance was observed for both cases in terms of side-lobe level, cross-polarization, and beam pointing which demonstrates relatively low coupling between the elements of the two bands.

In a different development, stacked patch cell element was used to design a reflectarray with distinct focal points for Tx/Rx Ka-band. The reflectarray configuration along with its cell are shown in Figure 4.10 Two different feeds are used for the V-polarization in the Tx band (30 GHz) and H-polarization in the Rx band (20 GHz) and orthogonal sides of the stacked patch cell elements were used to fo-

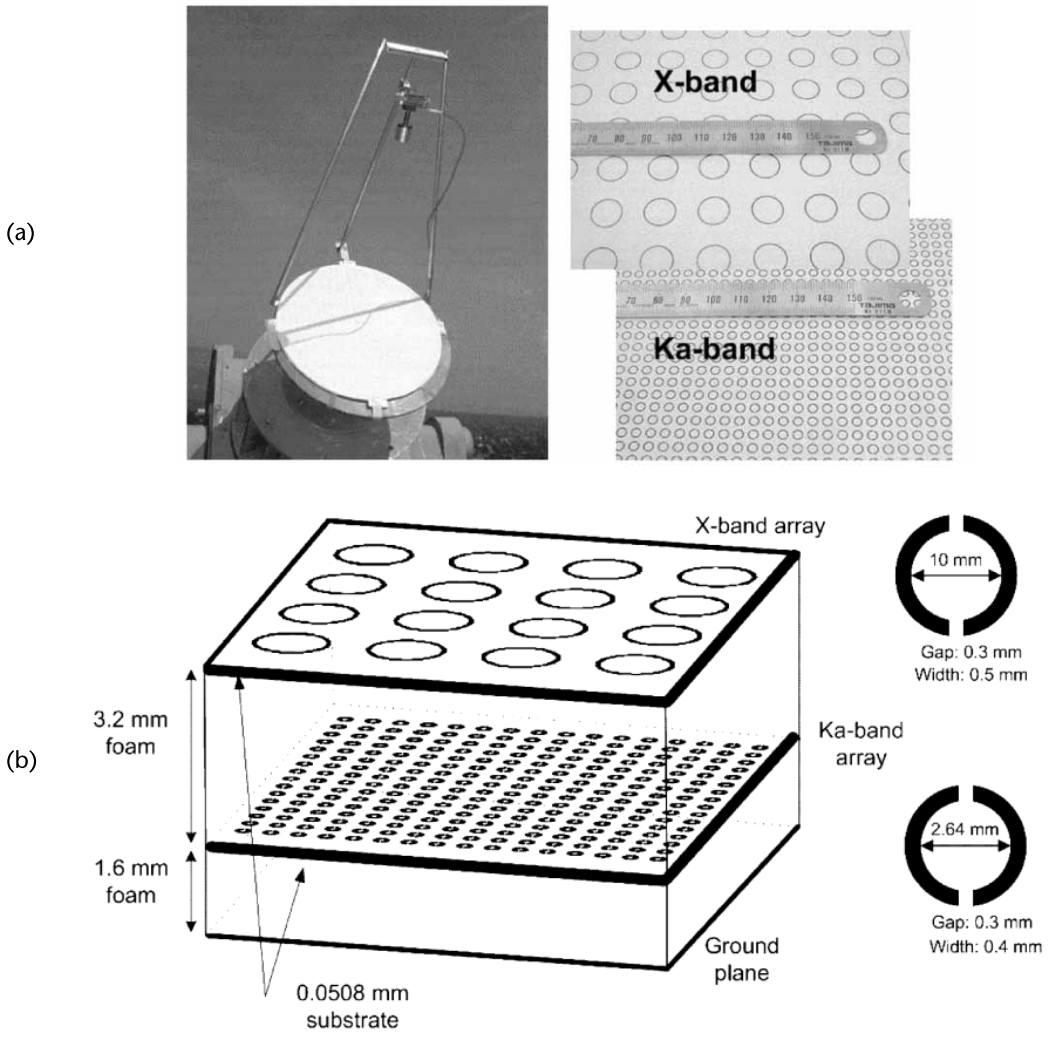

Figure 4.8 Dual-band reflectarray with stacked ring elements for X/Ka-band: (a) general view of the reflectarray and (b) configuration of the cell elements and their lattice structure. (© 2005 IEEE. *From:* [4].)

cus the given frequency band and polarization. Simulated and measured radiation patterns of the reflectarray within its operating bands are shown in Figure 4.11.

4.1.3 FSS-Backed Reflectarray

The flexibility endowed by innovative manipulation of the ground plane of a reflectarray has been largely neglected thus far. For instance, replacement of the ground plane with a frequency selective surface (FSS) that is reflective in the operating band of the reflectarray and transparent outside the same can provide a viable alternative for multiband/multipolarization operation [6–8]. Figure 4.12 shows two different implementations of FSS-backed reflectarrays.

In the first implementation that is shown in Figure 4.12(a), multiple FSS-backed reflectarrays are fed by separate feeds and cascaded to obtain multiband operation. Observing from the feed side, the reflectarray with higher operating band should

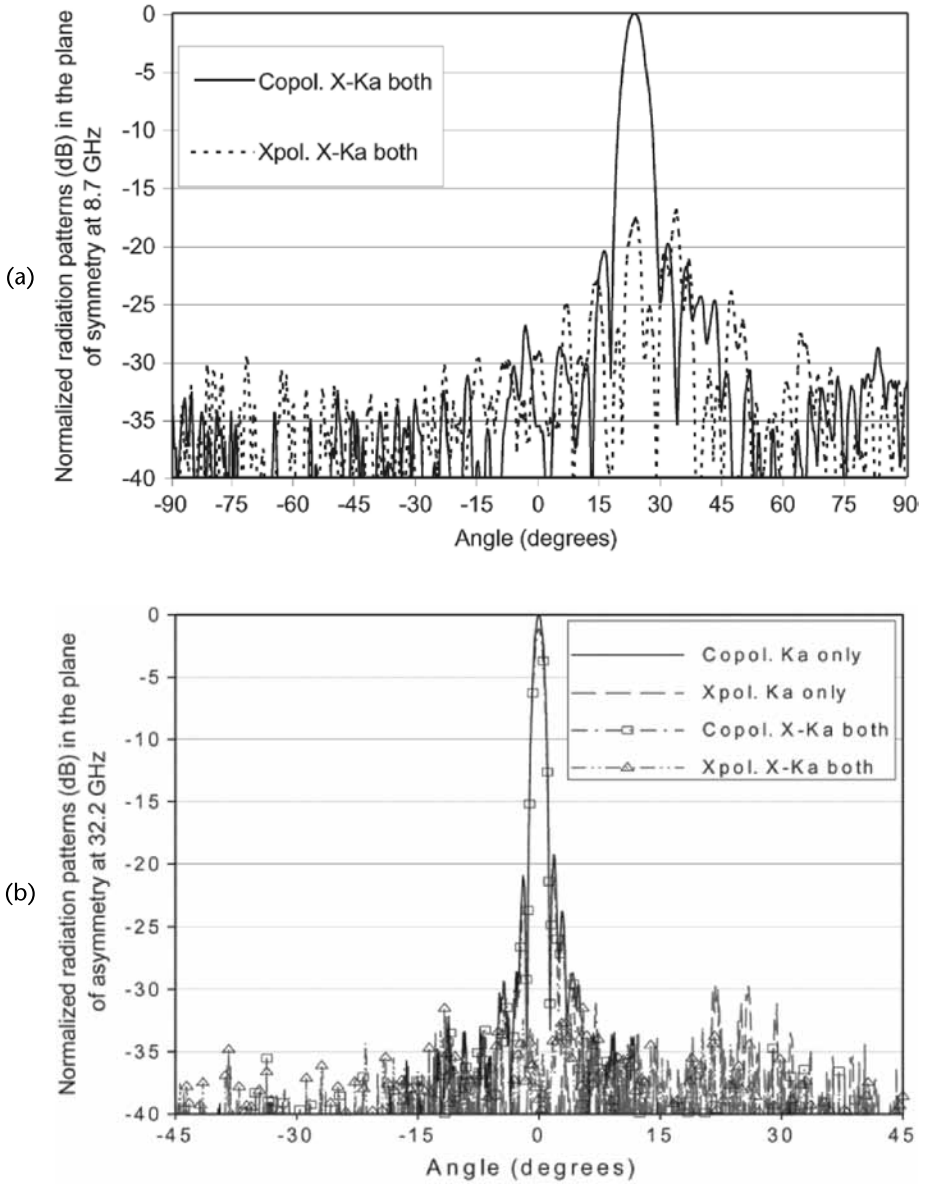

Figure 4.9 Measured radiation patterns of the X/Ka-band reflectarray in the (a) X-band and (b) Ka-band. (© 2005 IEEE. *From:* [4].)

precede the ones with lower operating band [6]. A reverse sequence in the placement of the reflectarrays might result in excitation of grating lobes at the higher bands. The second implementation that involves placement of an FSS-backed reflectarray on a conventional parabolic reflector is shown Figure 4.12(b). This section outlines the results for second implementation and more detailed information on the first implementation can be found in [7, 8].

The printed dipole was used as the cell element of both reflectarray and also FSS backing as shown in Figure 4.13. Reflected phase of the structure was calculated for constant size of elements on the FSS while the size of the elements on reflectarray side were changing and results are shown in Figure 4.14. It should be

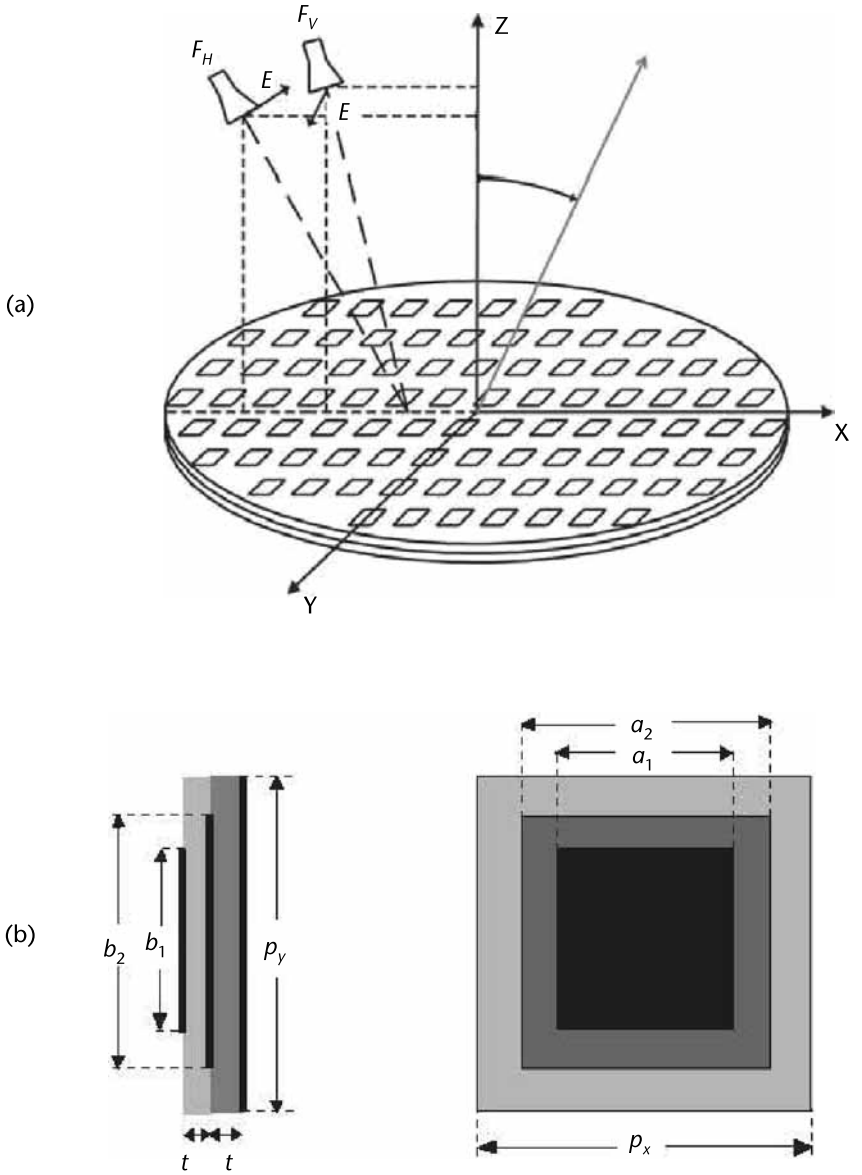

Figure 4.10 (a) Reflectarray with two separate feeds. (b) Stacked patch cell element. (© 2010 IEEE. *From:* [5].)

noted that both phase and amplitude have to be calculated in the design process as opposed to conventional reflectarray design that the focus is on the reflected phase response. Again, seemingly reverse orientation of the phase-length curve is caused by using $e^{-j\omega t}$ time dependence in the calculations.

A hybrid reflector-reflectarray structure is depicted in Figure 4.15. A foam housing was used to secure the relative location of the FSS-backed reflectarray with respect to the conventional solid offset-fed parabolic reflector. The operating frequency band of the reflector and reflectarray are the Ku-band and the Ka-band, respectively. The measured insertion loss of the FSS-backed reflectarray in the Ku-band was less 1.0 dB.

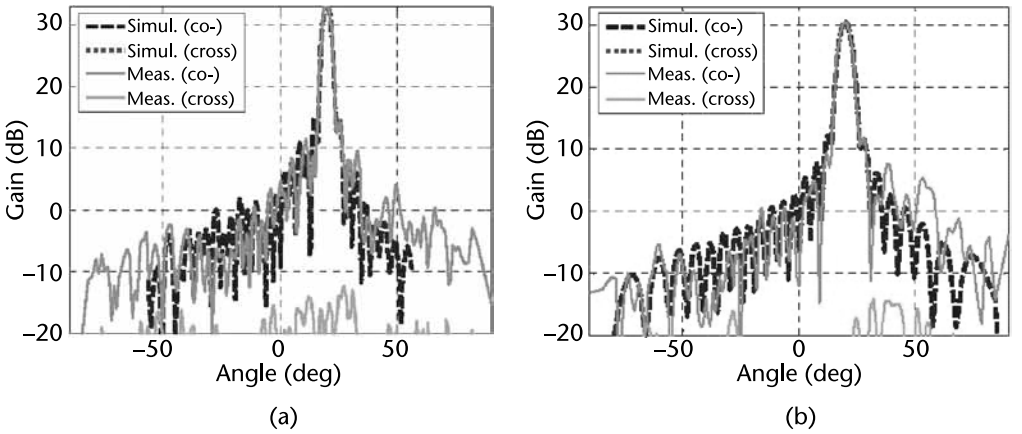

Figure 4.11 Radiation pattern of the dual-band reflectarray in the XZ plane at (a) 20 GHz and (b) 30 GHz. (© 2010 IEEE. *From:* [5].)

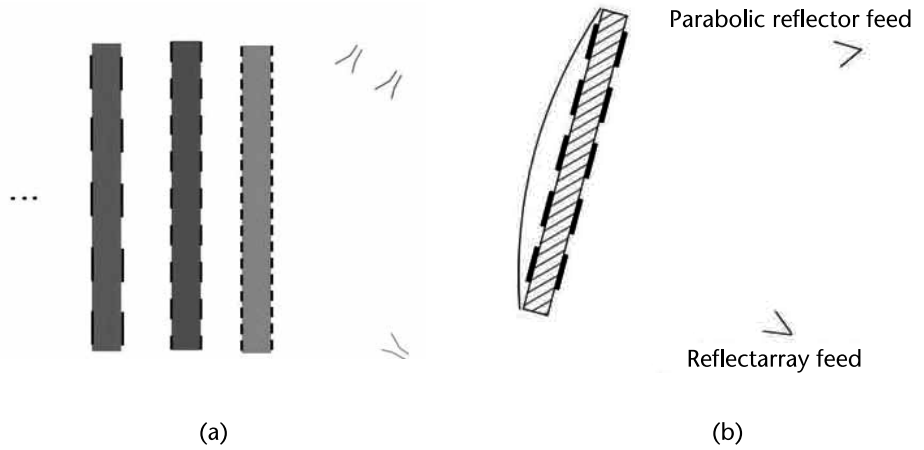

Figure 4.12 Two different scenarios for the application of FSS-backed reflectarray: (a) cascade of FSS-backed reflectarray structures and (b) cascade of a FSS backed reflectarray and conventional offset fed parabolic reflector. (© 2008 IEEE. *From:* [7]. Reprinted with permission.)

The radiation pattern of the whole assembly was measured in anechoic antenna chamber across its two operating bands and the results are shown in Figure 4.16. It is to be noted that the hybrid antenna maintains different beam pointing angles for its two operating bands, which shows the advantage of this hybrid structure with respect to a conventional reflector structure. Also, different positions for the operating bands focal points simplified feed structure significantly.

4.2 Circularly Polarized Reflectarrays

Two different methods have been introduced for the design of a circularly polarized (CP) reflectarray. In the first method, a CP feed illuminates the reflectarray comprised of elements that exhibit 180° phase difference in terms of their reflected

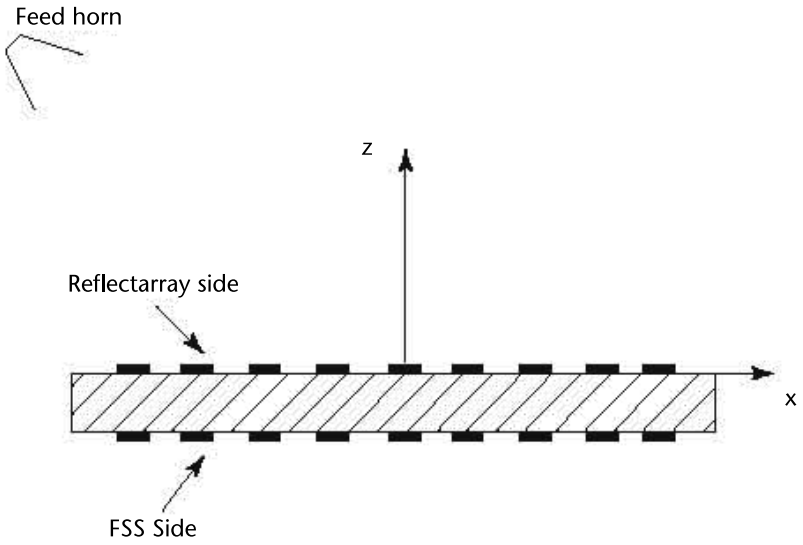

Figure 4.13 Side view of a typical FSS-backed reflectarray.

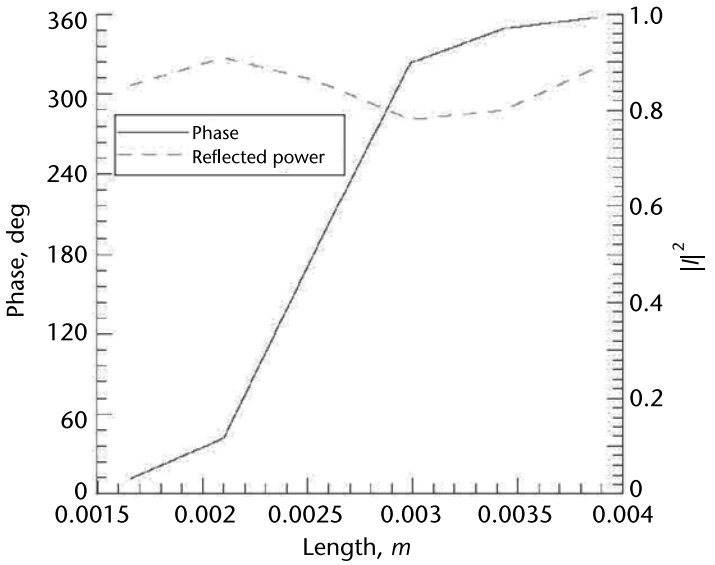

Figure 4.14 Simulation results for variation of phase and amplitude of reflected wave with respect to length of printed dipoles in upper surface, The following parameters were used in the simulation: $\varepsilon_r = 3.0$, substrate thickness = 0.0508 cm, length of dipoles on FSS side = 0.35 cm, dipole width = 0.2 cm, and lattice dimension is 0.6×0.6 cm, and $f = 27.6$ GHz. (© 2005 IEE. *From:* [6]. Reprinted with permission.)

phase response to the two orthogonal linear polarizations [9]. It was proven in [9] that rotation of such elements by ψ leads to 2ψ phase shift in the reflected phase when two-dimensional infinite lattice is illuminated by CP wave. The condition of 180° phase difference between the two orthogonal linear polarizations can be maintained by using dual stub-loaded patch cell element as shown in Figure 4.17.

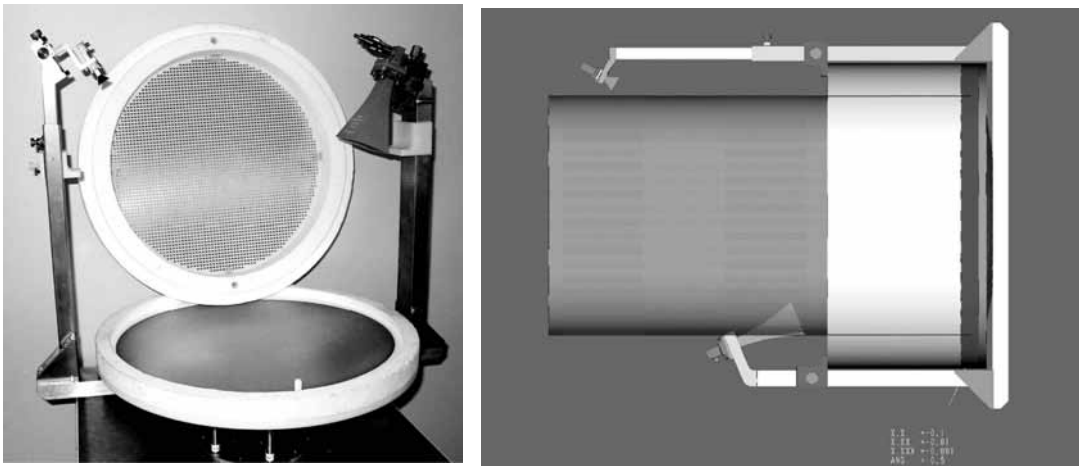

(a) (b)

Figure 4.15 Two different views of the hybrid antenna system. The position of the reflectarray focal point with respect to the reflectarray center: Xf = 24 cm, Yf = 0.0 cm, and Zf = 36.0 cm, the diameter of the reflectarray = 40.0 cm. The position of the focal point of the offset reflector with respect to the reflector center: Xf = 20 cm, Yf = 0.0 cm, and Zf = 32.0 cm, $\theta_i = 18.01$, $\theta_o = 78.01$, diameter of the offset reflector = 44.0 cm (Z-axis is normal to the surface of reflectarray). (a) Side view of the reflectarray and the offset reflector. Reflectarray is held by a foam frame 10.0 cm away from the offset reflector rim. (b) The foam holder is used to keep the reflectarray away from the offset reflector. (© 2005 IEE. *From:* [6]. Reprinted with permission.)

The radiation pattern and efficiency of a reflectarray that was designed based on this principle are shown in Figure 4.18.

A split square loop cell element is also introduced in [10] to generate CP at X-band using CP feed. In this method which is depicted in Figure 4.19, the position of slots along the perimeter of the square loop is moved instead of rotating the whole element as discussed before. It is observed that when the slot position is moved along the perimeter of the square loop, the resonant frequency of the structure will shift due to the corner effect. To maintain the same operating frequency, the slot width needs to be adjusted. Furthermore, it is important to point out that as shown in Figure 4.20 the phase variation is no longer a linear function of the rotation angle as the conventional method.

A second strand in the design of CP reflectarrays is to synthesize elements that simultaneously transform incoming linear polarization (LP) to CP and also collimate the beam [11]. The mechanism of LP to CP transformation is described in Figure 4.21. The incoming linearly polarized wave is aligned at 45° with respect to the two arms of the cross dipole and hence decomposed equally into components parallel to the arms. The lengths of the vertical arms have been adjusted to impart 90° phase difference between the two orthogonal vector components of the reflected wave which is equivalent to excitation of a CP wave, the handedness of which depends on phase lead or lag relationship between the phases of these two vector components. The same principle can be applied to any element with different phase response with respect to the two orthogonal linear polarizations. However, the amount of the phase shift can be adjusted to obtain beam collimation as well. Figure 4.22 shows a dual-band 20/30 GHz CP reflectarray with opposite CP handedness for the two bands. The reflectarray utilizes interlaced cross dipoles for the both operating bands.

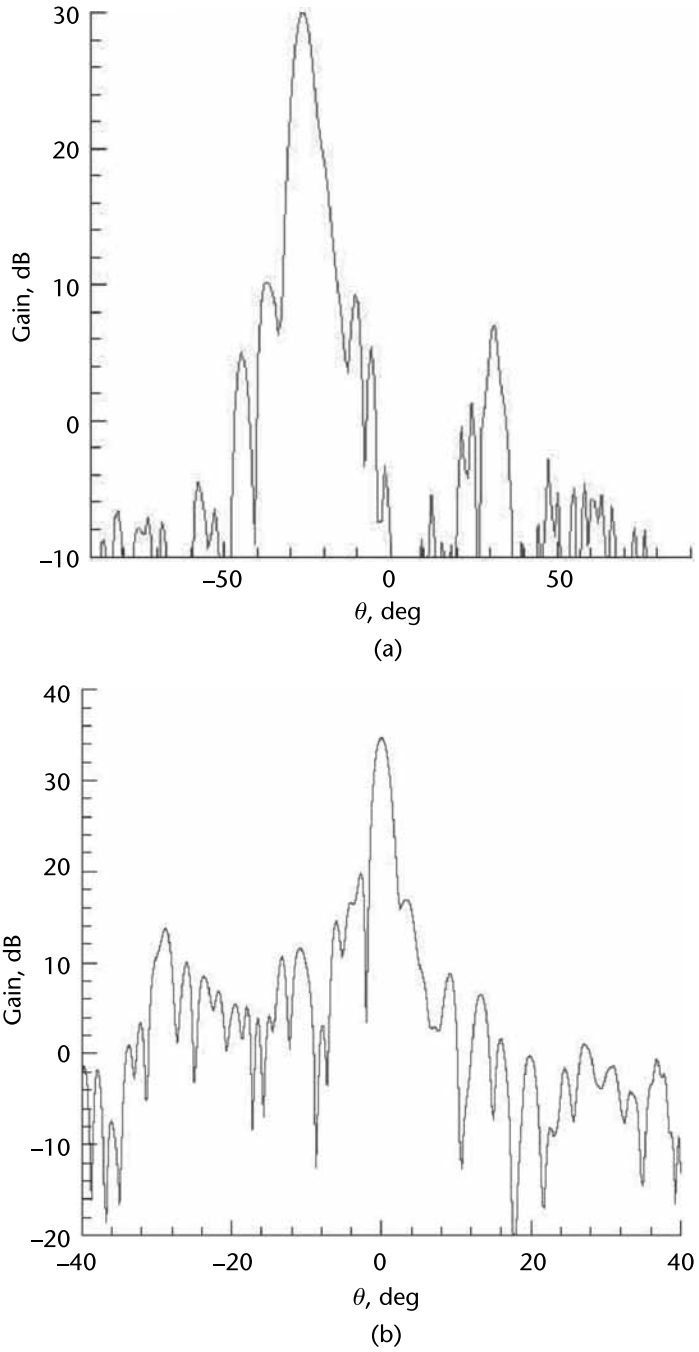

Figure 4.16 (a) Measured E-plane radiation pattern of hybrid antenna system at the lower band, $f = 11.0$ GHz. (b) Measured E-plane radiation patter of hybrid antenna system at the upper band, $f = 27.4$ GHz.

Coupling between cross arms at each given band and also between elements at the upper and lower bands were extensively studied. Such an analysis is required for the design of any dual band reflectarray to guaranty fulfillment of design specifications. To estimate the effect of the lower-band elements on the higher-band dipoles, the phase versus length curve of the higher-band dipoles was calculated,

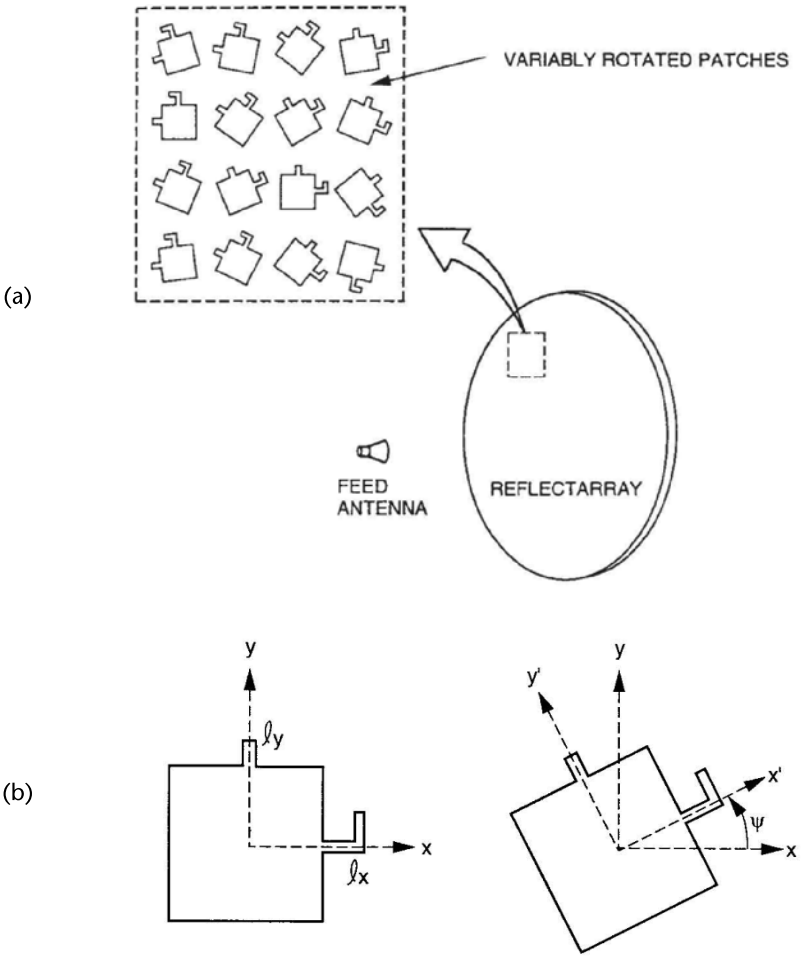

Figure 4.17 (a) Circularly polarized microstrip reflectarray with elements having variable rotation angles. (b) Cell element of the CP reflectarray and its rotated version. Rotation of the element by ψ leads to 2ψ shift in the reflected phase of the CP incident wave. (© 1998 IEEE. *From:* [9]. Reprinted with permission.)

while the lengths of the lower-band dipoles were kept constant. The same procedure was repeated for lower-band elements to estimate the effect of the higher-band elements on the lower-band operation. The structure was illuminated by a *y*-polarized normal incident plane wave. The unit cell that was used in the simulations is shown in Figure 4.23. The coupling between the cross dipoles of the two different bands are shown in Figures 4.24 and 4.25.

Using these concepts and design guidelines that were described in the preceding sections, a 45.0 cm × 45.0 cm dual-band CP single-layer reflectarray with *F/D* = 0.5, as shown in Figure 4.26, was designed and fabricated. The feeds of the two bands were set 5.0 cm apart from each other. The antenna was tested in the planar near-field facilities and the results are shown in Figure 4.27. Also, the gain and the axial ratio performance of the reflectarray are listed in Table 4.1 for single frequencies in the lower and upper bands. Aperture efficiency close to 34% was achieved for both the upper and lower bands and the axial ratio is less than 1.5 dB for the design frequencies.

(a)

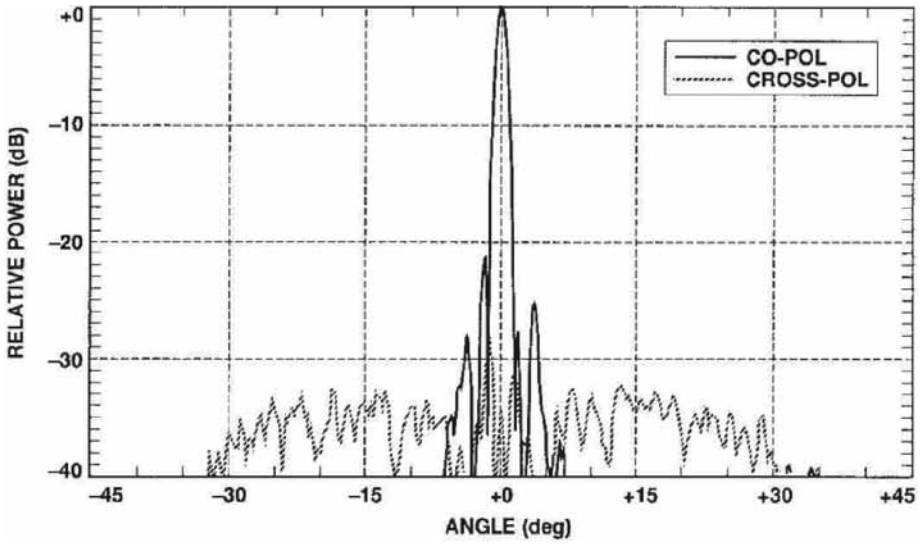

(b)

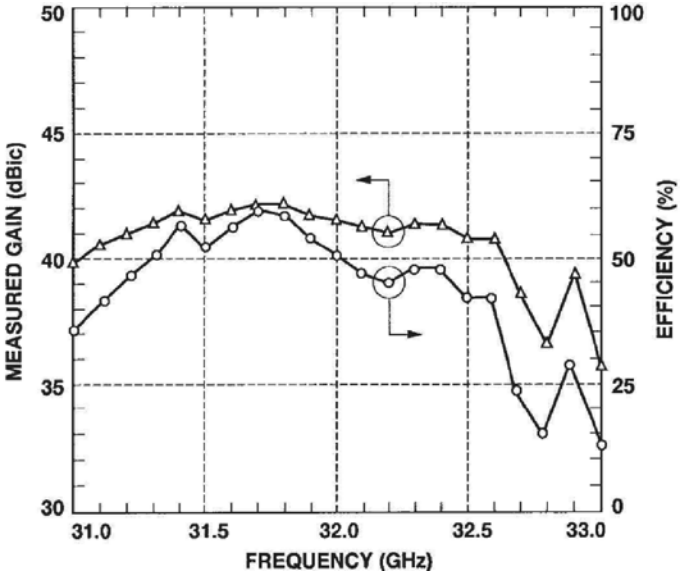

Figure 4.18 (a) Measured copolarization and cross-polarization radiation patterns of the reflectarray with rotated stub-loaded elements, f = 32 GHz. (b) Measured gain and efficiency of the reflectarray across its operating band. (© 1998 IEEE. *From:* [9]. Reprinted with permission.)

4.3 Folded Reflectarray

The attempt to reduce volumetric constraints has led to the design of folded reflectarray structure [12]. This type of reflectarray utilizes multiple reflections of the rays that emanate from the feed along with polarization rotation to increase their optical paths before launching them into the free space. Figure 4.28 shows a view of the folded reflectarray and the path traversed by a typical ray. As indicated, the path of the ray with a given linear polarization starts at the feed and then reflected by the top surface that reflects only a given sense of polarization. Upon reflection from the top reflector, the ray meets the bottom surface that acts simultaneously

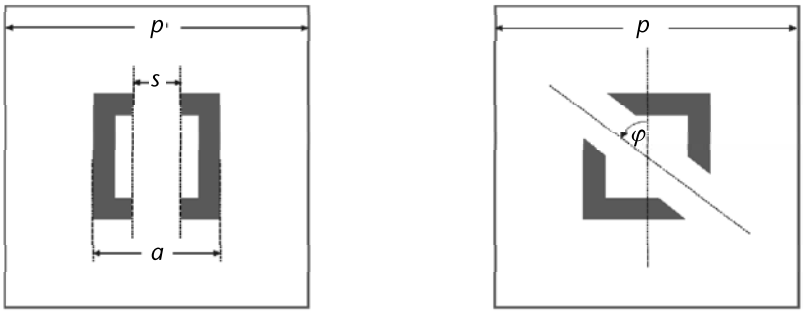

Figure 4.19 Single split square ring elements with (a) central slot and (b) offset slot. (© 2008 IEEE. *From:* [10]. Reprinted with permission.)

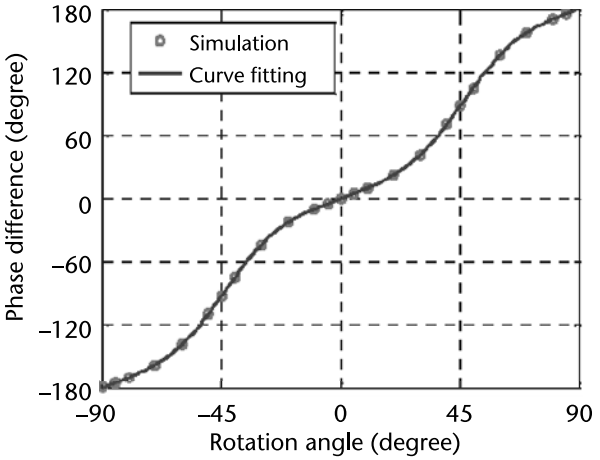

Figure 4.20 Reflected phase versus element rotation angle. (© 2008 IEEE. *From:* [10]. Reprinted with permission.)

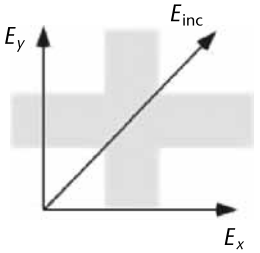

Figure 4.21 Description of LP to CP transformation for cross dipole cell element.

as a polarizer and also imparts the necessary phase shift onto that same ray to achieve a collimated beam in a given direction. The upper surface is a polarization filter comprised of strip of conductor which reflects the E-field with polarization parallel to the strips and is transparent to the E-field that is normal to the strip. The

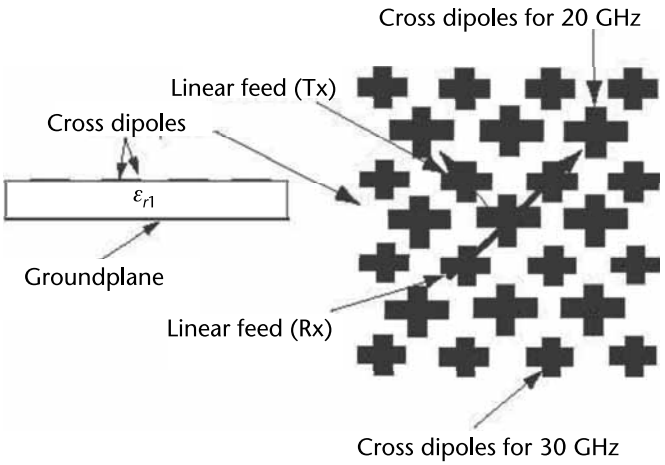

Figure 4.22 Schematic view of single-layer reflectarray antenna with cross dipoles of variable arm length on top surface (© 2006 IEE. *From:* [11]. Reprinted with permission.)

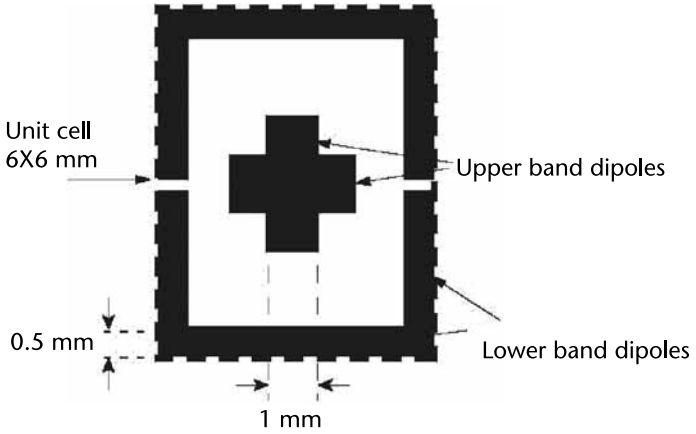

Figure 4.23 Schematic view of unit cell used for simulating the effect of lower-band dipoles on upper band dipoles (© 2006 IEE. *From:* [11]. Reprinted with permission.)

bottom reflectarray is composed of dipoles that are at 45° orientation with respect to the polarization of the wave that is reflected by the upper polarization filter. As described in Figure 4.28, the size of the dipoles is adjusted to rotate the E-field polarization by 90° and also provide the required phase shift for collimated beam.

The bottom surface of a typical folded reflectarray has been shown in Figure 4.29. The antenna was designed to operate in the V-band and the size of the antenna is 100 mm with $F/D = 0.5$. The measured 1-dB gain bandwidth of the antenna is about 6%. The measured radiation pattern of the antenna is shown in Figure 4.30.

Different versions of the folded reflectarray have been reported in the literature to obtain beam shaping and beam scanning [13]. In a novel implementation of this same concept, the top surface has been replaced by a reflectarray backed by a polarizer to provide both amplitude and phase control for beam shaping [13].

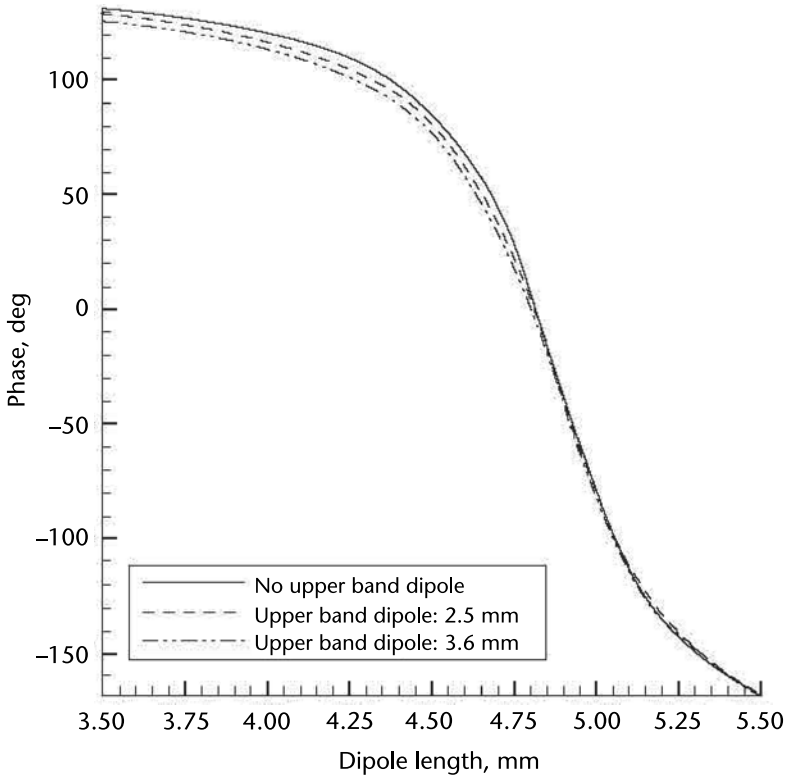

Figure 4.24 Effect of the upper-band dipoles on the lower-band dipoles of the single-layer reflectarray antenna with cross dipoles of variable arm length on top layer. (© 2006 IEE. *From:* [11]. Reprinted with permission.)

4.4 Power Combining and Beam Splitting

The structure of reflectarray is amenable to integration of active elements within the unit cell of the reflectarray or realization of phase front transformations that lead to novel application such as power combining and beam splitting. Power combining at higher millimeter-wave band is a measure to avoid the complexity of the design and operation of high-power amplifier. Figure 4.31 shows the cell element that is composed of a microstrip backed by orthogonal slots and used in [14] for the integration of amplifier within the cell element of the reflectarray. The microstrip captures a given polarization that is coupled into a given slot and passed through the microstrip line while being amplified by the amplifier. The amplified signal is coupled to the other slot and radiated by the microstrip in a polarization that is orthogonal to the incoming signal. This provides a degree of isolation between the input and output, which reduces the possibility of unwanted oscillation. The length of the microstrip line that connects the two slots is adjusted to achieve the desired phase front transformation.

Power combining can also be addressed at the feed level by using multiple feeds and adjusting reflectarray elements to achieve the phase shift required to combine the power of the multiple feeds. Figure 4.32 shows a reflectarray that is designed to combine the power of two feeds at $f = 30$ GHz [15]. The measurements demonstrated 33% radiation efficiency for the structure.

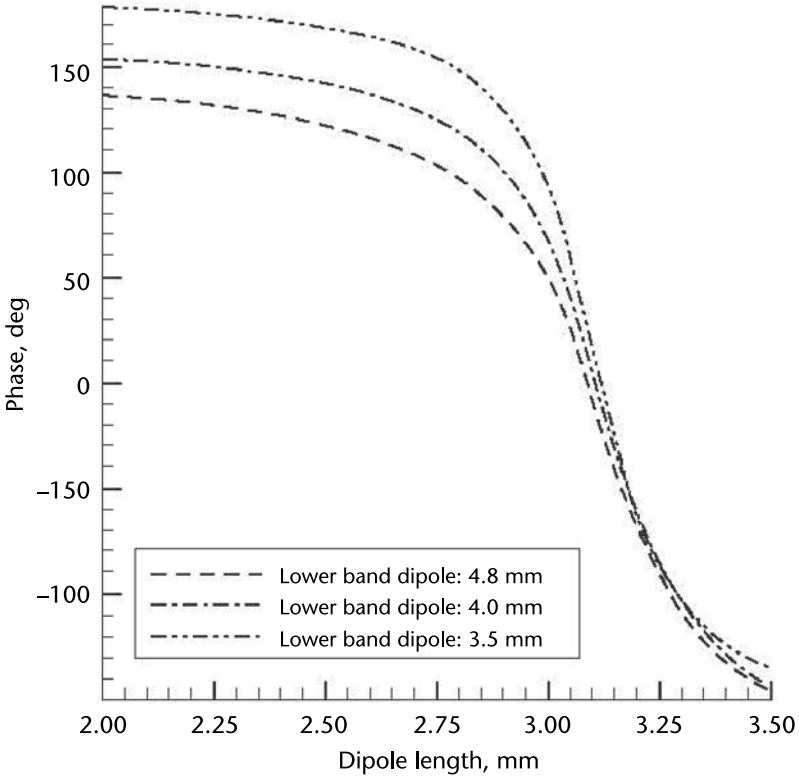

Figure 4.25 Effect of lower-band dipoles on upper-band dipoles of single-layer reflectarray antenna with cross dipoles of variable arm length on top layer. (© 2006 IEE. *From:* [11]. Reprinted with permission.)

Figure 4.26 Photograph of 45.0 cm × 45.0 cm dual-band CP reflectarray. (© 2006 IEE. *From:* [11]. Reprinted with permission.)

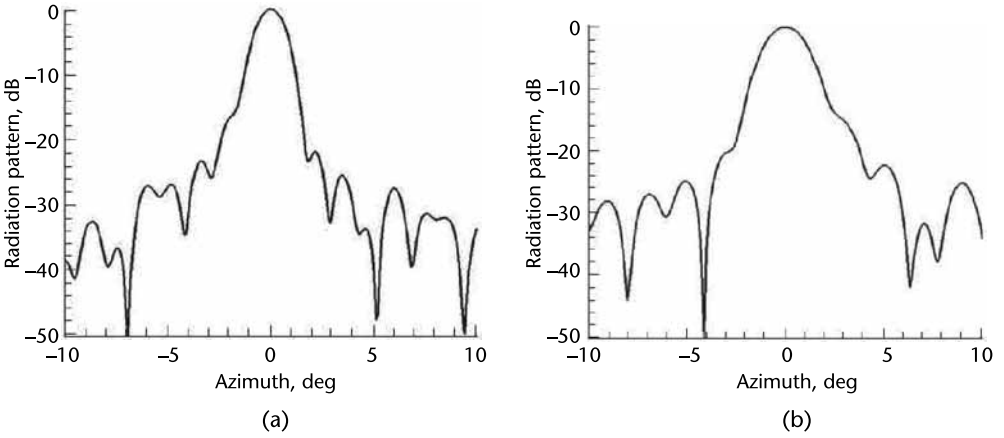

Figure 4.27 Measured radiation pattern of single layer 45 cm × 45 cm reflectarray (a) $f = 19.7$ GHz and (b) $f = 29.5$ GHz. (© 2006 IEE. *From:* [11]. Reprinted with permission.)

Table 4.1 Gain and Axial Ratio Performance of One-Layer 45 cm × 45 cm Reflectarray

	$f = 19.5$ GHz	$f = 29$ GHz	$f = 29.7$ GHz	$f = 30$ GHz
Gain, dB_{ic}	36.1	37.4	38.0	38.2
Axial Ratio, *dB*	1.2	1.3	1.2	1.2

Source: [11].

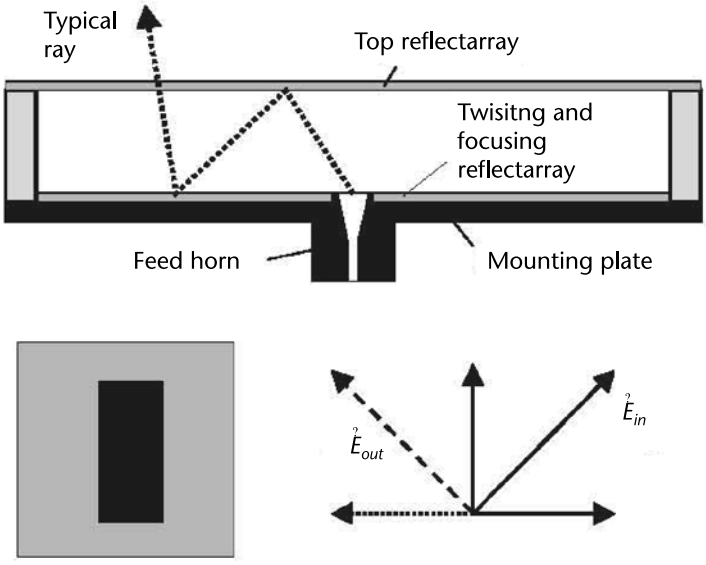

Figure 4.28 Cross section of a folded reflectarray setup. (© 2002 IEEE. *From:* [12]. Reprinted with permission.)

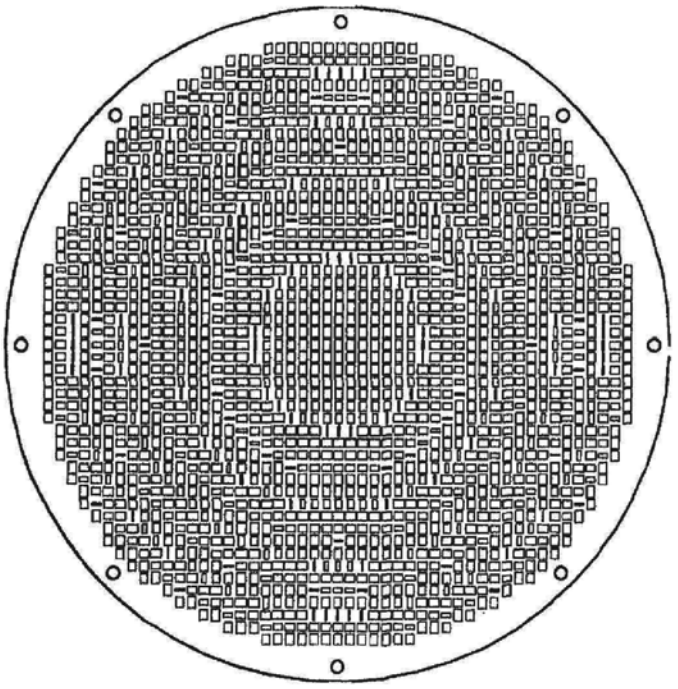

Figure 4.29 Layout of a V-band reflectarray for a folded reflectarray antenna. (© 2002 IEEE. *From:* [12]. Reprinted with permission.)

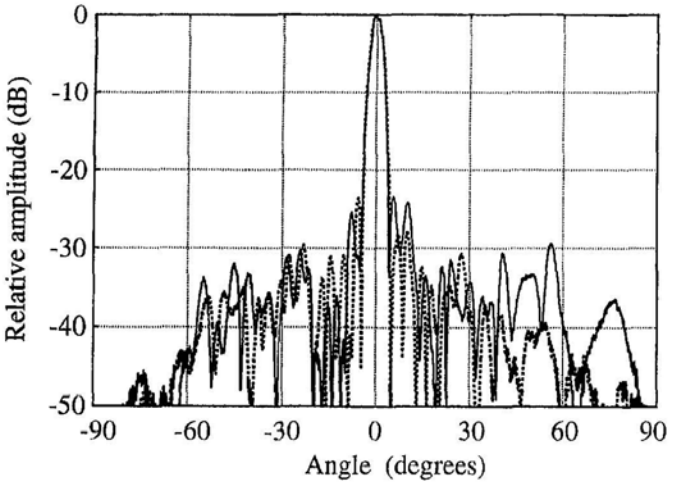

Figure 4.30 The E-plane (solid line) and H-plane (dotted line) radiation diagrams of the V-band folded reflector antenna. (© 2002 IEEE. *From:* [12]. Reprinted with permission.)

4.5 Subreflectarray Structures

Utilization of reflectarray technology in the context multiple reflector structures is a natural extension of earlier work on single reflectarray structures. Subreflectarray provides an appealing possibility for integration of active elements for beam shaping [16] and phase error correction on the main reflector [17].

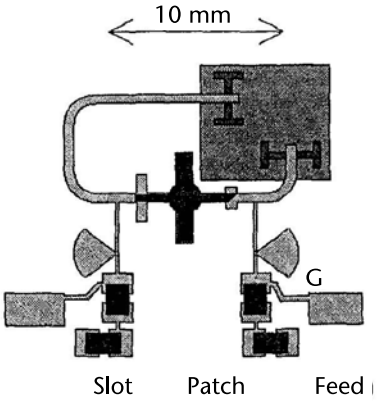

Figure 4.31 Cell element of the active reflectarray. (© 1997 IEEE. *From:* [14]. Reprinted with permission.)

The implementation of the subreflectarray in Cassegrain and Gregorian configurations involves the transformation of a given spherical wave that is generated by a feed located at one of the focal points of the subreflectarray into another spherical wave that emanates from the other focal point of the subreflectarray as depicted in Figure 4.33 for ellipsoidal or hyperboloid subreflectarray [18].

Noting the parameters that are defined in Figure 4.33, the required phase for the nth element on the ellipsoidal subreflectarray can be calculated from the following equation:

$$\psi_n = k\left(R_n + d_n\right) \pm 2p\pi \tag{4.1}$$

and similar equation can be derived for hyperboloid subreflectarray:

$$\psi_n = k\left(R_n - d_n\right) \pm 2p\pi \tag{4.2}$$

where k is free-space wavenumber in the above two equations and p is an integer. The geometrical parameters are defined in Figure 4.33. The similarity of these equations to similar equations to conventional subreflectors is quite interesting.

An ellipsoidal subreflectarray was designed based on (4.1) and fabricated and subsequently tested. The layout of the subreflectarray is shown in Figure 4.34. The size of the subreflectarray was 155 mm × 155 mm and the foci of the structure were $F_R = 155$ mm and $F_V = 61$ mm. The subreflectarray was etched on 0.020-inch-thick substrate with $\varepsilon_r = 3.0$. Both radiation pattern magnitude and phase were measured in anechoic far-field chamber. The phase pattern was initially measured with respect to a point at the center of the subreflectarray and then the phase center was shifted to the location of the other focal point of the ellipsoid through postprocessing of the measured phase data. Figure 4.35 shows HFSS simulation and measurement results for magnitude and phase of the subreflectarray structure.

Blockage was not accounted in the calculations which accounts for disagreement between simulated and measured results around boresight direction. It is observed that the reflectarray has managed to create a rather spherical phase front up to about 40°.

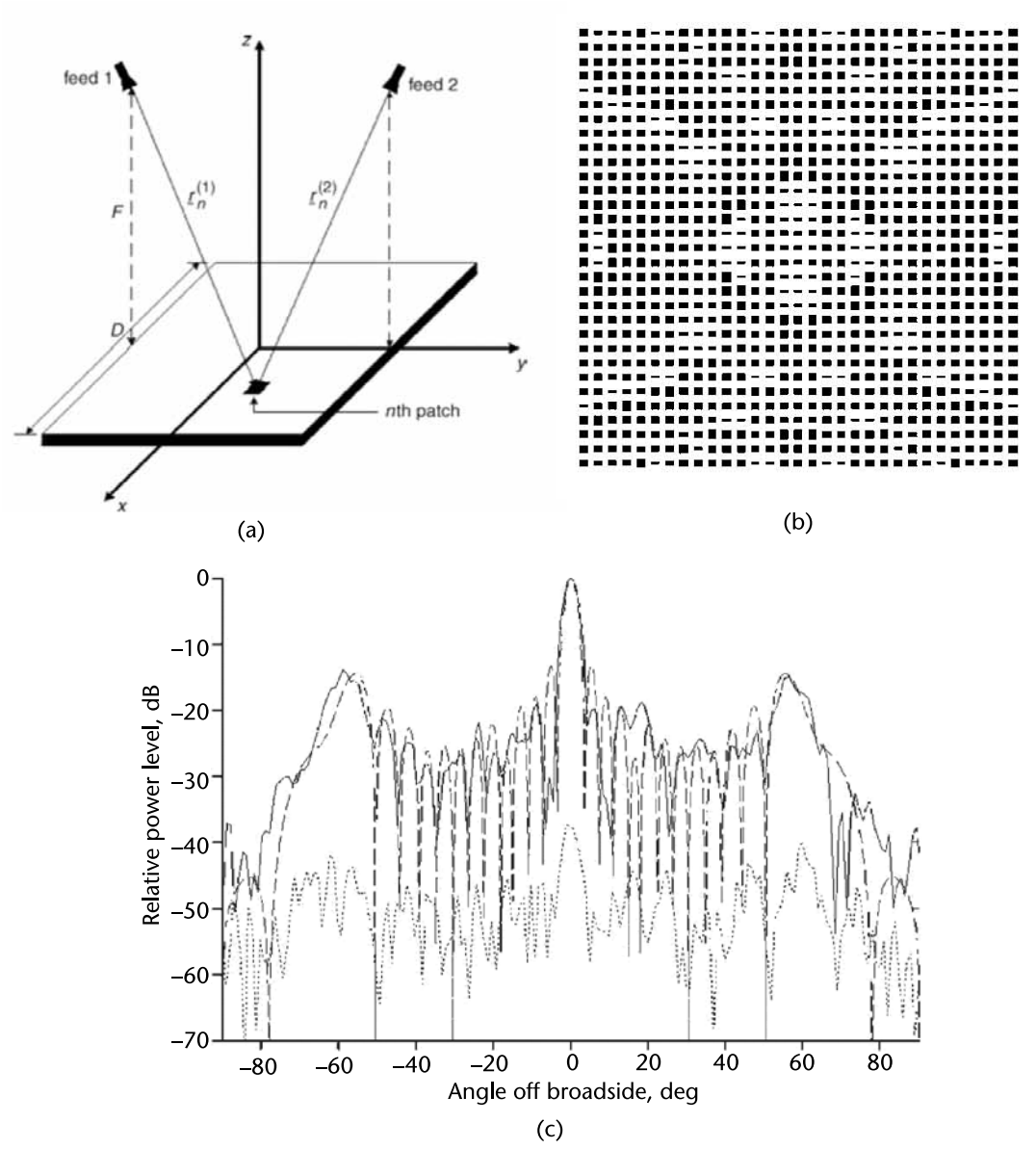

Figure 4.32 (a) Configuration of reflectarray with multiple feed, (b) top view of the reflectarray composed of microstrip patches, and (c) typical radiation pattern of the power combiner. (© 2004 IET. *From:* [15]. Reprinted with permission.)

4.6 Beam Shaping

Conventional solid reflectors are shaped in order to obtain a shaped beam [19]. As in the case of conventional solid reflectors, two different methods can be used for beam shaping in a reflectarray. One can either synthesize the main reflectarray to realize the specified phase front transformation [20, 21] or synthesize the subreflectarray of a dual reflector configuration to achieve the same [16, 22]. The subreflectarray approach is more advantageous when it comes to integration of

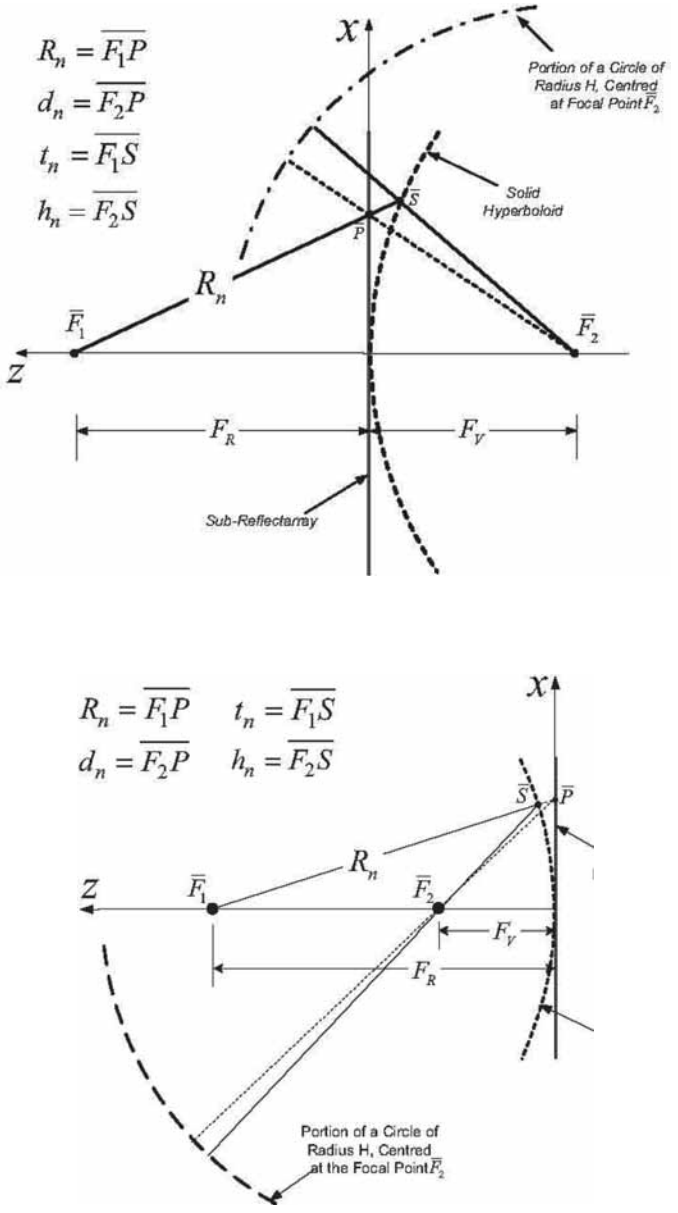

Figure 4.33 Diagram used in the derivation of the basic design equation for (a) hyperboloid subreflectarray and (b) ellipsoid subreflectarray. (© 2012 IEEE. *From:* [18]. Reprinted with permission.)

active elements for dynamic beam shaping because a much smaller number of active elements are required as compared to the main reflectarray with active elements. In both methods a given phase distribution over the reflectarray (whether main reflectarray or subreflectarray) is achieved by adjusting the cell elements. However, in the case of folded reflectarray, both phase and amplitude of the aperture field distributions can be optimized [13].

An early version of a shaped beam reflectarray was reported in [21] where the authors used microstrip patch as the cell element. The phase front transformation was projected onto the main reflectarray surface. Figure 4.36 shows the shaped

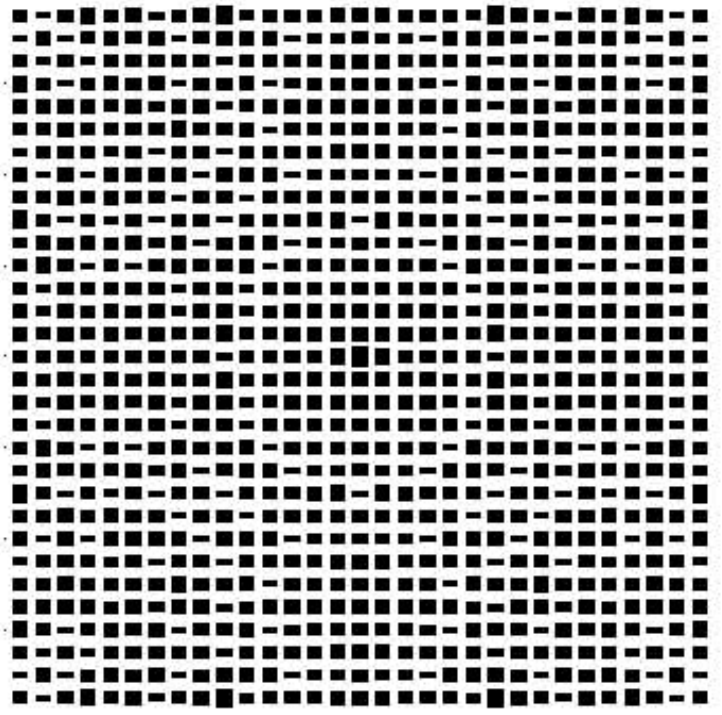

Figure 4.34 Layout of the ellipsoidal reflectarray. (© 2002 IEEE. *From:* [18]. Reprinted with permission.)

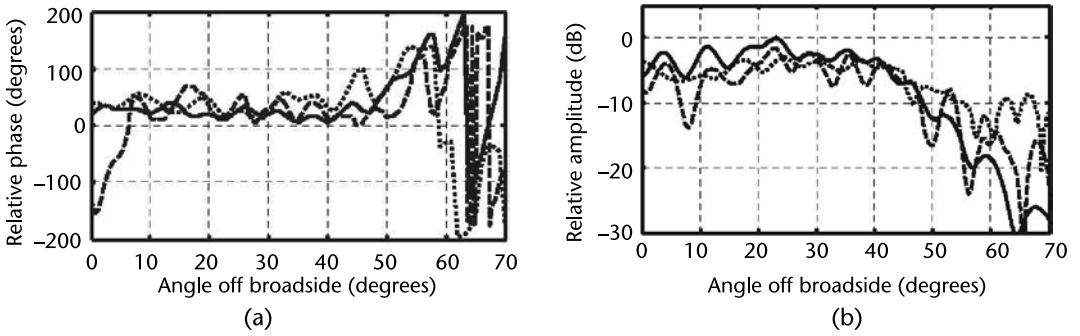

Figure 4.35 Measured (dashed line) and HFSS simulation (dotted line) array theory computed (solid line): (a) magnitude of the radiation pattern and (b) phase of the radiation pattern. (© 2002 IEEE. *From:* [18]. Reprinted with permission.)

reflectarray surface that was etched on the Duroid substrate of $\varepsilon_r = 2.2$ and was 0.062 inch thick. The cross section of the reflectarray was in the form of an ellipse with major and minor axes of 110.0 cm and 90 cm, respectively. It should be noted that the choice of microstrip patch as the element leads to a range of unattainable phase values that can lead to phase error. The shaped reflectarray was designed to illuminate continental Europe at 14.0 GHz with 5% bandwidth. The surface of shaped-beam reflector was first synthesized using TICRA [23] and it was then used to synthesize the required phase transformation on the face of the reflectarray. The reflectarray was fed by a corrugated horn. The antenna was designed for $f = 14.15$

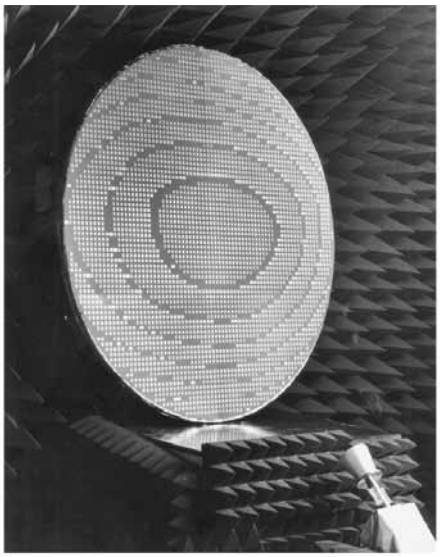

Figure 4.36 Photograph of prototype microstrip shaped-beam reflectarray. (© 1999 IEEE. *From:* [21]. Reprinted with permission.)

GHz as the center frequency and the measured coverage for three frequencies are shown in Figure 4.37. The measurement demonstrated that within 7% operating bandwidth, 99% of the coverage area receives a power in excess of 23 dB, which meets the system requirement.

To further increase the bandwidth of the reflectarray, a three-layer stacked patch was used as the cell element. This type of element was discussed in Chapter 3 and is shown in Figure 3.7. The nature of the elements leads to a more gradual slope for the phase plot of the structure and also the whole 360° phase range can be achieved. The antenna was designed for the center frequency of 11.95 GHz for South America and Florida coverage. The cross section of the reflectarray, which is shown in Figure 4.38, was near elliptical with major and minor axis of 83.2 cm and 80.6 cm, respectively. A phase-only technique was used to synthesize the reflectarray. The simulated contour plot of the structure is given in Figure 4.39, which shows 10% operating bandwidth for the shaped beam reflectarray.

The other possibility for exploitation of reflectarray technology to achieve shaped beams is to use a shaped beam subreflectarray. Figure 4.40 shows the cross of a dual reflector system that is composed of a solid parabolic reflector and a shaped-beam subreflectarray. Double-stacked patch elements were used as the cell element of the subreflectarray. The diameter of the parabolic reflector was 1.5m and subreflectarray was a square of 56.1 cm × 56.1 cm. The required phase for South American shaped-beam coverage is shown in Figure 4.41. The calculated contour beam of the dual reflector configuration is shown in Figure 4.42. Although the structure does not completely fulfill the requirements, it can be considered as a good starting point for further optimization.

Beam-shaping methods that have been outlined thus far pertain to phase-only beam shaping. A folded reflectarray structure can be used to optimize both amplitude and phase of the aperture field distribution [13]. A side view of such a folded reflectarray is shown in Figure 4.43.

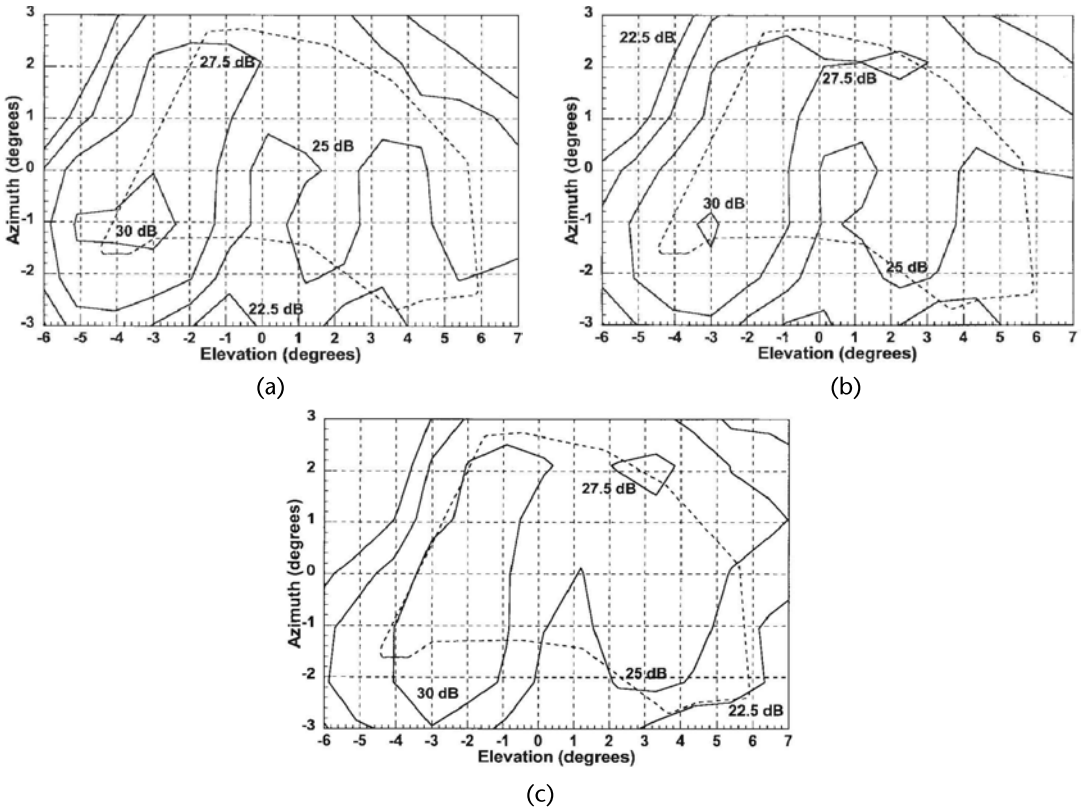

Figure 4.37 Measured copolarized contour plots of the shaped-beam reflectarray radiation pattern for (a) 13.80 GHz, (b) 14.15 GHz, and (c) 14.5 GHz. (© 1999 IEEE. *From:* [21]. Reprinted with permission.)

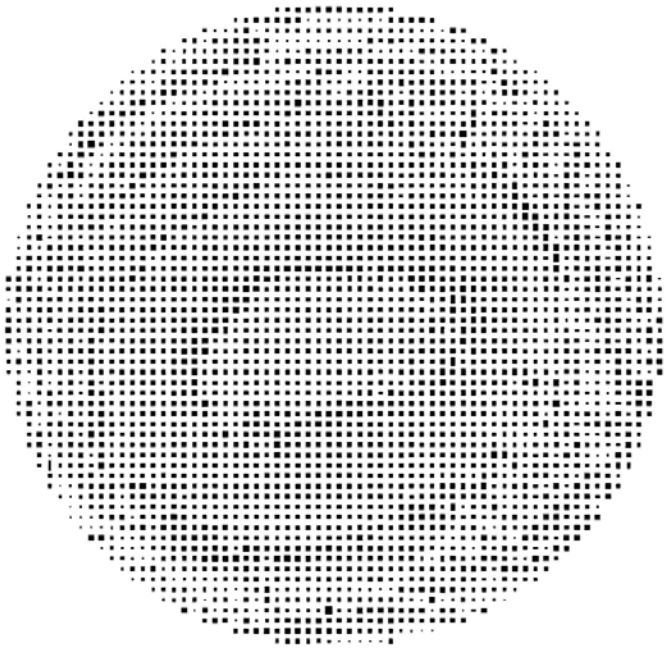

Figure 4.38 Photo-etching mask for the first layer of the shaped-beam reflectarray. (© 2004 IEEE. *From:* [20]. Reprinted with permission.)

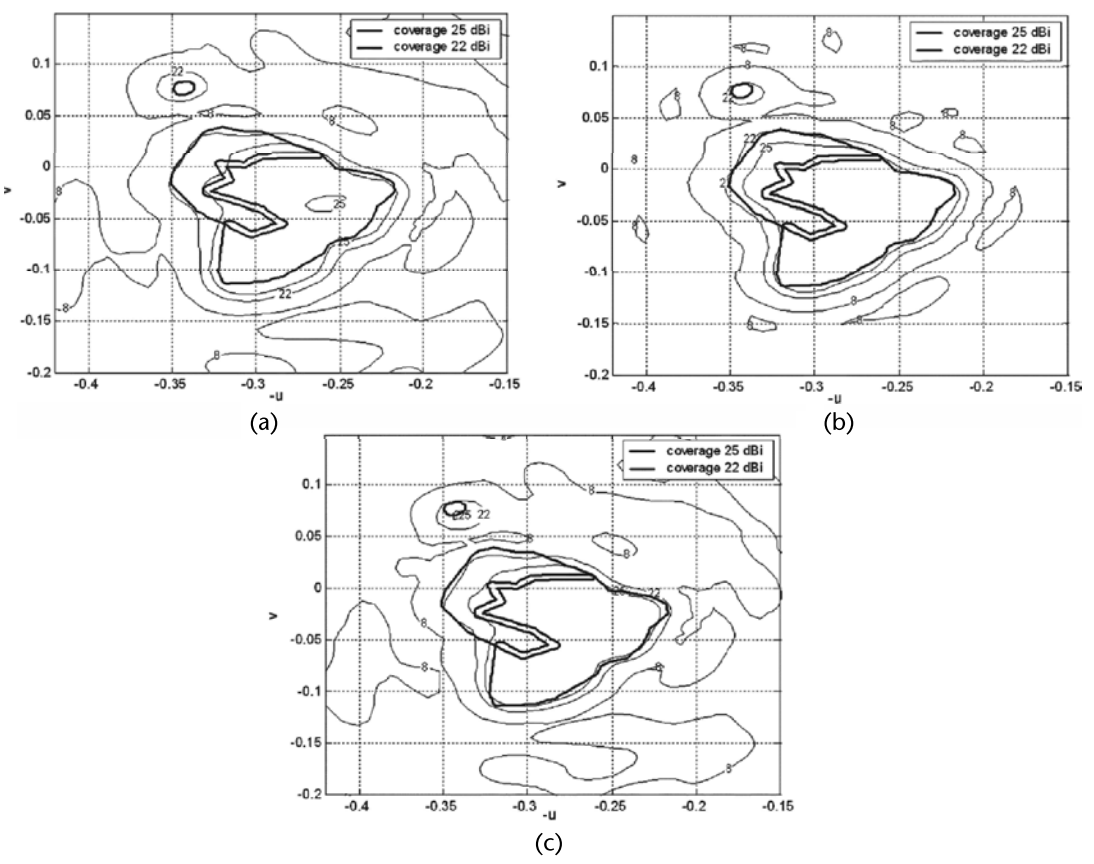

Figure 4.39 Radiation patterns at central and extreme frequencies for the reflectarray optimized in the 12.8–14.2-GHz band: (a) 12.8 GHz, (b) 13.5 GHz, and (c) 14.2 GHz. (© 2004 IEEE. *From:* [20]. Reprinted with permission.)

A reflectarray that is backed by strips is implemented at the top layer. The top surface reflects the radiation from the feed into a given field distribution. Subsequently, the bottom reflectarray that is illuminated by the field with given amplitude distribution imparts the required phase onto each ray to rotate its polarization by 90° and also provide the required phase distribution for the shaped beam. The polarization of the outgoing ray is orthogonal to the top layer strips and reflectarray dipoles, which makes the top layer invisible to outgoing rays. Figure 4.44 depicts the operation of the shaped-beam folded reflectarray. The horn has been placed at a null of field on the lower reflectarray to improve return loss performance. A 24° sector beam antenna with small beam width in the elevation was realized at 58 GHz. The reflectarrays were 25 mm apart and the size of the lower reflectarray was 130 mm × 95 mm and it was etched on 5880 Duroid material of 0.010-inch thickness and $\varepsilon_r = 2.2$. The measured three-dimensional radiation pattern of the antenna is shown in Figure 4.45, which shows a sector beam with narrow beamwidth in elevation.

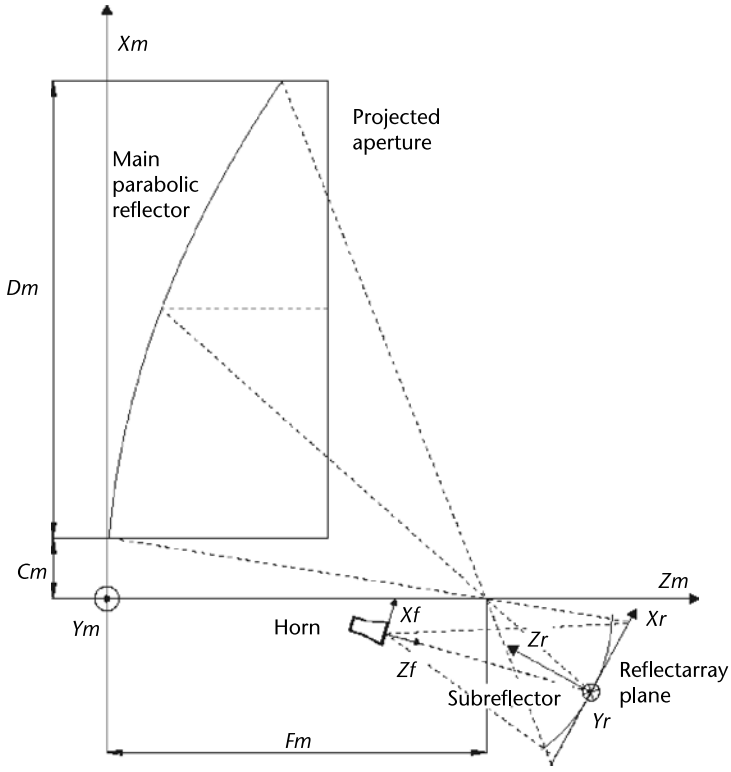

Figure 4.40 Side view of dual reflector-subreflectarray structure. (© 2007 IEEE. *From:* [16]. Reprinted with permission.)

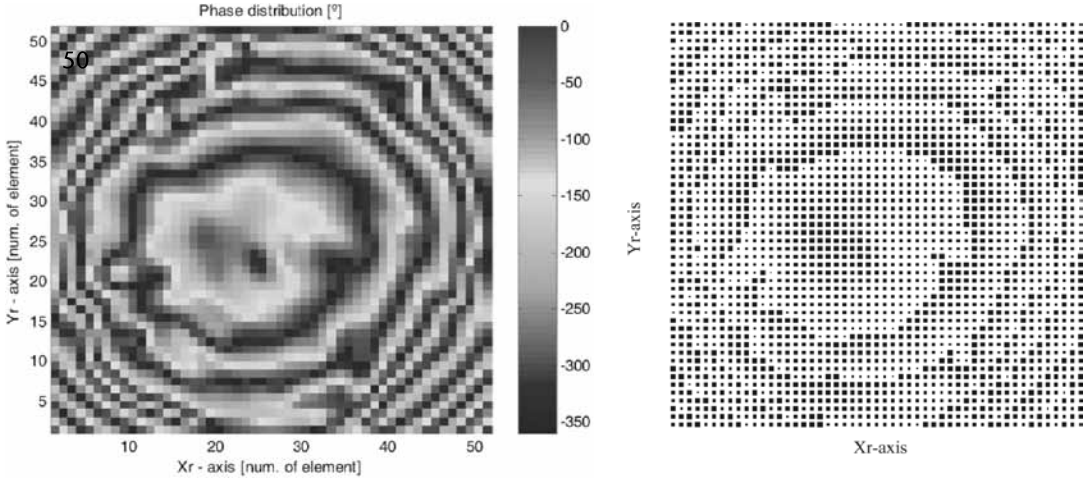

(a) (b)

Figure 4.41 (a) The required phase distribution on the aperture of the shaped subreflectarray. (b) The layout of the bottom layer of the shaped subreflectarray. (© 2007 IEEE. *From:* [16]. Reprinted with permission.)

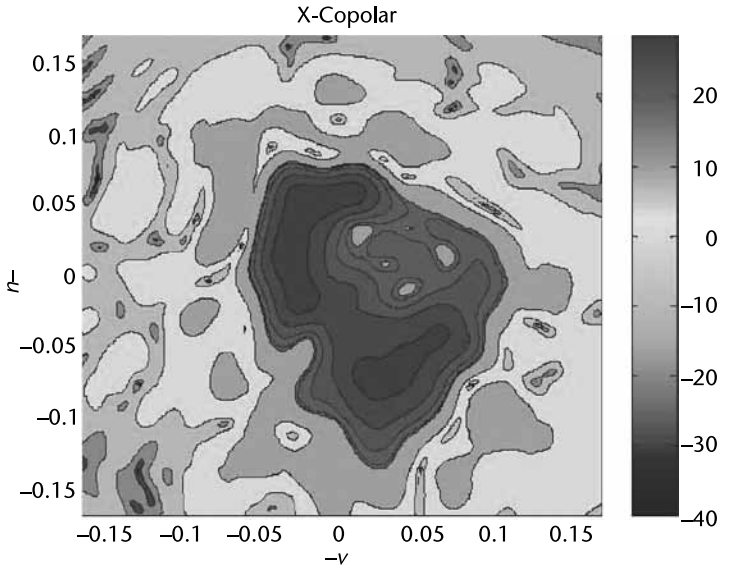

Figure 4.42 Copolar contour plot of dual reflector-subreflectarray configuration. (© 2007 IEEE. *From:* [16]. Reprinted with permission.)

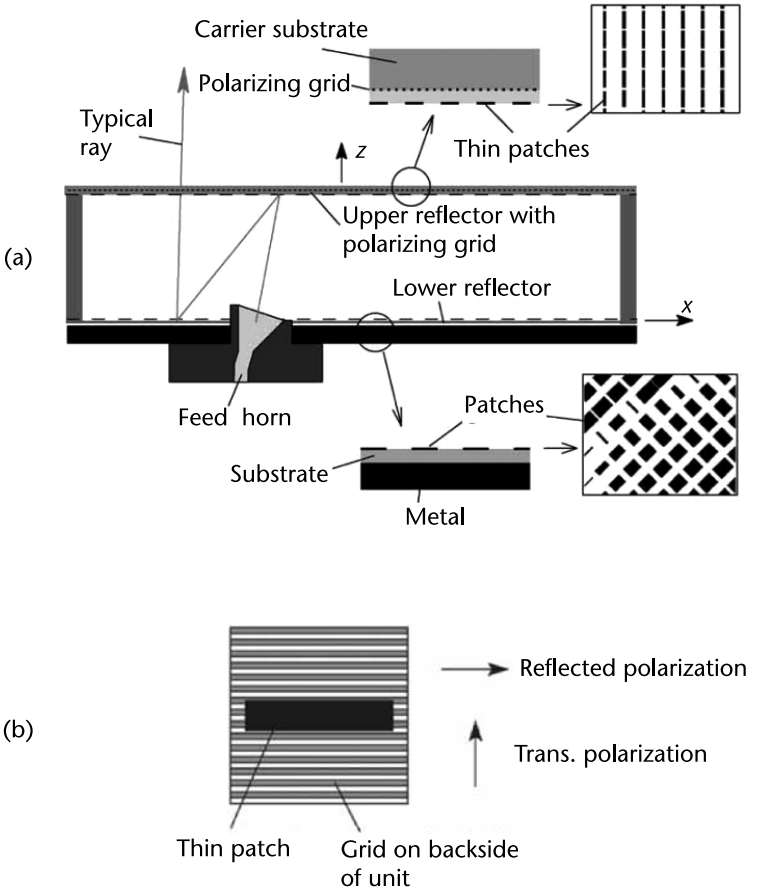

Figure 4.43 (a) Side view of the shaped-beam folded reflectarray. (b) Top layer of the shaped-beam folded reflectarray. (© 2005 IEEE. *From:* [13]. Reprinted with permission.)

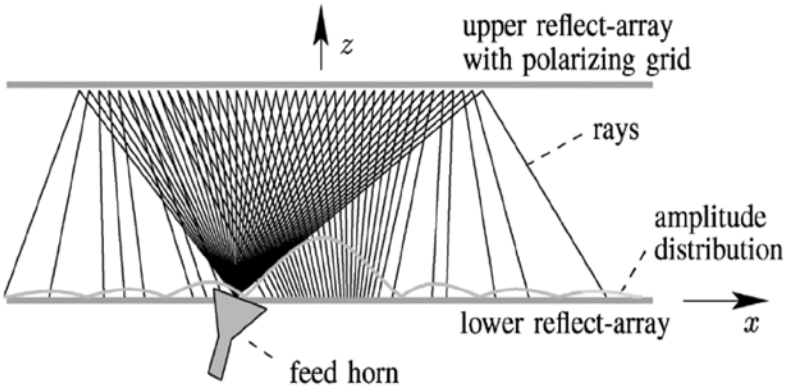

Figure 4.44 Side view depiction of the rays. (© 2005 IEEE. *From:* [13]. Reprinted with permission.)

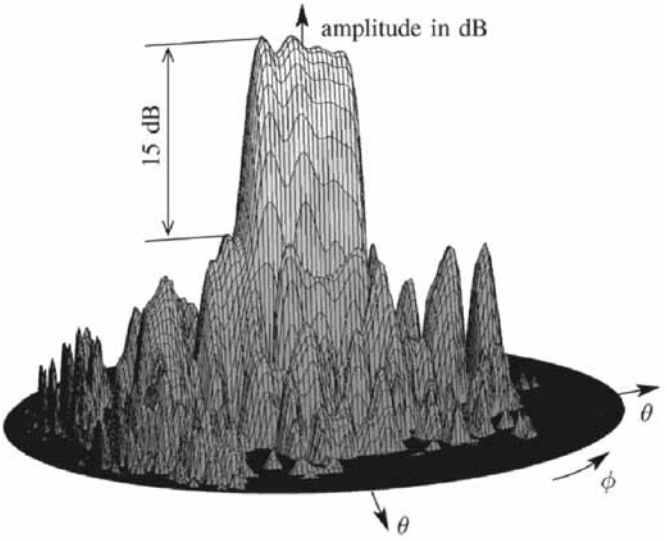

Figure 4.45 Measured normalized far-field characteristic at 57.6 GHz. (© 2005 IEEE. *From:* [13]. Reprinted with permission.)

References

[1] Shaker, J., C. Pike, and M. Cuhaci, "Dual-Band, Dual-Polarisation Transmit-Receive Cassegrain Flat Reflector," *Microwave and Optical Technology Letters*, Vol. 24, No. 1, January 5, 2000, pp. 7–11.

[2] Shaker, M. C., "A Novel Bifocal Dual-Band, Dual Orthogonal Polarisation Planar Reflector for SatCom Applications," *AP2000*, Davos, Switzerland, April 2000.

[3] Shaker, J., et al., "Investigation of the Performance of a Reflectarray Fed by an Active Feed Block to Establish Link with ACTS," *Proceedings of ANTEM 2002*, Montreal, Canada, August 2002, pp. 506–509.

[4] Han, C., J. Huang, and K. Chang, "A High Efficiency Offset-Fed X/Ka Dual Band Reflectarray Using Thin Membranes," *IEEE Transactions on Antennas and Propagation*, Vol. 53, No. 9, September 2005, pp. 2792–2798.

[5] Encinar, J., and M. Barba, "Design Manufacture and Test of Ka-Band Reflectarray Antenna for Transmitting and Receiving in Orthogonal Polarization," *Proceedings of 14th International Symposium on Antenna Technology and Applied Electromagnetics & the American Electromagnetics Conference (ANTEM-AMEREM)*, Ottawa, Canada, 2010.

[6] Shaker, J., and M. Cuhaci, "Multi-Band, Multi-Polarization Reflector-Reflectarray Antenna with Simplified Feed System and Mutually Independent Radiation Patterns," *IEE Proceedings on Microwaves, Antennas, and Propagation*, Vol. 152, No. 2, April 2005, pp. 97–101.

[7] Shaker, J., M. R. Chaharmir, and H. Legay, "Investigation of FSS-Backed Reflectarray Using Different Classes of Cell Elements," *IEEE Transactions on Antennas and Propagation*, Vol. 56, No. 12, December 2008, pp. 3700–3706.

[8] Chaharmir, M. M. R., J. Shaker, and H. Legay, "Dual-Band Ka/X Reflectarray with Broadband Loop Elements," *IEE Proceedings on Antennas, Microwaves, and Propagation*, Vol. 4, No. 2, 2010, pp. 225–231.

[9] Huang, J., and R. Pogorzelski, "A Ka-Band Microstrip Reflectarray with Elements Having Variable Rotation Angles," *IEEE Transactions on Antennas and Propagation*, Vol. 46, No. 5, May 1998, pp. 650–656.

[10] Yu, A., et al., "An X-Band Circularly Polarized Reflectarray Using Split Square Ring Elements and the Modified Element Rotation Technique," *Proceedings of IEEE Antenna and Propagation International Symposium*, 2008.

[11] Chaharmir, R., J. Shaker, and M. Cuhaci, "Development of Dual Band Circularly Polarized Reflectarray," *IEE Proceedings Microwaves, Antennas, and Propagation*, Vol. 153, No. 1, February 6, 2006, pp. 49–54.

[12] Menzel, W., D. Piltz, and M. Al-Tikriti, "Millimeter-Wave Folded Reflector Antennas with High Gain, Low Loss, and Low Profile," *IEEE Antennas and Propagation Magazine*, Vol. 44, No. 3, June 2002, pp. 24–29.

[13] Leberer, R., and W. Menzel, "A Dual Planar Reflectarray with Synthesized Phase and Amplitude Distribution," *IEEE Transactions on Antennas and Propagation*, Vol. 53, No. 11, December 2005, pp. 3534–3539.

[14] Robinson, A. W., and M. E. Bialkowski, "An X-Band Active Microstrip Reflectarray Antenna," *Proceedings of Asia-Pacific Microwave Conference*, 1997, pp. 925–928.

[15] Arpin, F., J. Shaker, and D. McNamara, "Multifeed Single-Beam Power-Combining Reflectarray Antenna," *Electronics Letters*, Vol. 40, No. 17, August 2004, pp. 1035–1037.

[16] Arrebola, M., et al., "Contoured-Beam Gregorian Antenna with a Reflectarray as Subreflector," *Proceedings of the 2nd European Conference on Antennas and Propagation, EUCAP 2007*, 2007.

[17] Yu, S., Y. Rahmat-Samii, and W. Imberiale, "Subreflectarrays for Reflector Surface Distortion Compensation," *IEEE Transactions on Antennas and Propagation*, Vol. 57, No. 2, February 2009, pp. 364–372.

[18] Almajali, E., et al., "Derivation and Validation of the Basic Design Equations for Symmetric Sub-Reflectarrays," *IEEE Transactions on Antennas and Propagation*, Vol. 60, No. 5, May 2012, pp. 2336–2346.

[19] Love, A., *Reflector Antennas*, New York: IEEE Press, 1978.

[20] Encinar, J., and J. Zornoza, "Three-Layer Printed Reflectarrays for Contoured Beam Space Applications," *IEEE Transactions on Antennas and Propagation*, Vol. 52, No. 5, May 2004, pp. 1138–1148.

[21] Pozar, D. M., S. D. Targonski, and R. Pokuls, "A Shaped-Beam Microstrip **Patch Reflec**tarray," *IEEE Transactions on Antennas and Propagation*, Vol. 47, No. 7, July 1999, pp. 1167–1173.

[22] Legay, H., et al., "Recent Developments on Reflectarray Antennas at Thales-Alenia," *Proceedings of the 3rd European Conference on Antennas and Propagation, EUCAP-2009*, 2009, pp. 2515–2519.

[23] TICRA, http://www.ticra.com/products/software.

CHAPTER 5

Numerical Methods: Pathway to a Better Understanding of Reflectarrays

As noted in previous chapters, each region of a quasi-periodic structure such as reflectarray antenna can be considered to be an infinite periodic structure illuminated by a plane wave that is incident along the line that connects the feed and that specific region. Then numerical methods that have been developed for infinite periodic structures can be utilized to calculate scattered field from that specific region. Total scattered field from a reflectarray is addition of the scattered fields from its constituent regions. The underlying assumption for the validity of this approach is smooth variation of the lattice structure to warrant its approximation as an infinite periodic structure. The objective of this chapter goes beyond the sheer presentation of numerical methods that have been used in the analysis of reflectarrays to draw useful physical insight from the application of such methods.

The method of moment (MoM) has been widely used in the analysis of periodic structures. A summary of the intricacies of this method in the context of periodic structures will be presented. The planar grating reflector is also presented to emphasize that one is not restricted to a direct reflected (0, 0) Floquet mode in the realization of a reflectarray. Later on, different methods that have been applied to calculate radiation pattern of a reflectarray, knowing the MoM current distributions on the cell elements, will be presented. As will be seen, such an analysis can be exploited to calculate contribution of each of the constituent components of the reflectarray (cell elements, ground plane, and dielectric substrate) to the far-field radiation pattern. Then utilization of circuit methods in the design of reflectarray will be presented. Considerations on using commercial software in the analysis of reflectarrays will be presented through an example to estimate gain-bandwidth performance of a large reflectarray. Characteristic mode (CM) theory, which is a promising method with a lot of flexibility in the design of reflectarrays, will also be presented.

5.1 Application on the Method of Moment in the Analysis of Reflectarrays

Scattering from a periodic structure that is illuminated by a plane wave will occur in the form of the discrete summation of Floquet modes in contrast to scattering

from finite scatters, which consist of a continuous spectrum of propagating and evanescent waves. This can be readily observed from an inspection of the Green's function integral for a typical infinite two-dimensional periodic structure shown in Figure 5.1:

$$\vec{E}_{scat}(x,y,z)=\frac{1}{T_xT_y}\sum_{m=-\infty}^{+\infty}\sum_{n=-\infty}^{+\infty}\int\vec{\vec{G}}\left(k'_{xm},k'_{yn}\right)\cdot\vec{J}\left(x',y',0\right)$$
$$e^{j\left(k'_{xm}(x-x')+k'_{yn}(y-y')\right)}e^{jk'_{zmn}}dx'\,dy' \tag{5.1}$$

where

$$k'_{xm}=\left(\frac{2\pi m}{T_x}+k_{x0}\right)\quad k'_{yn}=\left(\frac{2\pi n}{T_y}+k_{y0}\right)\quad k'_{zm}=\sqrt{k_0^2-k'^2_{xm}-k'^2_{yn}} \tag{5.2}$$

and k_{x0} and k_{y0} are Cartesian components of the wavenumber of the incident plane wave, k_0 is the free-space wave number, and lattice sizes are denoted as T_x and T_y as shown in Figure 5.1. It can be seen from (5.1) that the whole scattered wave is a summation of a finite number of outgoing propagating waves and an infinite number of evanescent waves depending on the real or imaginary nature of k'_{zmn}. Note that the sign of k'_{zmn} should be determined in consideration of radiation boundary

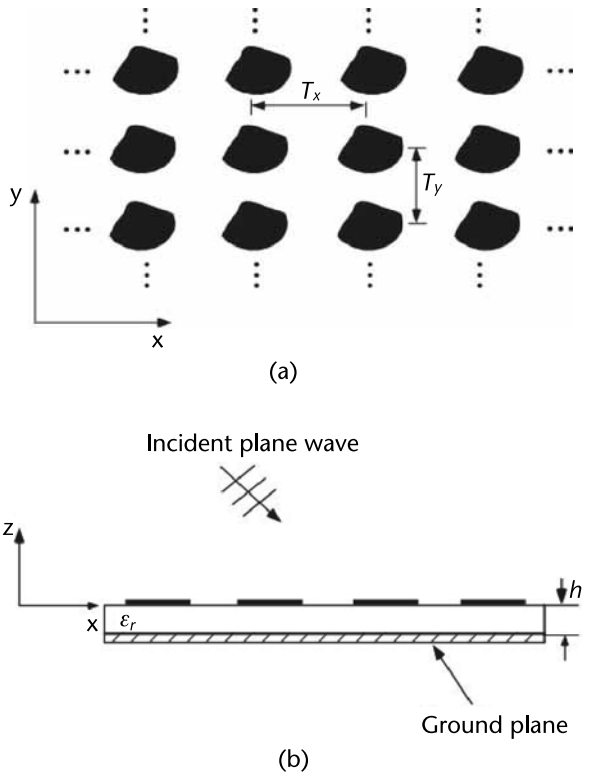

Figure 5.1 Typical infinite two dimensional periodic structure that is illuminate by a plane wave.

condition. Also, $\vec{J}(x',y',0)$ is surface current distribution on the (0, 0)th cell of the periodic structure which can be calculated using an MoM scheme [1]. Using appropriate expansion and testing basis functions, a linear system of equations is established in terms of unknown current amplitude (I_n) on the conducting cell elements:

$$[Z_{mn}][I_n]=[V_n] \tag{5.3}$$

where the square Z matrix gives the interaction between mth testing function and nth current expansion function and the excitation vector V on the right can be expressed as the inner product of the testing function with the excitation field:

$$V_m = \int_{S_m} \left(\vec{E}_{inc} + \vec{E}_{ref}\right).\vec{J}_m dS \tag{5.4}$$

It is important to note that excitation signal is not restricted to the incident field and it should also include the reflected field from the combination of substrate and ground plane.

The current distribution on the patch is decomposed into a given set of basic functions:

$$\vec{J}(x,y)=\sum_{n=1}^{N} I_n \vec{J}_n(x,y) \tag{5.5}$$

where $\vec{J}_n(x,y)$ is of a known functional form with a support through the whole scatterer (entire domain) or a limited portion of the scatterer. For a list of possibilities of the basic functions, the reader is referred to [2–4]. It is to be noted that the entire domain basic functions should reflect the modal currents of the scatterer. For instance, one can use sinusoidal entire domain basis functions to express the current distribution on a periodic arrangement of dipoles that are illuminated by plane wave [2].

It is important to note that (5.1) gives only a scattered wave from the cell elements and it does not include scattering (reflection) from the substrate and ground plane structure. Also, the cell size of a conventional reflectarray is small enough to exclude the excitation of higher-order modes other than the direct reflection (0, 0) order Floquet mode. The total direct reflection from the periodic structure can be summarized as follows:

$$\vec{E}_T = \vec{E}_r + \vec{E}_s \tag{5.6}$$

Noting the fact that the structure has a ground plane in the back, the whole incident power is reflected back which implies unity amplitude for the total scattered field:

$$\vec{E}_T = \hat{e}_T e^{j\phi_T} \tag{5.7}$$

The direction of the scattered field vector, $\hat{e}_T$, depends on the depolarization effects of the cell elements. In the absence of the cell element, the polarization of

the incident field is preserved. In other words, a *TE*(*TM*) incident field gives rise to a *TE*(*TM*) field. In the absence of excessive depolarization effects from the cell element of the reflectarray (which is usually the case for conventional geometries such as patches and loops), the most important design parameter is the phase response, $\phi_{T,}$ the determination of which is the basis of the reflectarray design. The starting point of the reflectarray design is calculation of the reflected phase as a function of a geometrical parameter of the cell element. A variety of phase versus geometrical feature size curves were presented in Chapter 4 for different types of cell elements.

The above analysis can be used for the design and operation of a reflectarray based on direct reflection. Therefore, the lattice size should be held close to half a wavelength or less to prevent the excitation of higher-order modes. However, the quasi-periodic nature of reflectarray gives rise to other possibilities in terms of the choice of the propagating mode by the appropriate choice of the lattice parameters. The concept of blazed grating is particularly useful in such a development [5]. The next higher-order mode of a periodic structure is (0, –1) Floquet mode. For a periodic structure composed of dipoles that are arranged in a lattice shown in Figure 5.2, the direction of propagation of this higher order mode is given as follows [6]:

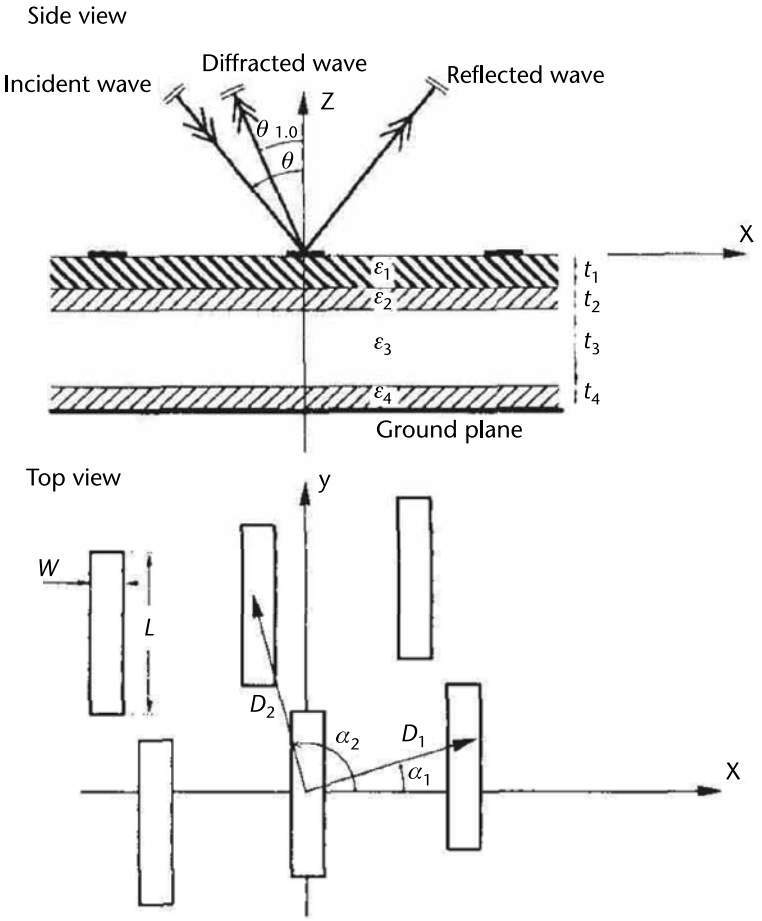

Figure 5.2 Side and top views of a blazed grating composed of dipoles etched on dielectric substrate. (© 1990 IEEE. *From:* [6]. Reprinted with permission.)

$$\sin\theta_{0,-1}\cos\varphi_{0,-1} = \sin\theta\cos\varphi - \frac{\lambda}{D_1}\frac{\sin\alpha_2}{\sin(\alpha_2-\alpha_1)} \tag{5.8}$$

$$\sin\theta_{0,-1}\sin\varphi_{0,-1} = \sin\theta\sin\varphi + \frac{\lambda}{D_1}\frac{\cos\alpha_2}{\sin(\alpha_2-\alpha_1)} \tag{5.9}$$

The lattice parameters have been shown in Figure 5.2 and θ and ϕ define the direction of the propagation of the incident wave. Equations (5.7) and (5.8) are independent of D_2. The other lattice parameters can be set to obtain a specific direction of propagation for (0, –1) mode. The grating reflector surface is assumed to be composed of regions of periodic structures illuminated by a plane wave that is propagating along the line that connects the feed point to the center of that particular region and then the local lattice parameters are determined to excite (0, –1) mode along a given direction. Assuming the desired outgoing field direction to be $(\theta_{0,-1}, \phi_{0,-1})=(\Psi_0, 180°)$, the last two equations can be rewritten as follows [6]:

$$\sin\Psi_0 + \sin\theta\cos\varphi = \frac{\lambda}{D_1}\frac{\sin\alpha_2}{\sin(\alpha_2-\alpha_1)} \tag{5.10}$$

$$\sin\theta\sin\varphi = -\frac{\lambda}{D_1}\frac{\cos\alpha_2}{\sin(\alpha_2-\alpha_1)} \tag{5.11}$$

The lattice parameters (D_1, α_1, α_2) are determined to excite (0, –1) mode along a specified direction. For a detailed overview of design procedure, the reader is referred to [6]. Once the lattice is knitted together to ensure excitation of higher-order mode along a given direction, the size of the dipole and the substrate thickness are optimized to ensure high coupling of incident field into the desired higher-order mode. Modal efficiency of a typical grating reflector is shown in Figure 5.3. One salient feature of grating reflector is frequency scanned beam as a result of the dependence of diffraction angle of the higher-order mode on the operating frequency, as can be seen from (5.10) and (5.11).

Numerical methods based on the finite-difference time domain (FDTD) have also been used for the analysis of the cell element of reflectarray in an infinite periodic medium [7]. However, because the method in its conventional form cannot handle the coupling between elements in infinite periodic structure, it has been applied to cell elements that have been located within a waveguide that minimizes interelement coupling [7]. Generally, spectral-domain methods handle a wider class of cell elements and also provide insightful information on the operation of reflectarray in the context of discrete set of scattered Floquet modes.

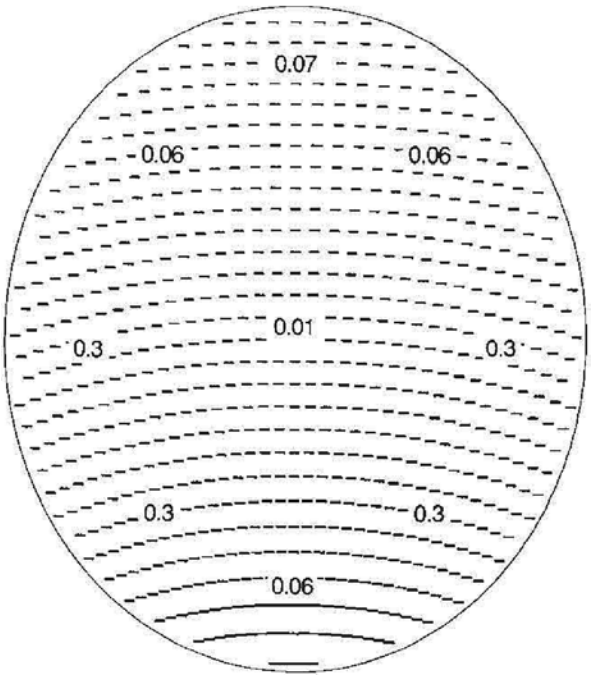

Figure 5.3 Computed local conversion loss in decibels of the incident field to the diffracted (0, –1) wave for a typical grating reflector. (© 1990 IEEE. *From:* [6]. Reprinted with permission.)

5.2 Application of Circuit Models in the Analysis of Reflectarray Cell Element

The concept of equivalent circuit has been widely used in EM analysis with the aim of speeding up calculations by replacing the lengthy full-wave simulation with the analysis of equivalent circuit. The equivalent circuit of a cell element is based on the physical understanding of that particular cell element. Therefore, the applicability of method is restricted to that particular cell element. A different frequency band, lattice configuration, and/or polarization of excitation might require a different equivalent circuit to capture the operation of cell element. The reader is henceforth cautioned to comply with the restrictions of applying the equivalent circuit and also conclusions that can be drawn from such a model.

The equivalent circuit method was used in [8] to obtain design curves for patch and square loop that were arranged in a subwavelength square lattice. The cell elements along with their equivalent circuits are shown in Figure 5.4. The equivalent circuits were based on the common knowledge that the edges normal to the polarization of the incident E-field tend to create a capacitive effect, whereas conductors parallel to E-polarization have an inductive effect. The extent of capacitive/inductive effect depends on the separation between adjacent edges, lattice size, and conductor width. Detailed formulas can be found in [8, 9]. Figure 5.5 shows a comparison between the circuit method and full-wave analysis for patch and loop element within the subwavelength lattice. Therefore, rather than relying on lengthy full-wave simulations to calculate the phase design curves of reflectarray, a quick circuit analysis is sufficient to provide the designer with the same piece information.

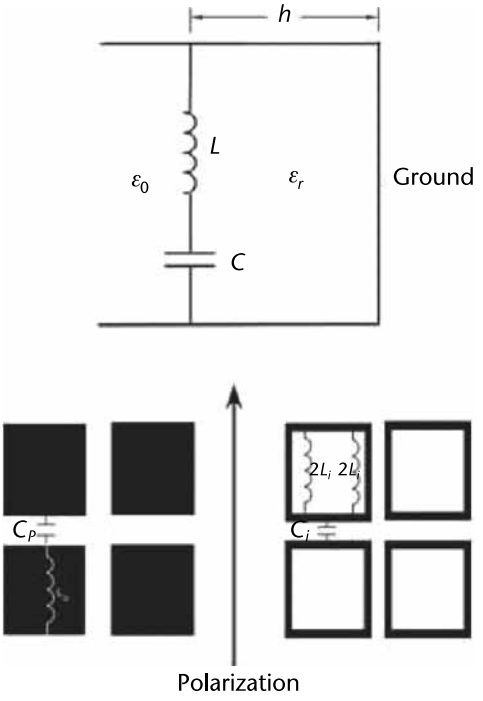

Figure 5.4 Circuit model for subwavelength patch and loop elements. (© 2011 IET. *From:* [8]. Reprinted with permission.)

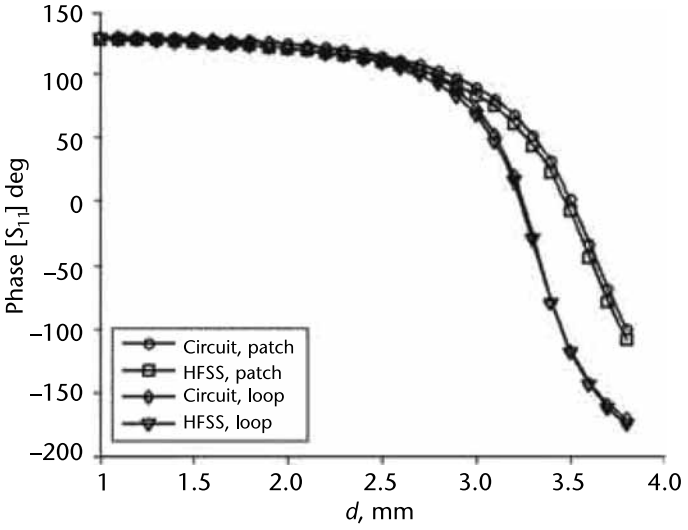

Figure 5.5 Reflection phase against length d for the subwavelength loop and patch based on circuit model and HFSS, $f = 12.5$ GHz. The lattice size was 4.0 mm × 4.0 mm, the substrate thickness was 0.060 inch, and permittivity was 3. (© 2011 IET. *From:* [8]. Reprinted with permission.)

It is common to integrate active elements into the cell element of the reflectarray to achieve switched-beam and beam-steering capabilities. One example of such a development is shown in Figure 5.6 where MEM switches were embedded within the cell element to change phase response of the cell element through a combination of the states of switches [10]. The redundancy in achieving a given phase

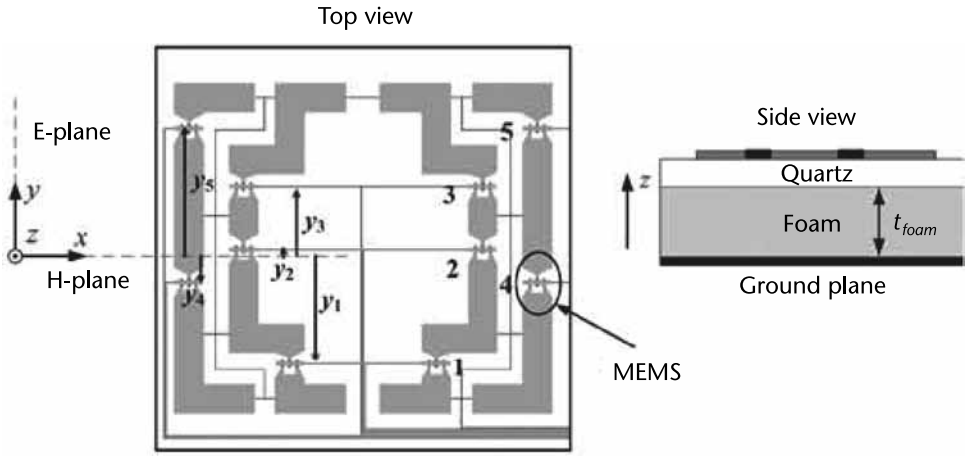

Figure 5.6 View of the element that consists of two pseudo-rings loaded with two state MEMS variable series capacitors. (© 2010 IEEE. *From:* [10]. Reprinted with permission.)

using different combinations of the states of switches is used to mitigate frequency dispersion of the reflectarray. It is very cumbersome to run the full-wave simulation for all combinations of the states of MEM switches. The whole cell element is simulated as an N-port structure where the first port is set as the surface of the cell element that is excited by the incident plane wave and the openings on the cell element, where the switches were placed, were treated as the rest $N - 1$ ports as shown in Figure 5.7 [11]. A single full-wave simulation was run to obtain scattering parameters of the cell in the absence of MEM switches. Knowing the equivalent circuits for ON/OFF states of MEM, it is a matter of circuit analysis to find the phase response of the cell elements for different states of MEM switches [10, 11].

5.3 Calculation of the Radiation Pattern of a Reflectarray

The most straightforward method to find the radiation pattern of a reflectarray is to use direct summation of the field radiated by each of the cell elements [12, 13]. In this method, the cell element currents are determined by resorting to infinite

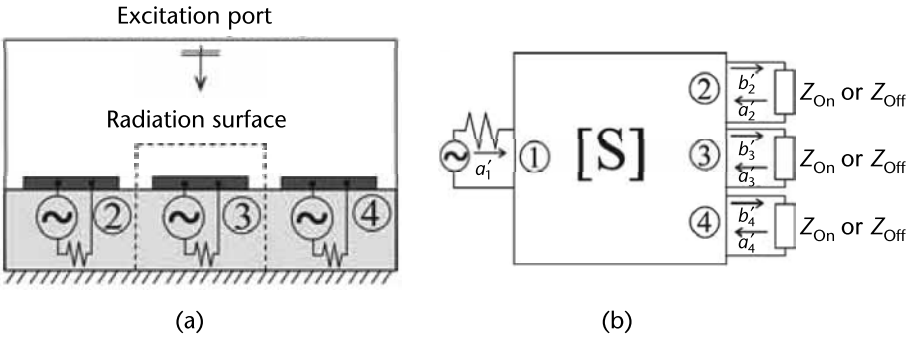

Figure 5.7 Description of the method used for the analysis of an active cell element: (a) electromagnetic of the cell element and (b) circuit simulation of the loaded structure. (© 2012 IEEE. *From:* [11]. Reprinted with permission.)

periodicity assumption subject to plane wave excitation and then the dyadic Green function is used to find the radiated field from a given cell element. Total radiated field along an arbitrary $\hat{u}$ direction is summation of the radiated fields of cell elements [14]:

$$E(\hat{u}) = \sum_m F\left(\vec{r}_m.\vec{r}_f\right)A\left(\hat{u}.\hat{u}_0\right)\exp\left\{-jk_0\left[\left|\vec{r}_m - \vec{r}_f\right| + \vec{r}_m.\hat{u}\right] + j\alpha_m\right\} \tag{5.12}$$

where F is the feed radiation pattern, A is the radiation pattern of the cell element, $\vec{r}_m$ is location vector for the mth cell element, $\hat{u}_0$ is the desired direction of the beam, and α_m is the phase shift imparted by that same element. The shortcoming of this method is the assumption of infinite ground plane in the calculation of the radiated field from each given cell element. Therefore, a second method was suggested in [15] to overcome this shortcoming. In this method, the reflected field on each cell is calculated based on the same assumptions that were used in the first method. Then the total radiated field is obtained by calculating equivalent electric and magnetic current distributions right above the surface of reflectarray using the following expressions:

$$\vec{J}_s = \hat{n} \times \vec{H} \tag{5.13}$$

$$\vec{M}_s = -\hat{n} \times \vec{E} \tag{5.14}$$

The free-space dyadic Green function can then be used to find the radiated field. The emergence of discontinuity on borders of adjacent cells is inherent to this method and leads to erroneous results in image beam direction of the feed. To smooth out these discontinuities, the spectral integral expressions can be used to find the field distribution on the reflectarray surface as the third method. Similar to the previous two methods, the current distributions is calculated based on periodic structure assumptions and then the following expression is used for spectral E-field on surface of reflectarray:

$$\vec{E}\left(k_x, k_y\right) = \overline{\overline{G}}\left(k_x, k_y\right).\left(\vec{J}\left(k_x, k_y\right) - b\left(k_x, k_y\right)\right) \tag{5.15}$$

where $\overline{\overline{G}}(k_x, k_y)$ is the multilayer dyadic Green function, $\vec{J}(k_x, k_y)$ is the spectral expression for current distribution on the cell element, and $b(k_x, k_y)$ is obtained from the following relationship:

$$b\left(k_x, k_y\right) = \frac{2}{\eta_0 k_0 \gamma_0}\begin{bmatrix} k_0^2 & k_x k_y \\ k_x k_y & k_0^2 - k_x^2 \end{bmatrix}.\vec{E}_i\left(k_x, k_y\right) \tag{5.16}$$

where η_0 and k_0 are characteristic impedance and wavenumber of free space, $E_i(k_x, k_y)$ is the spectral expression for incident wave on the reflectarray and $\gamma_0 = \sqrt{k_0^2 - k_x^2 - k_y^2}$. It is to be noted that the propagating portion of the spectrum is sufficient for the calculation of the field on the reflectarray:

$$\vec{E}(x,y)=\frac{1}{4\pi^2}\int\limits_{k_x^2+k_y^2<k_0^2}\vec{E}(k_x,k_y)e^{-j(k_x x+k_y y)}dk_x dk_y \tag{5.17}$$

The magnetic field can be obtained from electric field using the following integral expression:

$$\vec{H}(x,y)=\frac{1}{4\pi^2}\int\limits_{k_x^2+k_y^2<k_0^2}\frac{1}{\eta_0}\hat{k}\times\vec{E}(k_x,k_y)e^{-j(k_x x+k_y y)}dk_x dk_y \tag{5.18}$$

where $\hat{k}=\hat{x}k_x+\hat{y}k_y\pm\hat{z}\gamma_0$ represents the direction of propagation. Having calculated the field distribution on the surface of reflectarray, (5.13) and (5.14) can be used to find the equivalent currents. The field expressions in the third method are based on the continuous plane wave spectrum as opposed to fundamental Floquet space harmonics [15]. Figure 5.8 shows comparison of the calculated radiated using the above three methods and the measured radiation pattern. The second and third methods show a relatively good agreement with measurement. The full range of measured radiation pattern and calculated radiation pattern from the second and third methods are shown in Figure 5.9. The disagreement between the second method and measurement around $\theta = 145°$ pertains to direct reflection direction from the feed.

It is instructive to use the current and field distribution on the constituent parts of the reflectarray (cell elements, ground plane, and dielectric substrate) to calculate contribution of each these elements to the total radiated field of a reflectarray [16]. Commercial HFSS [17] software has been used in [16] to find H-field distribution on the ground plane and right above and below substrate air interface of the reflectarray that is illuminated by a given feed horn. Because the current distribution is

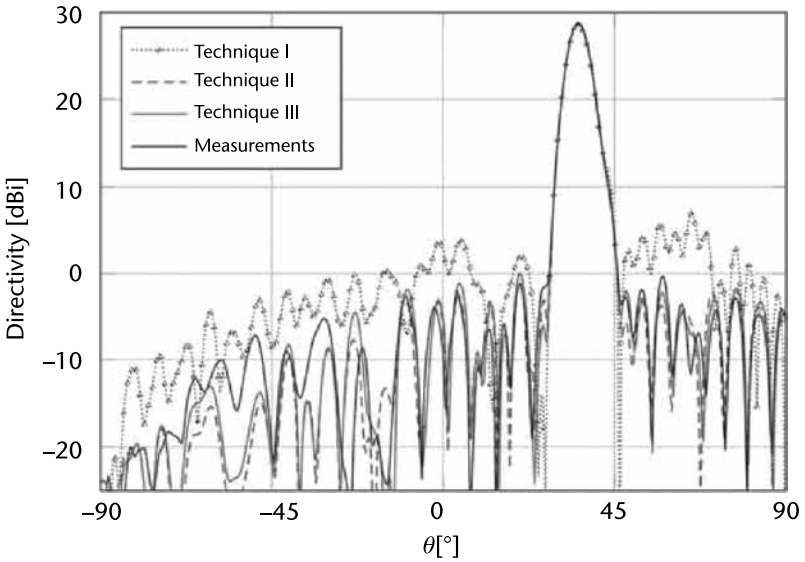

Figure 5.8 Simulated and measured radiation patterns of the copolar component at $\phi = 135°$. (© 2011 IEEE. *From:* [15]. Reprinted with permission.)

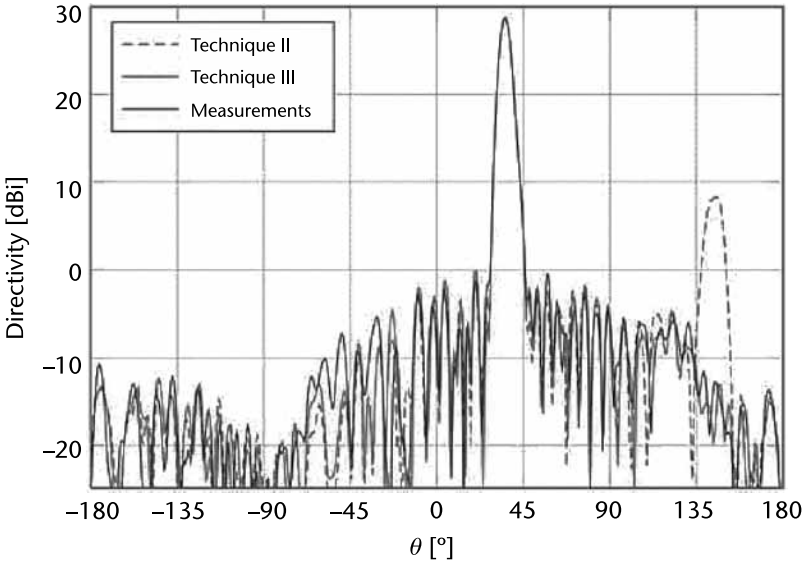

Figure 5.9 Simulated and measured co-polar radiation patterns for the second and third methods. (© 2011 IEEE. *From:* [15]. Reprinted with permission.)

the results of discontinuity of H-field (see Figure 5.10), the following relationship can be used to calculate field distribution on the cell elements and ground plane:

$$\vec{J}_s = \hat{n} \times \left(\vec{H}_2 - \vec{H}_1 \right) \tag{5.19}$$

Criteria have been presented in [16] on how far above and below the interface the observation points are to be located in order to get convergence for the

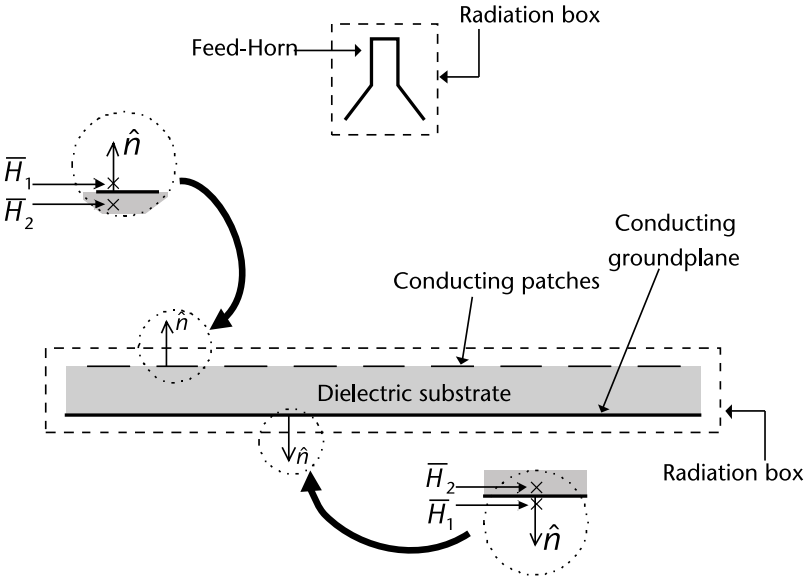

Figure 5.10 Cross-section of reflectarray antenna geometry showing the radiation boxes and the quantities used in calculation of conduction current. (© 2012 IEEE. *From:* [16]. Reprinted with permission.)

calculated current distribution. To investigate the contributions of the reflectarray components to its far-field pattern, a single-layer, center-fed reflectarray of rectangular patches was designed and simulated at a center frequency of 30 GHz ($\lambda_0 = 10$ mm). Dielectric permittivity of $\varepsilon_r = 3.0$ and thickness $h = 0.508$ mm were selected for the substrate. The reflectarray size is $15.5\lambda_0 \times 15.5\lambda_0$ and the feed phase center is located at $F = 15.5\lambda_0$ from its surface. The current distributions on patches and ground plane were calculated from the knowledge of simulated HFSS field and application of (5.19) and the results are shown in Figure 5.11.

The symmetry of the reflectarray has been exploited to restrict the computational domain to a quarter of the reflectarray surface. The regions of the ground plane that are underneath resonant or near-resonant patches support strong current almost equal to the amplitude of the current on those same patches. This observation tends to establish similarity between these patches and open resonators with upper patch and the underneath ground plane regions as their top and bottom conducting surfaces. It is to be noted that the regions of the ground plane that are highly exposed to the radiated field from the feed do not support strong current. Similarity of the order of current distribution on patches and ground plane, as shown in Figure 5.11, implies almost similar radiation patterns for these individual current components as shown in Figure 5.12. These radiation patterns suffer from high sidelobe level, which disappears after their complex addition. Figure 5.13 shows a comparison of the complex addition of the radiation patterns of ground plane and patch elements with the total HFSS [17] calculated radiation pattern of the reflectarray. The discrepancy between the two radiation patterns represents contribution of substrate polarization current to the total radiation.

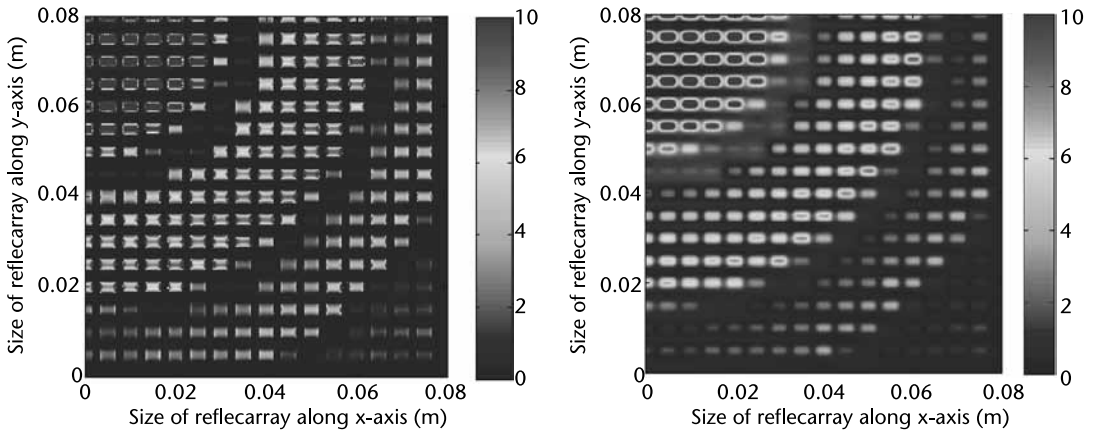

Figure 5.11 The extracted conduction surface current density on (a) the patch elements and (b) the ground plane. One quadrant shown due to symmetry. (© 2012 IEEE. *From:* [16]. Reprinted with permission.)

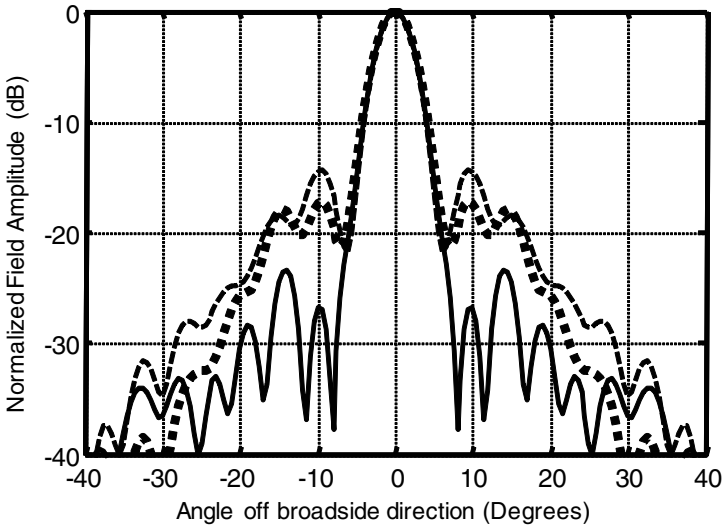

Figure 5.12 E-plane (scattered) far-field radiation patterns due to conduction currents on the patches (.....), the ground plane (– – –), and both the patches and the ground plane (—), calculated using the extracted current densities at 30 GHz. (© 2012 IEEE. *From:* [16]. Reprinted with permission.)

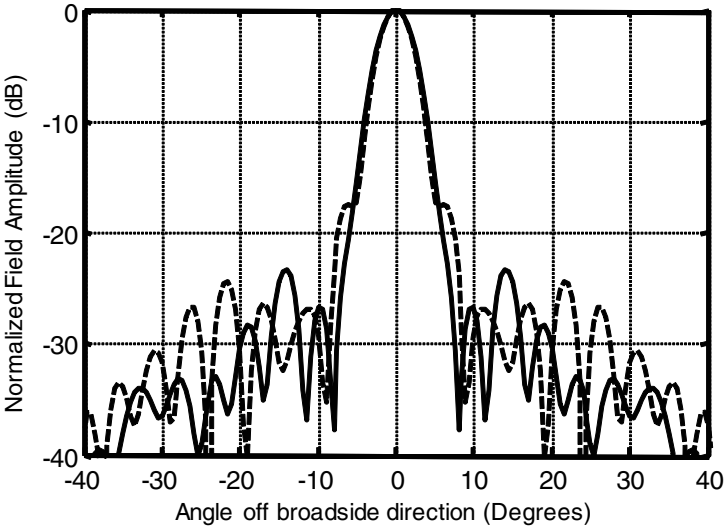

Figure 5.13 E-plane (scattered) far-field patterns computed from extracted conduction currents on both the patches and the ground plane (—), and obtained directly from HFSS (– – –) and due to conduction and polarization currents. (© 2012 IEEE. *From:* [16]. Reprinted with permission.)

5.4 Application of Commercial Software in the Design and Analysis of Reflectarrays

Currently, there is no specialized software dedicated to the design and synthesis of reflectarrays. Computation and memory resources of current computers prevent the synthesis of full reflectarray structure. The best one could hope for is calculation of

phase response of the cell element with the assumption of infinite periodicity and then utilization of that same response to synthesize the reflectarray.

There are a number of commercial full-wave electromagnetic software such as HFSS [17], CST [18], and EMCUBE [19] that can be used for the calculation of the phase response of the cell element. Generally, any software that can accommodate periodic boundary condition can be used for the calculation of the phase response of cell element.

Although the phase response of the cell element is dependent on the angle of incidence of the incoming plane wave, it might still be acceptable to restrict the analysis to normal incidence. This statement is particularly valid for a dense periodic structure with a lattice size below a half-wavelength. The periodic nature of the structure can be captured by appropriately surrounding the cell element with electric and magnetic walls. Pursuing this strategy broadens the range of software that can handle calculation of the phase response of cell element to closed-region full-wave software that accommodates electric and magnetic walls. However, it should be noted that the cell element should have double transverse symmetry to span the desire periodic structure by repeated replication through electric and magnetic walls of the waveguide simulator [11]. For instance, the waveguide simulator shown in Figure 5.14(a) spans the infinite periodic structure composed of microstrip patches whereas it is easy to verify that the waveguide simulator of Figure 5.14(c) fails to span infinite periodic structure composed of open square rings shown in Figure 5.14(b). The multiple reflections of cell element with respect to waveguide walls give rise to the structure shown in Figure 5.14(d), which is different from the structure in Figure 5.14(b). This restriction should be noted carefully when applying electric and magnetic walls to emulate normal incidence onto a periodic structure.

Having synthesized the reflectarray following the procedure that was outlined above, one can use electromagnetic tools with scattering computation capability to analyze the performance of the reflectarray. Obviously, the largest reflectarray size that can be handled by the software depends on available computational resources and also the complexity of the software. However, using the available commercial software intelligently, one can draw useful information on the performance of the reflectarray without simulating the whole structure. For instance, calculation of scattering from the center row of a center-fed or offset-fed reflectarray gives a good estimate of the operating bandwidth of the structure. One of the challenges in the design of reflectarray is estimation of gain bandwidth, which is usually hampered by the large size of the structure. It was suggested in [20] that scattering from single central row of the reflectarray provides a good estimate of the gain bandwidth performance. An offset-fed 1.2m $\times$ 1.2m Ku-band reflectarray with the radiated beam along the direct reflection ray from the feed was used in [20] to demonstrate this method. The single row of the reflectarray is highlighted in Figure 5.15. A single row of the reflectarray was imported into HFSS and PMC walls were placed around it to establish its periodicity. Then the single row was illuminated by a plane wave along the direction of the main beam of the original reflectarray and the field intensity at the focal point was calculated across the frequency band. The variation of the field intensity at the focal point, which is shown in Figure 5.16, provided an estimation of the gain bandwidth performance of the reflectarray.

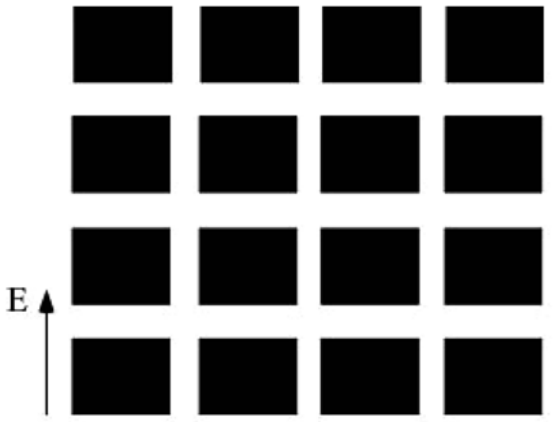

Infinite periodic structure

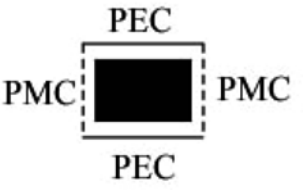

Waveguide simulator

(a)

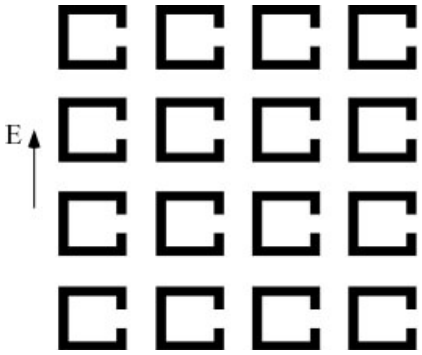

(b)

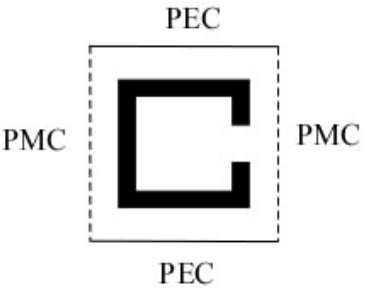

(c)

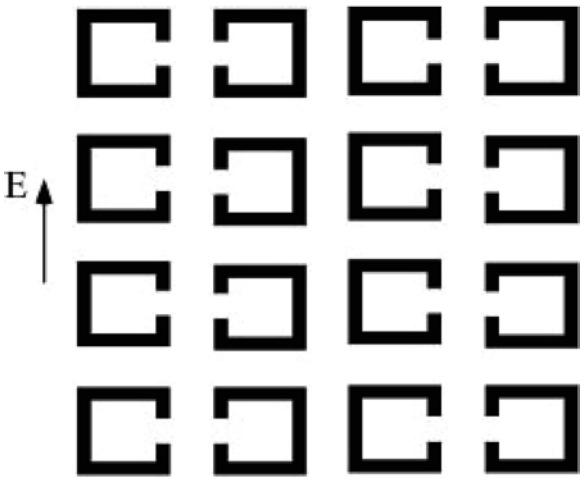

(d)

Figure 5.14 Two periodic structures illuminated by a normal incident plane wave along with their waveguide simulator implementation. (a) Infinite array of microstrip patch and the cell element within a waveguide simulator. (b) Infinite periodic structure of open square ring. (c) Single open square ring enclosed within the waveguide simulator. (d) Infinite periodic structure resulting from multiple reflections with respect to waveguide simulator walls.

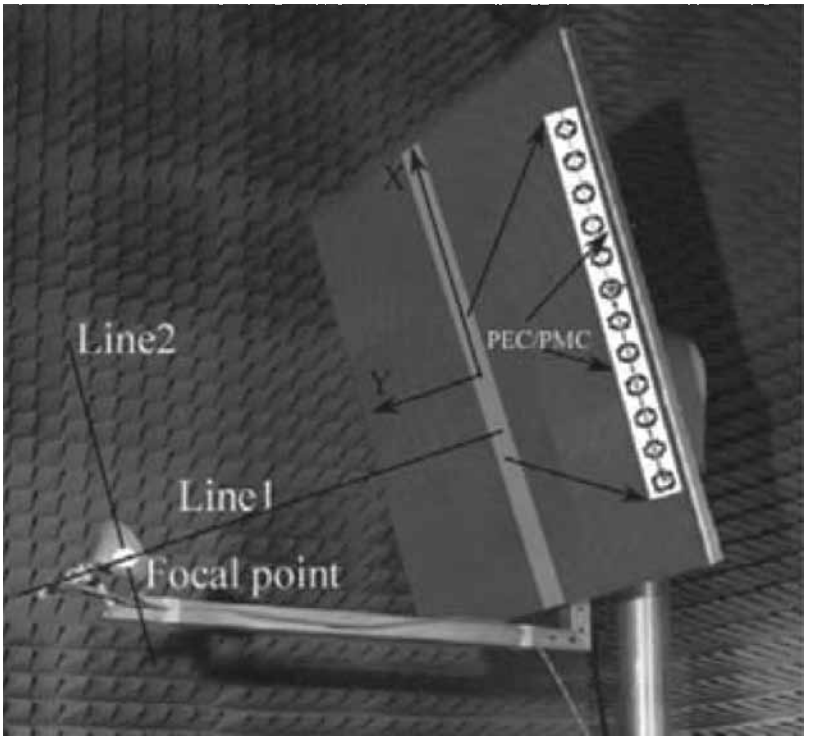

Figure 5.15 The simulation setup in HFSS to evaluate the bandwidth of reflectarray. (© 2010 IEEE. *From:* [20]. Reprinted with permission.)

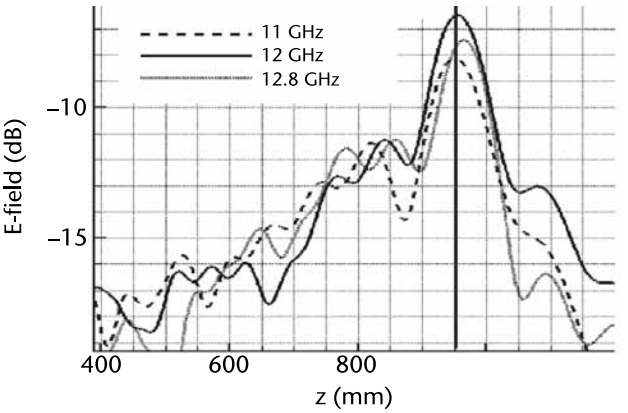

Figure 5.16 Calculated near field in HFSS on line 1 of Figure 5.11. (© 2010 IEEE. *From:* [20]. Reprinted with permission.)

5.5 The Infinite-from-Finite Method

The bulk of electromagnetic simulations involving infinite periodic structures make use of absorbing boundary conditions (FDTD and FEM) or periodicity of the governing Green function (MoM) to extract the desired properties of the infinite array. These approaches offer computationally efficient techniques from both the computation time and the computational resource (i.e., memory) perspectives. However,

the enforcement of infinite periodicity suffers from two shortcomings: (1) the numerical method must necessarily employ more complex coding over finite structural analysis (this is especially true in MoM implementations), and (2) the inability to assess the properties of finite arrays.

One technique that can address these two issues is the infinite-from-finite (IFF) method [21]. The technique makes one mandatory assumption: all elements in a finite periodic structure are illuminated identically (i.e., an incident plane wave) and one optional assumption that all elements exhibit identical excitation currents. The assumption of identical excitation (perhaps allowing for phase differences to account for non-normal plane wave incidence) allows one to probe the properties of a finite array without needing to analyze the array in its entirety. If one does indeed assume identical excitation currents among all elements, the properties of the infinite periodic structure can be extracted using a numerical code that need only be capable of analyzing a finite structure, thus forgoing the need to develop new numerical codes.

The IFF method begins by considering a finite periodic structure as shown in Figure 5.17. Assume that this periodic structure has M total elements. Any arbitrary moment method code would describe the entire structure using the impedance matrix

$$\begin{bmatrix} [Z_{11}] & [Z_{12}] & \cdots & [Z_{1M}] \\ [Z_{21}] & [Z_{22}] & \cdots & [Z_{2M}] \\ \vdots & \vdots & \ddots & \vdots \\ [Z_{M1}] & [Z_{M2}] & \cdots & [Z_{MM}] \end{bmatrix} \begin{bmatrix} [I_1] \\ [I_2] \\ \vdots \\ [I_M] \end{bmatrix} = \begin{bmatrix} [V_1] \\ [V_2] \\ \vdots \\ [V_M] \end{bmatrix} \tag{5.20}$$

where each submatrix has dimension equal to the number of expansion functions describing the particular element. Note that at this point all elements have unique excitation and current. To ensure that each element has identical excitation (a normally incident plane wave) and identical currents (the infinite periodic structure condition), we enforce the following conditions

$$[V_m] = [V] \forall m = 1 \ldots M \tag{5.21a}$$

$$[I_m] = [I] \forall m = 1 \ldots M \tag{5.21b}$$

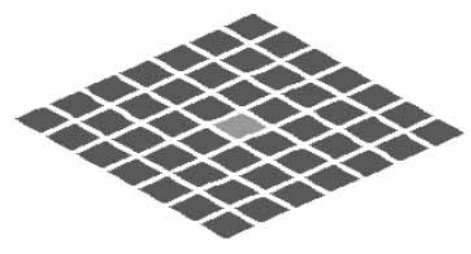

Figure 5.17 Example of a finite collection of periodic structure elements with the light gray element as the central element and dark gray denoting periphery elements.

This leads to an alternative impedance matrix given as follows

$$\begin{bmatrix} [Z_{11}] & [Z_{12}] & \cdots & [Z_{1M}] \\ [Z_{21}] & [Z_{22}] & \cdots & [Z_{2M}] \\ \vdots & \vdots & \ddots & \vdots \\ [Z_{M1}] & [Z_{M2}] & \cdots & [Z_{MM}] \end{bmatrix} \begin{bmatrix} [I] \\ [I] \\ \vdots \\ [I] \end{bmatrix} = \begin{bmatrix} [V] \\ [V] \\ \vdots \\ [V] \end{bmatrix} \tag{5.22}$$

There is substantial redundancy in its structure. In particular, we note that for periodic structures with identical elements throughout implies that one actually has M identical equations. Thus, we need only to solve a single equation, namely, the solution to the first block row of the impedance matrix, expressed as

$$\begin{aligned} &[Z_{11}][I]+[Z_{12}][I]+\ldots+[Z_{1M}][I]=[V] \\ &\{[Z_{11}]+[Z_{12}]+\ldots+[Z_{1M}]\}[I]=[V] \end{aligned} \tag{5.23}$$

allowing us to denote a new impedance operator

$$\begin{aligned} \left[Z^{(M)}\right]_{ps} &= [Z_{11}]+[Z_{12}]+\ldots+[Z_{1M}] \\ &= [Z_{11}]+\sum_{n=2}^{M}[Z_{1n}] \\ &= [Z_{11}]+\left[Q^{(M)}\right] \end{aligned} \tag{5.24}$$

that obeys a current and excitation relationship

$$\left[Z^{(M)}\right]_{ps}[I]_{ps}=[V]_{ps} \tag{5.25}$$

Thus, we conclude that $[Z^{(M)}]_{ps}$ is the impedance operator for the infinite periodic structure. Note that this operator only becomes exact in the limit of $M \rightarrow \infty$ where M is the number of periphery elements to include in the summation. Nevertheless, one expects acceptable convergence for a finite number of iterations, as discussed further in [21].

Consider Figure 5.18(a) where a dogbone element is considered and Figure 5.18(b), which shows the reflection magnitude of the periodic structure as a function of the number of rings of elements to include in the IFF method compared to the reflection magnitude obtained from a well-established commercial code. Note that an acceptable amount of convergence is obtained for five rings. Note that reflection coefficients can be obtained using the traditional method of exciting the structure and observing the scattered field, although a potentially superior technique is described next using modal techniques.

(a)

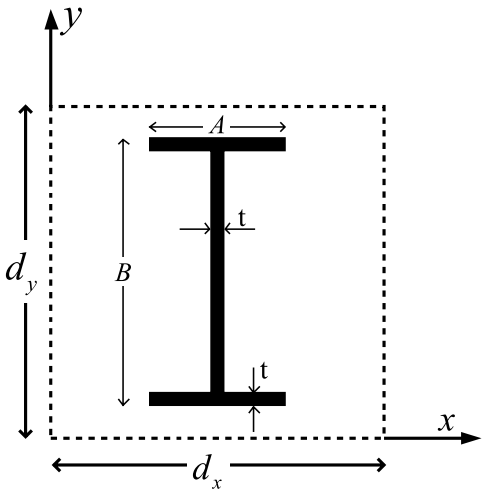

(b)

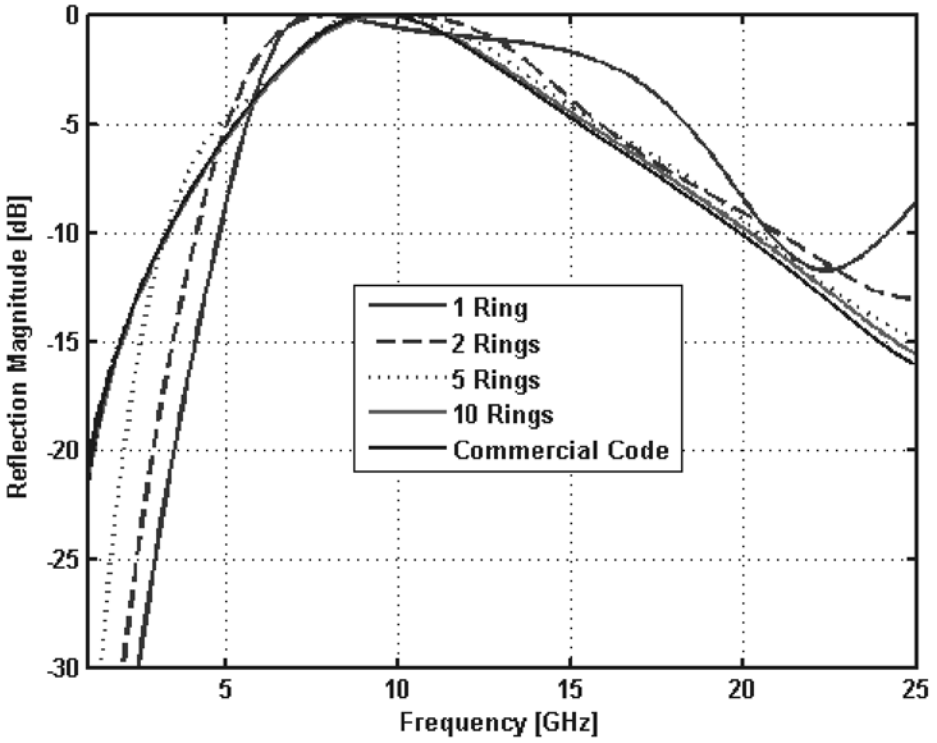

Figure 5.18 Example of (a) a dogbone reflectarray element and (b) a convergence of reflection magnitude as a function of the number of rings of elements included, compared to commercial simulation code.

5.6 Characteristic Mode Analysis of Periodic Structures

5.6.1 Fundamentals of Characteristic Mode Analysis

Characteristic modes (CMs) are a useful numerical analysis tool that determines a set of scattered field modes that yield mutually orthogonal far field patterns [23, 24]. The technique has near exclusive use in finite scatterers, with the exception

of [22]. CMs were used as a numerically efficient technique to extract important parameters such as transmission and reflection coefficients for periodic structures in [22]. Rather than applying an incident field, computing excitation currents and then determining the scattered field, one can alternatively rely on eigenvalue information alone to determine these parameters. The problem to be solved uses the impedance operator $Z = R + jX$ cast in an eigenvalue problem (and readily obtained in any moment method formulation) as follows

$$X\left(\underline{J}_n\right) = \lambda_n R\left(\underline{J}_n\right) \tag{5.26}$$

It can be shown that the eigenvalues are significant electromagnetic quantities, representing the ratio of stored energy to radiated power. Consequently, one is then able to determine a host of important parameters from these eigenvalues. Of particular interest is the computation of the transmission and reflection coefficients of a free-space periodic structure using the following formulas [22]:

$$T = T_n = \frac{j\lambda_n}{1 + j\lambda_n} \tag{5.27}$$

$$\Gamma = \Gamma_n = \frac{-1}{1 + j\lambda_n} \tag{5.28}$$

allowing us to state that a resonant mode ($\lambda_n = 0$) implies complete reflection while an anti-resonant mode ($\lambda_n \rightarrow \pm \infty$) implies complete transmission. Furthermore, if a ground plane is present, the transmission coefficient is zero and the reflection coefficient has unity magnitude, while the reflection phase can be obtained from the argument

$$\Gamma = \Gamma_n = \frac{1 - j\lambda_n}{1 + j\lambda_n} \tag{5.29}$$

Implying zero reflection phase is obtained in the presence of a resonant mode ($\lambda_n = 0$).

5.6.2 Efficient and Unambiguous Extraction of Reflection and Transmission Coefficients

In the previous section, one was able to compute transmission and reflection coefficients of periodic structures without having to neither excite with an incident field nor extract currents or scattered field; the computation was performed excitation-free using the eigenvalue alone. However, eigenanalysis is a costly computational endeavor. Fortunately, it can be shown that the following operator identity exists for periodic structures that operate a single characteristic mode [22]:

$$\Psi = Trace\left(\left[Z\right]^{-1}\left[R\right]\right) \approx \frac{1}{1+j\lambda_1} \tag{5.30}$$

where trace is simply the sum of the diagonal entries of the matrix in question. Through simple algebra, we can then show that for a free-space periodic structure the transmission and reflection coefficients can be written in terms of the function Ψ

$$\Gamma = \Gamma_n = -\Psi \tag{5.31}$$

$$T = T_n = 1 - \Psi \tag{5.32}$$

Similarly, the reflection coefficient of a ground plane-backed single-mode periodic structure can be easily extracted as well using Ψ

$$\Gamma = \Gamma_n = \frac{Trace\left(\left[Z\right]^{-1}\left[R\right]\right)}{Trace\left(\left[Z\right]^{-1}\left[R\right]\right)^*} = \frac{\Psi}{\Psi^*} = \frac{1-j\lambda_n}{1+j\lambda_n} \tag{5.33}$$

Should a periodic structure element be dual-mode but exhibit perfect four-quadrant symmetry, there exist two dominant modes of identical eigenvalues. The resulting trace function Ψ becomes

$$\Psi = Trace\left(\left[Z\right]^{-1}\left[R\right]\right) \approx \frac{2}{1+j\lambda} \tag{5.34}$$

In such a scenario, the desired coefficients in free space can be written simply as

$$\Gamma = \Gamma_n = -\frac{1}{2}\Psi \tag{5.35}$$

$$T = T_n = 1 - \frac{1}{2}\Psi \tag{5.36}$$

And in the ground plane-backed scenario, the coefficient actually remains unchanged

$$\Gamma = \Gamma_n = \frac{Trace\left(\left[Z\right]^{-1}\left[R\right]\right)}{Trace\left(\left[Z\right]^{-1}\left[R\right]\right)^*} = \frac{\Psi}{\Psi^*} = \frac{\frac{2}{1+j\lambda}}{\frac{2}{1-j\lambda}} = \frac{1-j\lambda_n}{1+j\lambda_n} \tag{5.37}$$

These are advantageous expression for two main reasons:

1. They are computationally straightforward. No fields are computed, no currents are extracted, and the approach makes use of the computationally efficient trace.
2. There is no need to select a reference plane and be concerned with measuring the scattered field at a sufficient distance from the surface of the periodic structure. Phase values are referenced to the origin and are independent of excitation as no measurement is actually performed.

(a)

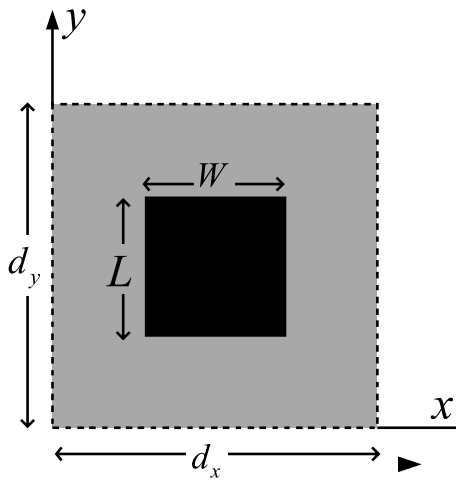

(b)

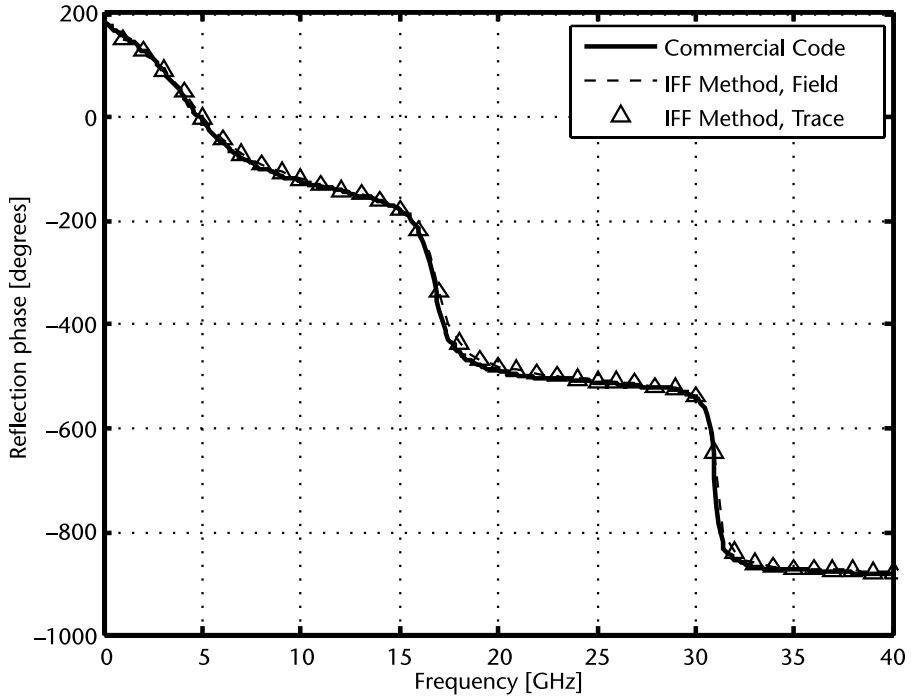

Figure 5.19 Examples of (a) patch and (b) reflection phases using different methods.

In Figure 5.19 the reflection phase of a ground plane backed patch element is computed over a very wide frequency range from dc to 40 GHz using: (1) a commercial code, (2) the traditional scattered field approach, and (3) the efficient trace method. Good agreement is seen over all frequencies.

References

[1] Harrington, R. F., *Field Computation by Moment Methods*, New York: IEEE Press, 2000.

[2] Munk, B., *Frequency Selective Surfaces: Theory and Design*, New York: John Wiley & Sons, 2000.

[3] Mittra, R., C. Chan, and T. Cwik, "Techniques for Analyzing Frequency Selective Surfaces: A Review," *Proceedings of the IEEE*, Vol. 75, No. 12, December 1998, pp. 1593–1615.

[4] Shaker, J., "Analysis of Multilayer Double Periodic Structures and Their Performance," Ph.D. dissertation, Department of Electrical and Computer Engineering, University of Manitoba, 1995.

[5] Hessel, A., and J. Shmoys, "Bragg-Angle Blazing of Diffraction Gratings," *Journal of the Optical Society of America*, Vol. 65, No. 4, April 1975, pp. 380–384.

[6] Johansson, F. S., "A New Planar Grating Reflector Antenna," *IEEE Transactions on Antennas and Propagation*, Vol. 38, No. 9, September 1990, pp. 1491–1495.

[7] Guirard, E., R. Moulinet, and R. Gillard, "An FDTD Optimization of a Circularly Polarized Reflectarray Unit Cell," *IEEE Antennas and Propagation Soc. Intl. Symposium*, San Antonio, TX, Vol. 3, June 2002, pp. 136–139.

[8] Ethier, J., M. R. Chaharmir, and J. Shaker, "Novel Reflectarray Design Comprised of Sub-Wavelength Coupled-Resonant Square Loop Elements," *Electronics Letters*, Vol. 47, No. 22, October 27, 2011, pp. 1215–1217.

[9] Marcuvitz, N., *Waveguide Handbook*, New York: McGraw-Hill, 1951.

[10] Perruisseau-Carrier, J., et al., "Contributions to the Modeling and Design of Reconfigurable Reflecting Cells Embedding Discrete Control Elements," *IEEE Transactions on Antennas and Propagation*, Vol. 58, No. 6, June 2010, pp. 1621–1628.

[11] Yann, C., et al., "A New Approach Combining Surrounded-Element and Compression Methods for Analyzing Reconfigurable Reflectarray Antennas," *IEEE Transactions on Antennas and Propagation*, Vol. 60, No. 7, July 2012, pp. 3215–3221.

[12] Pozar, D. M., "Radiation and Scattering from a Microstrip Patch on a Uniaxial Substrate," *IEEE Transactions on Antennas and Propagation*, Vol. AP-35, No. 6, June 1987, pp. 613–621.

[13] Huang, J., and J. A. Encinar, *Reflectarray Antennas*, New York: IEEE Press, 2008.

[14] Huang, J., "Analysis of a Microstrip Reflectarray Antenna for Microspacecraft Applications," TDA Progress Report 42-120, February 15, 1995.

[15] M. Zhou, et al., "An Accurate Technique for Calculation of Radiation from Printed Reflectarrays," *IEEE Antennas and Wireless Propagation Letters*, Vol. 10, 2011, pp. 1081–1084.

[16] Almajali, E., et al., "An Investigation of Reflectarray Operation Using Its Component Current Contributions," *Proceedings of 6th European Conference on Antennas and Propagation*, 2012, pp. 1603–1607.

[17] HFSS, http://www.ansys.com/hfss.

[18] CST, http://www.cst.com/.

[19] EMCUBE, http://www.emagtech.com/products/emagware/emcube

[20] Chaharmir, M. R., et al., "Design of Broadband, Single Layer Dual-Band Reflectarray Using Multi Open Loop Elements," *IEEE Transactions on Antennas and Propagation*, Vol. 58, No. 9, September 2010, pp. 2875–2883.

[21] Ethier, J., and D. McNamara, "Predicting Infinite Periodic Structure Properties from Finite Structure Models," *Microwave and Optical Technology Letters*, Vol. 54, No. 10, October 2012, pp. 2416–2420.

[22] Ethier, J., "Antenna Shape Synthesis Using Characteristic Mode Concepts," Doctoral Thesis, University of Ottawa, 2012.

[23] Garbacz, R. J., "A Generalized Expansion for Radiation and Scattered Fields," Ph.D. dissertation, Ohio State University, Columbus, 1968.

[24] Harrington, R. F., and J. Mautz, "Theory of Characteristic Modes for Conducting Bodies," *IEEE Transactions on Antennas and Propagation*, Vol. AP-19, No. 5, September 1971, pp. 622–628.

CHAPTER 6

Reflectarray Bandwidth

6.1 Introduction

The most severe drawback in reflectarray antennas is their inherent narrowband performance, and much effort has been made in recent years to overcome this limitation. There are two separate factors that play an important role in setting an upper bound on the bandwidth of a reflectarray antenna. The first is the narrowband of the radiating elements and the second is the differential spatial phase delay resulting from different paths lengths between the feed and each point on the wave front of the radiated beam. The first factor has a severe impact on the bandwidth of moderate size reflectarrays (<20λ) and $F/D > 0.5$, while the second factor becomes dominant in the case of large reflectarrays (>30λ) and $F/D > 0.5$. However, as will be seen later, the second factor can adversely affect the bandwidth for $F/D < 0.25$ even for a moderate size reflectarray.

The required phase value that is to be imparted by the reflectarray element to achieve a specific phase front transformation can be obtained using the following equation:

$$\psi_{di}(f) = k(R_i - r_i.r_0) + \psi_0(f) \tag{6.1}$$

where $\vec{R}_i$ is the distance from the feed horn to the ith element, $\vec{r}_i$ is the position vector of the ith element, and $\vec{r}_o$ represents the main beam direction as shown in Figure 6.1. A constant phase Ψ_0 is added here at each frequency, indicating that it is the relative refection phase rather than the absolute refection phase that matters in reflectarray design. Without loss of generality, let us consider a reflectarray with a main beam at the broadside direction (r_i, $r_0 = 0$) and assume that $\Psi_0(f) = 0$.

$$\psi_{di}(f) = kR_i \tag{6.2}$$

The center element can be used as a reference and the phase of the other elements can be normalized to this reference phase.

$$\psi_{ni}(f) = k(R_i - F) \tag{6.3}$$

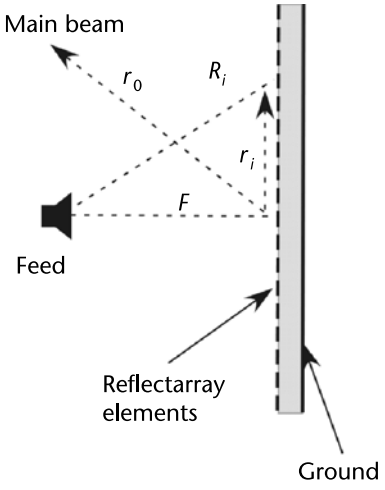

Figure 6.1 A schematic view of a reflectarray.

The phase difference between the normalized phase in (6.3) and the real phase generated by the reflectarray element ($\Phi_{ei}(f)$) is defined as error function. It is obvious that this error function is zero at the design frequency f_0.

$$E_i(f) = \psi_{ni}(f) - \phi_{ei}(f) \tag{6.4}$$

Assume

$$\phi_{ei}(f) = A(f)\phi_{ei}(f_0) \tag{6.5}$$

It will be seen later that the above assumption is indeed correct for a large class of cell elements. It is clear from (6.5) that $A(f_0) = 1$. Equations (6.4) and (6.5) can be combined to obtain the following equation:

$$E_i(f) = k(R_i - F) - A(f)\phi_{ei}(f_0) \tag{6.6}$$

Knowing that the error function diminishes at $f = f_0$:

$$\therefore E_i(f_0) = k_0(R_i - F) - A(f_0)\phi_{ei}(F_0) = 0 \tag{6.7}$$

The following relation can be obtained for the desired phase at $f = f_0$:

$$\phi_{ei}(f_0) = k_0(R_i - F) \tag{6.8}$$

which can be used along with (6.6) to derive the following relationship:

$$E_i(f) = k(R_i - F) - k_0 A(f)(R_i - F) = (R_i - F)(k - A(f)k_0) \tag{6.9}$$

It is clear that to constrain the error function to zero at all frequencies ($E_i(f) = 0$), the following relationship should be maintained for $A(f)$:

$$if\ \therefore E_i(f)=0 \Rightarrow k-A(f)k_0=0 \Rightarrow A(f)=\frac{f}{f_0} \tag{6.10}$$

This means if the element has the following phase behaviour the reflectarray has infinite bandwidth performance regardless of the reflectarray size.

$$\phi_{ei}(f)=\frac{f}{f_0}\phi_{ei}(f_0) \tag{6.11}$$

Such an element is a true time delay (TTD) element that completely removes the frequency dispersion from unequal path lengths and results in infinite bandwidth for large reflectarrays.

In the case of an element with infinite bandwidth ($\Phi_{ei}(f)=A\Phi_{ei}(f_0)$), A is constant (assume $A = 1$) and the error function in (6.9) is:

$$E_i(f)=\frac{2\pi}{c}(R_i-F)(f-f_0) \tag{6.12}$$

This equation shows that for the element with infinite bandwidth the phase error has a direct relationship with the size of reflectarray (R_i–F), and for small and moderate size reflectarray as will be explained in next section, bandwidth of the element is the main factor of reducing reflectarray bandwidth.

This chapter is focused on a more detailed presentation of the above factors that set an upper bound on the reflectarray bandwidth and also techniques to overcome their adverse effect. Due to the flatness of the reflectarray structure, the focal point of a reflectarray is moved along a line as the frequency is shifted across the operating band. This phenomenon will also be discussed in this chapter for a broadband reflectarray.

6.2 Bandwidth Limitation by the Reflectarray Element

The phase value that is to be imparted by the elements of reflectarray to achieve a specific phase front transformation can be obtained using (6.1). Figure 6.2 shows a plot of the required phase for a moderate size (16λ) Ku-band reflectarray at three different frequencies. A similar plot has been generated and shown in Figure 6.3 for a large size reflectarray (40λ) in the same frequency band and the same *F/D* as the moderate size reflectarray. For the case of moderate size reflectarray, the required phase is changed almost linearly as the frequency is swept across the band. This phase variation can be compensated by a broadband cell element because a linear phase variation with changing the frequency can be achieved using these cell elements. However, for large reflectarrays as shown in Figure 6.3, the required phase is not changed linearly across the band and the broadband cell element cannot compensate this phase variation and the gain drops due to this phase error for the large size reflectarrays. Elements with linear phase response are usually used to improve

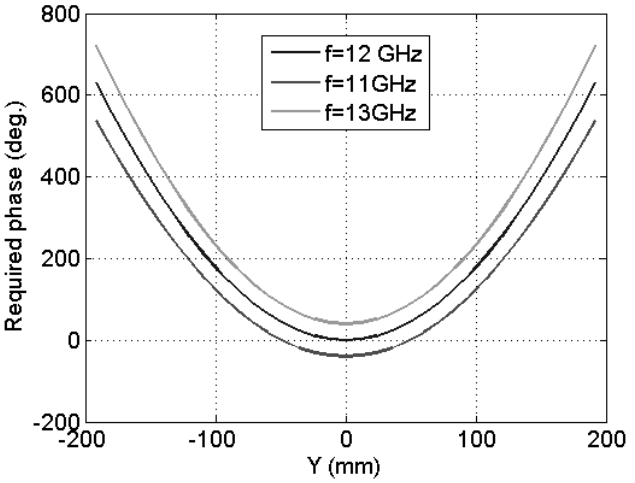

Figure 6.2 Required phase for reflectarrays of $16\lambda \times 16\lambda$ size at the edge and center frequencies.

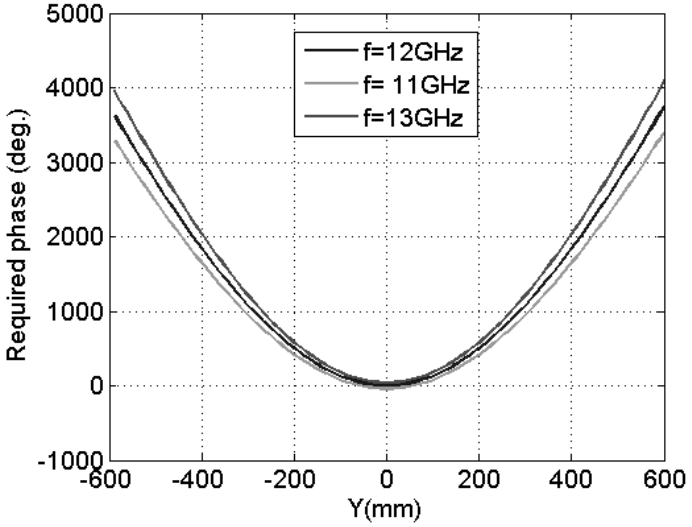

Figure 6.3 Required phase for a large reflectarrays of $40\lambda \times 40\lambda$ size at the edge and center frequencies.

the element bandwidth. Utilization of thick substrates for single-layer reflectarray composed of patches is one of the techniques that were used in the early days of reflectarray research to improve the bandwidth. However, reduced attainable phase shift for such structures was synonymous to reduced gain [2]. Inspired by earlier research in the field of wideband microstrip patch, stacked patch was later suggested as the reflectarray cell element to achieve wideband operation [3]. This latter technology suffers from complexity in fabrication and reduced flexibility for multiband or multipolarization application. Recently, single-layer multiresonance elements were introduced to enhance reflectarray bandwidth. Different cell elements such as patch loaded with slot [4], windmill elements [5], and multidipole [6] were

introduced in the literature. In this section, the research on realization of broadband reflectarray in the context of ring type cell elements is presented. The underlying physics behind this choice is described in the next section. Different types of ring type cell elements, namely, square ring type, cross ring type, and hybrid square and cross-ring cell elements were studied. As will be seen in the case of multiloop structures, the same multiresonance effect that is the basis of stacked patch design [7] is exploited to obtain the optimum phase response.

Recently, subwavelength elements were introduced as another viable alternative for broadband reflectarray. Subwavelength elements have dimensions and periodicity below the typical resonant half-wavelength interelement spacing. Subwavelength rings are discussed in this section as a representative of such elements.

6.3 Multiresonant Elements

Any attempt for broadening the bandwidth of the reflectarray should not solely rely on the common knowledge of the behavior of single element in isolation but should also exploit the rich literature on periodic structures [8]. Particular constraints and restrictions set on the broadband operation of such extensively studied periodic structures as frequency selective surfaces (FSS) are quite relevant and advantageous in the design of broadband reflectarrays. A prominent example of such an outlook is the class of cell elements known as loop elements in FSS nomenclature. The relatively small resonant size of this class of cell elements allows for densely packed FSSs that are superior in bandwidth performance and stability of angular response.

The small size of the resonant element serves the twofold objective of exclusion of higher-order modes excitation and enhancement of the validity of the commonly used infinite periodic structure approximation that is applied in the design stage. A smaller reflectarray cell element is also more efficient in capturing sharp and abrupt phase reversals on the reflectarray.

6.3.1 Square-Loop Cell Element

Single- and double-loop elements [9] were thoroughly discussed in Chapter 4 and it was demonstrated that each additional loop leads to an additional resonance and added range of attainable phase. The phase response of the element can be smoothed out by adjusting the coupling between multiloop elements as shown in Figure 3.11.

The wider attainable phase range and also smoother phase versus length characteristics of the double loop cell element leads with wider operating bandwidth.

A reflectarray was fabricated at Ku-band using double ring cell element and tested in the far-field anechoic chamber [10]. The gain-frequency response for this particular antenna is shown Figure 6.4, which shows 14% bandwidth for 1-dB gain reduction. The reflectarray is offset-fed with 40 cm $\times$ 40 cm dimensions. To mitigate beam squint across the frequency band, the direction of the outgoing beam was set along the direction of the direct reflected ray with respect to the ray from the focal point to the center of the reflectarray [11]. The same practice was followed in all offset reflectarrays in this section.

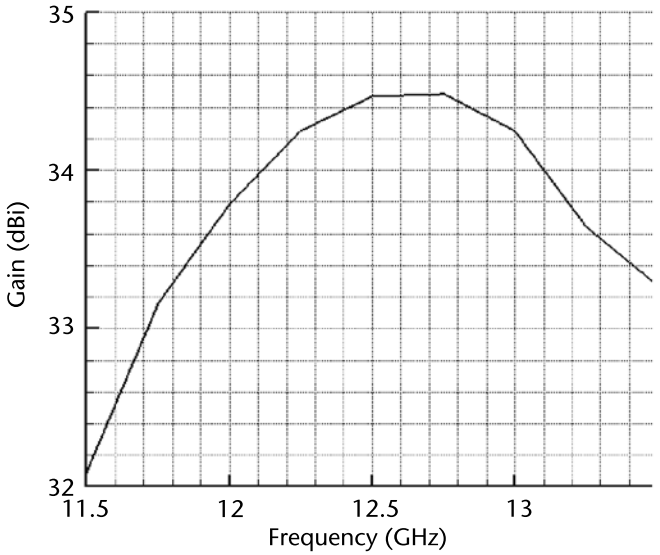

Figure 6.4 Directivity-frequency plot for a reflectarray composed of double square rings. (© 2009 IEEE. *From:* [10].)

6.3.2 Cross-Loop Cell Element

The cross-loop cell element as was introduced in Chapter 3 and shown in (3.13) is another variation of the class of loop elements that can achieve wideband operation.

As it was mentioned in Section 3.2 and Figure 3.14, a gradual variation of phase with respect to the loop length is a prerequisite for a wideband element. An offset-fed reflectarray composed of cross ring cell elements was designed, fabricated, and tested at Ku-band. The reflectarray dimensions was set at 40 cm × 40 cm. Gain versus frequency bandwidth of this reflectarray is shown in Figure 6.5, which shows a 16% bandwidth for 1-dB gain reduction.

6.3.3 Hybrid Cell Element

Following an extensive set of simulations for square-ring and cross-loop cell elements, it was shown that the number of resonances is increased as more rings are added to the structure and these resonances can be decoupled from each other by maintaining a certain relationship between the sizes of concentric rings. Also, it is important to note that simultaneous resonance of the rings results in steeper phase characteristics within the coupling region. Therefore, the rings are ought to be decoupled in order to obtain more gradual variation of the phase with respect to the ring size. The gap between the rings needs to be adjusted to reduce the coupling between adjacent rings of the same cell element to achieve gradual phase versus ring size characteristic in all regions. These geometrical considerations led to the hybrid modified square (rectangular) and cross ring cell elements as the optimized element to achieve the necessary phase shift range and gradual phase-ring size variation [13]. The phase versus ring size plot of this optimized element based on cell element dimensions of [13] is shown in Figure 6.6.

An offset-fed reflectarray composed of such elements was designed, fabricated, and tested. Measured gain versus frequency plot and the radiation pattern of the

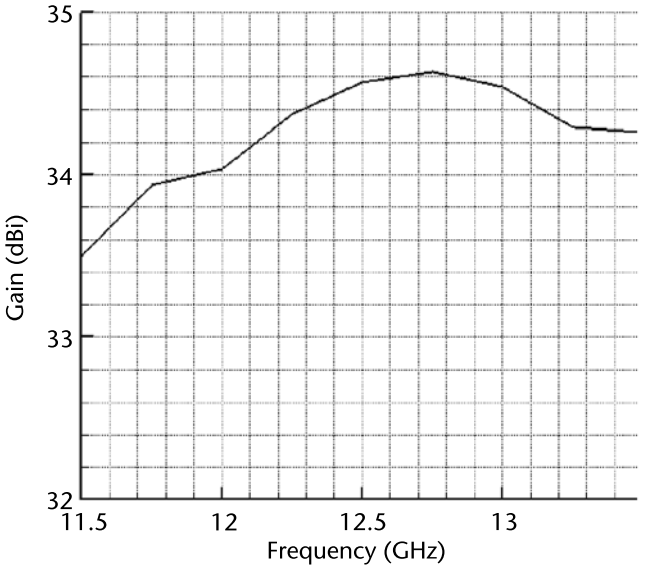

Figure 6.5 Measured directivity versus frequency of the double cross loop reflectarray: unit cell= 12 mm, W_1 = 3.4 mm, W_2 = 0.4 mm, and $d_1 = d_2 = g$ = 0.5 mm. (© 2009 IEEE. *From:* [10].)

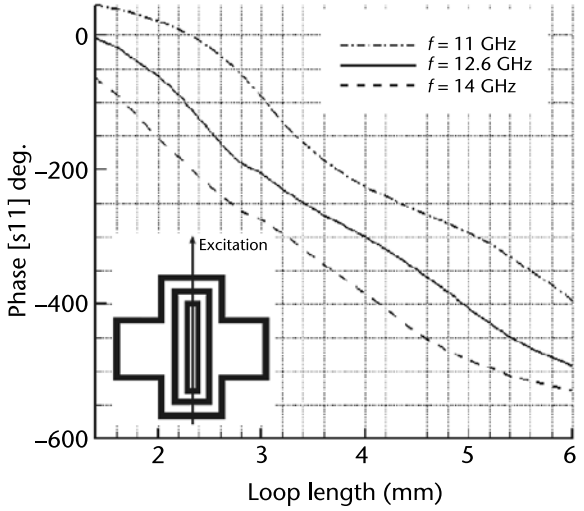

Figure 6.6 Phase-ring size characteristics for cell elements composed one cross loop and two rectangular loops. (© 2009 IEEE. *From:* [13].)

antenna are shown in Figures 6.7 and 6.8. A measured 1-dB gain versus bandwidth of 24% was achieved using this novel cell element. The efficiency at the center frequency was measured to be 60%.

6.4 Subwavelength Elements

Reflectarray cell elements are traditionally designed with lattice sizes around $\lambda/2$. It was shown recently that the bandwidth of reflectarray can be improved by using

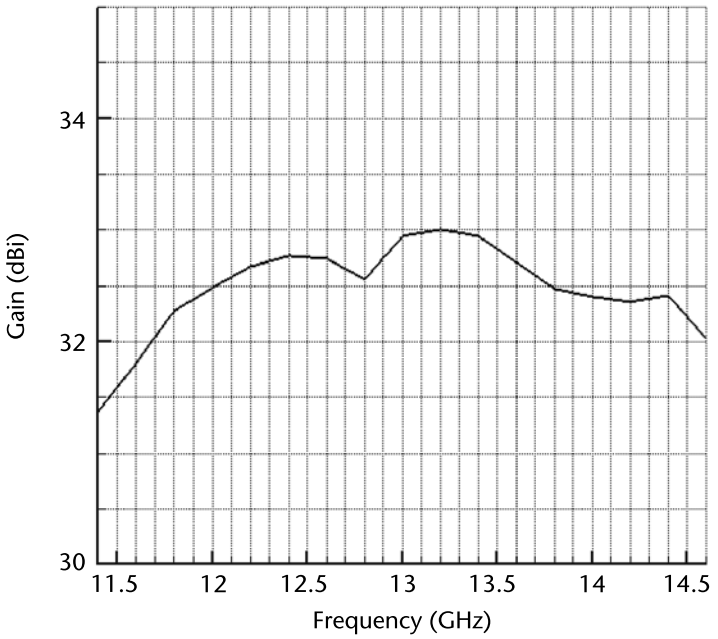

Figure 6.7 Phase-ring size characteristics for cell elements composed of one cross ring and two rectangular rings. (© 2008 IEEE. *From:* [13].)

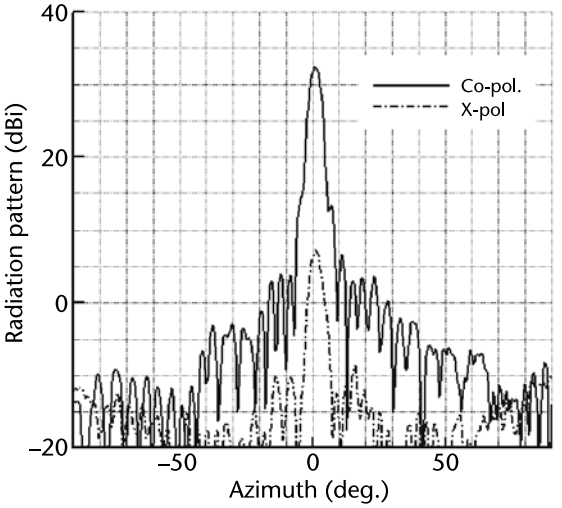

Figure 6.8 Radiation pattern of the reflectarray composed of cell elements described in Figure 6.7. (© 2008 IEEE. *From:* [13].)

closely spaced element with cell size smaller than $\lambda/2$ so-called subwavelength elements, which were explained in Chapter 3. Smaller lattice size along with subwavelength coupled-resonant elements can act as artificial impendence surface which substantially improve the bandwidth. It was shown in [14] that there is a direct relationship between reflectarray cell size and gain bandwidth of reflectarray lattice size. In this reference a reflectarray using array of 20×20 near-resonant patches on 31-mil substrate with spacings of 9 mm is compared with three alternative designs

using subwavelength patches with different cell sizes. The grid spacings and the number of elements are selected so that aperture area is the same for all four cases. Figure 3.32(a) in Chapter 3 showed the gain versus frequency for all four cases. It appears that gain bandwidth increases as the grid spacings become smaller (with a fixed aperture size).

Reflectarrays composed of subwavelength patch elements have been widely studied in the literature [15]. The minimum gap size between the patch elements is a critical factor in controlling the maximum achievable phasing range.

It was shown in [16] that the phase variation of the reflected wave with frequency is decreased by reducing the cell size of a subwavelength patch, which can improve the bandwidth of small and moderate size reflectarrays as shown in (6.12). While reducing the cell size can improve the bandwidth of the subwavelength reflectarray, it sets tight constraints on etching tolerance. Two-layer subwavelength patch elements have been suggested in [17] to achieve the desired phase range while maintaining reasonable etching tolerances nevertheless the higher fabrication complexity because of the additional layer of cell elements. Other subwavelength elements such as loop and dogbone were introduced in Chapter 3, which can be used as reflectarray subwavelength element with smaller cell size as compared to subwavelength patch. These subwavelength elements are better candidates for broadband operation. Figure 6.9 shows the reflection phase dispersion which is defined as the frequency derivative of the reflected phase ($Dispersion = \frac{d\phi}{df}$) versus frequency of a subwavelength loop for different cell sizes [18]. The phase dispersion decreased significantly by reducing the lattice size which confirms the observation in [16]. However, the subwavelength loop can still furnish the desired phase range of 300° with lattice size of $\lambda/6$.

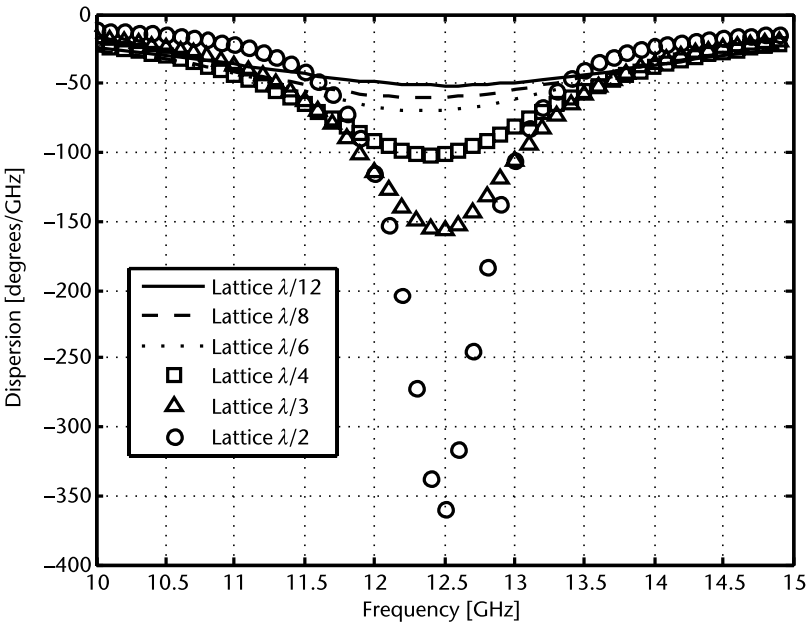

Figure 6.9 Plot of dispersion versus frequency for square loop element for various electrical lattice sizes. (© 2011 IEEE. *From:* [18].)

The measured gain versus frequency for a reflectarray with subwavelength loop element [19] was shown in Figure 3.35. A 1-dB gain bandwidth of nearly 19% was measured for the reflectarray, which is the same as the simulated bandwidth of the double layer patch element with cell size of $\lambda/3$ reported in [17].

6.5 Bandwidth Limitation by Differential Spatial Phase Delay

The bandwidth limitation due to differential spatial phase delay resulting from different path lengths for the rays emanating from the feed to each reflectarray element is the most restrictive factor in bandwidth performance of large-sized reflectarrays. The separation between the phase center of feed and each reflectarray element produces a different phase delay at each location, which is compensated with the reflected phase generated by reflectarray elements. This phase delay can be in a range of several multiples of 360° in given regions of a large reflectarray. The conventional technique of reflectarray design calls for adjustment of the elements to compensate the phase delay at the center frequency without taking into account the dispersion phase value ($\Delta\Phi/\Delta f$), which is the variation of the required phase as the frequency is swept across the band. Because of the appreciable amount of frequency dispersion for a large reflectarray, and very limited capability of the element to compensate for the dispersion, the antenna bandwidth suffers significantly. This pathological investigation into the causes of reduced bandwidth in the case of large reflectarray might lead the attentive reader to possible solutions to overcome this restriction. For instance, the reflectarray elements are ought to be selected from among a pool of elements that realize the required phase at the center frequency and at the same time are the best fit considering the phase requirements at the edge frequencies. In other words, the cell element at a particular location on the reflectarray has a twofold function of realizing the desired phase to attain the phase transformation at the center frequency and edge frequencies. Having different phase requirements at these frequencies would force the designer to select from among a pool of elements [20, 21]. The following relationship is used as the error function to choose from among a pool of elements:

$$e(m,n) = \sum_{i=l,c,u} \left| \Phi_i^{desired}(f_i)(m,n) - \Phi_i^{achieved}(f_i)(m,n) \right| \tag{6.13}$$

where *l, c, u* refer to lower, center, and upper frequencies, *m*, *n* refers to element indices on the reflectarray grid, and Φ is the phase shift. This error function can be used as the objective function in an optimization routine to be presented in next section to design moderate and large size reflectarrays.

The issue of frequency dispersion in the case of the large reflectarray can be understood from a different perspective. Figure 6.10 shows the phase difference between the phase of the elements at the center and the rim of the reflectarray when there is no restriction on the amount of phase that can be realized by the elements. In other words, the elements are capable of realizing phase values in excess of 360°. Wavelength is the yardstick that is to be used in the quantification of the desired phase. The physical size of this yardstick changes as the frequency is swept across

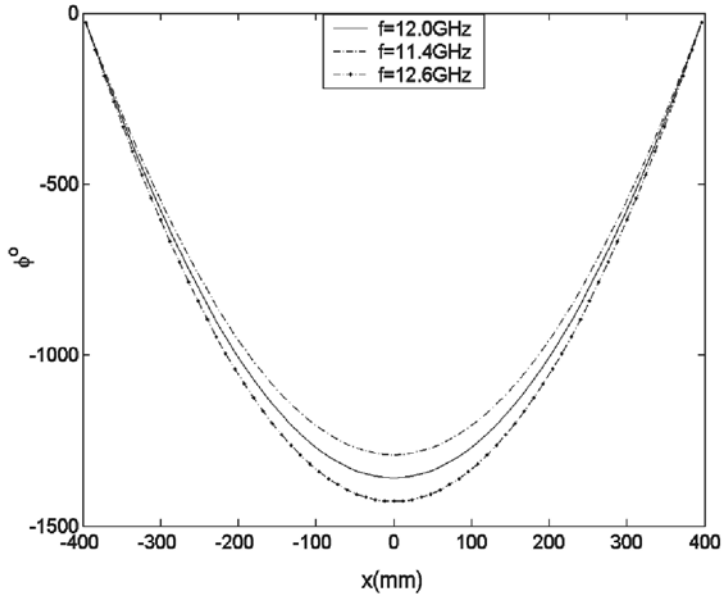

Figure 6.10 Desired phase for the large reflectarray when there is no restriction on the amount of phase that can be attained from the cell element.

the band, which demonstrates the frequency dispersion. This is equivalent to different phase constraints at different frequencies in order to realize the same phase transformation. Now, if a mechanism can be contrived to account for the time delay of the signal as it travels from the feed to different points on the reflectarray, the bandwidth can be increased significantly.

As was shown in (6.13), the ideal solution to have infinite bandwidth is to use element with true time delay (TTD) capability. Figure 6.11 shows slot coupled time delay lines that have been introduced in [22] as a TTD measure to improve bandwidth. The phase response can be very linear if a proper adjustment of the geometry is performed to alleviate the effects produced by multiple resonances. Depending on the phase values required at the reflectarray elements, the phase-shifter is chosen with a simple $L1$ line segment or with a U-shaped TTD line. The phase and amplitude of the reflection coefficient for this type of element is shown

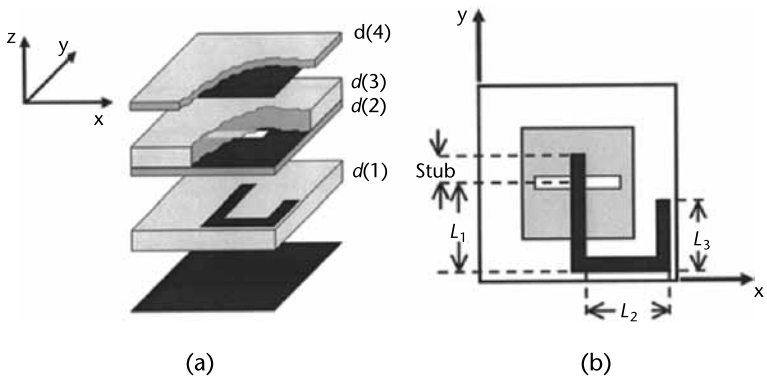

Figure 6.11 Reflectarray element based on patches aperture-coupled to delay lines: (a) expanded view and (b) top view. (© 2008 IEEE. *From:* [22].)

in Figure 6.12. The phase variation covers 3 × 360° phase range required for the phase-delay distribution and it is compared with an ideal delay line, in which the phase should be $-2\beta L$, where β is the propagation constant at the corresponding frequency and L is the length of the delay line.

A reflectarray using this element is designed and fabricated at X-band and a gain bandwidth of 26% (1.5-dB gain drop) was measured for this reflectarray [22].

6.5.1 Verification of the Optimization Method

The differential spatial phase delay is the main reason of bandwidth limitation of large reflectarrays. The idea of optimization as was mentioned in the previous section is to select the reflectarray elements from among a pool of elements that realize the required phase at the center frequency and at the same time are the best fit considering the phase requirements at the edge frequencies. A method was introduced in [20] to overcome the bandwidth limitation of large reflectarrays by using an optimization routine to adjust all the dimensions of a three-layer printed reflectarray to compensate for the frequency dispersion, but using a multilayer configuration leads to other shortcomings such as additional fabrication complexity, increased weight, and higher loss. The optimization technique introduced in this section is based on a single-layer structure and different classes of multicross loop elements were utilized in this optimization [23, 24].

For an offset-fed reflectarray that is shown in Figure 6.13 (for simplification, only the one-dimensional problem was addressed here and the figure shows the cross section of the reflectarray and feed in the *xoz* plane), the phase value that is to be imparted by the elements of the reflectarray to transform the spherical phase front of the feed to plane wave at θ_b can be calculated from the following equation:

$$\phi_n(f) = 2\pi \frac{f}{c}\left(R_n - x_n \sin\theta_b\right) \tag{6.14}$$

where xn is x-coordinate of nth reflectarray element with respect to geometrical center of reflectarray along the x-axis, θ_b is the angle of main beam with respect to

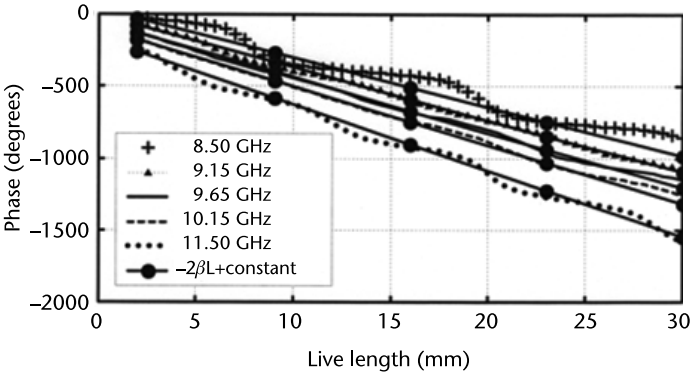

Figure 6.12 Reflection coefficient for reflectarray element as a function of line length for normal incidence. (© 2008 IEEE. *From:* [22].)

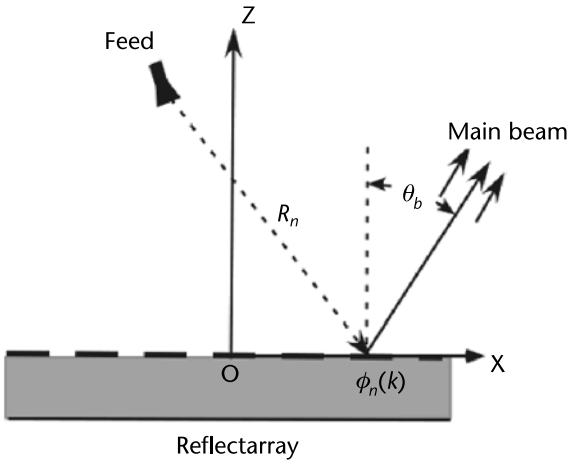

Figure 6.13 Schematic one-dimensional view of an offset-fed reflectarray.

the z-axis, R_n is distance from the feed to the nth element, and f and c represent the operating frequency and the speed of light, respectively.

This phase can be normalized to the minimum phase, ($\Phi_{min}(f)$) (global minimum of the required phase shift throughout the reflectarray), for each frequency to impose 0° global minimum phase shift for the phase templates at all optimized frequencies. An arbitrary phase ($\Phi_{ref}(f)$) can be added as shown in (6.15) to satisfy the dispersion frequency constraint as described here:

$$\phi_{n\_norm}(f) = 2\pi\frac{f}{c}\left(R_n - x_n \sin\theta_b\right) - \phi_{\min}(f) + \phi_{ref}(f) \tag{6.15}$$

Φ_{ref} is selected in a way to meet $\Delta\Phi_{n\text{–}norm}/\Delta f \le 0$ constraint for all the reflectarray elements (physical restriction). The parameter $\Phi_{ref}(f)$ is adjusted to get zero frequency dispersion for the elements at the reflectarray edge while maintaining negative frequency dispersion for the rest of elements. This guarantees negative (or zero) frequency dispersion for all the other reflectarray elements to make the structure physically realizable by appropriate choice of cell elements. As pointed out, negative frequency dispersion condition is a universal condition that is to be met regardless of the type of element that is used. For a simple case of a broadside, center-fed reflectarray ($\theta_b = 0$), the maximum $\Delta\Phi_{ref}/\Delta f$ can be calculated according to the following equation:

$$\Delta\phi_{ref}/\Delta f = \frac{2\pi}{c}\left(R_{\max} - F\right) \tag{6.16}$$

where Φ_{ref} is calculated for the center element, R_{max} is the distance from the feed to the edge of reflectarray, and F is reflectarray focal length. This equation was calculated by assuming $\Delta\Phi_{n\text{–}norm}/\Delta f = 0$ for the element at the edge ($R_n = R_{max}$) and $\Phi_{min} = 2\pi fF/c$ in (6.15).

Figures 6.14 and 6.15 show the required phase on a row/column passing through the center of a center-fed reflectarray for the center frequency and extreme frequencies of a Ku-band 1.2-m reflectarray. These phases were calculated for two different $\Delta\Phi_{ref}/\Delta f$ values. The desired phase in Figure 6.14 is calculated based on (6.14) to get $\Delta\Phi_{n-norm}/\Delta f = 0$ for the elements at the edge of reflectarray. In Figure 6.15 to get $\Delta\Phi_{ref}/\Delta f$ is not assigned correctly and it is slightly smaller than the one calculated in Figure 6.14, therefore the $\Delta\Phi_{n-norm}/\Delta f > 0$ for some elements at the edge, which cannot be compensated by any choice of reflectarray cell element. The phase of center element at center frequency was set to $\Phi_0 = 0°$ but it can be treated as design parameter to obtain a better convergence and less error as a result of frequency dispersion.

Different classes of double-cross loop elements with variable length (see Figure 6.16) were used for designing the reflectarray. Different loop elements were defined by changing the line width (di), loops separation ($g1$), and cross width (w) (see Table 6.1). These sets of loops form the search space for the selection of the elements according to the criteria outlined in the previous section.

In practice, the error function introduced in (6.13) is tested with all elements within the search space and the element with the lowest error function is selected as the optimum element from the point of view of bandwidth performance. This same procedure was repeated for all the elements to get minimum frequency dispersion for all reflectarray elements. In other words, from among all the members of the search space that provide a given phase at the center frequency, the one that minimizes the objective function is chosen as the optimum element. Figure 6.17 shows the phase of reflected wave versus loop length (L) for the double-cross loop element when $d1 = d2 = g1$ for different cross widths (w). Changing the parameters of the cell element generates different slope values.

The optimization technique was used to design a 1.2-m offset-fed reflectarray for a frequency band of 11.4 GHz–12.8 GHz. As noted before the value of $\Delta\text{ref}/\Delta f$ for the center element is selected in such a way that $\Delta\Phi/f = 0$ for the edge elements

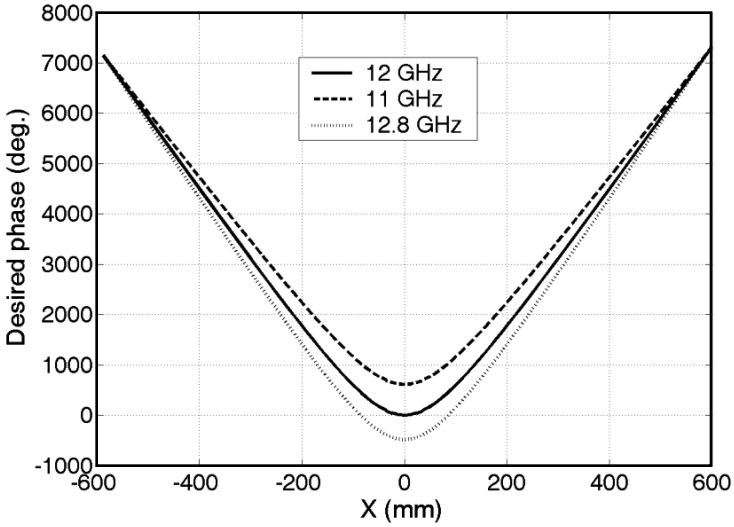

Figure 6.14 The desired on-axis phase of 120-cm-square center-fed reflectarray with F/D = 1 for three different frequencies when $\Delta\Phi_{ref}/\Delta f$ is calculated according to (6.16). (© 2010 IEEE. *From:* [24].)

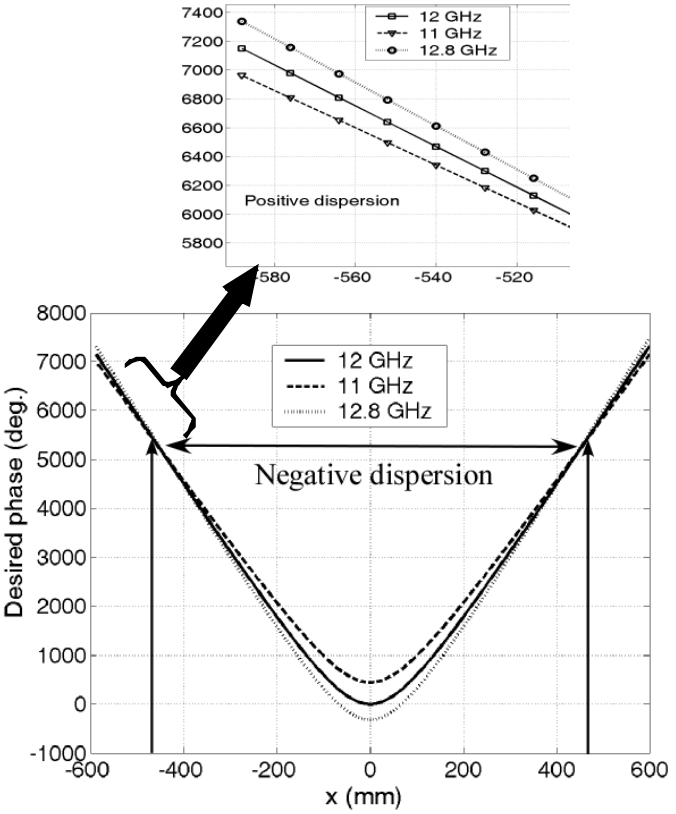

Figure 6.15 The desired on-axis phase of 120-cm-square center-fed reflectarray with F/D = 1 for three different frequencies when $\Delta\Phi_{ref}/\Delta f$ is smaller than the one calculated in (6.16). (© 2011 IEEE. *From:* [24].)

Table 6.1 Parameters of the Cell Element for Different Configuration

Loop Type	*d1, d2 (mm)*	*g1 (mm)*	*w (mm)*
Double-cross loop	0.2 – 0.5 step:0.1	0.2 – 0.5 step:0.1	3.5
Double-cross loop	0.2 – 0.5 step:0.1	0.2 – 0.6 step: 0.1	4
Double-cross loop	0.2 – 0.5 step:0.1	0.2 – 0.6 step: 0.1	4.5

Source: [24].

and $\Delta\Phi/\Delta f < 0$ for the rest of the elements. Reflectarrays were designed when the selection pool is composed of a single type of element or 66 types of elements (see Table 6.1). Radiation patterns were calculated for each case using array theory and results are shown in Figure 6.18. Comparison between Figures 6.18(a) and 6.18(b) demonstrates significant improvements of radiation pattern characteristics as the selection pool is enlarged.

Figure 6.19 shows a histogram of the cross-loop elements that are selected in the design of the reflectarray when 66 different cross-loop configurations, as

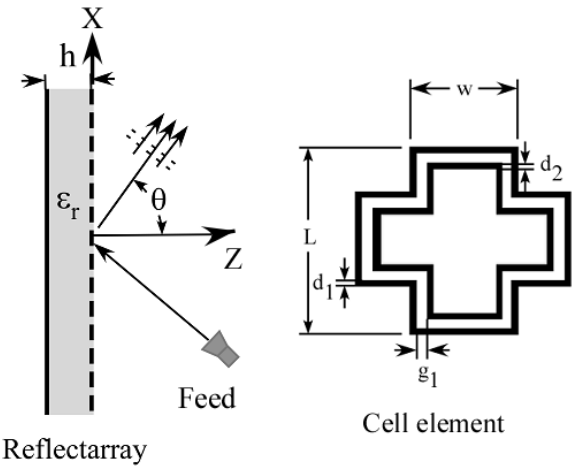

Figure 6.16 A schematic view of the reflectarray and the cell element. (© 2010 IEEE. *From:* [23].)

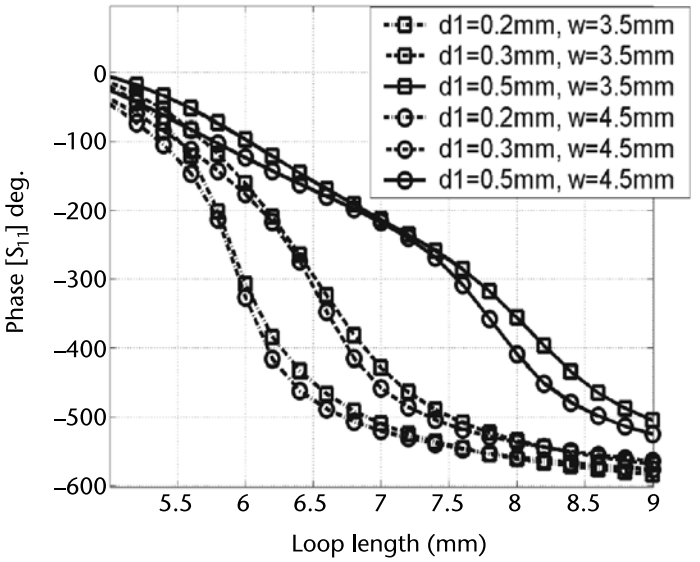

Figure 6.17 Phase of the reflected wave versus loop length for different loop configurations $d_1 = d_2 = g_1$. (© 2010 IEEE. *From:* [24].)

tabulated in Table 6.1, were used in the optimization. It is evident in this figure that element numbers 16, 41, and 66 were used the most in this design. These curves have same line width (*di*) and gap (*g*1) with cross widths of 3.5 mm, 4 mm, and 4.5 mm, respectively. Inspection of the phase versus cross loop length of these elements reveals their broadband nature.

This reflectarray was designed and fabricated [24] and the measured H-plane radiation pattern for the design and edges frequencies is shown in Figure 6.20. The pattern is quite stable for all these frequencies and gain drops less than 1 dB and sidelobe level stays below –20 dB within the frequency band. The measured gain bandwidth is better than 12% for this antenna, which shows a significant improvement as compared to conventional single-layer reflectarrays with same size.

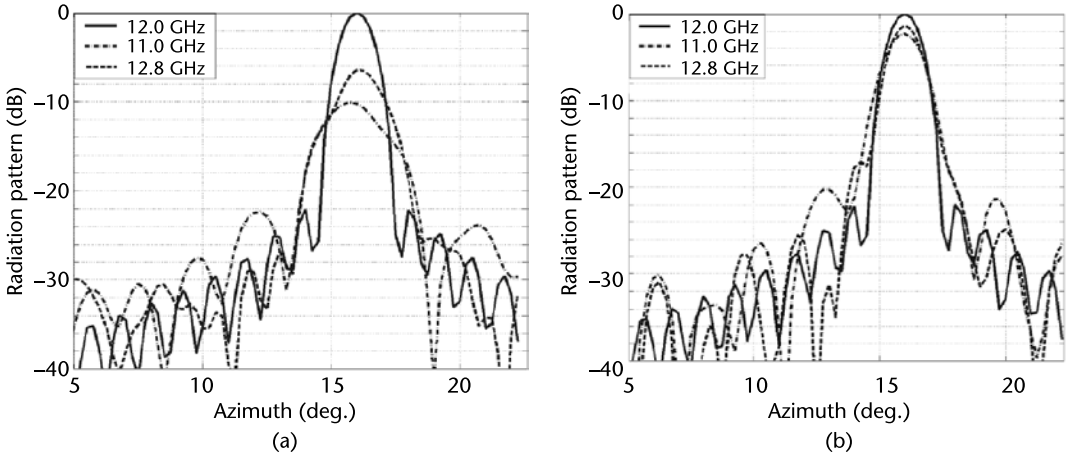

Figure 6.18 Calculated radiation pattern for the 1.2-m reflectarray for different cross loop configurations in Table 6.1: (a) one cross loop, $d_1 = d_2 = g = 0.2$ mm, $w = 3.5$ mm and (b) 66 different cross-loop configurations (see Table 6.1). (© 2010 IEEE. *From:* [24].)

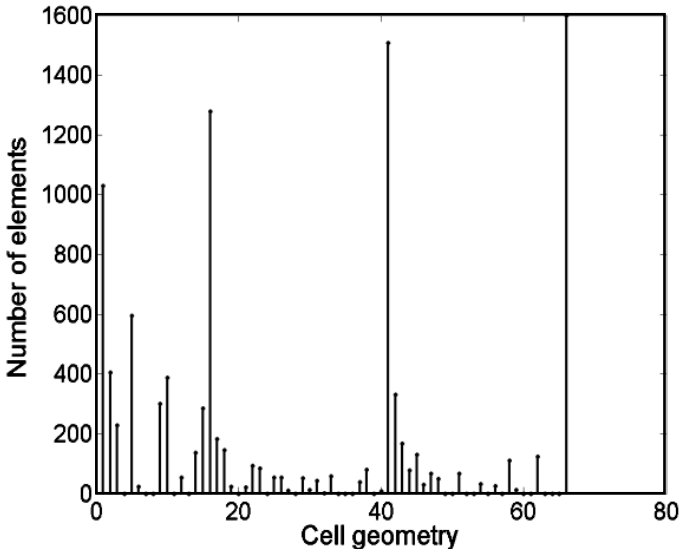

Figure 6.19 A histogram of number of times each cross-loop type in Table 6.1 is used in the design of the reflectarray. (© 2010 IEEE. *From:* [24].)

6.6 Impact of the Feed Position on the Bandwidth of Broadband Reflectarrays

Whereas the physical shape of reflector antenna is modeled by adjusting the frequency-dependent phase of elements in the case of its reflectarray counterpart, there is a focal point shift as the frequency is swept within the operating band of reflectarray. In this section, a study is undertaken to investigate the effect of changing feed location (the distance from horn aperture to the reflectarray center) on the bandwidth performance of reflectarray [26, 27]. An offset-fed reflectarray as shown in Figure 6.21 with $D = 160$ mm and $F/D = 1$ is used in this study. The reflectarray is designed at center frequency of $f = 30$ GHz with a main beam at broadside

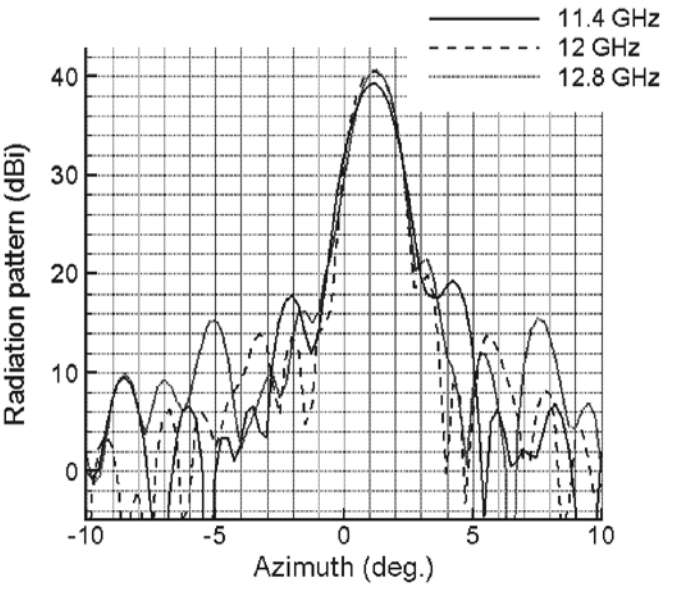

Figure 6.20 Measured radiation pattern (H-plane) for three different frequencies of 11 GHz, 12 GHz, and 12.8 GHz. (© 2010 IEEE. *From:* [24].)

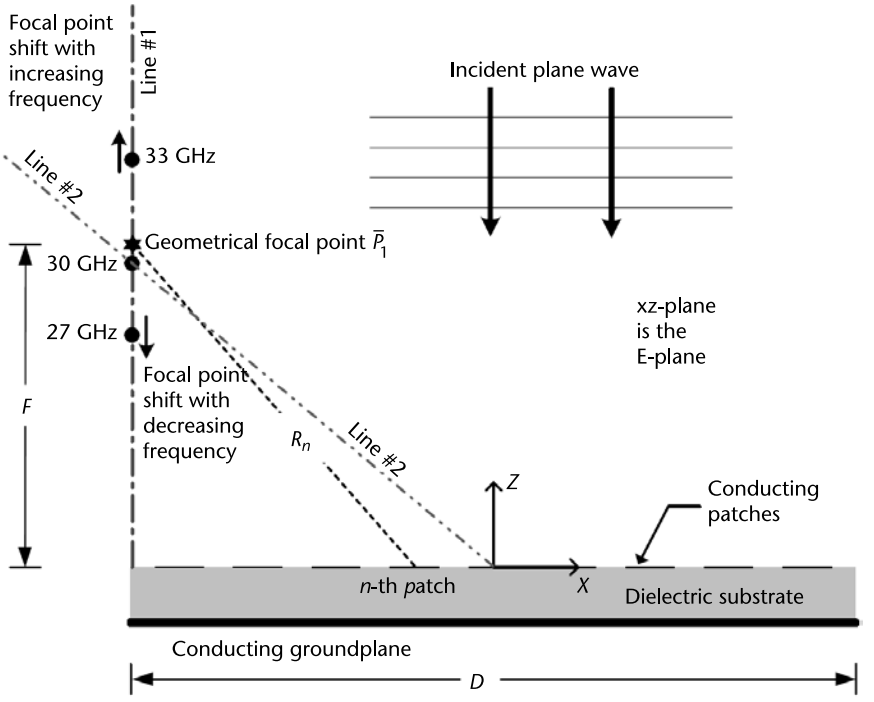

Figure 6.21 Offset-fed reflectarray geometry showing a normally incident plane wave. The coordinate origin is at the center of the reflectarray aperture. The shift of the actual focal point from the geometrical one is shown exagerrated. (© 2012 IEEE. *From:* [27].)

direction. The focal point ($P1$), hereafter referred to as the geometrical focal point, is at location ($x = x\text{off}$, $y = y\text{off}$, $z = F$).

To derive an approximate expression for the focal shift with frequency that we recognize, with reference to Figure 6.22, the boundary of the first Fresnel zone is defined by the following equation [25]:

$$\left|P_1P_3\right| - \left|P_1P_2\right| = \sqrt{\left(x_{fz} - x_{off}\right)^2 + F^2} - F = \frac{c}{f} \tag{6.17}$$

It is evident that the focal point moves to keep the Fresnel zones boundary intact as the frequency is swept across the band. That means the values of *x*off and *xfz* are fixed for a given reflectarray. Implicit differentiation of (6.17) with respect to frequency *f* allows us to write the focal point shift (ΔF) from its center-frequency value, along Line #1 shown in Figure 6.21, for a shift (Δf) in the operating frequency from the center frequency:

$$\Delta F = \left(\frac{\left|P_1P_3\right|}{\left|P_1P_3\right| - F}\right)\frac{c}{f^2}\Delta f \tag{6.18}$$

where *P*1*P*3 is the distance from focal point to the boundary of the first Fresnel zone at center frequency. It is assumed that the reflectarray elements have elements with infinite bandwidth in this expression so the reflected phase shift by elements is constant throughout the frequency band.

The method that was described in Chapter 5 is utilized here to study this feed movement further and verify the accuracy of the above equation. The near-field intensity on predefined lines in HFSS is used to track the feed movement. An offset-fed 15-cm-square reflectarray with subwavelength patch elements designed at 30 GHz is used in this study. The reflectarray is illuminated with a normal plane wave and near-field intensity was calculated on Line #1 in Figure 6.21 at different frequencies inside frequency band of 27 GHz to 33 GHz. As frequency is changed the maximum field value (the focal point), shifts vertically along Line #1 (normal to the reflectarray) as shown in Figure 6.23. In other words, the focal point moves towards (away from) the reflectarray surface as the frequency decreases below (increases above) the center frequency of 30 GHz. Specific shifts along Line #1 are given in Table 6.2. The feed movement calculated using (6.18) is also shown in this

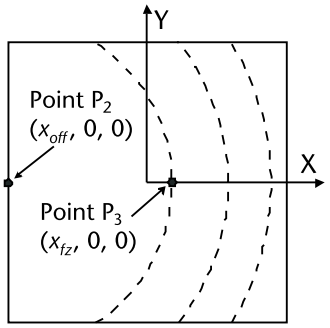

Figure 6.22 Schematic top view of a reflectarray, with dashed lines indicating Fresnel zone boundaries. Point P1 is shown in Figure 6.21. (© 2012 IEEE. *From:* [27].)

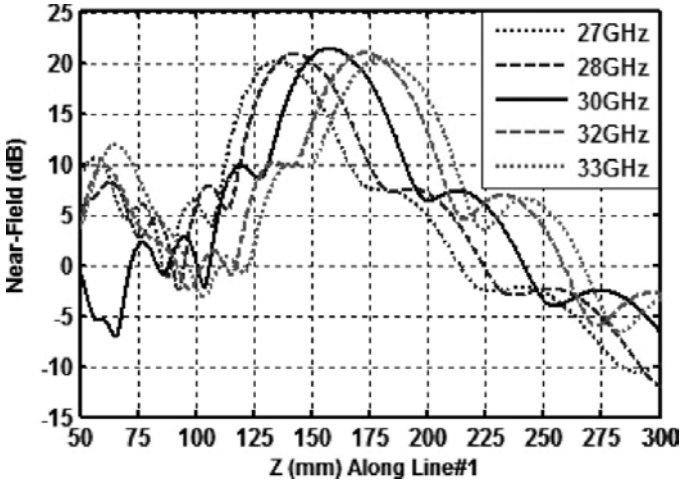

Figure 6.23 Focal field region shift with frequency along Line #1 ($\lambda/3$ lattice). (© 2012 IEEE. *From:* [27].)

Table 6.2 Focal Point Shift Along Line #1

Frequency (GHz)	*Focal Point Position z (mm): Full-Wave Model*	*Shift from Geometrical Focal Point Using Full-Wave Model Result*	*Shift from Geometrical Focal Point Using [3]*
27	*F*2 = 136.5	–23.5	–21.7
30	*F*1 = 157.3	2.7	2.7
33	*F*3 = 180.6	20.6	16.3

Source: [27].

table and there is a good agreement between the simulation results in HFSS and the results calculated using (6.18).

Understanding of this feed movement can help us to change the frequency operation of reflectarrays by moving the feed location along the line of the feed movement without redesigning the reflectarray as long as the reflectarray elements are wideband enough to cover the whole frequency band.

References

[1] Pozar, D. M., "Bandwidth of Reflectarray," *Electronics Letters*, Vol. 39, No. 21, October 2003, pp. 1490–1491.

[2] Pozar, D. M., S. D. Targonski, and H. D. Syrigos, "Design of Millimeter Wave Microstrip Reflectarrays," *IEEE Transactions on Antennas and Propagation*, Vol. 45, No. 2, February 1997, pp. 287–295.

[3] Encinar, J., "Design of Two Layer Printed Reflectarrays Using Patches of Variable Size," *IEEE Transactions on Antennas and Propagation*, Vol. 49, No. 10, October 2001, pp. 1403–1410.

[4] Cadoret, D., et al., "A New Reflectarray Cell Using Microstrip Patches Loaded with Slots," *Microwave and Optical Technology Letters*, Vol. 44, No. 3, February 5, 2005, pp. 270–272.

[5] Zhao, J. -J., et al., "A Novel Broadband Reflectarray Antenna Using Windmill Elements," *9th International Symposium on Antennas Propagation and EM Theory (ISAPE)*, 2010.

[6] Li, L., et al., "Novel Broadband Planar Reflectarray with Parasitic Dipoles for Wireless Communication Applications," *IEEE Antennas and Wireless Propagation Letters*, Vol. 8, 2009, pp. 881–885.

[7] Encinar, J., and J. A. Zornoza, "Broadband Design of a Three-Layer Printed Reflectarray," *IEEE Transactions on Antennas and Propagation*, Vol. 51, No. 7, July 2003, pp. 1662–1664.

[8] Munk, A., *Frequency Selective Surfaces: Theory and Design*, New York: John Wiley & Sons, 2000.

[9] Chaharmir, M. R., et al., "A Broadband Reflectarray Antenna with Double Square Rings," *Microwave and Optical Technology Letters*, Vol. 48, No. 7, July 2006, pp. 1317–1320.

[10] Chaharmir, R., et al., "Wideband Reflectarray Research at the Communications Research Center Canada," *Proceedings ANTEM Conference*, Banff, Alberta, Canada, February 2009.

[11] Targonski, D., and D. M. Pozar, "Minimization of Beam Squint in Microstrip Reflectarrays Using an Offset Feed," *Antennas and Propagation Society International Symposium,* Vol. 2, July 21–26, 1996, pp. 1326–1329.

[12] Chaharmir, M. R., et al., "Broadband Reflectarray Antenna with Double Cross Loops," *Electronics Letters*, Vol. 42, No. 2, January 2006, pp. 65–66.

[13] Chaharmir, R., and J. Shaker, "Broadband Reflectarray with Combination of Cross and Rectangle Loop Elements," *Electronics Letters*, Vol. 44, No. 11, May 22, 2008, pp. 658–659.

[14] Pozar, D. M., "Wideband Reflectarrays Using Artificial Impedance Surfaces," *Electronics Letters*, Vol. 43, No. 3, February 2007, pp. 148–149.

[15] Nayeri, P., F. Yang, and A. Z. Elsherbeni, "A Broadband Microstrip Reflectarray Using Sub-Wavelength Patch Elements," *IEEE Antennas and Propagation Society International Symposium*, 2009.

[16] Nayeri, P., F. Yang, and A. Z. Elsherbeni, "Bandwidth Improvement of Reflectarray Antenna Using Closely Spaced Elements," *PIER*, Vol. 18, 2011, pp. 19–29.

[17] Nayeri, P., F. Yang, and A. Z. Elsherbeni, "Broadband Reflectarray Antennas Using Double-Layer Subwavelength Patch Elements," *IEEE Antennas and Wireless Propagation Letters*, Vol. 9, 2010, pp. 1139–1142.

[18] Ethier, J., R. Chaharmir, and J. Shaker, "Novel Approach for Low-Loss Reflectarray Design," *APS 2011*, Toronto, July 4–8, 2011.

[19] Ethier, J., M. R. Chaharmir, and J. Shaker, "Reflectarray Design Comprised of Sub-Wavelength Coupled-Resonant Square Loop Elements," *Electronics Letters,* Vol. 47, No. 22, October 27, 2011, pp. 1215–1216.

[20] Encinar, J., and J. A. Zornoza, "Broadband Design of a Three-Layer Printed Reflectarray," *IEEE Transactions on Antennas and Propagation,* Vol. 51, No. 7, July 2003, pp. 1662–1664.

[21] Encinar, J. A., "Design of Two-Layer Printed Reflectarrays Using Patches of Variable Size," *IEEE Transactions on Antennas and Propagation,* Vol. 49, 2001, pp. 1403–1410.

[22] Carrasco, E., M. Barba, and J. A. Encinar, "Bandwidth Improvement in Large Reflectarray by Using True-Time Delay Line," *IEEE Transactions on Antennas and Propagation,* Vol. 56, No. 8, August 2008, pp. 2496–2503.

[23] Chaharmir, M. R., J. Shaker, and N. Gagnon, "Broadband Design of a Single Layer Large Reflectarray Using Multi Cross Loop Elements," *IEEE Transactions on Antennas and Propagation,* Vol. 57, No. 10, October 2010, pp. 3363–3366.

[24] Chaharmir, M. R., J. Shaker, and N. Gagnon, "Design of Broadband, Single Layer Dual-Band Large Reflectarray Using Multi Open Loop Elements," *IEEE Transactions on Antennas and Propagation,* Vol. 58, No. 9, September 2010, pp. 2875–2883.

[25] Petosa, A., and A. Ittipiboon, "Design and Performance of a Perforated Dielectric Fresnel Lens," *Inst. Elect. Eng. Proc. Microw., Antennas Propag.,* Vol. 150, October 2003, pp. 309–314.

[26] Mohammadirad, M., et al., "The Effect of Feed Position on the Performance of a Broadband Reflectarray," *APS 2011, Toronto,* July 4–8, 2011.

[27] Almajali, E., et al., "On Beam Squint in Offset-Fed Reflectarrays," *IEEE Antennas and Wireless Propagation Letters*, Vol. 11, 2012, pp. 937–940.

CHAPTER 7

Reflectarrays on Lossy Substrates

7.1 Introductory Remarks

Reflectarray antennas are versatile devices as they can be used in a myriad of applications with their patterns and functionality spanning a wide range of possible specifications. The most common use of reflectarrays, however, is the synthesis of pencil beam antenna patterns. An analog to this type of reflectarray is the solid parabolic reflector antenna [1]. Such solid reflectors can be mass-produced with low costs as evidenced by the pervasiveness nature of commercial satellite digital broadcast systems (DBS). Traditional reflectarrays are often designed using Teflon-based and other low loss microwave substrates. The use of these substrates leads to high-aperture efficiency and gain commensurate with solid parabolic reflectors. However, low-loss substrates are often quite costly and thus preclude their competitiveness with solid reflectors from the cost perspective. Naturally, reflectarray costs can be reduced through use of low-cost substrates (e.g., FR4), but such materials tend to have high loss tangents and hence will have reduced gain as compared to their solid reflector counterparts [2–5]. At present, it would seem that concessions must be made in the deployment of reflectarrays either through increased material costs or decreased electrical performance. In this chapter, we will show that this is not the case and that costs can be decreased while still maintaining excellent electrical performance. In Section 7.2, we will explore the physical mechanisms that lead to reflectarray losses followed with a cataloging of reflectarray elements based on their loss performance in Section 7.3. In Section 7.4 we shall further investigate the use of subwavelength elements and the relationship between frequency dispersion of reflection phase and losses. Lastly, in Section 7.5 we will provide examples of high-gain reflectarray designs on lossy substrates with ample experimental measurements to confirm that low-cost, high-performance reflectarrays can indeed be realized.

7.2 A Description of the Loss Mechanism in Reflectarray Elements

The loss mechanism in reflectarray elements has been explored previously in [2–5]. In all cases, the authors investigate the losses through the use of equivalent circuit

models. One important conclusion made in these prior inquiries is that dielectric losses are of paramount importance in describing losses, with metal losses (assuming high-conductivity metals such as copper, silver, or gold) being nearly negligible in describing total loss when a lossy substrate is present. This is unsurprising, as conductors such as copper and silver are often assumed to be perfectly conducting at microwave frequencies with no detriment to the accuracy of the electromagnetic modeling. The losses in reflectarrays can be modeled quite simply using a parallel RLC network, as shown in Figure 7.1, with the resistor R being responsible for the losses while the phase response is largely determined by the reactive LC components. A pole-zero analysis of the RLC circuit modeling square patch elements is performed in [4, 5], with the conclusion that the simplistic circuit model is capable of modeling low to moderate losses, while struggling to model very lossy structures. Losses were noted as quite significant, leading to substantial reduction in antenna gain if used in a pencil beam reflectarray configuration. It was noted, however, that thicker substrates leads to lowered losses with the immediately apparent consequence of higher material costs, weight and profile, and a reduction in the achievable phase variability of the patch element. This behavior is confirmed and shown in Figure 7.2.

A study of various elements was also performed in [2], where the authors compared the loss performance of dipole, patch, and dogbone-shaped elements and concluded the dogbone element exhibited lower losses as compared to the other elements for the same substrate thickness. The metric used in this comparison was the Q of the element, leading to the conclusion that lower Q elements exhibit lower losses. This is in fact of benefit to reflectarray designs, since reflectarrays designed with low Q elements tend to be wideband structures.

7.3 Cataloging Elements Based on Loss Performance

7.3.1 Loss Performance of Narrowband Versus Wideband Elements

It is clear that we seek elements with low Q if we are to successfully use lossy substrates in reflectarray designs. Elements such as resonant patches and dipoles are high Q elements and thus absorb an unacceptable amount (with regard to high-aperture efficiency designs) of incident power. There is the temptation to select a wideband element, since wide bandwidth and low Q are often synonymous. However, one must be cautioned with this approach, because many wideband elements are not simple single-resonance structures and hence are not accurately modeled using a single RLC circuit for which Q is unambiguously defined. Consider the narrowband patch element shown in Figure 7.3(a) and the wideband double cross-loop element in Figure 7.3(b). The reflection phase and magnitude versus element length

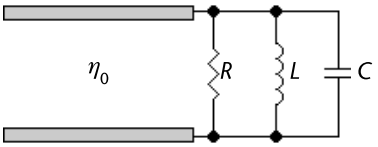

Figure 7.1 Equivalent RLC circuit model of reflectarray element.

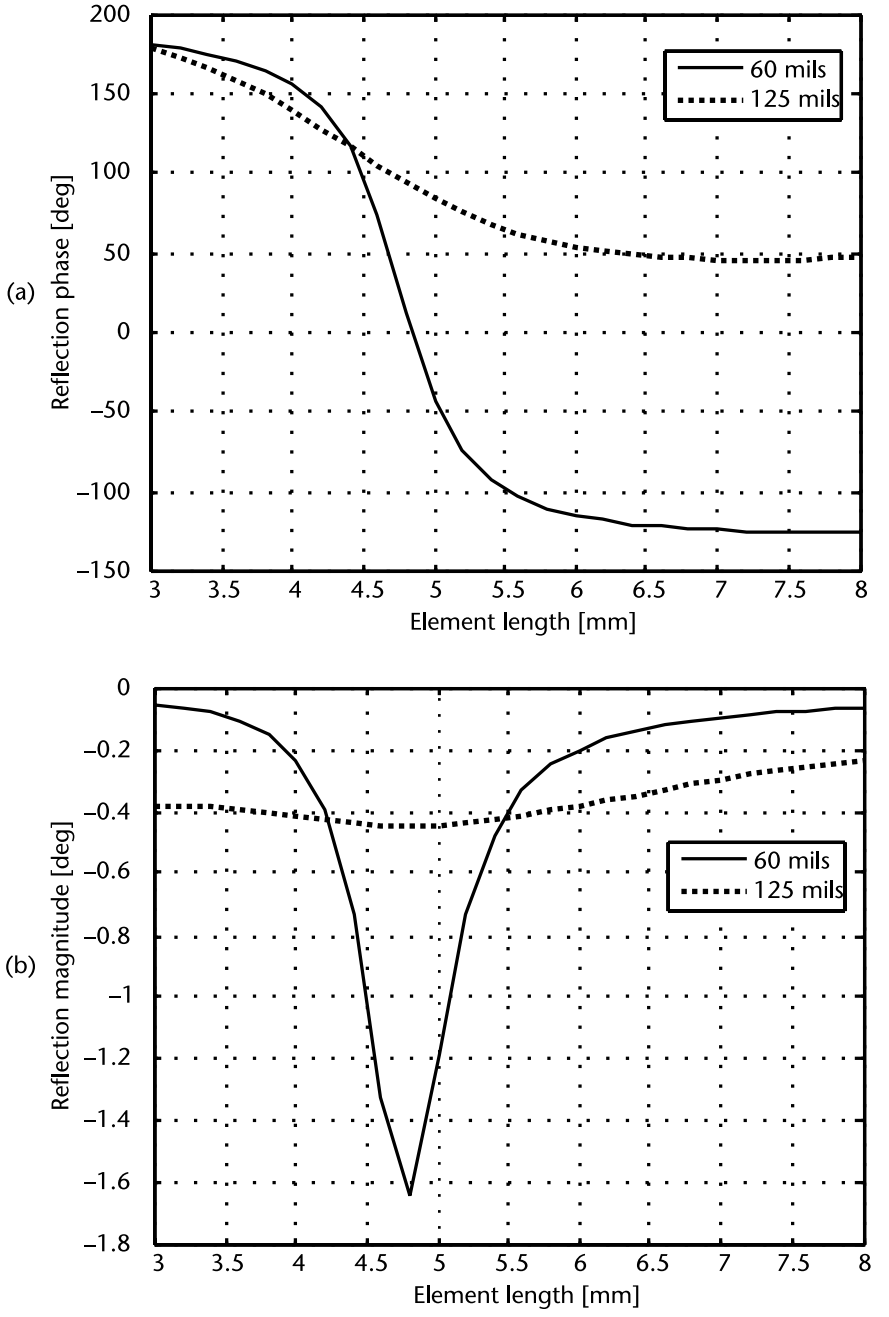

Figure 7.2 Plot of (a) reflection phase and (b) reflection magnitude versus frequency for various substrate thicknesses. The reflectarray element considered is a square patch with variable dimensions residing in a 12-mm-square lattice, simulated at 12.5 GHz with an FR4 substrate with $\varepsilon_r = 4.45$ and $\tan\delta = 0.016$.

of these two elements is shown in Figures 7.4(a) and 7.4(b), respectively. Note that while the patch is quite lossy, the double cross loop is as well, despite being a wide-band element. The peak loss of the patch is much higher than the double cross loop, but the double cross loop is lossy for nearly all element lengths. These scenarios are representative cases of concentrated loss compared to distributed loss. In the end,

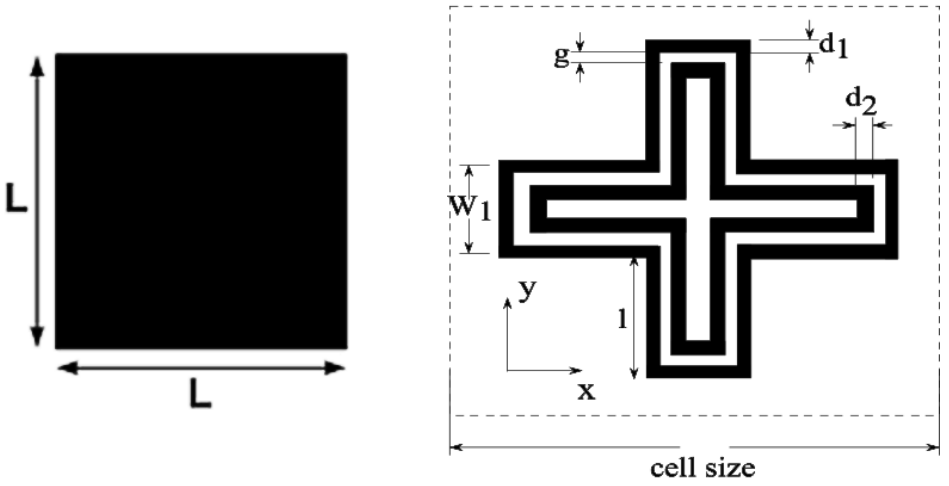

Figure 7.3 Examples of (a) narrowband (patch) and (b) wideband (double cross loop) elements.

a reflectarray designed using either element would result in unacceptable gain loss due to substrate power losses.

7.3.2 Loss Performance of Subwavelength, Coupled Resonant Elements

A class of reflectarray elements known as subwavelength, coupled resonant (SCR) elements provides an alternative means of reducing the losses in reflectarray designs. By reducing the lattice size below that of the traditional $\lambda/2$ spacing, the losses of the element tend to be reduced. This has been confirmed for various canonical elements including patches, loops, dogbones, and Jerusalem crosses [6, 7], although exceptions certainly exist. In particular, consider the reflection magnitude and phase as a function of element length for the square patch and loop, as shown in Figure 7.5. Both elements exhibit high reflection magnitudes, despite residing on a lossy FR4 substrate. However, the patch element exhibits a narrower phase variability (260°) as compared to the loop (310°). Therefore, the subwavelength loop element offers advantages over the patch in this regard. It is possible for subwavelength patches to have wider phase range, but one must resort to impractical gap sizes between adjacent patches [8] or the use of multiple layers of patches [9], either of which lead to increased fabrication costs (a more detailed discussion on the implications of fabrication tolerance can be found in Chapter 10). A more reasonable approach would involve the use of the subwavelength loops, which can be used to design a reflectarray on a single-layer with reasonable element feature sizes.

To emphasize the reduction in losses that occurs due to lattice size reduction, consider Figure 7.6 where the reflection magnitude of loop elements residing in various lattice sizes is considered. Even for a minor decrease in lattice size from $\lambda/2$ to $\lambda/3$, there is significant loss reduction. A summary of the properties of these loop elements is found in Table 7.1. One finds sufficient phase variability to design a reflectarray with a lattice as small as $\lambda/6$, perhaps even $\lambda/8$. It should be noted that for lattice sizes below $\lambda/8$, there is insufficient phase variability to design a high-gain

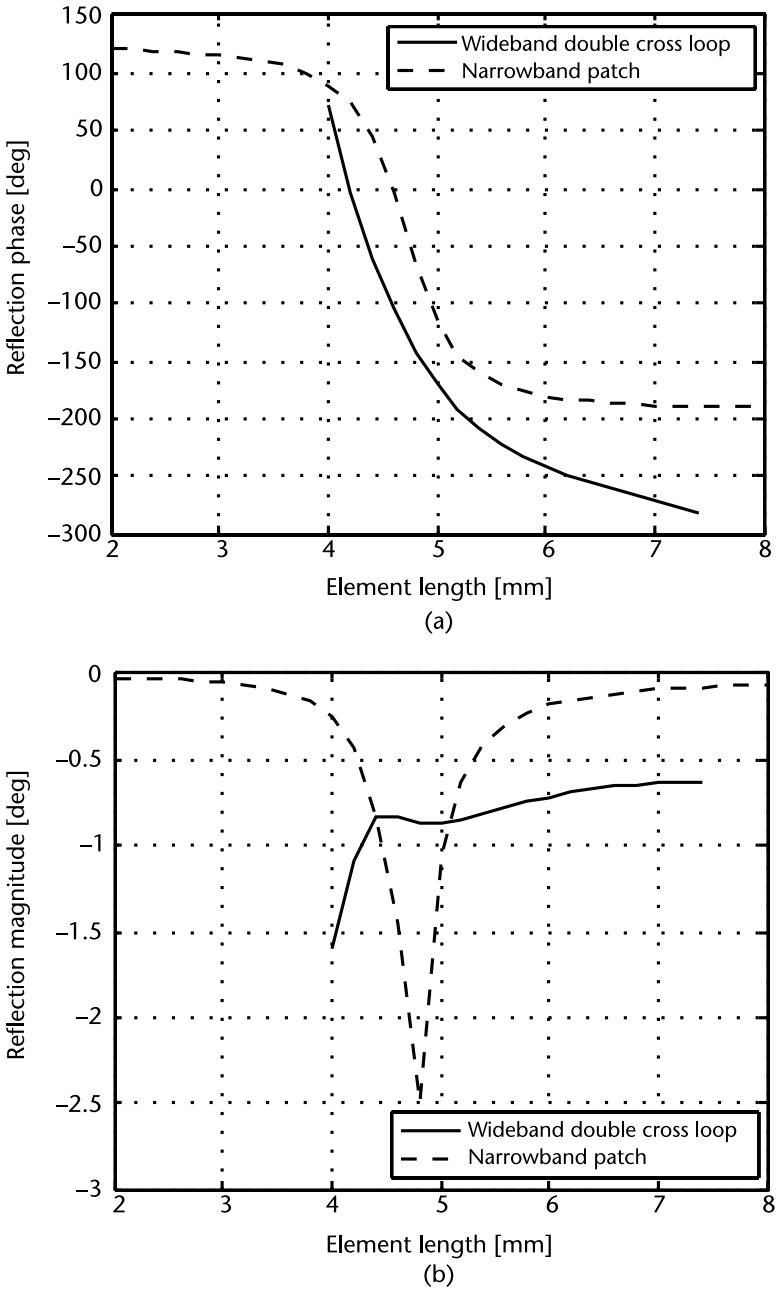

Figure 7.4 Examples of narrowband patch and wideband double cross loop elements and their respective (a) phase and (b) reflection magnitude on 125 mils FR4, relative permittivity 4.45, loss tangent 0.016, W1 = W2 = 4 mm, d1 = d2 = 0.6 mm, and g = 0.2 mm.

reflectarray, making the very low losses superfluous to the overall antenna design. Lastly, consider that the resonant length of the elements reduces as the lattice size reduces. This indicates that the interelement coupling leads to a reduction in resonant frequency and hence the element itself is no longer resonant and is strongly dependent on the adjacent elements: a coupled-resonance.

Table 7.1 Minimum |S11| and Phase Range of Loop Element for Various Unit Cell Sizes, Computed at 12.5 GHz on Substrate of FR4 with $\varepsilon_r = 4.45$ and $\tan\delta = 0.016$, 1.524-mm Thick Loop Line Width d = 0.2 mm

Lattice Size			*Resonant*	
Physical	*Electrical*	*Min|S11|*	*Length*	*Phase Range*
2 mm	$\lambda/12$	–0.50 dB	NA	115.6°
2.4 mm	$\lambda/10$	–0.56 dB	2.10 mm	202.3°
3 mm	$\lambda/8$	–0.61 dB	2.45 mm	274.1°
4 mm	$\lambda/6$	–0.70 dB	2.93 mm	309.3°
6 mm	$\lambda/4$	–1.02 dB	3.50 mm	330.5°
8 mm	$\lambda/3$	–1.58 dB	3.70 mm	338.9°
12 mm	$\lambda/2$	–3.32 dB	3.76 mm	382.0°

See Chapter 3 for the physical layout of the loop element.

In general, it can be said that subwavelength, coupled-resonant elements exhibit low losses and are therefore ideally suited for reflectarray designs where the use of lossy substrates is required.

7.4 Frequency Dispersion of the Reflection Phase and Its Relationship with Loss

We have shown in Section 7.3.1 that both narrowband and wideband elements can exhibit significant reflection losses. An alternative configuration was shown in Section 7.3.2, which involved the reduction in lattice size below that of the typical $\lambda/2$ spacing, which leads to very low losses. It is worthwhile exploring the mechanisms that lead to this reduction in losses [7].

7.4.1 Qualitative Description of Loss Reduction

It is important to address the question as to why subwavelength elements exhibit substantially lower losses than their resonant counterparts. The answer can be given qualitatively by observing and describing the mechanism by which resonance occurs in both cases. First, one can excite the resonant and subwavelength loop elements with identical normally incident y-polarized plane waves and observe the total fields and power dissipation surrounding the loops. The substrate considered in both of the cases presented in this section is 1.524-mm-thick FR4, identical to the material discussed in Section 7.3.2. The loop elements are always placed at the $z = 0$ plane with the lengths given in Table 7.1 for the case of $\lambda/2$ and $\lambda/6$ lattice spacing at 12.5 GHz. The near-field distributions of the resonant-spaced loop element are shown in Figures 7.7(a), 7.7(c), and 7.7(e). It is essential to recognize that the fields are predominantly confined in the lossy substrate and more specifically, immediately surrounding and directly beneath the element itself, as shown in Figures 7.7(a) and 7.7(c) for the field components E_y and E_z. This is indicative of a self-resonant

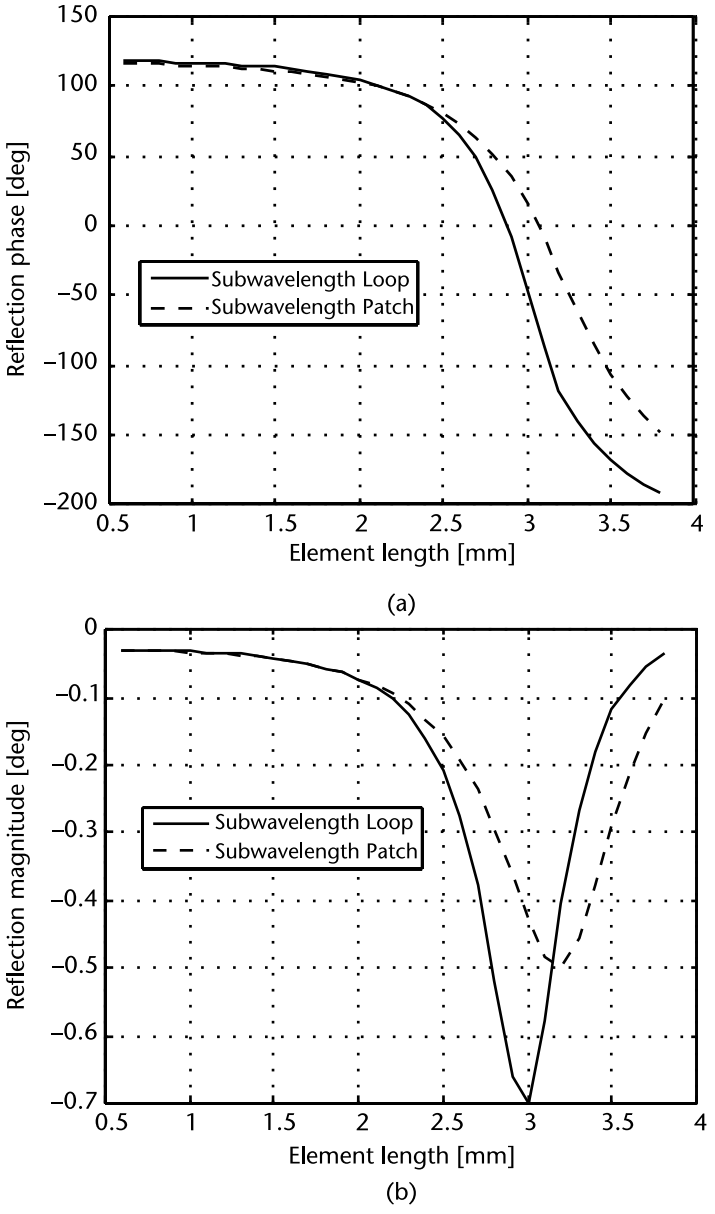

Figure 7.5 Reflection (a) phase and (b) magnitude for a subwavelength patch and loop element on 60-mil FR4 substrate at 12.5 GHz; loop line width is 0.2 mm. (© 2011 IEEE. *From:* [7]. Reprinted with permission.)

structure since the field strength is orders of magnitude lower as one approaches the adjacent elements as compared to the central element. In other words, the coupling between elements in the periodic array does not play a great role in the resonant behavior of the loop. These surrounding elements are not shown due to the use of periodic boundary conditions. This confinement of fields in the lossy regions leads to significant reduction in the reflection magnitude.

Conversely, as shown in Figures 7.7(b), 7.7(d), and 7.7(f), the fields surrounding the subwavelength loop element are evenly distributed in both the substrate and air superstrate with E_y predominantly existing between adjacent elements rather

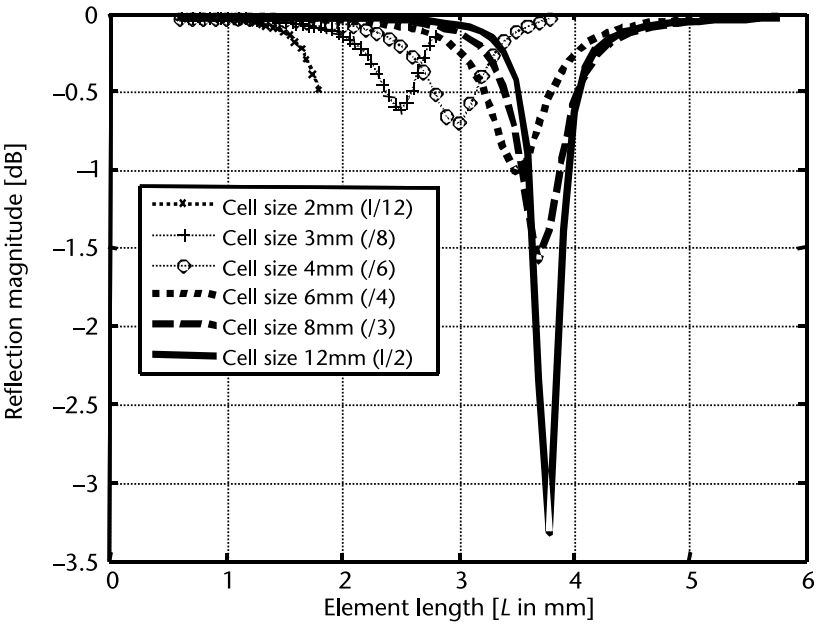

Figure 7.6 Reflection magnitude for loop element as a function of element length. Curves computed at 12.5 GHz on substrate of FR4 with $\varepsilon_r = 4.45$ and $\tan\delta = 0.016$, 1.524-mm-thick loop line width d = 0.2 mm. (© 2011 IEEE. *From:* [7]. Reprinted with permission.)

than being associated with individual elements. This is indicative of a coupled resonance since the field magnitudes remains quite large at the median position between elements (at the periodic boundary). This further suggests that the adjacent elements in the array are critical in maintaining resonant behavior. The fact that the fields are not strongly confined to lossy regions leads to lowered overall losses. Additionally, it should be noted that the fields in the air and dielectric regions as well as the currents on the conductors have significantly lower magnitudes as compared to their resonant counterparts. In particular, the peak E_y and E_z field magnitudes are 12 dB and 3 dB lower for the subwavelength loop as compared to the field magnitudes in the resonant loop case, respectively. To ensure a fair comparison, identical plane wave excitation is used in both cases. The relaxing of field confinement and the reduced intensity for the field and current suggests the subwavelength elements have a lower quality factor (Q) than their resonant counterparts with numerical confirmation of this fact in Section 7.4.2.

7.4.2 Quantitative Description of Loss Reduction

For a quantitative explanation of reduced losses, we can compute the frequency dispersion of the reflection phase [Figure 7.8(a)] and reflection magnitudes [Figure 7.8(b)] for square loop elements for various lattice sizes. The reflection phase frequency dispersion is defined as the frequency derivative of the reflection phase:

$$\text{Dispersion} = \frac{d\phi}{df} \tag{7.1}$$

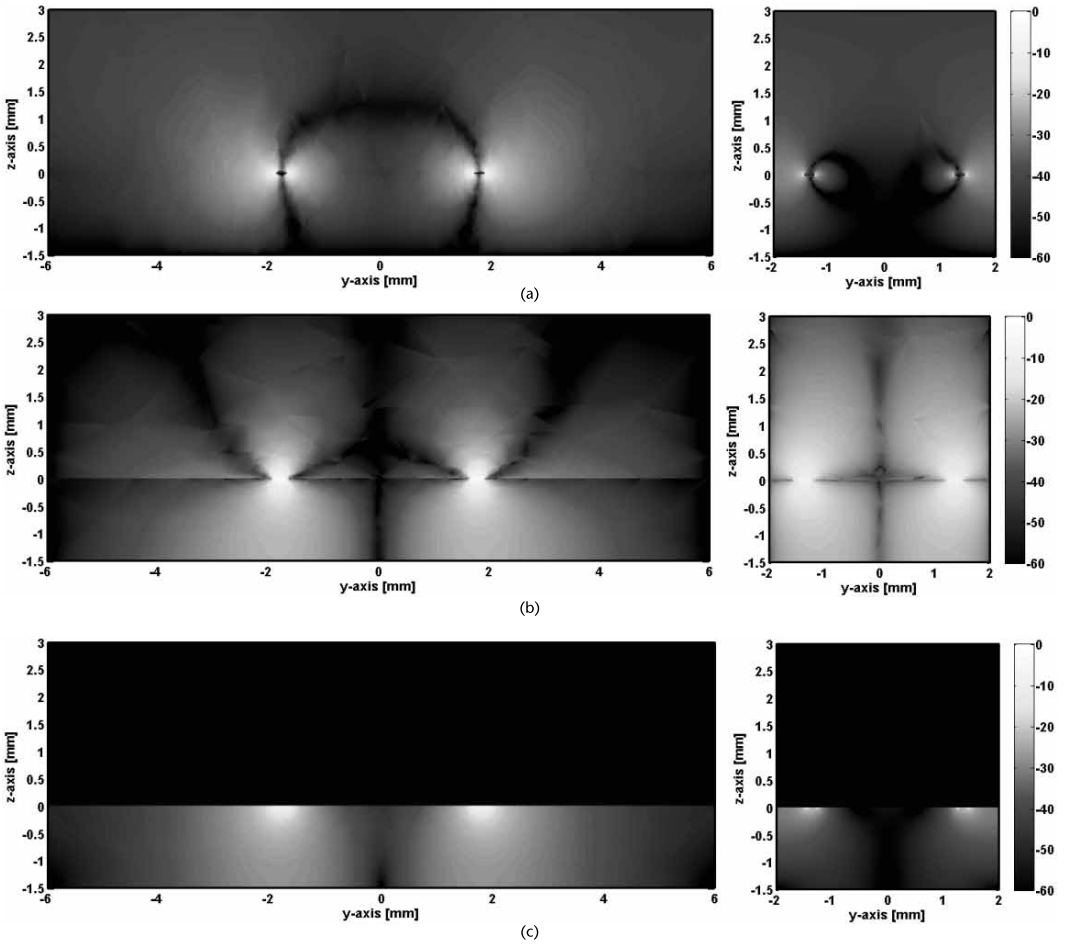

Figure 7.7 Near-field behavior of a loop element with dimensions corresponding to the fourth row (subwavelength, lattice $\lambda/6$) and last row (resonant, lattice $\lambda/2$) of Table 7.1 with identical substrate and element parameters. (a) Ey field magnitude, resonant loop, (b) Ey field magnitude, subwavelength loop, (c) Ez field magnitude, resonant loop, (d) Ez field magnitude, subwavelength loop, (e) resonant loop, power dissipation per mm3, and (e) subwavelength loop, power dissipation per mm3. All units are normalized to resonant case (plots a, c, e) and expressed in decibels. Excitation is along y and the coordinate x = 0 in all cases. (© 2012 IEEE. *From:* [11]. Reprinted with permission.)

where ϕ is the reflection phase in degrees and f is the frequency in gigahertz. Element length is selected such that their resonance falls approximately at the desired frequency of 12.5 GHz, with the lengths equal to the resonant lengths listed in Table 7.1. The $\lambda/2$-spaced loop has greater dispersion than its subwavelength counterparts, and consequently has the greatest loss. Notice also the glaring similarity between the frequency dependency of dispersion [Figure 7.8(a)] and loss [Figure 7.8(b)], confirming that dispersion and loss are deeply interdependent quantities. The plots are nearly identical but for a change in the variable along the y-axis. If one were to plot frequency dispersion of reflection phase versus the reflection magnitude, a nearly linear relationship between these quantities becomes apparent, as shown in Figure 7.9. This would appear to have implications on the amount of loss we must incur if a particular dispersion is required and vice versa. It also suggests that to design a low-loss reflectarray, the elements must have low reflection phase

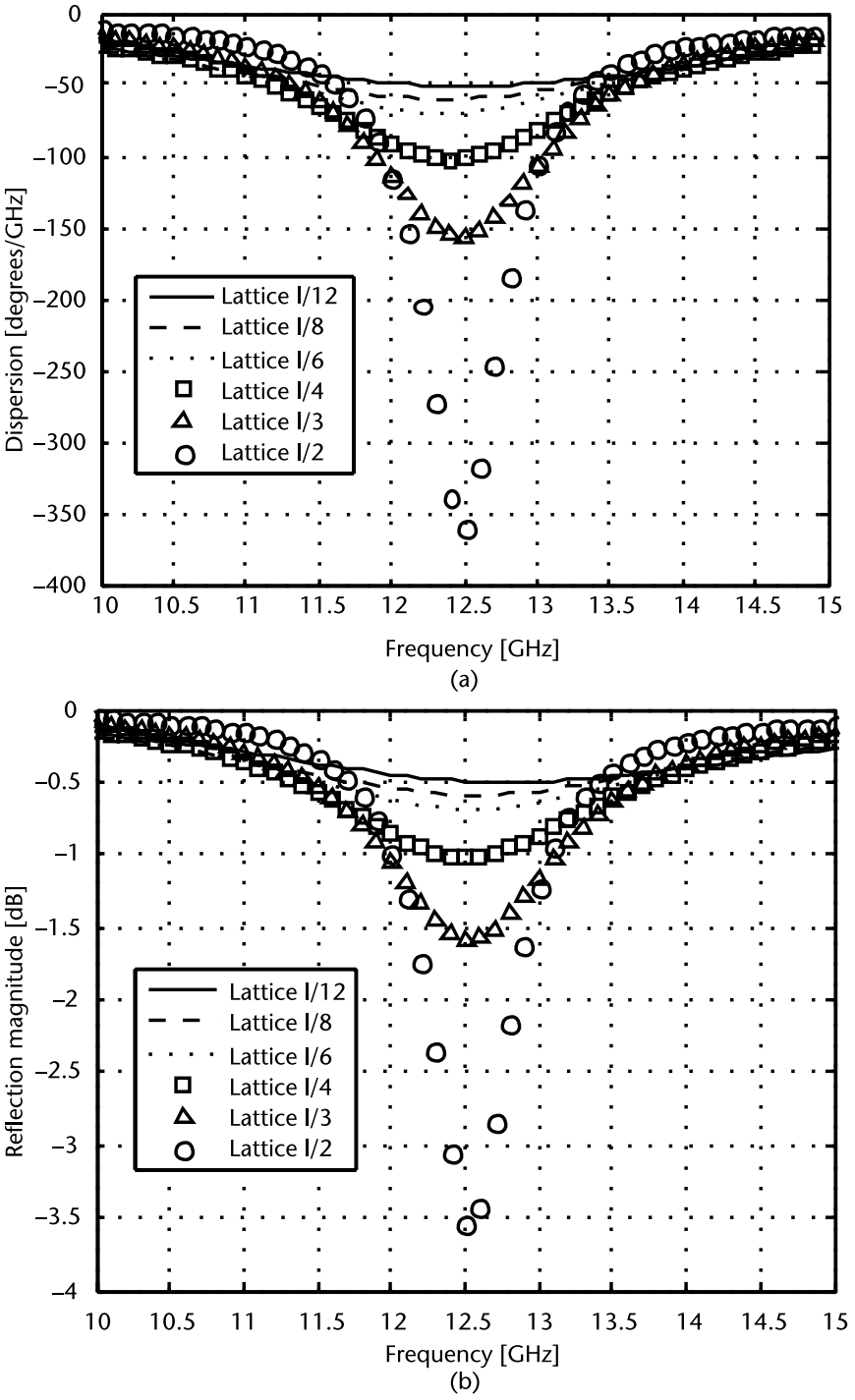

Figure 7.8 Plot of (a) frequency dispersion of reflection phase and (b) reflection coefficient magnitude versus frequency for square loop element for various electrical lattice sizes.

frequency dispersion, which, in turn, places restrictions on the bandwidth and aperture efficiency of reflectarray designs in general (see Chapter 6).

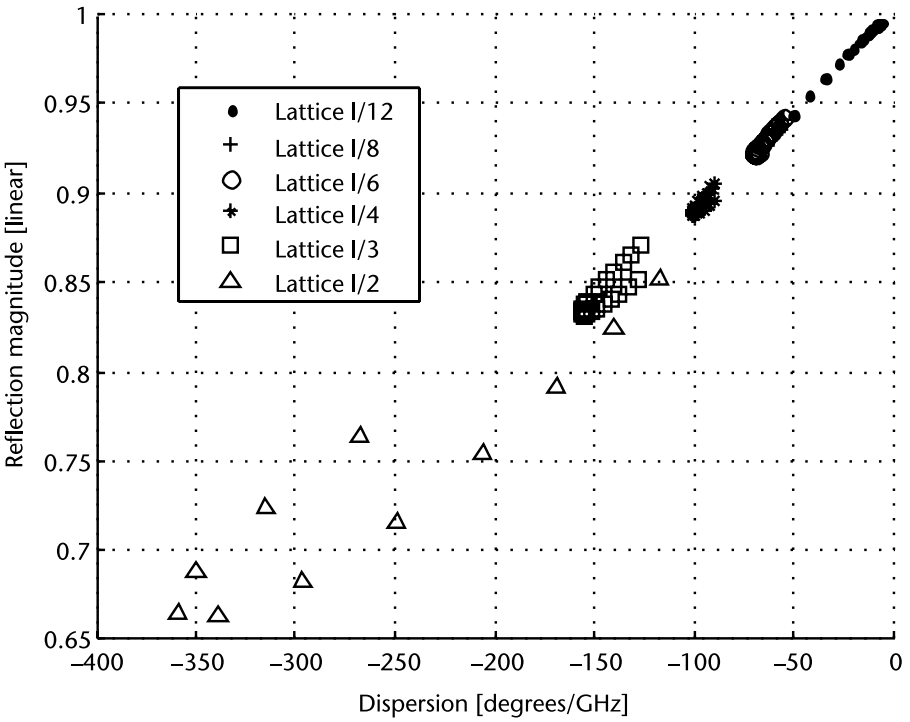

Figure 7.9 Reflection magnitude (linear units) as a function of frequency dispersion of reflection phase. Notice the near linear relationship between these two quantities. (© 2011 IEEE. *From:* [7]. Reprinted with permission.)

7.5 High-Performance Reflectarrays Using Lossy Substrates

In this section we will consider reflectarray design examples that make use of elements with low reflection phase frequency dispersion. Four offset-fed direct-reflection reflectarrays were designed, fabricated, and measured, all having identical design specifications (denoted reflectarray designs A through D with their details summarized in Table 7.2). The design aperture size used was 396 mm × 396 mm with the design center frequency of 12.5 GHz (Ku-band). The coordinate origin was placed at the center of the reflectarray, with the phase center of the feed located at $(x_f, y_f, z_f) = (-124 \text{ mm}, 0 \text{ mm}, 432 \text{ mm})$ corresponding to a main beam directed 16° off broadside. The feed used is a Q-par QSG17S15S with a mid-band gain of 15 dBi leading to an approximate 10-dB edge taper illumination. The reflectarray

Table 7.2 Summary of Reflectarray Design Parameters

Design	*Substrate Variety*	*Substrate Thickness*	*Loss*	*Lattice Physical*	*Lattice Electrical*
A	Arlon 880	125 mils	Low	12 mm	$\lambda/2$
B	FR4	125 mils	High	12 mm	$\lambda/2$
C	Rogers 3003	60 mils	Low	4 mm	$\lambda/6$
D	FR4	60 mils	High	4 mm	$\lambda/6$

configuration is shown in Figure 7.10 with photographs of the designs shown in Figure 7.11.

Designs A and B were traditional reflectarray designs using $\lambda/2$ spaced loop elements with a lattice size of 12 mm. Design A was designed on 125-mil-thick Arlon Diclad 880, while Design B was designed on 125-mil-thick FR4 with relative permittivity $\varepsilon_r = 4.45$ and loss tangent $\tan\delta = 0.016$. While designs A and B utilize substrates with different permittivity, they should both achieve the same aperture efficiency at the center design frequency, save for the material losses due to the high loss tangent in Design B.

However, Designs C and D were reflectarray designs using square loop elements in a nontraditional subwavelength lattice size of $\lambda/6$. Design C used 60-mil-thick Rogers 3003 while design D used 60-mil-thick FR4 (identical substrate as Design B). It should be noted that a thicker substrate is used for the traditional resonant-spaced designs. This was performed purposefully as the losses in Design B would be too large to make sensible comparisons between the various designs. In this sense, we are being generous to the traditional resonant-spaced design technique for comparison purposes. The traditional reflectarrays using resonant elements consisted of 1,089 elements while the subwavelength based reflectarrays had 9,801 elements all using the same aperture size, etching tolerance, and fabrication process, thus making material costs the only financially discernible difference between designs.

The reflection coefficient magnitude of Designs B and D are shown in Figures 7.12(a) and 7.12(b), respectively (lighter colors representing larger reflection magnitude). Recall that Designs B and D use resonant and subwavelength element spacing, respectively, with both designs residing on lossy FR4. The subwavelength reflectarray has substantially larger reflection magnitude over the entire reflecting surface as expected. Moreover, we see substantial losses over the entire reflectarray designed using wideband resonant elements. From these simulation results, we

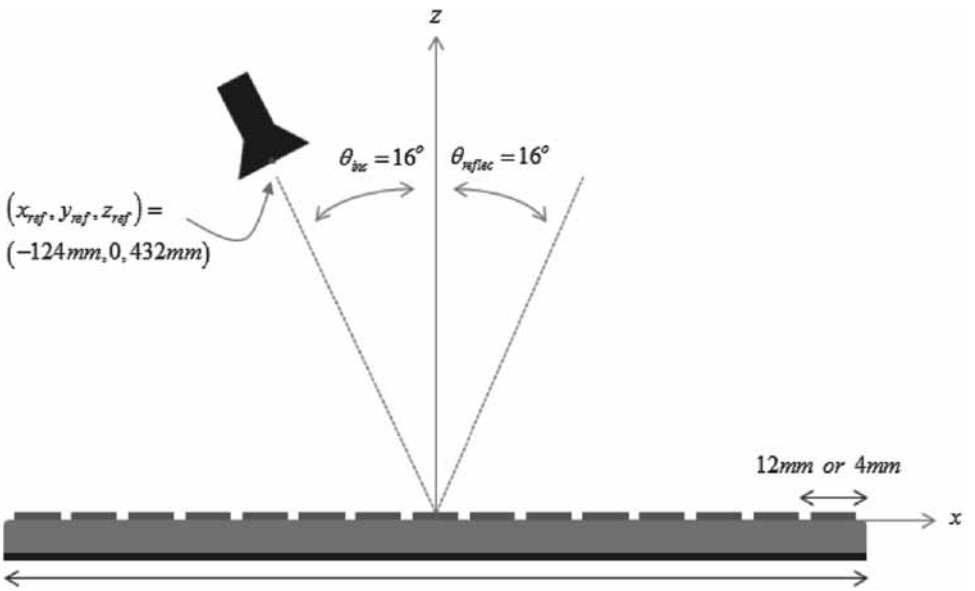

Figure 7.10 Reflectarray configuration used for comparisons between high- and low-loss designs.

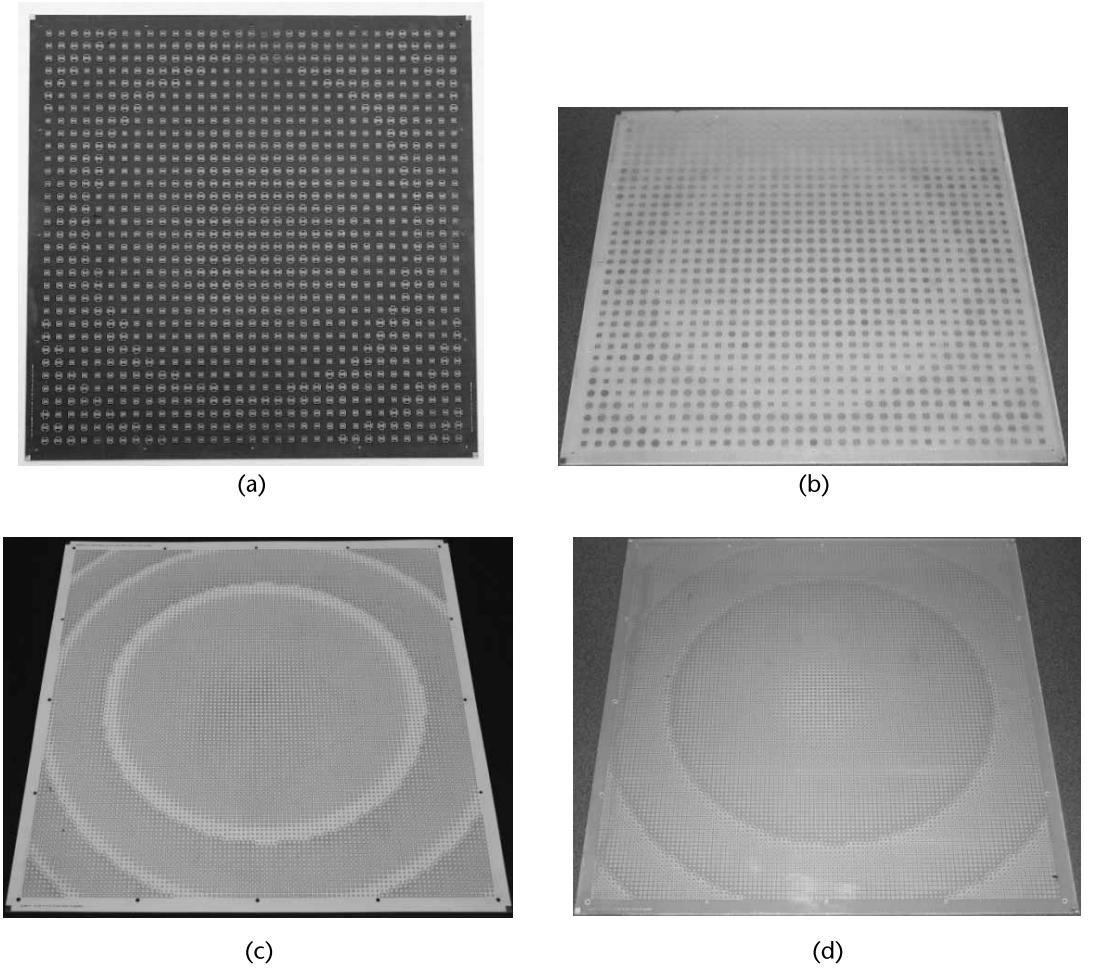

Figure 7.11 Photographs of four reflectarrays, Designs A through D numbered as such.

expect the subwavelength-based Design D to achieve higher aperture efficiency and thus higher gain as compared to the resonant element-based Design B.

The far-field patterns of the four reflectarrays were measured with the gain versus frequency curves for the four reflectarrays shown in Figure 7.13. The two reflectarrays designed using subwavelength elements (Designs C and D) achieved a 19% 1-dB gain bandwidth, with the lossy FR4 based design losing at most 0.7 dB of gain at center frequency compared to its low loss (and more costly) Rogers 3003-based reflectarray. These experimentally measured bandwidths are similar to those shown both via simulation and experiment in [6, 9]. Additionally, the low-loss subwavelength design achieved higher peak gain than the resonant based design, though the low loss resonant design from [10] exhibits a wider bandwidth of 25% for 1-dB gain.

However, the reflectarray designed using an FR4 substrate with resonant spaced elements (Design B) suffers from a significant gain drop principally due to losses in the FR4 material. Note also the dramatic drop in gain around 13.4 GHz, which

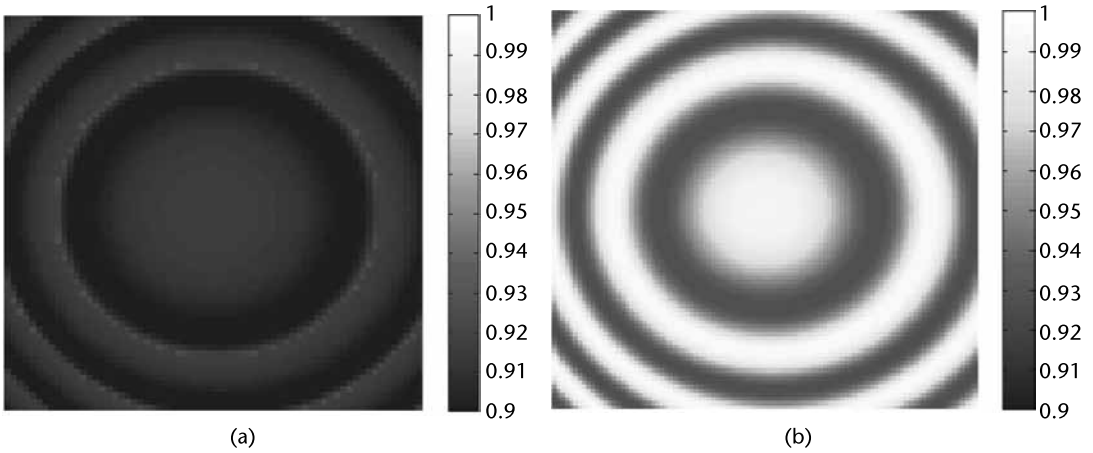

Figure 7.12 Plot of element reflection magnitude (in linear) over the aperture of the reflectarray for (a) resonant loop elements (Design B) and (b) subwavelength loop elements (Design D); both designs reside on lossy FR4. (© 2011 IEEE. *From:* [7]. Reprinted with permission.)

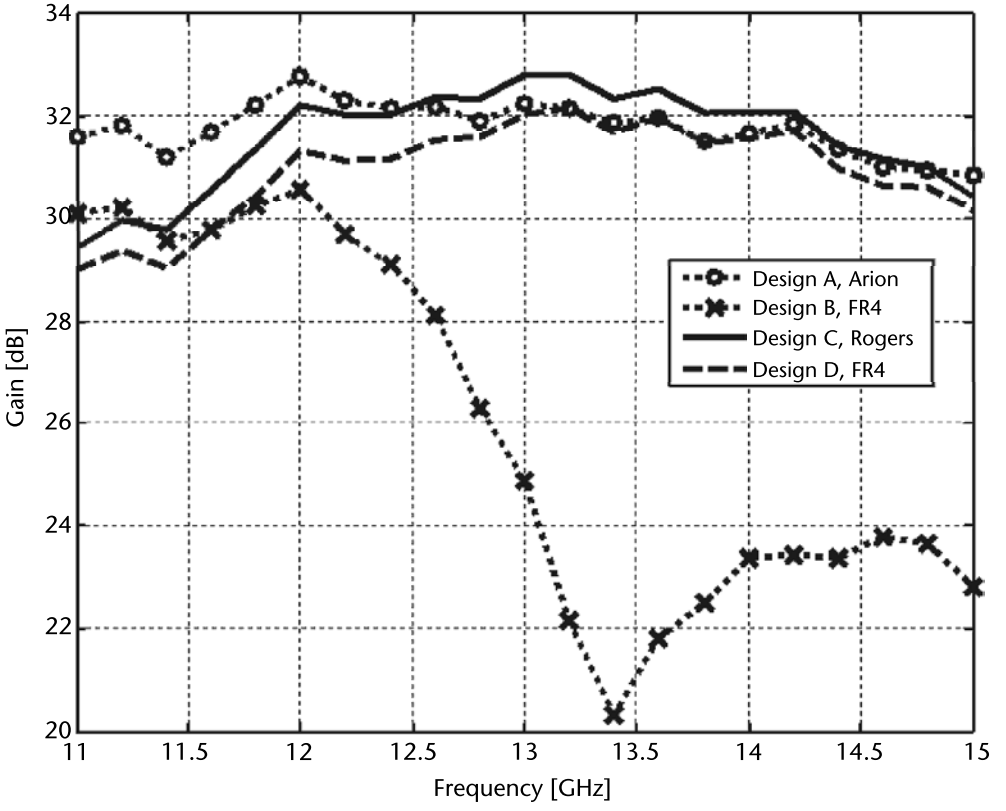

Figure 7.13 Plot of measured gain versus frequency for the four reflectarray designs (© 2011 IEEE. *From:* [7]. Reprinted with permission.)

is attributed to the fact that the elements at the center of the reflectarray are all in the vicinity of a very high-Q resonance, thus providing the worst-case scenario for losses in reflectarray design: the greatest illumination occurring in regions where the reflectarray exhibits the greatest loss.

It is important to note that the reflectarray designed using resonant elements on FR4 is by no means optimized for low loss. However, it is representative of a typical reflectarray design that would perform quite well on a typical low-loss substrate and yet exhibits poor electrical performance due to the lossy substrate. Without any optimization and strictly through the reduction of lattice size (and thus element size), the subwavelength loop-based reflectarray performs nearly as well on lossy FR4 as it does on low loss Rogers 3003 material. A comparison of the far-field gain patterns at the center frequency of 12.5 GHz of these two subwavelength-based reflectarrays are shown in Figure 7.14. Note that the patterns are nearly identical, save for a marginal reduction in gain due to the lossy substrate. There is a stark difference in material costs between the two designs, thereby making the slight reduction in gain a reasonable price to pay in scenarios where cost reduction is of paramount importance.

7.6 Concluding Remarks

In this chapter we have explored the design of reflectarray antennas on lossy substrates. The main motivation for this examination is to take advantage of the lower costs associated with lossy substrates. As shown, if attention is not given to the selection of reflectarray elements, an otherwise high-performance design would perform quite poorly on a lossy substrate. This leads to a discussion of the mechanisms by which losses occur in reflectarray elements, showing that both narrowband and wideband elements can exhibit a large amount of loss. A class of elements known

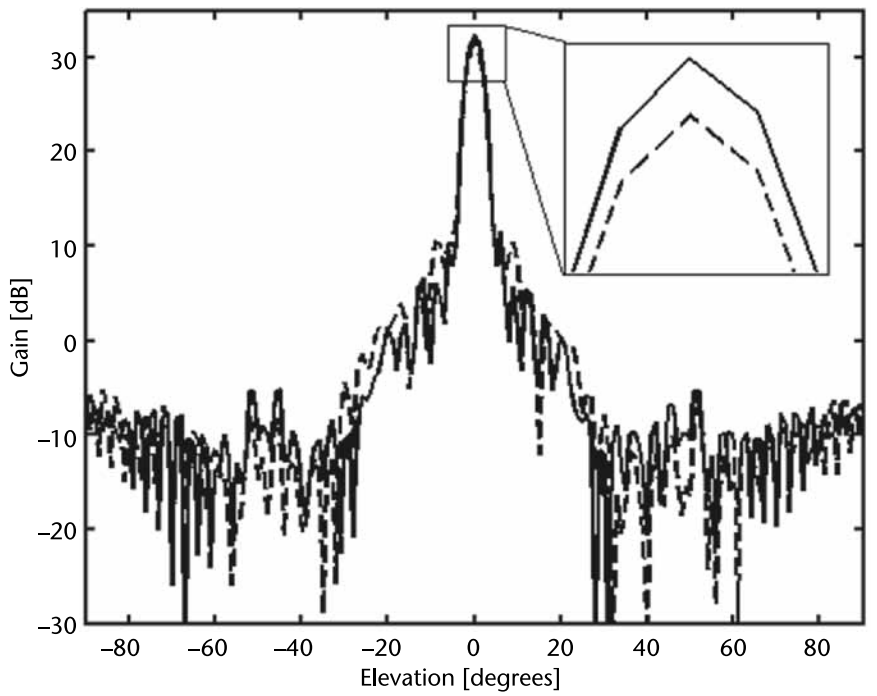

Figure 7.14 Measured far-field patterns of reflectarrays at center frequency of 12.5 GHz (—— design C on Rogers 3003, - - - design D on FR4).

as subwavelength, coupled-resonant (SCR) elements was shown to exhibit very low losses with sufficient phase variability for the design of high-gain reflectarrays. It was further shown that SCR loop elements exhibit superior performance over SCR patches as they require less restrictive etching tolerance and reduced fabrication complexity.

A comparative study of the near-field behavior of resonant-spaced and subwavelength elements was given, with the conclusion that the strong near-field coupling in SCR elements reduces the overall intensity of the near fields (lower Q) as well as a reduction in the confinement of the near fields within the lossy substrate. Quantitatively, the SCR elements exhibit lower reflection phase frequency dispersion, which is shown to be inextricably linked to the reflection magnitude and hence loss.

Lastly, a collection of reflectarray designs were considered, culminating in a high-performance reflectarray residing on a low-cost, lossy FR4 substrate. Comparisons were made with reflectarrays designed on high-cost, low-loss substrates with only marginal reduction in gain observed due to material losses. Moreover, a reflectarray designed using dispersive elements in conjunction with a lossy substrate such as FR4 leads to a significant reduction in reflectarray gain. At no additional fabrication cost and with significant material cost reduction, a high-performance reflectarray antenna can be designed and fabrication on low-cost, high-loss substrate materials.

References

[1] Love, A. W., *Reflector Antennas*, New York: IEEE Press, 1978.

[2] Bozzi, M., S. Germani, and L. Perregrini, "A Figure of Merit for Losses in Printed Reflectarray Elements," *IEEE Antennas and Wireless Propagation Letters*, Vol. 3, 2004, pp. 257–260.

[3] Hu, W., et al., "Phase Control of Reflectarray Patches Using Liquid Crystal Substrate," *Proceedings of European Conference on Antennas and Propagation*, Nice, France, November 2006.

[4] Rajagopalan, H., and Y. Rahmat-Samii, "Dielectric and Conductor Loss Quantification for Microstrip Reflectarray: Simulation and Measurements," *IEEE Transactions on Antennas and Propagation*, Vol. 56, No. 4, April 2008, pp. 1192–1196.

[5] Rajagopalan, H., and Y. Rahmat-Samii, "On the Reflection Characteristics of a Reflectarray Element with Low-Loss and High-Loss Substrates," *IEEE Antennas and Propagation Magazine*, Vol. 52, No. 4, 2010, pp. 73–89.

[6] Nayeri, P., F. Yang, and A. Z. Elsherbeni, "Bandwidth Improvement of Reflectarray Antennas Using Closely Spaced Elements," *Progress in Electromagnetics Research C*, Vol. 18, 2011, pp. 19–29.

[7] Ethier, J., M. R. Chaharmir, and J. Shaker, "Novel Approach for Low-Loss Reflectarray Designs," *IEEE International Symposium on Antennas and Propagation (URSI/APS)*, Spokane, WA, July 3–8, 2011.

[8] Pozar, D. M., "Wideband Reflectarrays Using Artificial Impedance Surfaces," *Electronics Letters*, Vol. 43, No. 3, February 1, 2007, pp. 148–149.

[9] Nayeri, P., F. Yang, and A. Z. Elsherbeni, "Broadband Reflectarray Antennas using Double-Layer Sub-Wavelength Patch Elements," *IEEE Antennas and Wireless Propagation Letters*, Vol. 9, 2010, pp. 1139–1142.

[10] Chaharmir, M. R., et al., "Broadband Reflectarray Antenna with Double Cross Loops," *Electronics Letters*, Vol. 42, No. 2, January 2006, pp. 65–66.

[11] Ethier, J., M. R. Chaharmir, and J. Shaker, "Loss Reduction in Reflectarray Designs Using Sub-Wavelength Coupled-Resonant Elements," *IEEE Transactions on Antennas and Propagation*, Vol. 60, No. 11, 2012, pp. 5456–5459.

CHAPTER 8

Transmitarray

8.1 Introduction

Offset-fed reflectarray structures are designed to avoid feed blocking loss. However, the offset geometry gives rise to higher cross polarization, beam squint, and feed image. A transmitarray that combines the features of a traditional dielectric lens and phased array can overcome the shortcomings of offset reflectarray. In transmitarray, the incident electromagnetic wave transmits through the multilayer structure and is converted from spherical phasefront into any desired phasefront [1]. The advancement of lithographic etching technology has realized the possibility of low-cost and simple methods for fabrication of planar lens structures. However, the design of a transmitarray is more complicated than that of a reflectarray antenna because the radiating element must provide both the high transmission and phase compensation concurrently as compared to reflectarray where only the desired phase compensation for the reflected wave is required.

Different techniques for designing transmitarray and a number of its applications are introduced in this chapter.

8.2 Antenna-Filter-Antenna Transmitarray

A basic transmitarray structure is divided into two principal devices as shown in Figure 8.1 [2]: radiating interfaces for reception and transmission and the processing interface for array phase configuration in each transmitarray cell. The early transmitarrays using this technique were introduced in [3, 4]. Figure 8.2 shows an example of such transmitarray configuration where resonant patches constitute the radiation interfaces and a transmission line delay with varying length was utilized between the resonant patches as the processing interface to obtain the required phase transformation. Two different types of interconnections between elements of opposing faces were used, as illustrated in Figure 8.2. Shorting pin through an aperture in the common ground plane is the first interconnection type and slot-coupled aperture is the second type.

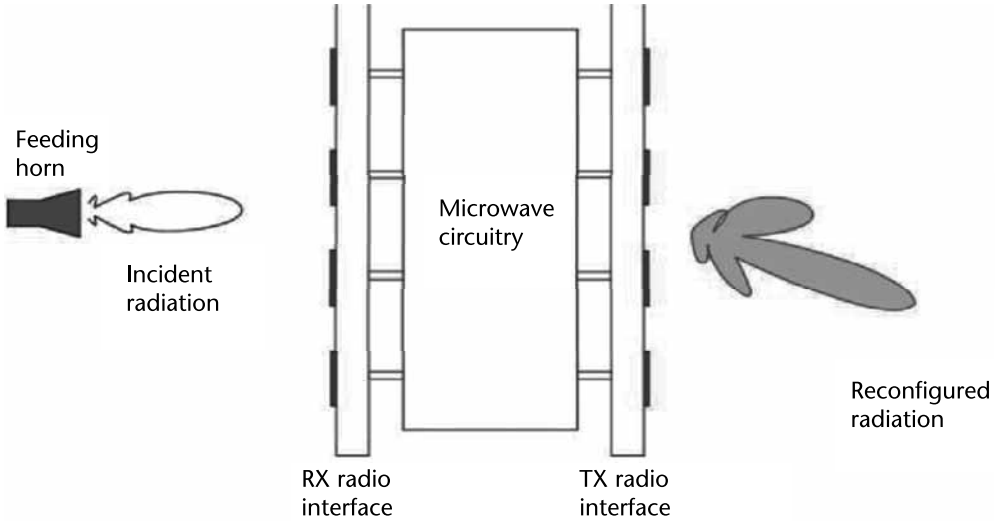

Figure 8.1 Schematic view of an antenna-interface-antenna transmitarray. (© 2010 IEEE. *From:* [2].)

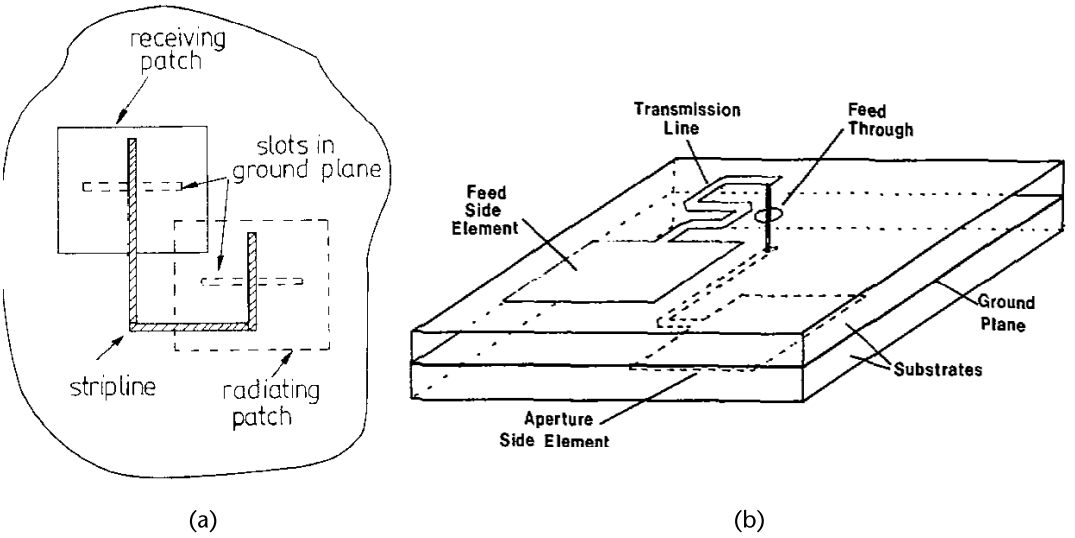

Figure 8.2 Different types of antenna-phase delay-antenna planar lenses: (a) metal vial coupled (© 1986 IEEE. *From:* [3]) and (b) slot coupled. (© 1996 IEEE. *From:* [4].)

Fabrication complexity, limited bandwidth, and reduced phase shift range that reduce the aperture efficiency are some of the main drawbacks of these planar lenses.

An alternative approach was developed based on nonuniform array of antenna-filter-antenna (AFA) elements [5, 6]. These elements have been previously demonstrated and used in uniform arrays for designing frequency-selective surfaces (FSS) [7]. Different types of bandpass filter with required phase delays, acting as the processing interface in Figure 8.1, can be used for the design of the transmitarray.

A three-pole bandpass AFA element composed of two back-to-back patch antennas and a coplanar waveguide (CPW) resonator ground plane as shown in

Figure 8.3 was introduced in [8] to design an AFA planar lens. The antenna elements are hexagonal patches, etched on glass substrates. The middle resonator is a half-wave resonator that couples the power between top and bottom patches with 180° phase difference at its flared ends. A circuit model for this structure is shown in Figure 8.4. As shown in this figure, the AFA structure can be viewed as a bandpass filter between two radiation ports. The cell elements of the structure were single-polarized and present the required frequency response only for the incident waves polarized in parallel with the CPW resonators as shown in Figure 8.3.

To use this element in a transmitarray, the desired phase-shift between the input and output of each array cell should be realized. To achieve different values of phase shift, the elements are retuned in the vicinity of the operating frequency by scaling the transversal dimensions. The maximum range of phase shift that can be obtained in this method is equal to the in-band variations of the phase delay, which is close to 180° in the case of a three-pole AFA.

The main drawback of the structures introduced so far is relatively large interelement spacing between the array elements which makes the phase response more sensitive to the angle of incidence. Additionally, the cell elements of these

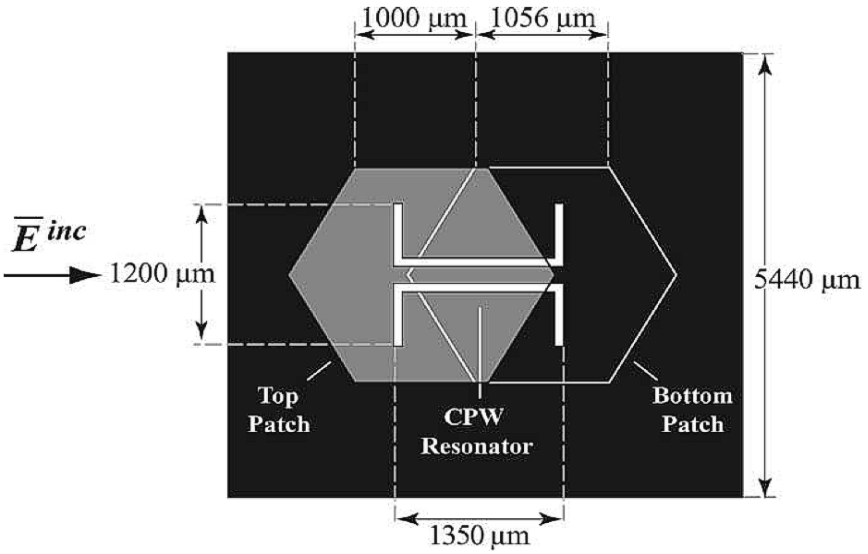

Figure 8.3 A view of the AFA cell element. The patches are located on top and the bottom layers and the CPW resonator lies on the common ground plane. (© 2004 IEEE. *From:* [7].)

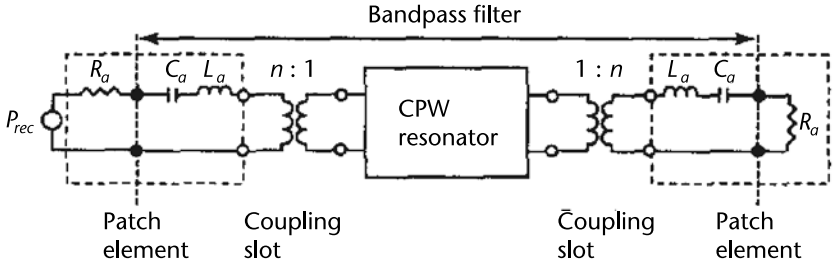

Figure 8.4 A circuit model of the AFA element as a bandpass filter with radiation ports. (© 2004 IEEE. *From:* [8].)

transmitarrays have limited phase variation which results in reducing the aperture efficiency.

Recently, a new technique was introduced to design transmitarray where frequency selective surfaces (FSS) were used as phase processing interface [9]. The phase shift required for beam collimation was achieved from the phase response of the transfer functions of the cascade of FSSs. The phase shift that can be achieved from a bandpass FSS is directly related to the type and order of its frequency response. In this transmitarray a multilayer stack of subwavelength patch-grid as shown in Figure 8.5 is utilized to design an nth-order passband FSS [10] that has n capacitive layers of subwavelength patches and $n - 1$ inductive layers of grids. The phase and amplitude of transmission coefficients of this bandpass FSS with second, third, and fourth orders are shown in Figure 8.6. As seen from Figure 8.6, the higher the order of the response, the larger is the achievable phase shift range.

According to Figure 8.6, a fourth-order frequency response would be sufficient if a phase variation of more than 270° but less than 360° is needed for the high transmission frequency band. The synthesis procedure described in [10] was used

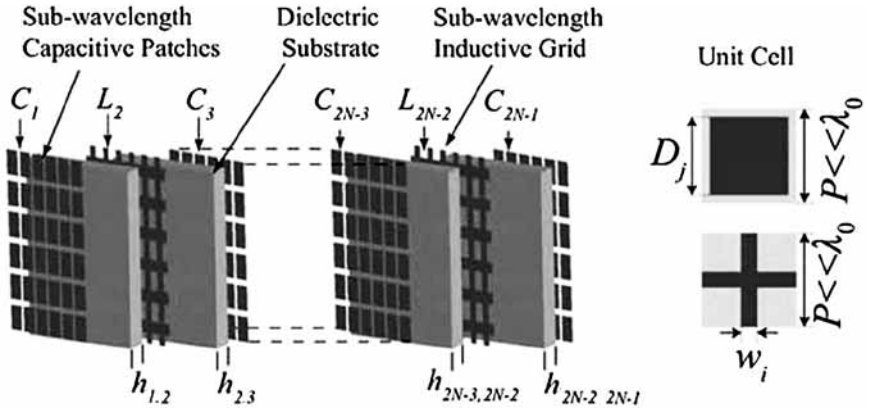

Figure 8.5 A view of multilayer of nth-order bandpass FSS. (© 2011 IEEE. *From:* [9].)

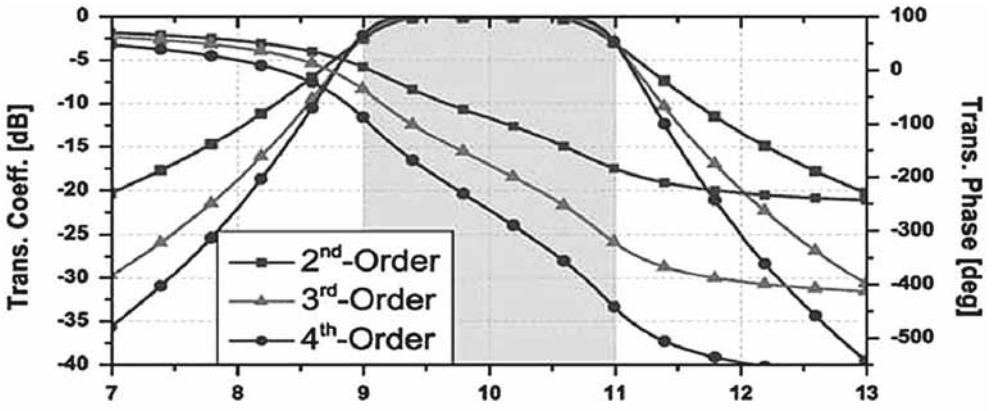

Figure 8.6 Simulated transmission coefficients (magnitude and phase) of three FSSs having second-, third-, and fourth-order bandpass responses. (© 2010 IEEE. *From:* [10].)

to achieve the required phase front on the aperture of the transmitarray. The dimensions of subwavelength patches, grids, and separation between adjacent layers can be adjusted to synthesize the required phase response. Figure 8.7 shows the phase and amplitude of the transmission coefficient of this FSS for different configurations [9]. As shown in this figure about 170° phase variation was achieved at 10 GHz.

8.3 Multilayer Transmitarray Using Matching Impedance

In this method, multilayer FSS with appropriate surface impedance values were cascaded and the separations between them were adjusted to have the entire wave transmitted at design frequency with a specified phase front. As will be outlined next, different configurations were used for designing transmitarray based on this technique, some of which are introduced here.

8.3.1 Transmitarray with Multilayer of Dipoles

A multilayer dual-polarized transmitarray composed of cross dipoles [11, 12] is shown in Figure 8.8(a). The size of the dipoles was changed to control the impedance of each layer and the separation between the layers is adjusted to maximize transmission at the design frequency. The s-parameters of two infinite FSS with airgap d between the substrates under a normally incident plan wave illumination as shown in Figure 8.8(b) can be calculated using matrix propagator method [13]. In this method the scattering matrix of single layer is calculated and then the following equations are utilized for the calculation of the scattering parameters of the whole structure.

$$\begin{bmatrix} E_{1r} \\ E_{4r} \end{bmatrix} = \begin{bmatrix} S_{\alpha\alpha} & S_{\alpha\gamma} \\ S_{\gamma\alpha} & S_{\gamma\gamma} \end{bmatrix} \begin{bmatrix} E_{1i} \\ E_{4i} \end{bmatrix} \tag{8.1}$$

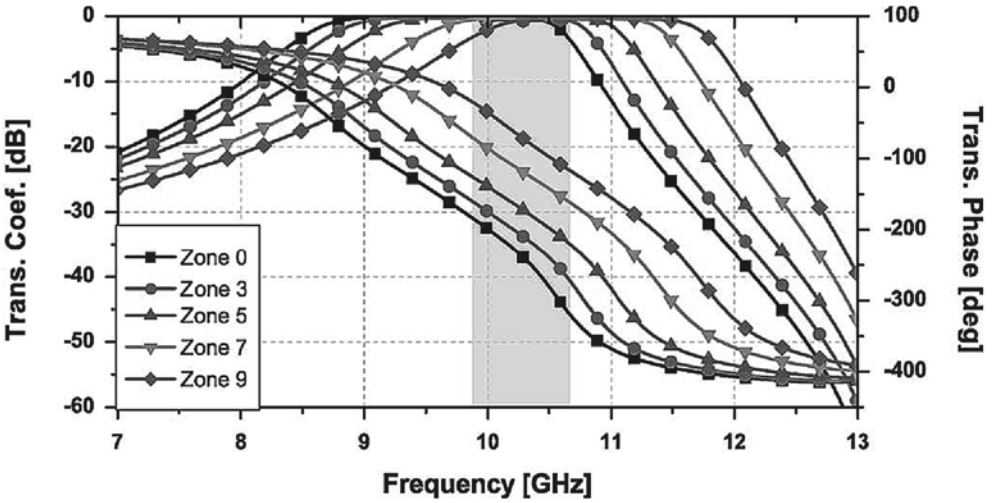

Figure 8.7 Phase and amplitude of transmission coefficient for different configurations of the transmitarray. (© 2011 IEEE. *From:* [9].)

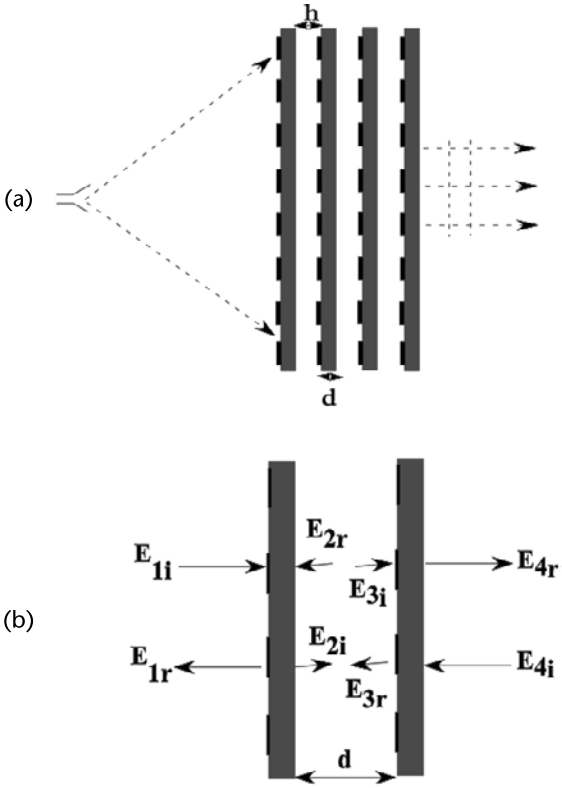

Figure 8.8 (a) Side view of multilayer lens. (b) Cascading two FSSs (© 2006 IEEE. *From:* [12].)

where

$$S_{\alpha\alpha} = S_{11} + S_{12}H_2S_{44}PS_{21} \tag{8.2}$$

$$S_{\alpha\gamma} = S_{12}H_2S_{34} \tag{8.3}$$

$$S_{\gamma\alpha} = S_{43}H_1S_{21} \tag{8.4}$$

$$S_{\gamma\gamma} = S_{44} + S_{43}H_1S_{22}PS_{34} \tag{8.5}$$

$$H_1 = \left(P^{-1} - S_{22}PS_{44}\right)^{-1} \tag{8.6}$$

$$H_2 = \left(P^{-1} - S_{44}PS_{22}\right)^{-1} \tag{8.7}$$

$$P = e^{-jk_0 d} \tag{8.8}$$

Repeated application these equations yields total reflection and transmission coefficients of any number of uniform layers that are set in cascade.

The number of layers and separation between layers are adjusted to maximize the phase and magnitude of the transmitted wave. Figure 8.9 shows the phase and

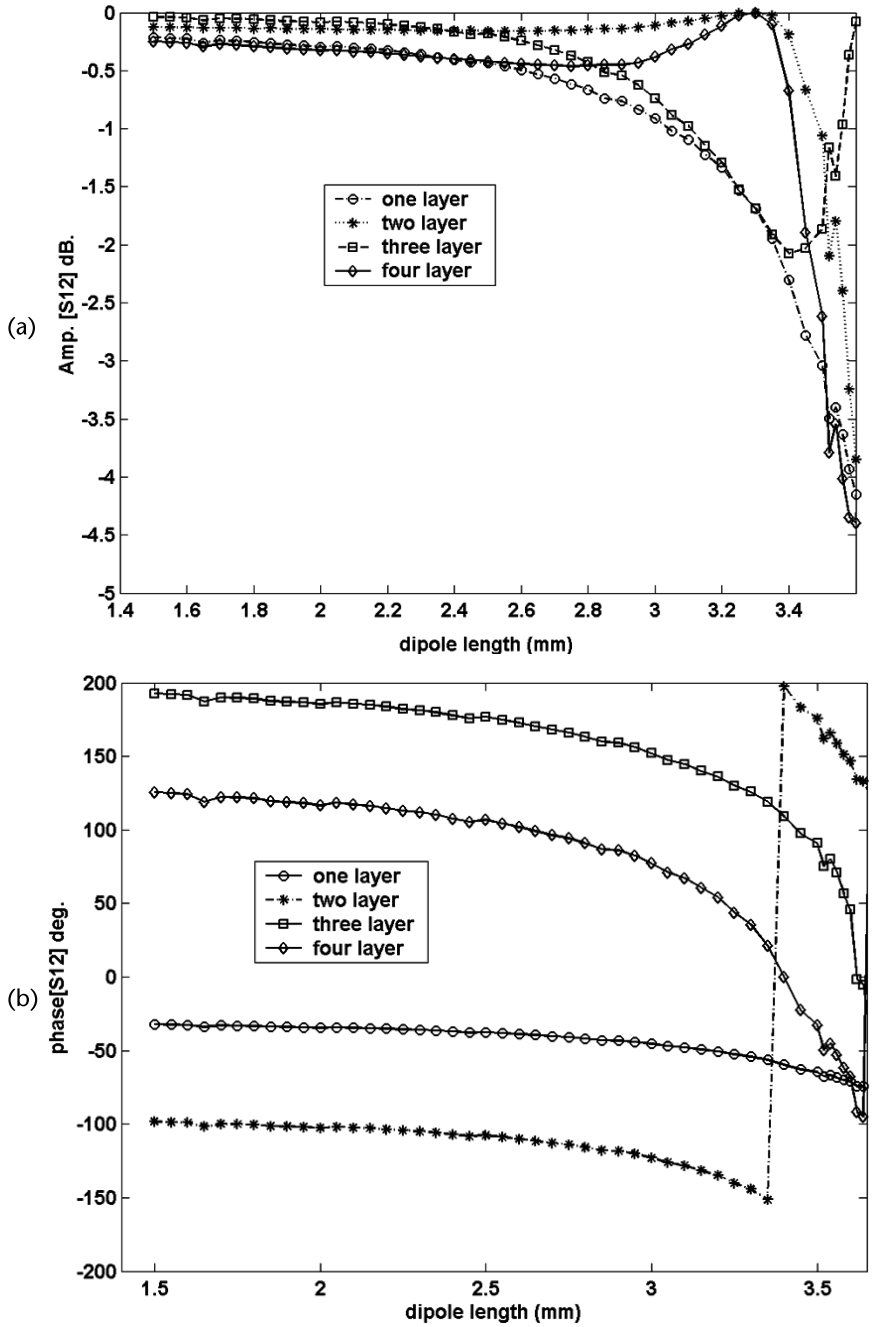

Figure 8.9 (a) Amplitude and (b) phase of a transmitarray with cross-dipole elements for different number of layers, f = 30 GHz. (© 2006 IEEE. *From:* [12].)

magnitude of transmitted wave for different number of layers up to four layers as a function of the dipole length. Both the phase and magnitude of the transmitted wave are improved by increasing the number of layers. The phase and magnitude of the transmitted wave of a four-layer transmitarray for different separations between layers are shown in Figure 8.10. A phase variation close to 300° with a magnitude less than 3 dB was achieved for 1-mm separation between the layers.

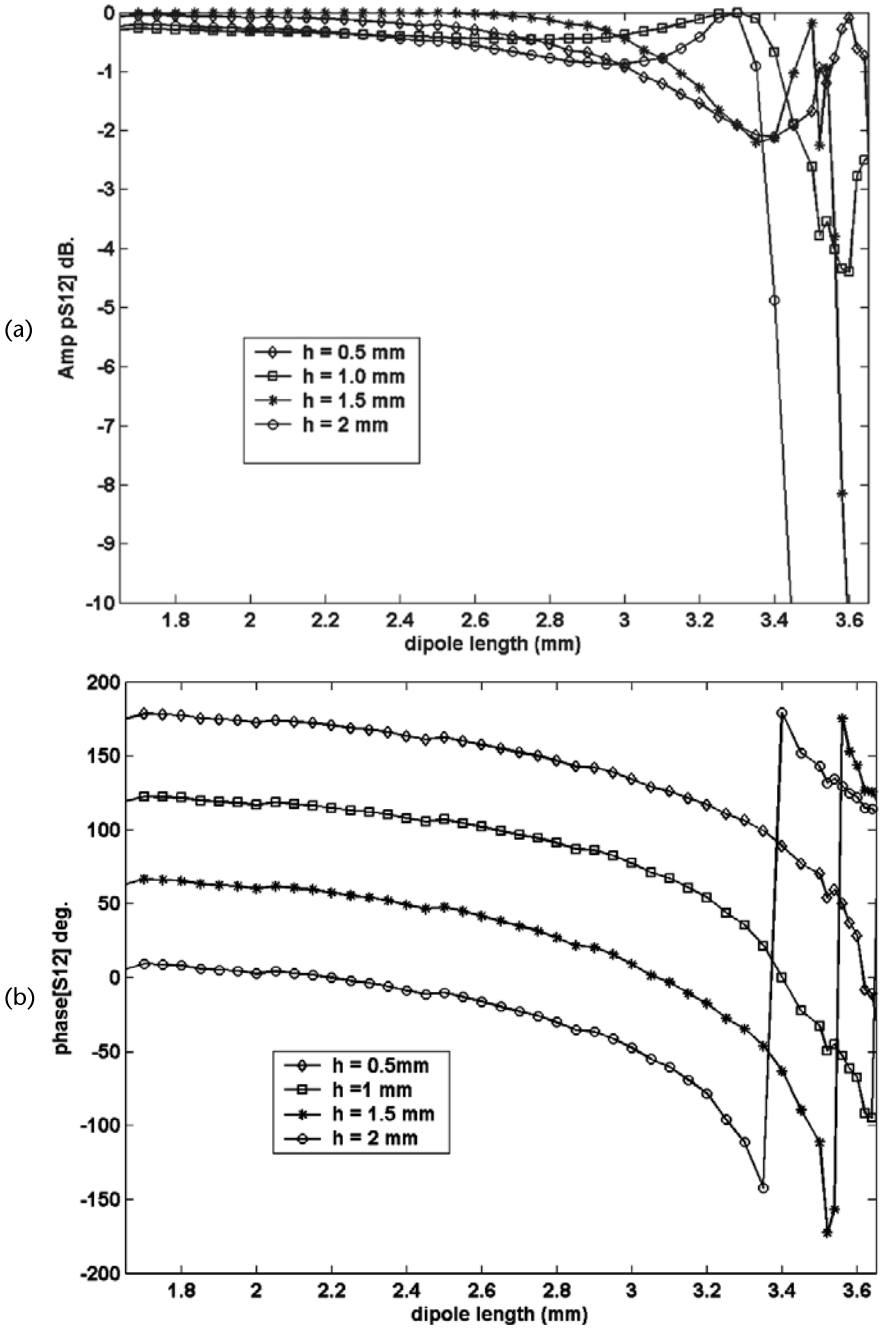

Figure 8.10 (a) Amplitude and (b) phase of a four-layer transmitarray with cross dipole elements for different separations between the layers, $f = 30$ GHz. (© 2006 IEEE. *From:* [12].)

A lens that consists of four substrates with identical thickness of 0.508 mm and permittivity of $\varepsilon_r = 3$ as shown in Figure 8.11 was designed and fabricated at for operation at 30 GHz The cross dipoles with identical arms were etched on top of each substrate and the size of cross dipoles were adjusted to collimate the beam of spherical wave emanating from the feed. The size of cross dipoles with similar transverse coordinate on substrates was identical. There is an air-gap of $d = 1$ mm between adjacent layers. The transmitarray was designed for $F/D = 0.9$ with dimensions of 15 cm × 15 cm and the cell size of 6 mm × 6 mm. The radiation pattern of this antenna is shown in Figure 8.12.

8.3.2 Dual-Band Transmitarray

A dual-band transmitarray designed for two frequency bands of 20 GHz and 30 GHz has been reported which was essentially the same as single-band transmitarray except that cross dipoles for two bands were interlaced on each layer of the structure as shown in Figure 8.13. The pyramidal horns were located at the focal point of the structure with 4-cm separation between the centers of two feeds to minimize coupling between the feeds. The phase versus arm length for both bands is shown in Figure 8.14. The coupling between the bands is taken into account in this simulation by assigning the length of the 20-GHz dipole at resonance for the simulation of the 30-GHz dipoles and vice versa. A four-layer transmitarray with same substrate configuration (dielectric constant, thickness, and separation between adjacent layers) as for the single-band transmitarray that was described in the previous subsection, was designed and fabricated and the gain versus frequency for both bands are depicted in Figure 8.15.

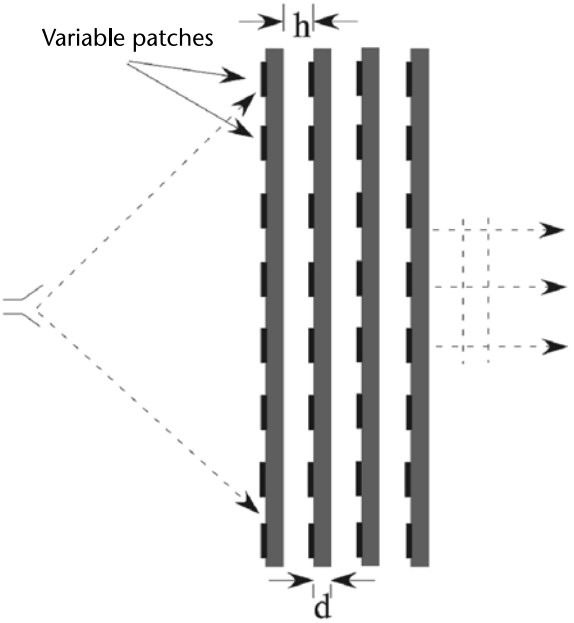

Figure 8.11 Side view of a multilayer lens. (© 2006 IEEE. *From:* [12].)

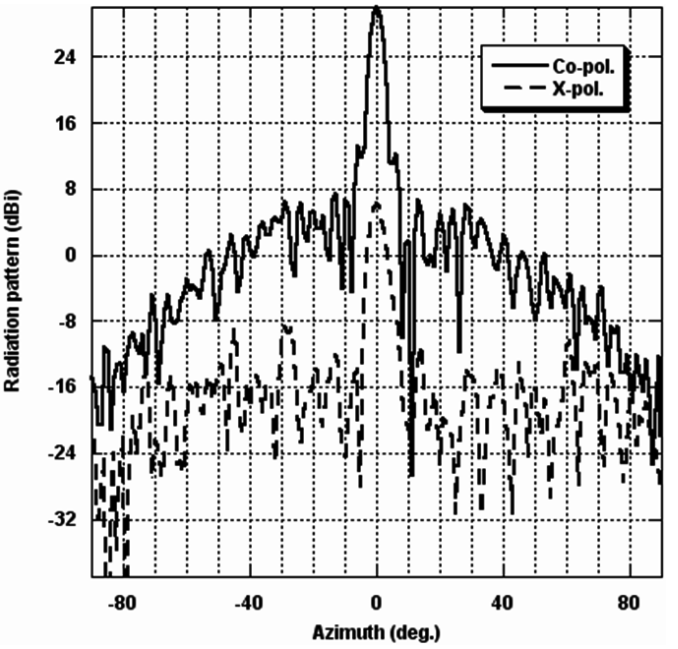

Figure 8.12 Radiation pattern of the four-layer transmitarray, f = 30 GHz. (© 2006 IEEE. *From:* [12].)

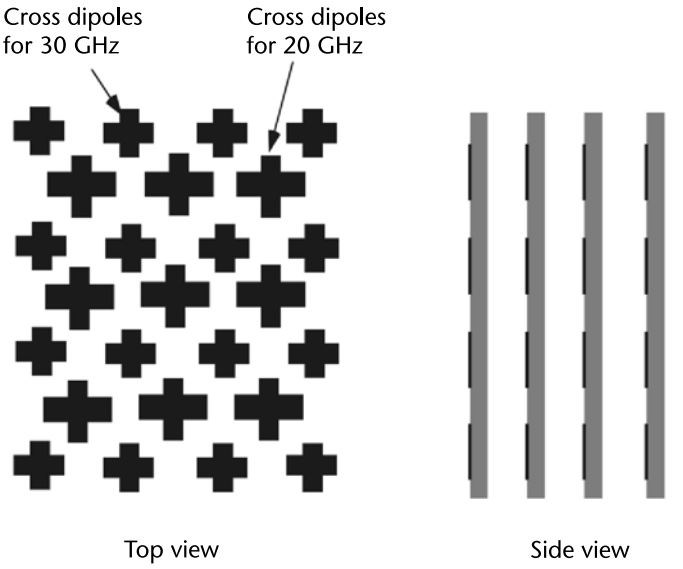

Figure 8.13 Side and top view of dual-band multilayer lens. (© 2006 IEEE. *From:* [12].)

8.3.3 Multilayer Transmitarray Using Loop Elements

One of the main disadvantages of the method explained in the previous section is infeasibility of achieving the full 360° phase shift using a single layer that enforces utilization of multilayers to achieve the full phase span [14]. In this section square loop is introduced as an alternative cell element to cross dipole to increase the phase variation and enhance transmitarray bandwidth.

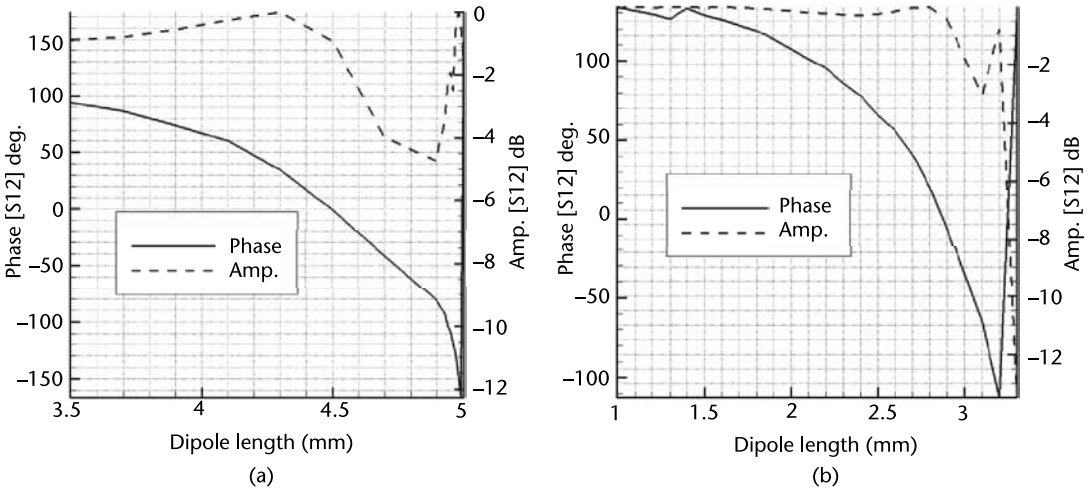

Figure 8.14 (a) Lower-band (20 GHz), upper cross dipoles set at resonance (3 mm). (b) Upper-band (30 GHz), lower cross dipoles set at resonance (5.1 mm). (© 2006 IEEE. *From:* [12].)

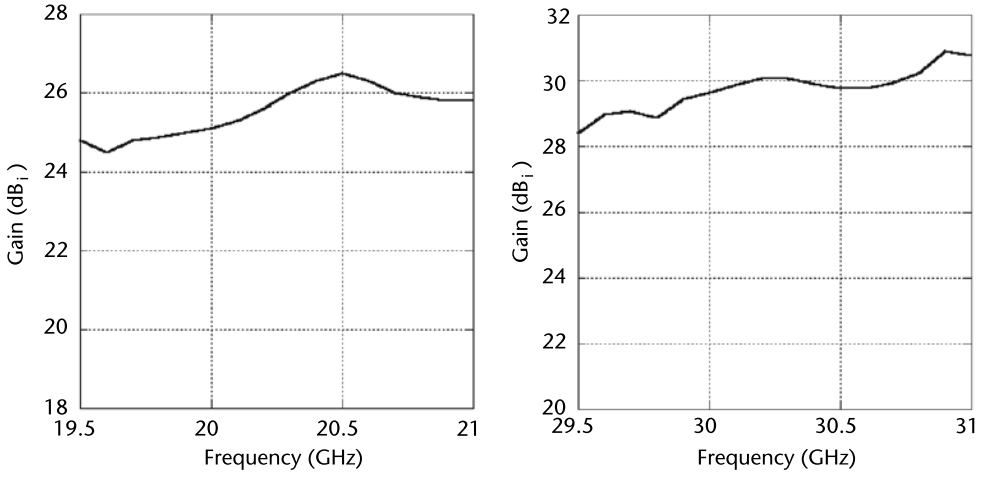

Figure 8.15 Measured gain versus frequency of dual-band multilayer lens for two frequency bands of 20 GHz and 30 GHz [12].

To reduce the number of layers that are required in the transmitarray antenna, the magnitude of phase shift per layer of the transmitarray should be maximized. Therefore, a second concentric ring has been added to yield the double square ring element, as shown in Figure 8.16(b). The transmission magnitude and phase versus frequency graphs are illustrated for generic single- and double-square ring geometries in Figure 8.17. As the dimensions of the element change, the magnitude and phase responses shift higher or lower in frequency, and thus the phase change seen at a particular frequency can be controlled. In optimizing the position of the two resonances, the extra degree of freedom of the inner ring can be used to find the best balance between the phase change and the transmission magnitude bandwidth. From Figure 8.17, it is seen that the addition of the second inner ring has introduced a second resonance in the frequency response and has increased the slope

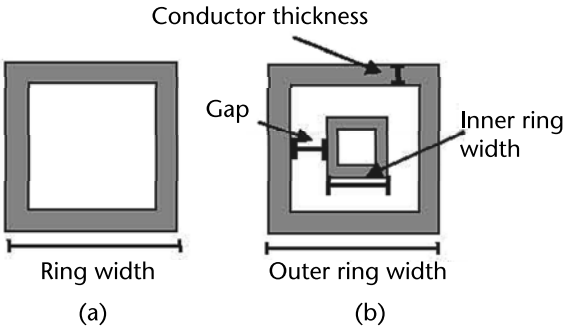

Figure 8.16 (a) Single square ring element and (b) double square ring element. (© 2010 IEEE. *From:* [14].)

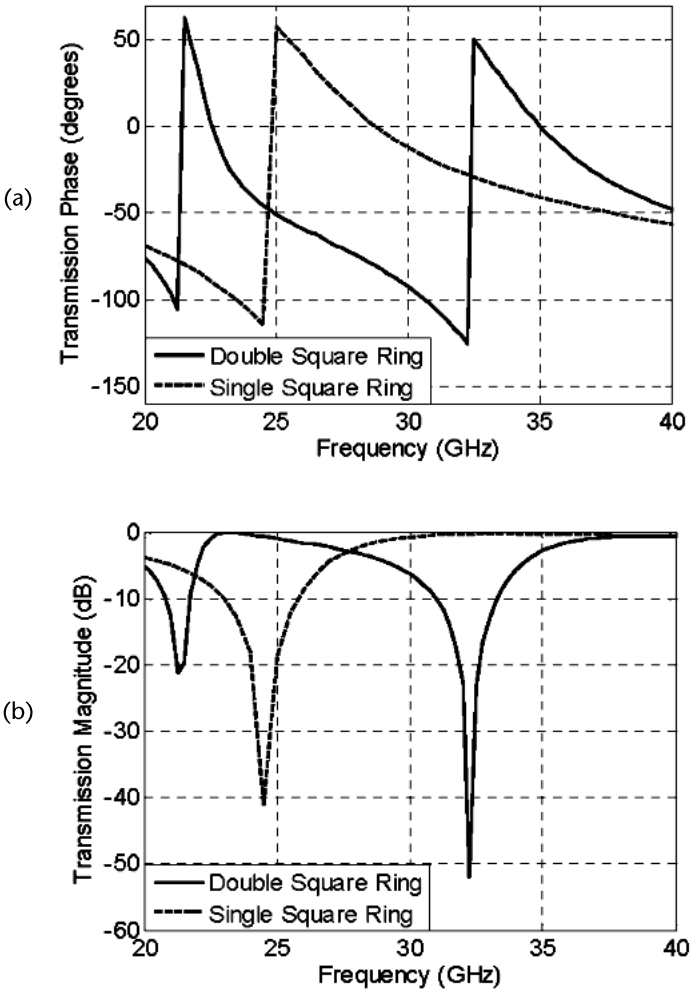

Figure 8.17 Illustration of (a) phase response and (b) magnitude response for generic single- and double-square ring elements. (© 2010 IEEE. *From:* [14].)

of the phase-versus-frequency curve between the two resonances. At a cost of a reduced transmission magnitude bandwidth (i.e., good transmission is obtained be-

tween the two resonances at 22 GHz and 32.5 GHz), a greater total phase change can be obtained from the double square ring element as its dimensions are varied.

Four different design strategies were investigated as illustrated in Figure 8.18. In the "fixed-gap" approach, the gap size between the inner and outer rings was set to a constant value and the width of the element was varied in order to control the phase variation. In an effort to improve the bandwidth, the second strategy employed a variable gap, in which the gap size is a function of the element width; this

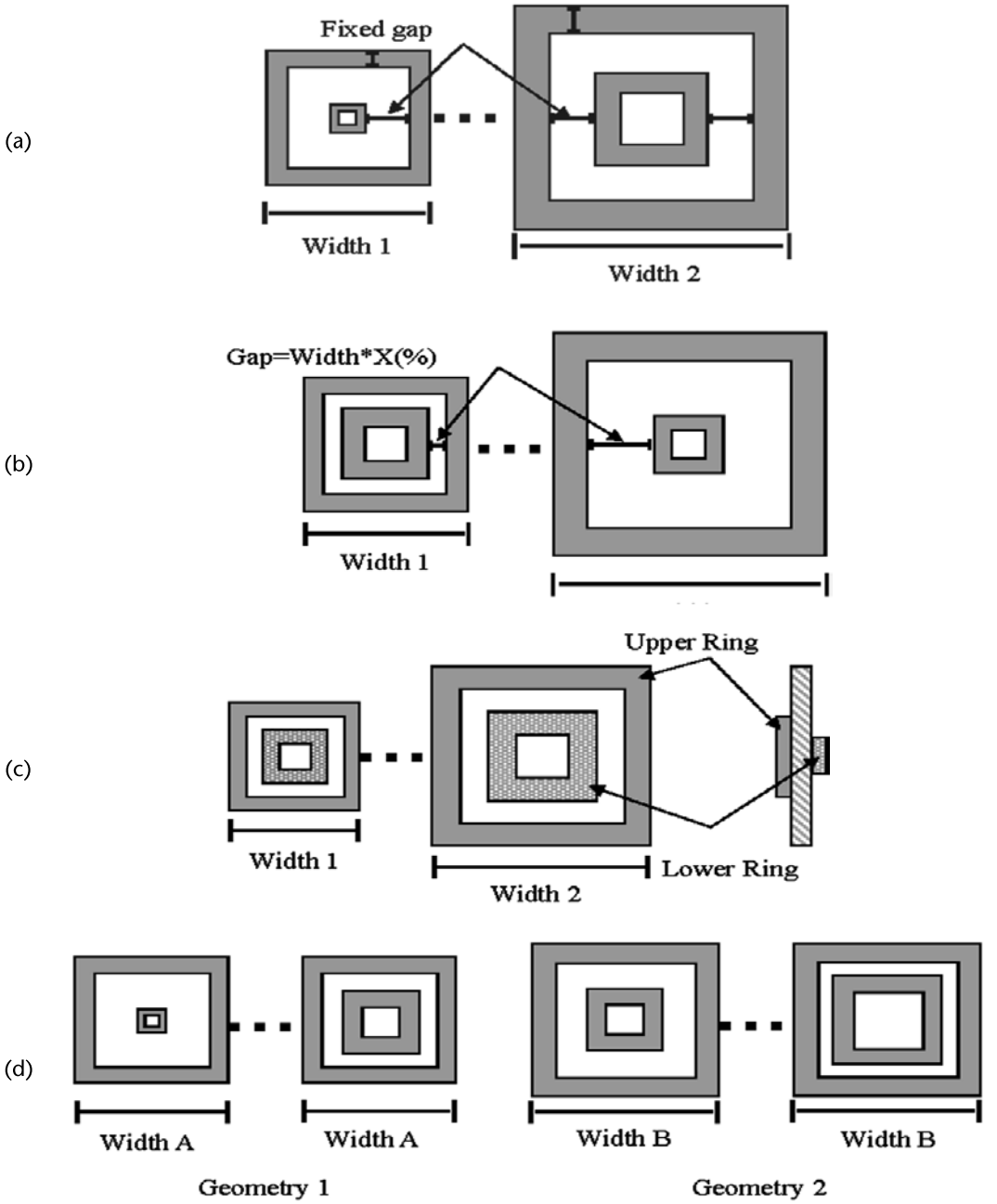

Figure 8.18 Possible unit cell designs: (a) fixed-gap, (b) variable-gap, (c) double-sided, and (d) fixed-outer ring. (© 2010 IEEE. *From:* [14].)

approach was used to delay the onset of the second resonance into the desired 30-GHz operating band. A double-sided design was also investigated to determine if an increased coupling between the rings could either widen the element bandwidth or lead to a larger per-layer phase change. Finally, an element with a fixed outer ring width was simulated; in this case the phase variation is controlled by specifying the width of the inner ring. This last design is unique in that it combines two different geometries which together are meant to cover the full 360° phase range.

Having selected the fixed-outer-ring approach and determined the optimized single-layer dimensions for this unit cell, the next step is to simulate the multilayer structure. To avoid time-consuming full-wave simulations, the matrix propagator method as explained in the previous section was used to calculate the magnitude and phase responses of the proposed design for two-, three-, and four-layer structures for a variety of layer separations from 1 mm up to 10 mm. An identical 3-mm air gap between each of the layers was found to yield the highest 30-GHz transmission magnitude over the intended inner ring width range for all three multilayer designs. The multilayer structures for this optimum layer spacing were then simulated in HFSS and Figure 8.19 shows the 30-GHz transmission magnitude and phase curves versus inner ring width for multilayer geometries ranging from two to four layers; in each case, the separation between layers is 3 mm. The four-layer magnitude and phase responses calculated from the matrix propagator method are also superimposed on the graphs and good agreement between the two approaches

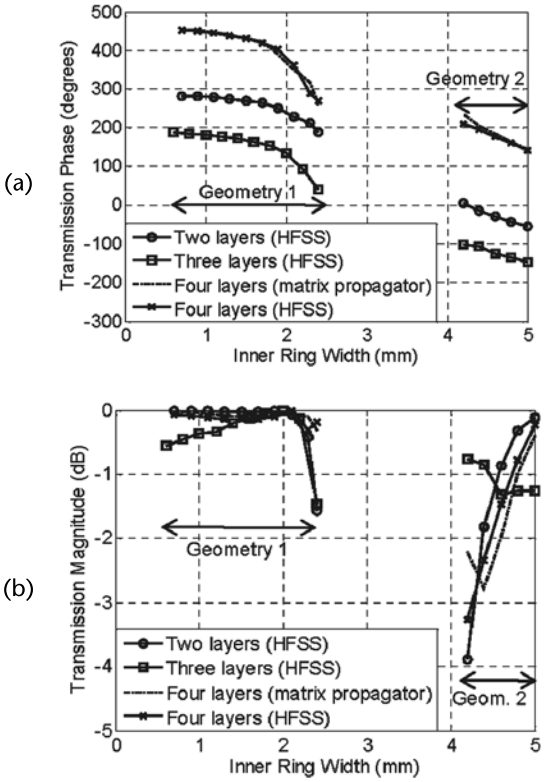

Figure 8.19 Comparison at 30 GHz of multilayer transmission (a) phase and (b) magnitude versus inner ring width for two, three, and four cascaded identical layers with a 3-mm layer separation. (© 2010 IEEE. *From:* [14].)

is obtained. Note that the graphs also indicate the range of values covered by each of the two geometries. The results show that the minimum transmission magnitude experienced by the configurations is –4 dB with close to 270° phase variation in total. Figure 8.20 plots the transmission magnitude and phase responses versus inner ring width for a four-layer structure for several frequencies ranging from 28 GHz to 31 GHz. A minimum of 270° phase variation is achieved at each frequency across the band and the transmission magnitude over the width range is usually above –3 dB. The transmission magnitude begins to decrease for frequencies above 31 GHz.

The four-layer transmitarray with the fixed-outer-ring unit cell was fabricated according to the dimensions of Table 8.1 with an F/D ratio of 0.9. A Rogers RT/Duroid 5880 substrate was used and foam spacers were inserted between the layers to create the air gaps. Figure 8.21 shows the measured far-field H-plane and E-plane radiation patterns for both copolarized and cross-polarized signals at 30 GHz as well as the measured peak H-plane gain versus frequency.

8.3.4 Phase Shifting Surface (PSS)

As its name suggests, the phase shifting surface (PSS) is a free-standing surface or screen that allows for controlled changing of the phase of an electromagnetic

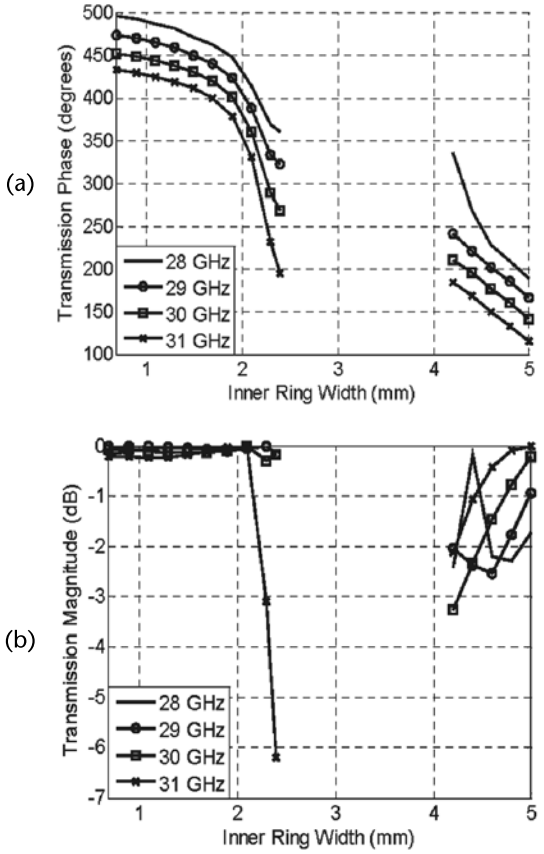

Figure 8.20 (a) Transmission phase and (b) magnitude versus inner ring width for a four-layer structure for several different frequencies. (© 2010 IEEE. *From:* [14].)

Table 8.1 Dimensions of Unit Call Configurations and of Transmitarray

Parameter	*Fixed Gap*	*Variable Gap*	*Double Sided*	*Fixed Outer Ring*	
				Geometry 1	Geometry 2
Conductor Width	0.2 mm	0.2 mm (outer) 0.2 mm (inner)	0.2 mm (upper) 0.9 mm (lower)	0.2 mm	0.2 mm
Gap	1.3 mm	0.2mm+(W-2 mm) · Rate	0.4 mm	NA	NA
Inner Ring Width	N/A	N/A	N/A	0.6–2.4 mm	4.2–5.0 mm
Outer Ring Width	4.0–5.4 mm	3.2–5.4 mm	2.6–3.8 mm	5.4 mm	5.8 mm
Cell Size	6.0 mm	6.0 mm	6.0 mm	6.0 mm	6.0 mm
Substrate Thickness (t)	0.127 mm	0.127 mm	0.127 mm	0.127 mm	0.127 mm
Relative Permittivity	3	3	2.2	2.2	2.2
Transmitarray Dimentions	(Not constructed)	(Not constructed)	(Not constructed)	12.6 cm X 12.6 cm	
Layer Separation				d_1 = 3 mm, d_2 = 3 mm, d_3 = 3 mm	

Source: [14].

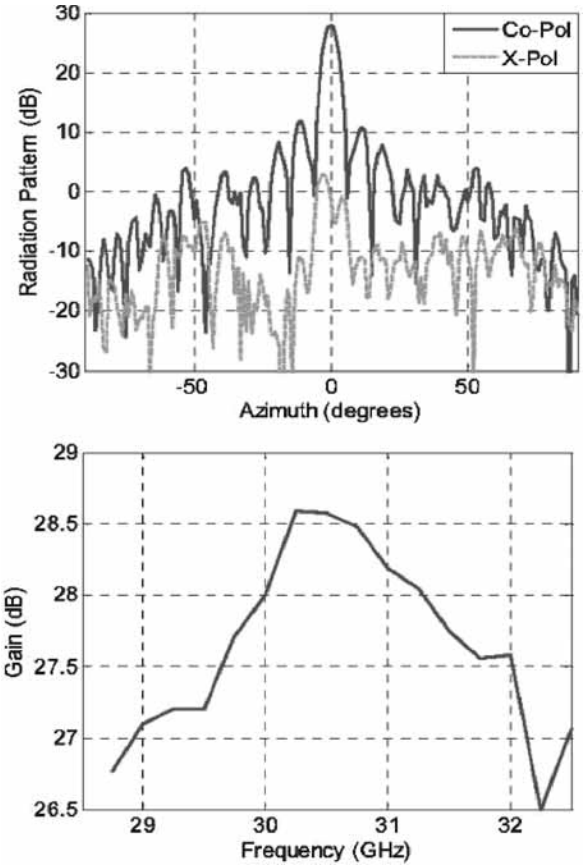

Figure 8.21 Measured 30 GHz radiation pattern (top) and gain versus frequency (bottom). (© 2010 IEEE. *From:* [14].)

wave propagating through it. The PSS can work like a transmitarray when it is excited with a horn and the phase on its aperture is adjusted to generate any desired

radiation pattern in the far field. These structures generally consist of conductive patches/strips etched on multilayer substrate the same as the configurations introduced in Section 8.2.1. However, the layers of PSSs are cascaded closely to get the advantage of the coupling between the layers which reduces the thickness of the structure. A unit cell as shown in Figure 8.22 was introduced in [15] to design an electrically thin PSS antenna. The structure is composed of two thin dielectric substrates with conducting strips etched on two sides (inner and outer) of one substrate and on one side (outer) of the second substrate. The objective is to control the value of the local phase shift of the transmitted wave while simultaneously minimizing the reflected wave. A circuit model for this structure is shown in Figure 8.23. The parameter extraction capability in the commercial code [16] was used to determine

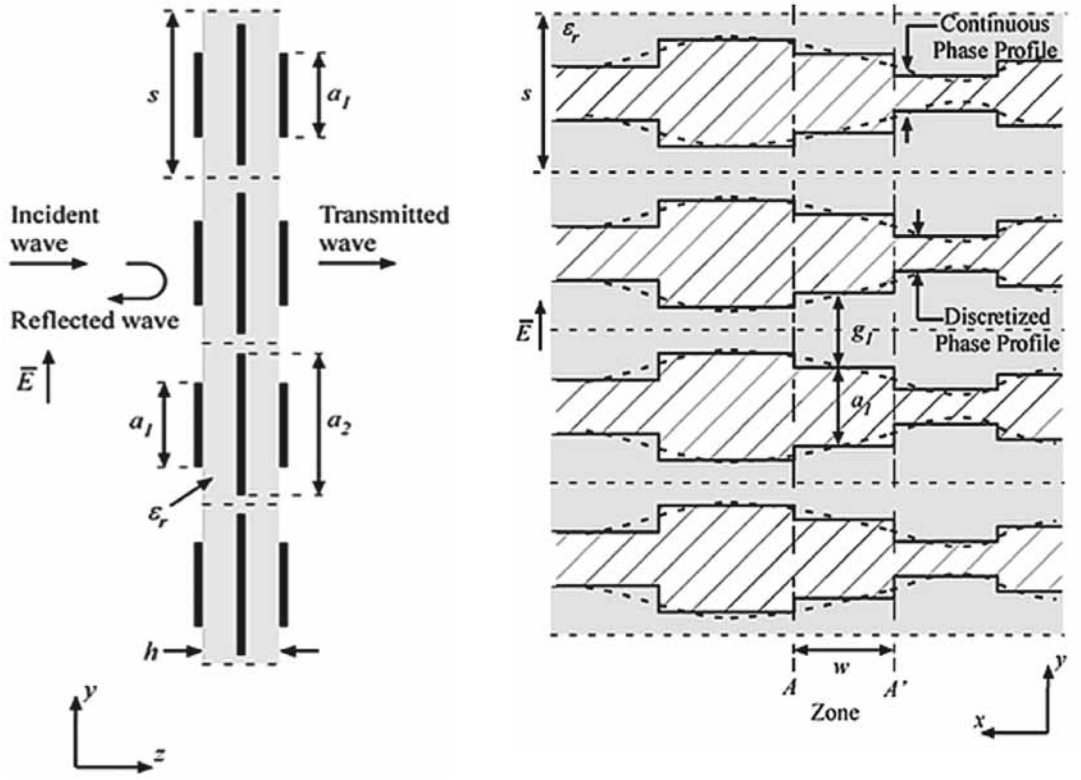

Figure 8.22 The phase-shifting surface layout: (a) side view and (b) front view. (© 2010 IEEE. *From:* [15].)

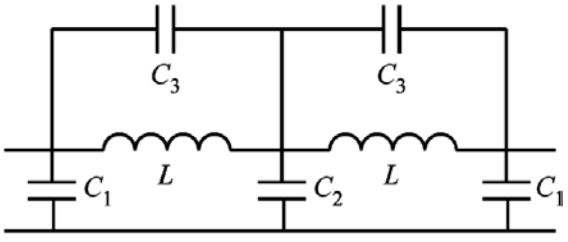

Figure 8.23 Equivalent circuit model of a unit cell of the PSS structure. (© 2010 IEEE. *From:* [15].)

the value of the equivalent circuit components. The shunt capacitances C_1 and C_2 result from the charge accumulation at the edge of the strips of two adjacent unit cells, located on the same layer, but separated by a gap along the *y*-axis. The series inductance L is function of the dielectric constant ε_r. It was observed in the simulation models that the electric field, which was assumed to be initially polarized in the *y*-direction, was bent between two strips of the same unit cell, providing a *z*-component of the field and hence the resulting series capacitance . The structure is clearly physically symmetrical, and hence so is the equivalent circuit.

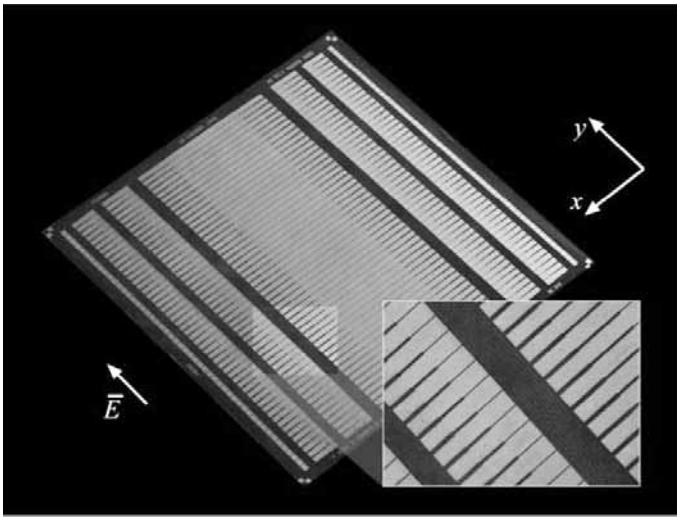

Figure 8.24 A photograph of the cylindrical PSS. (© 2010 IEEE. *From:* [15].)

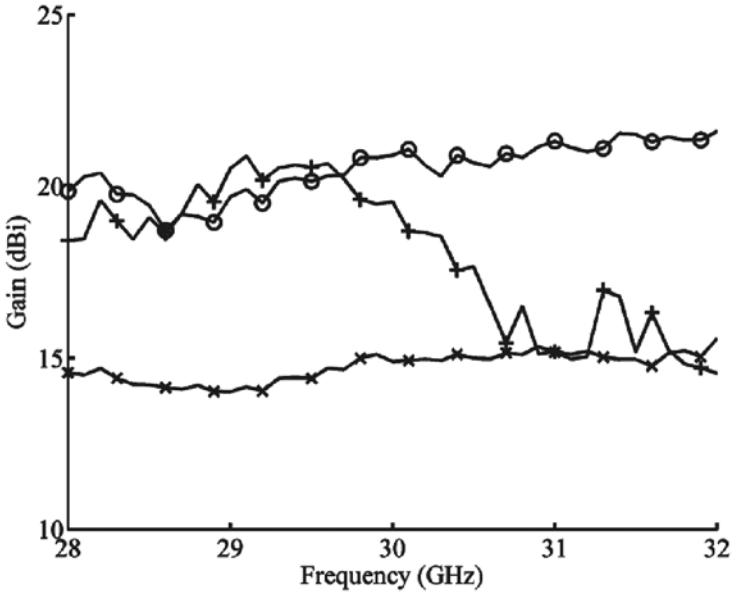

Figure 8.25 Measured boresight gain of the cylindrical lens antenna: thin PSS lens +; dielectric lens O; feed horn ×. (© 2010 IEEE. *From:* [15].)

A 15-cm-square cylindrical PSS with *F/D* = 0.5 was designed and fabricated based on this cell element. A photograph of this cylindrical lens is shown in Figure 8.24. Figure 8.25 shows the measured gain versus frequency for this PSS. A dielectric lens with the same size as PSS and the same *F/D* was also designed and the gain versus frequency of this lens is shown in Figure 8.25 for comparison. The same feed was used for both lenses. The same efficiency was measured for both lenses at the design frequency (30 GHz). However, the bandwidth of the PSS is significantly narrower than the dielectric lens as was expected.

A two-dimensional PSS with patch instead of strips was also investigated and details of the design process and measurement can be found in [17].

References

[1] Lam, K. W., et al., "Implementation of Transmitarray Antenna Concept by Using Aperture Coupled Microstrip Patches," *Asia Pacific Microwave Conference,* Hong Kong, 1997.

[2] Padilla, P., A. Muñoz-Acevedo, and M. Sierra-Castañer, "Passive Planar Transmit-Array Microstrip Lens for Microwave Purpose," *Microwave and Optical Technology Letters,* Vol. 52, No. 4, April 2010, pp. 940–947.

[3] McGrath, D. T., "Planar Three-Dimensional Constrained Lens," *IEEE Transactions on Antennas and Propagation*, Vol. 34, No. 1, January 1986, pp. 46–50.

[4] Pozar, D. M., "Flat Lens Antenna Concept Using Aperture Coupled Microstrip Patches," *Electronics Letters*, Vol. 32, No. 23, November 7, 1996, pp. 2109–2111.

[5] Abbaspour-Tamijani, A., K. Sarabandi, and G. M. Rebeiz, "A Planar Filter-Lens Array for Millimeter-Wave Applications," *IEEE AP-S Intl. Symp*., Vol. 1, No. 20–25, June 2004, pp. 657–658.

[6] Cheng, C. -C., and A. Abbaspour-Tamijani, "Study of 2-Bit Antenna-Filter-Antenna Elements for Reconfigurable Millimeter-Wave Lens Arrays," *IEEE Transactions on Microwave Theory and Techniques*, Vol. 54, No. 12, December 2006, pp. 4498–4506.

[7] Abbaspour-Tamijani, A., K. Sarabandi, and G. M. Rebeiz, "Antenna-Filter-Antenna Arrays as a Class of Bandpass Frequency-Selective Surfaces," *IEEE Transactions on Microwave Theory and Techniques*, Vol. 52, No. 8, August 2004, pp. 1781–1789.

[8] Abbaspour-Tamijani, A., K. Sarabandi, and G. M. Rebeiz, "A Planar Filter-Lens Array for Millimeter-Wave Applications," *Antenna and Propagation Symposium*, Vol. 1, 2004, pp. 675–678.

[9] Al-Joumayly, M. A., and N. Behdad, "Wideband Planar Microwave Lenses Using Sub-Wavelength Spatial Phase Shifters," *IEEE Transactions on Antennas and Propagation*, Vol. 59, No. 12, December 2011, pp. 4542–4552.

[10] Al-Joumayly, M., and N. Behdad, "A Generalized Method for Synthesizing Low Profile, Bandpass Frequency Selective Surfaces with Non Resonant Constituting Elements," *IEEE Transactions on Antennas and Propagation*, Vol. 58, No. 12, December 2010, pp. 4033–4041.

[11] Milne, R., "Dipole Array Lens Antenna," *IEEE Transactions on Antennas and Propagation*, Vol. AP-30, No. 4, July 1982, pp. 704-712.

[12] Chaharmir, M. R., A. Ittipiboon, and J. Shaker, "Single-Band and Dual-Band Transmitarray," *ANTEM*, Montreal, Canada, 2006, pp. 491–494.

[13] Redheffer, R., "On the Relation of Transmission-Line Theory to Scattering and Transfer," *Journal of Mathematics and Physics*, Vol. 41, 1962, pp. 1–41.

[14] Ryan, C. G. M., et al., "A Wideband Transmitarray Using Dual-Resonant Double Square Rings," *IEEE Transactions on Antennas and Propagation*, Vol. 58, No. 5, May 2010, pp. 1486–1493.

[15] Gagnon, N., A. Petosa, and D. A. McNamara, "Thin Microwave Quasitransparent Phase-Shifting Surface (PSS)," *IEEE Transactions on Antennas and Propagation*, Vol. 58, No. 4, April 2010, pp. 1193–1201.

[16] Advanced Design System (ADS) Agilent Technologies Inc., California.

[17] Gagnon, N., A. Petosa, and D. A. McNamara, "Thin Microwave Phase-Shifting Surface Lens Antenna Made of Square Elements," *Electronics Letters*, Vol. 46, No. 5, March 2010.

CHAPTER 9

New Techniques for Beam Switching or Steering in Reflectarray and Transmitarray

9.1 Introduction

Steerable beam antennas have been used for many decades for many applications such as radar, wireless communications, radiometric remote sensing, and imaging [1, 2]. Beam steering can be realized by mechanical rotation of the antenna, electronic phase control of large arrays, or a combination of these two methods (e.g., mechanical for azimuth and electrical for elevation). Purely mechanical solutions have the advantage of being low-cost compared to their electronic counterparts. However, they offer lower-speed beam control, which can be a limiting factor in certain imaging and wireless applications especially for the millimeter-wave band where more resolution is required. In addition, mechanical steering is more prone to correction for vibrations. Replacing these with electronically steered antennas would reduce power consumption and remove the need for lubrication and hence improve reliability. However, this is currently an unviable option because of technological limitations, which are imposed on producing reliable and low-loss phase shifters in the upper millimeter-wave and submillimeter-wave bands.

Electronically reconfigurable reflectarray and transmitarray antennas are receiving an increasing interest in key areas such as space and terrestrial communications, remote sensing, microwave imaging and radar systems [3]. Such antennas, in fact, potentially exhibit exceptional performance in scanning/tracking velocity, tolerance to vibrations, coverage modification, and robustness against interference. The low loss associated with the quasi-optical feeding system makes this solution preferable to its conventional counterpart represented by direct radiating arrays, especially at millimeter-wave frequencies. Reconfigurability is typically accomplished by employing solid state tuning devices (PIN or varactor diodes, FET). Recent advances in RF MEMS [4] technology eventually enable the use of such components in RF and millimeter-wave systems. Thanks to their inherent low cost and high performance, RF MEMS can potentially bring in completely new classes of tunable devices and circuits, particularly at high frequencies where the semiconductor-based counterparts suffer from inevitable limitations such as loss, nonlinearities, and cost. In this framework, reflectarrays are of special interest particularly at

millimeter-wave frequencies, where the loss associated with the feeding network makes it impractical to use directly radiating phased arrays.

Some of the most recent developments in reconfigurable reflectarrays and transmitarrays will be explained in this chapter. Different mechanical techniques for beam scanning of reflectarray and transmitarray will be addressed. The chapter will continue by introducing a photonically controlled technique for beam scanning of reflectarray and some novel photoconductive polymer materials will be introduced to enhance the efficiency of this technique. Recently, liquid crystal devices (LCD) have been introduced for reflectarray beam scanning at the millimeter-wave band. This method will be explained. Different electronically reconfigurable reflectarray antennas will be introduced at the end of this chapter.

9.2 Mechanical Techniques for Beam Scanning of Reflectarray and Transmitarray

Recently, there has been intense research in the field of beam-scanning antenna using a mechanical system [5]. The response time of such antennas is about a millisecond, which is slower than electrical methods; however, these antennas are excellent in terms of loss, cost, and power consumption compared with those made of a semiconductor.

Different mechanical techniques have been introduced to scan the main beam of reflectarrays. The simplest on is to put the reflectarray on a two axis steering system driven by the desired elevation and azimuth angles. However, these mechanical systems are bulky and heavy and scanning speed is slow. Previously, it has been shown that if a periphery shorted circular patch antenna is illuminated with a circularly polarized signal, it provides upon electrical or mechanical rotation of the disk a means for spatially phase shifting the incident circularly polarized signal. A method is introduced in [6] that uses the above concept to steer reflectarray beam by rotating the elements of the reflectarray. In this method, the reflectarray is illuminated with a CP feed and the phase of elements is controlled by mechanical rotation of cell element.

An active Fresnel reflector was also introduced in [7, 8] as a mechanical technique to scan the pattern of a Fresnel reflector. In this technique the Fresnel surface is divided to small cells and the level of the phase imparted by each cell is controlled mechanically using an actuator as shown in Figure 9.1. The actuator is placed under each reflecting cell, and it allows a displacement of the reflecting cell for two different states of 0 and 1, which correspond to 0° and 180° reflection phases, respectively. This can control the position of the Fresnel configuration on the surface of the antenna and scan the beam of the Fresnel reflector.

In both of the above techniques, we need a separate motor or actuator for each element to control the cell elements individually, which makes the mechanical system very complex and heavy. In this chapter, alternative mechanical techniques will be introduced for beam scanning or beam switching of reflectarray and transmitarray that proves to be simpler.

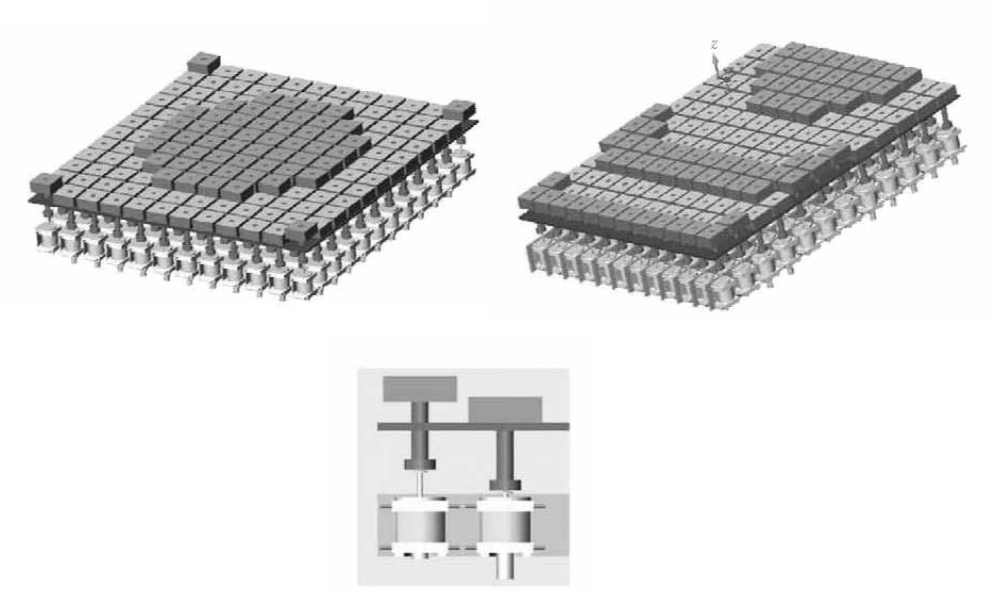

Figure 9.1 Views of the active Fresnel reflector with two different configurations and close up view of the actuator at two different states. (© 2009 IEEE. *From:* [7]. Reprinted with permission.)

9.2.1 A Mechanical Method for Beam Switching of Reflectarray

The first method is based on a reflectarray cell element [9] introduced in Chapter 3. The cell element is composed of patches with identical sizes, loaded with slots of varying length on ground plane. A view of this cell element is shown in Figures 9.2 and 9.3 shows the configuration of a mechanically steerable reflectarray that utilizes this type of cell element. The top layer was composed of identical size patches and the middle and bottom layers were composed of two sets of slots. In the middle layer, the first set of slots (1) all had identical sizes and the second set of slots (2) was several groups of slots of dissimilar length. There is no air gap between these two sets of slots and each group of slots of varying length corresponds to one and only one beam. The slots of identical length acted as a window through which only one set of variable slots can be seen by the patches. The slots that belonged to other sets were covered by the ground plane. Figure 9.3 shows three sets of such slots in each unit cell on layer 2 for collimating the beam at –30°, 0°, and +30 depending on the set of slots that are visible to the patch through the "window" in the second

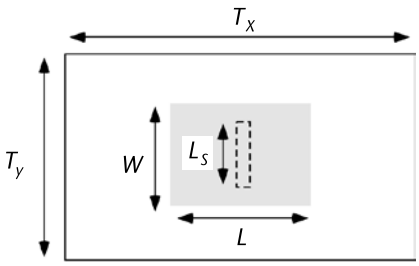

Figure 9.2 Typical slot loaded patch element. Slot length is variable to change the loading on the patch. The patch size is constant throughout the lattice.

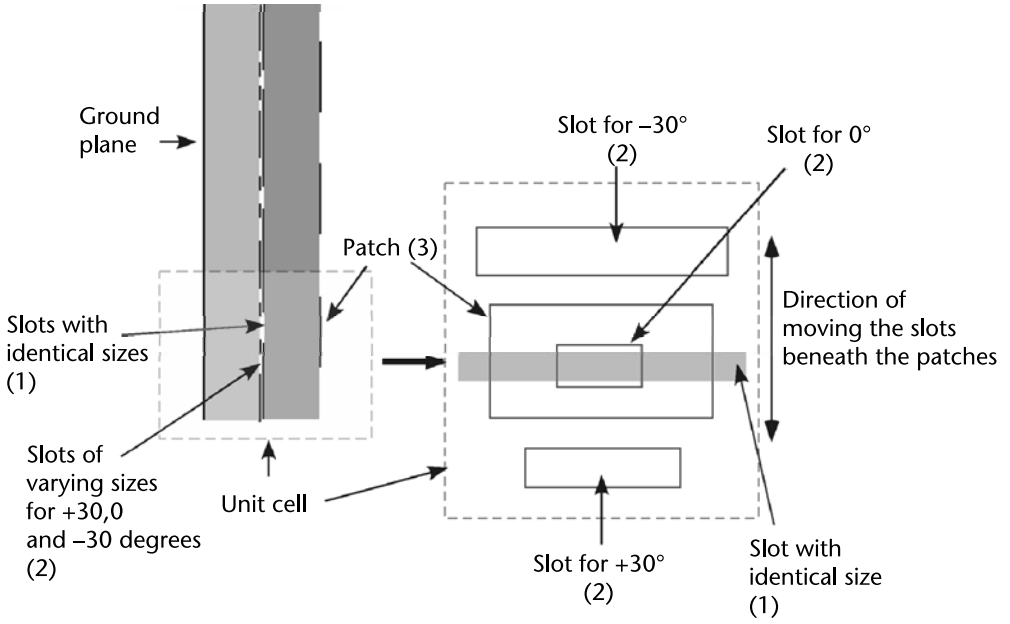

Figure 9.3 A schematic diagram of the mechanically steerable reflectarray call element. (© 2003 IEEE. *From:* [9]. Reprinted with permission.)

layer. It should be noted that only the slots aligned with the uniform slots are seen by the incoming wave. The separation between the slots within the same unit cell is 1.0 mm. Therefore, upward or downward displacement of the second layer with respect to the first layer is ±1 mm, which resulted in three different beams pointing to –30°, 0°, +30°.

A prototype was made based on the above principle and the fabricated reflectarray is shown in Figure 9.4. The normalized radiation pattern for this antenna at

Figure 9.4 A photograph of the fabricated reflectarray. (© 2003 IEEE. *From:* [9]. Reprinted with permission.)

30 GHz is shown in Figure 9.5. As shown in this figure, the beam can be switched between +30°, 0°, and –30° by moving layer (2) with respect to upper patch layer.

9.2.2 A Mechanical Method for Beam Scanning of Transmitarray

A cylindrical lens based on the multilayer transmitarray introduced in Chapter 8 is used to design a one-dimensional beam scanning cylindrical transmitarray at Ka-band [10]. A photograph of this lens with a schematic front view is shown in Figure 9.6. This antenna is fed by an array of 2×16 microstrip patch elements. The feed generate a fan-shaped pattern which illuminate the cylindrical lens. The cylindrical transmitarray is designed to change the fan-shaped beam received from the feed into a symmetrical pencil-shaped pattern. The beam is scanned by rotating the feed mechanically. Because this lens is designed for beam scanning by rotating the feed mechanically, the distance between the feed and the transmitarray should be identical for all feed angles. To do so, the transmitarray is design in a cylindrical shape and the elements are designed to collimate the fan-shaped beam coming from the feed in elevation plane without changing the feed pattern in azimuth plane. The feed is located at the center of cylinder. The transmitarray consists of four identical layers of substrate with permittivity of $\varepsilon_r = 3$ and thickness of 0.020 inch (see Chapter 8). There is a 1-mm air gap between adjacent layers. The transmitarray elements are cross dipoles and the phase is adjusted by changing the length of dipoles arms. Figure 9.7 shows the measured radiation pattern of this antenna for different feed angles in both azimuth and elevation planes. As shown in this figure, the fan-shaped beam of the feed is collimated to a symmetrical pencil-shaped beam and ±30° beam scanning can be achieved with this antenna without compromising gain and sidelobe performance of the transmitarray.

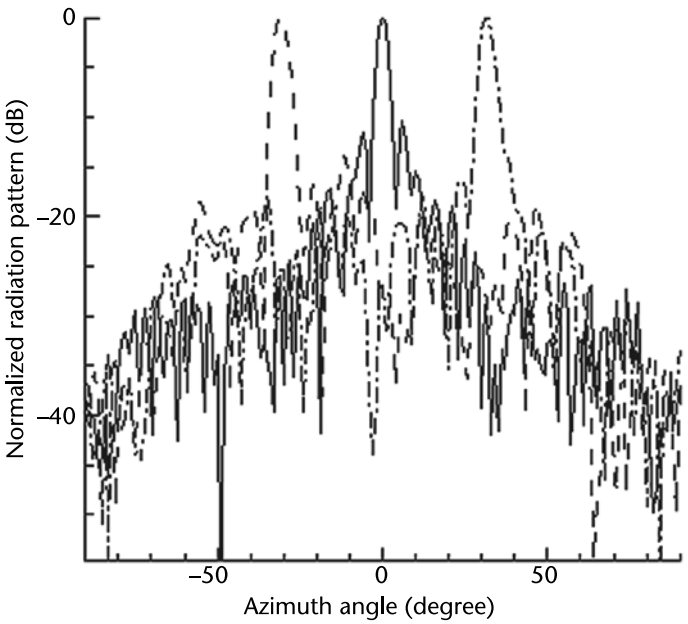

Figure 9.5 Radiation pattern of the reflectarray for the different positions of the moving screen. (© 2007 IEEE. *From:* [9]. Reprinted with permission.)

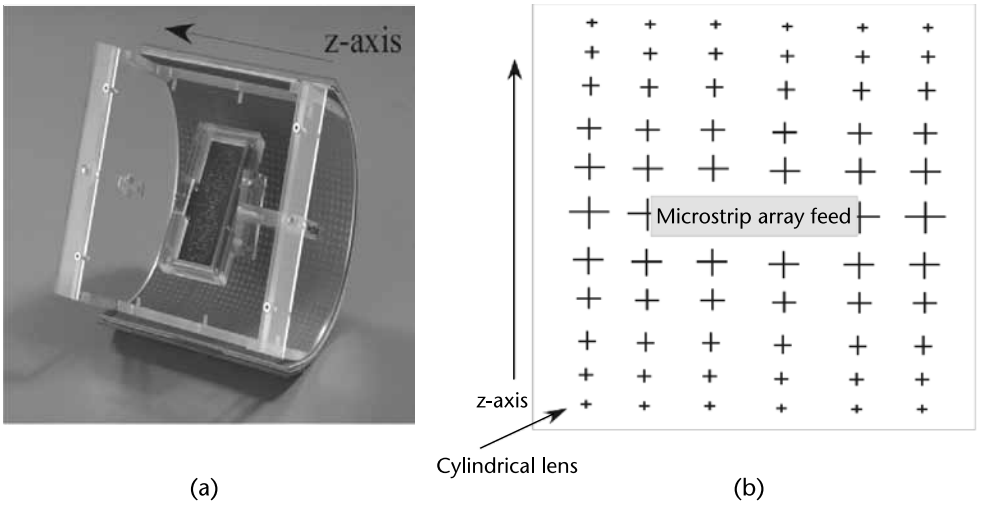

Figure 9.6 (a) A photograph of the cylindrical transmitarray. (b) A schematic front view of the transmitarray. (© 2007 IEEE. *From:* [10]. Reprinted with permission.)

9.3 Reflectarray Beam Scanning Using Reconfigurable Materials

Changing the properties such as permittivity, permeability, and conductivity of materials, which are used as substrate or radiating elements of reflectarray is one way to design reconfigurable reflectarray elements for beam scanning applications. Different tunable materials such as photoconductive materials, liquid crystals (LC), and ferroelectric materials are used to design reconfigurable reflectarray elements. In this section, tunable reflectarray elements using photoconductive and LCs will be presented.

9.3.1 Photonically Controlled Method for Beam Scanning of Reflectarray

Photo-induced plasma in a semiconductor medium is a promising solution for inexpensive beam steering in the microwave and millimeter-wave bands [11, 12]. The key element in these antennas is the interaction of the RF energy with an electron-hole plasma grating created by optical means. Recently a new photonic technique based on photo-induced plasma is presented for beam scanning of reflectarray antennas [13]. The proposed technique is based on varying the slot length by employing the photo-induced plasma, which establishes the phase shift mechanism in a reflectarray configuration. The reflectarray antenna consists of three layers. A schematic view of this structure is depicted in Figure 9.8. The first layer is a dielectric substrate layer onto which an array of microstrip patches of identical sizes is etched. The second layer is a silicon wafer with slots of identical size etched on its lower surface. An optically transparent substrate layer (glass) is located beneath the silicon. There is a small air gap between this glass plate and the silicon wafer. An indium tin-oxide (ITO) film is interposed on top of the glass between the silicon wafer and glass layer. The ITO sheet is optically transparent but reflective at the wavelength of the RF signal. The optical mask is attached to the glass. An optical

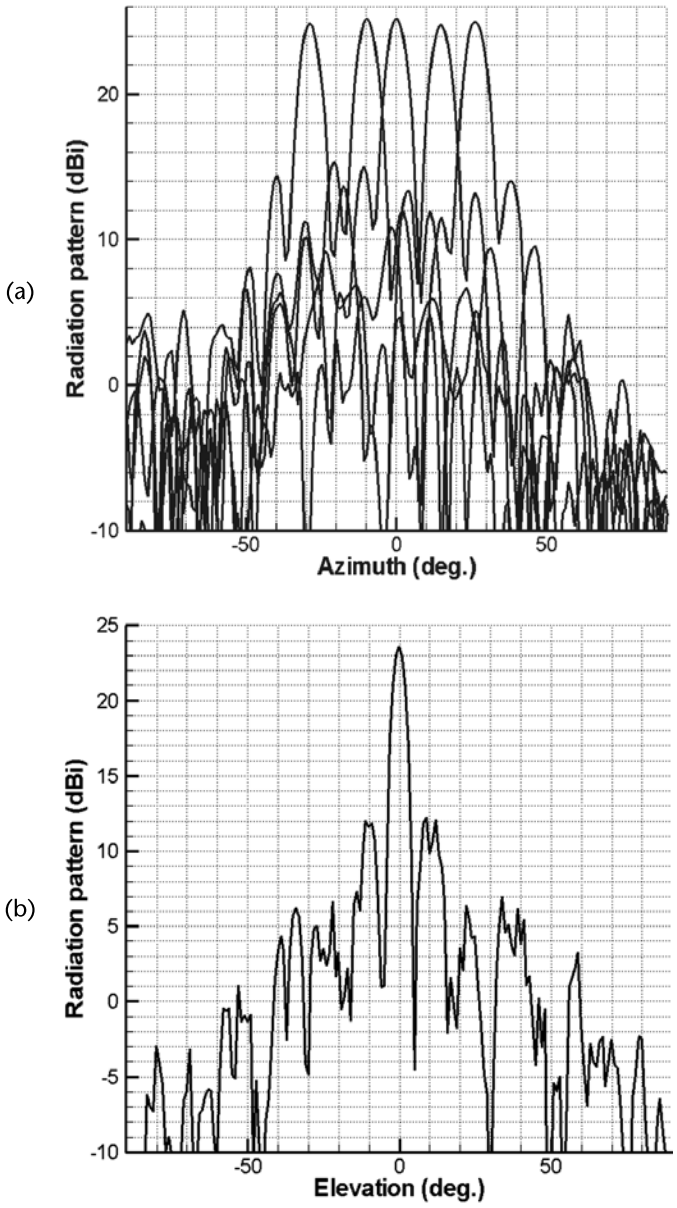

Figure 9.7 Measured radiation pattern of lens: (a) azimuth plane (xy-plane) and (b) elevation plane (xz-plane). (© 2007 IEEE. *From:* [10]. Reprinted with permission.)

source illuminates the reflectarray from the glass side. The photo-induced plasma generated inside the silicon changes the slot length which can control the phase distribution of the reflectarray to scan the beam of the reflectarray in a desire direction.

Figure 9.9 shows the phase and amplitude of the reflected wave versus the slot length when the slot length is changed by photo-induced plasma. The carrier density of plasma is set to 10^{17} cm^{-3}, 10^{18} cm^{-3}, and infinite (perfect conductor). As shown in this figure, as the carrier density of the plasma is decreased, the plasma loss is increased, and this adversely affects the reflection coefficient of the structure.

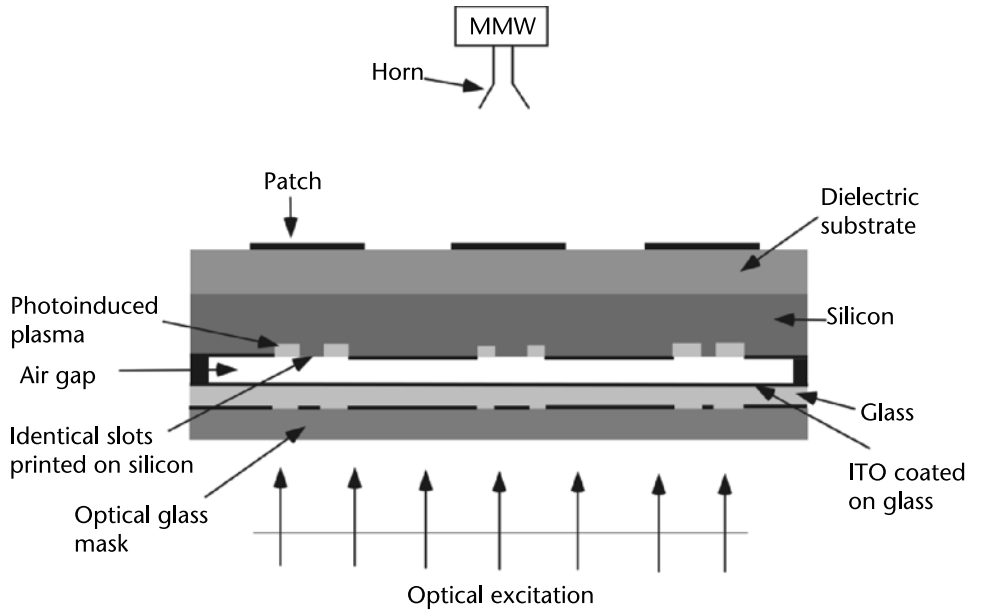

Figure 9.8 Schematic view of a three-layer reflectarray with optically controlled slots on the ground plane. (© 2006 IEEE. *From:* [13]. Reprinted with permission.)

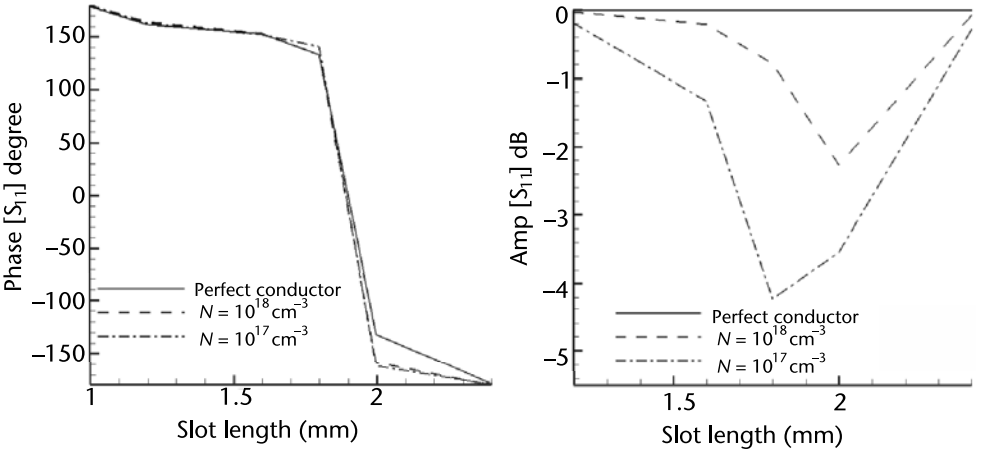

Figure 9.9 Phase and amplitude of the reflected versus the slot length of the three-layer reflectarray for the different carrier densities of plasma. (© 2006 IEEE. *From:* [13]. Reprinted with permission.)

Figure 9.10 shows the measured radiation pattern of this reflectarray when the optical signal is switched ON and OFF, respectively. The pattern is collimated at 0° when the reflectarray is illuminated with optical excitation.

The photo-induced plasma generated in semiconductor suffers from a number of shortcomings, including:

1. High-power optical sources are required to avoid excessive losses and obtain adequate efficiency, due to the inverse proportionality of losses inside the plasma to the optical power intensity.

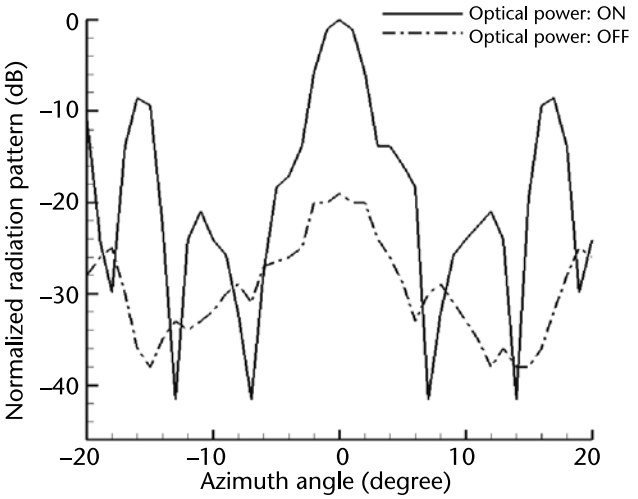

Figure 9.10 Measured radiation pattern of the reflectarray when optical signal is ON and OFF. (© 2006 IEEE. *From:* [13]. Reprinted with permission.)

2. Technological restrictions on processing large high-resistivity semiconductor wafers preclude the design of monolithic high-gain antenna arrays.
3. Coating a thin layer of high-resistivity semiconductor on a substrate is not currently feasible with the present technologies.

To overcome these shortcomings, polymeric materials are being considered as an alternative to semiconductors. These materials have many advantages over conventional semiconductors [14]. They are low-cost, easy to process, more efficient, and lightweight. A thin layer of the polymer can also be easily coated over a large surface area. A photoconductive polymer derived from poly (N-vinyl carbazole) (PVK) is introduced in [15]. A thin layer of this polymer is coated on one size of a glass substrate. To characterize the polymer, the glass substrate coated with the polymer is located in front of an open waveguide as shown in Figure 9.11. The polymer is illuminated through a slot. The reflection coefficient with and without optical excitation is measured using a vector network analyzer (VNA). Figure 9.12 compares the reflectivity versus frequency of a dark polymer sample and with the sample illuminated by an optical intensity of 2.3 W/cm^2 (maximum optical power generated by halogen lamp). The reflection coefficient of the sample when a metal plate is located in front of the slot is also shown as a comparison to the conductivity of photo-induced plasma generated in the polymer. The similarity of the S11 of the optically illuminated sample with that of the metal plate indicates highly conductive nature of the optically excited polymer sample.

9.3.2 Reconfigurable Reflectarrays Using Liquid Crystals

Liquid crystal (LC) is an anisotropic material showing both properties of a crystal and a liquid. The LC state depends on temperature and varies from solid to liquid. In the nematic state the rod like molecules float around as in a liquid phase; however, these are ordered in their orientation. The permittivity of the material can therefore be varied at microwave frequencies by changing the molecular orientation

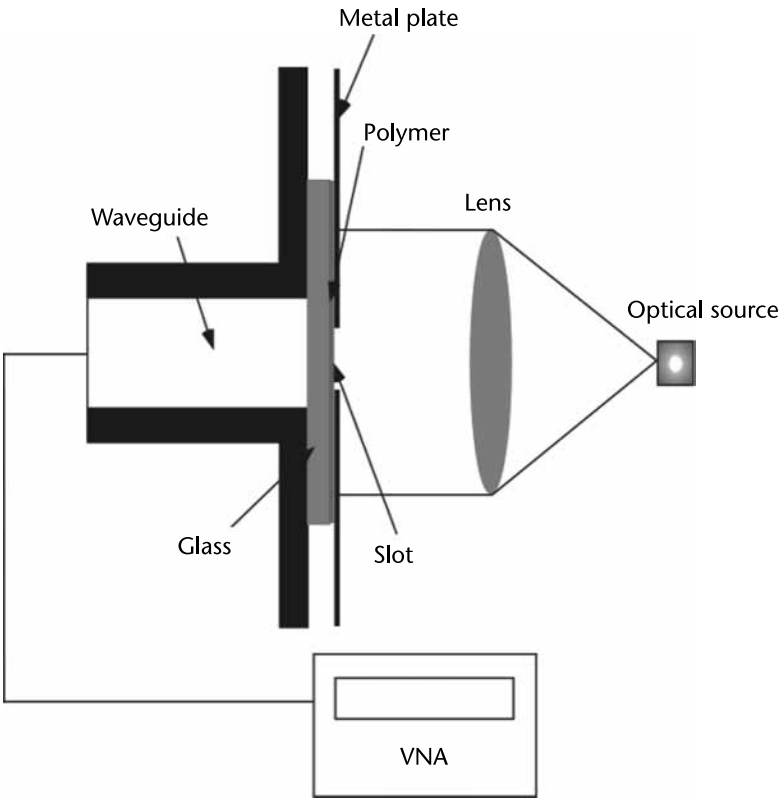

Figure 9.11 Schematic view of waveguide setup. (© 2005 IEEE. *From:* [15]. Reprinted with permission.)

relative to the RF field through application of dc voltage on the LC sample [16, 17]. When this technique is employed to design a phase agile reflectarray cell, the permittivity can be varied between two extreme values; $\varepsilon//$ when the fringing field is aligned parallel to the director of the molecules and $\varepsilon\perp$ when these are aligned perpendicular to the RF field.

The effective dielectric anisotropy is defined as:

$$\Delta\varepsilon = \varepsilon_{//} - \varepsilon_{\perp} \tag{9.1}$$

Figure 9.13 shows schematic of the cross section of a LC tunable reflectarray unit cell. The cell consists of a patch printed on a carrier substrate, the ground plane printed on a carrier as well, and the LC cavity between patch and ground. A thin polyimide film (about 300 nm) is spin coated both on the ground plane and on the patches, cured and finally mechanically rubbed, to provide the prealignment of the LC molecules. The director of the LC molecules is initially aligned parallel to the patch and ground, owing to the polyimide layer [Figure 9.13(a)]. The applied bias voltage between patch and ground generates the external electric field for reorientating the director of the LC molecules. The RF field, given by the microstrip patch fundamental mode is mainly confined in the LC volume and is essentially perpendicular to the director. Thus, the RF field will perceive an effective permittivity $\varepsilon_{r,eff} = \varepsilon_{\perp}$. Applying an increasing bias voltage, the director will begin to

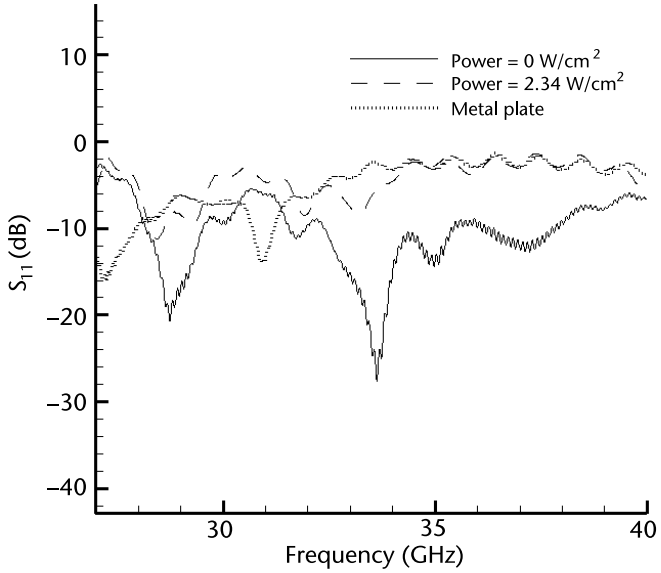

Figure 9.12 Measured S11 versus frequency for dark polymer sample (solid line), for the case illuminated with 2.3 W/cm2 optical intensity (dashed line) and when a metal plate is located in front of slot (dotted line). (© 2005 IEEE. *From:* [15]. Reprinted with permission.)

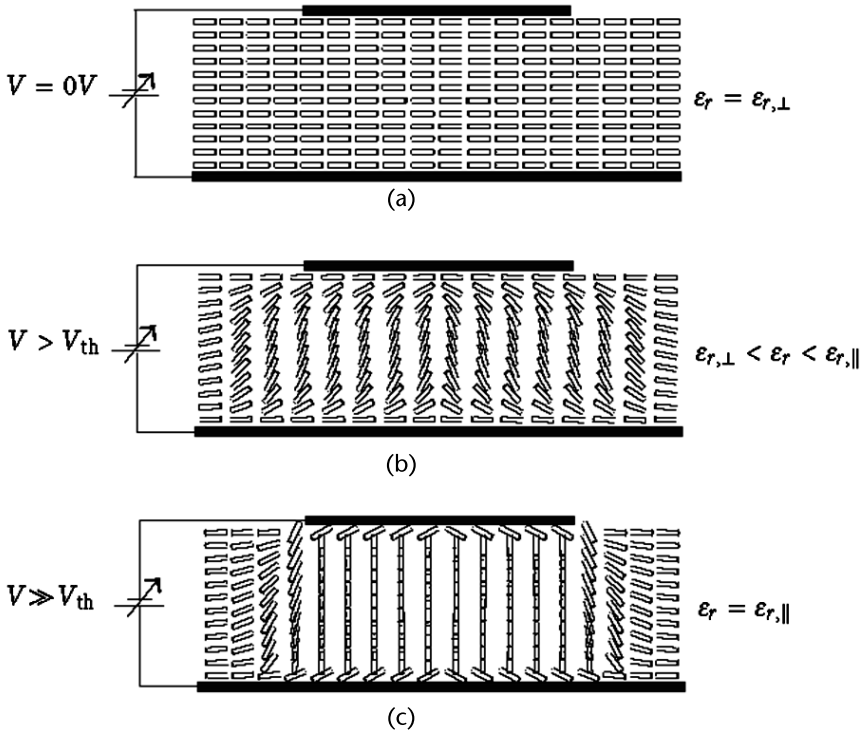

Figure 9.13 Functioning principle of the LC tunable reflectarray unit cell with single microstrip patch. (© 2008 IEEE. *From:* [18]. Reprinted with permission.)

rotate as soon as the voltage exceeds a certain threshold voltage *V*th of a few volts [Figure 9.13(b)]. When the bias voltage is increased even further, the director of

the LC molecules will tend to align with the bias field lines, until the molecules are completely aligned parallel to the bias E-field. In this state, the average direction of the main axes of all molecules become parallel to the RF-field and the experienced effective permittivity becomes $\varepsilon_{r,eff} = \varepsilon_{r//}$ [see Figure 9.13(c)]. The change in relative effective permittivity, $\Delta_{\varepsilon r}$,eff produces a change in the capacitance per unit length of the microstrip patch. This leads to a shift in the resonance frequency, ωr, and also to a shift of the phase characteristic as shown in Figure 9.14. As shown in this figure, about 180° phase variation was achieved at design frequency of f = 101.72 GHz, between this range of discrete phase variation the amplitude (loss) is predicted to vary between 3 and 7 dB. It has been shown that the loss improves in LC as the frequency increases [18].

9.4 Electronically Controlled Reflectarray Antennas

Electronically reconfigurable reflectarray antennas are receiving an increasing interest in key areas such as space and terrestrial communications, remote sensing, microwave imaging and radar systems [19]. Such antennas, in fact, potentially exhibit exceptional performance in scanning/tracking velocity, tolerance to vibrations, coverage modification, and robustness against interference. Reconfigurability is typically accomplished by employing solid state tuning devices (PIN or varactor diodes, FET, MEMS). Different electrically controlled reflectarray elements using different technologies such as PIN, varactor diodes, and MEMS are introduced in this section. The pros and cons of these technologies which are used to design electrically reconfigurable reflectarray elements are summarized in Table 9.1 [20].

PIN diode and MEMS can be used as a switch for changing the length and size of reflectarray elements or rotate the elements for CP applications. Depend

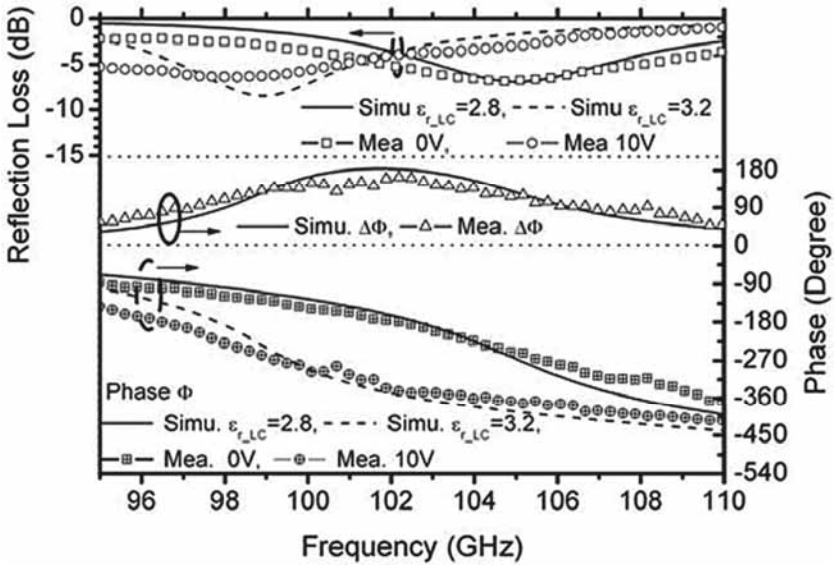

Figure 9.14 Simulated and experimental reflection loss (upper plot), phase (lower plot), and phase agility (center plot) of a reflectarray with LC as tunable substrate. (© 2008 IEEE. *From:* [18]. Reprinted with permission.)

Table 9.1 Potential Electrically Reconfigurable Technologies and Their Impact on Some Key Parameters

	RF MEMS	*PIN Diode*	*Varactor Diode*
Costs	Medium	Low	Medium/High
Loss	Very Low	Low	High
Power Consumption	Negligible	High	Negligible
Speed	Mircoseconds	Nanoseconds	Nanoseconds
Technology Readiness	Foundry required	Market available (COTS)	Market available (COTS)
Mounting Complexity	Low	Low	Low
Biasing Complexity	High voltage (60V)	Low voltage (1V)	Medium voltage (0–30V)

Source: [20].

on number of switches for each element, different level of phase quantization can be achieved. Various types of tunable reflectarray cell elements have been reported based on PIN diode and MEMS. A microstrip patch which is connected with short circuit stub-loaded with a PIN diode is reported in [21] as a single-bit quantized phase shifter to design a tunable reflectarray cell element at 60 GHz. The length of stub is adjusted to get 180° phase change when the PIN diode switches. The design of the dc bias line is the main challenge in this method due to the high coupling between dc bias circuit and reflectarray elements.

The other reconfigurable reflectarray element introduced in [22], used PIN diode to change the delay line of a patches aperture-coupled to a microstrip delay lines as shown in Figure 9.15. MEMS can also be used for this application as reported in [22]. In the method presented in [22], reflectarray elements are grouped in a cluster of two or four and the length of a common microstrip delay line is controlled through a PIN to save the number of control devices and their associated dc biasing lines. One PIN diode is used for each pair for producing two phase values to realize a reflectarray with beam switching capability. The same technique can be extended to N phase states if more electronic devices are inserted in the microstrip line. The main drawback of this gathering method is the high risk of generating grating lobe because the period of the subarray becomes much greater than half a wavelength although this undesirable grating lobe might appear to be far away from the main beam region. The reflectarray is designed to simplify the voltage control system [24].

Tunable reflectarrays using RF MEMS have also been reported recently [25–27]. The RF MEMS has many advantages such as: low insertion loss, low power consumption, small size, and low cost.

However there are some drawbacks of using these components in tunable reflectarray element such as low speed, the speed of MEMS in the range of microsecond, power handling, the inability of most MEMS elements to handle more than 100 mw, reliability, and packaging.

A reconfigurable MEMS reflectarray element is introduced in [28]. In this method, double cross loop is loaded with variable digital series MEMS capacitors as shown in Figure 9.16. In this approach, five pairs of MEMS are implemented for each cell which generates 2^5 discrete states in order to achieve a good

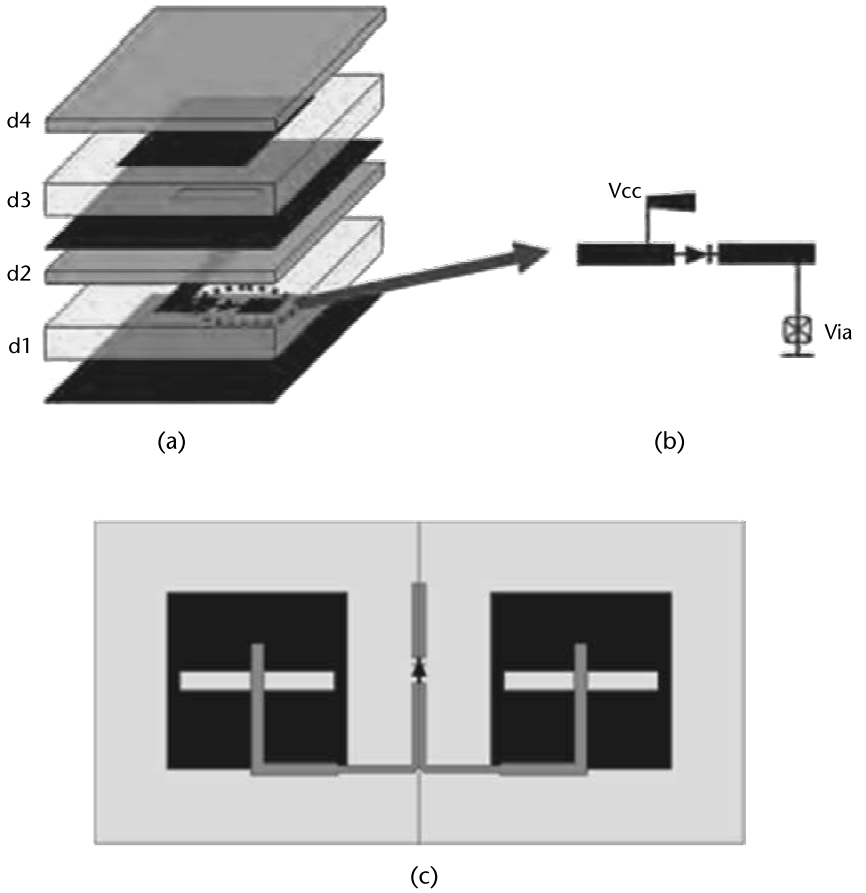

Figure 9.15 Phase shifter. (a) Expanded view of the individual element based on a patch aperture-coupled to a delay line controlled by a PIN diode. (b) Series configuration of a PIN diode. (c) Top view of two gathered elements controlled by a common delay line with a PIN diode. (© 2010 IEEE. *From:* [22]. Reprinted with permission.)

phase resolution. The 360° phase variation can be achieved using these 32 different states. The redundancy in the phase states can be exploited to mitigate frequency dispersion in large reflectarrays, which is tantamount to a wider bandwidth. A method was introduced in Chapter 5 to analyze such a complex configuration and reduce the simulation time. In this method first a full-wave simulation of the cell is made using commercial software such as HFSS where the MEMS are represented by internal ports. The overall structure with MEMS elements then will be analysed by the connection of the obtained multiport scattering matrix with impedances representing the MEMS as depicted in Figure 9.17.

Another technique to design a tunable reflectarray element using MEMS is introduced in [30]. This technique is used when the reflectarray elements are illuminated with a CP feed. The phase of scattered wave is controlled by rotating the cell element. This can be done by switching the status of the switches in Figure 9.18 to actually display a rotated element to the incoming wave.

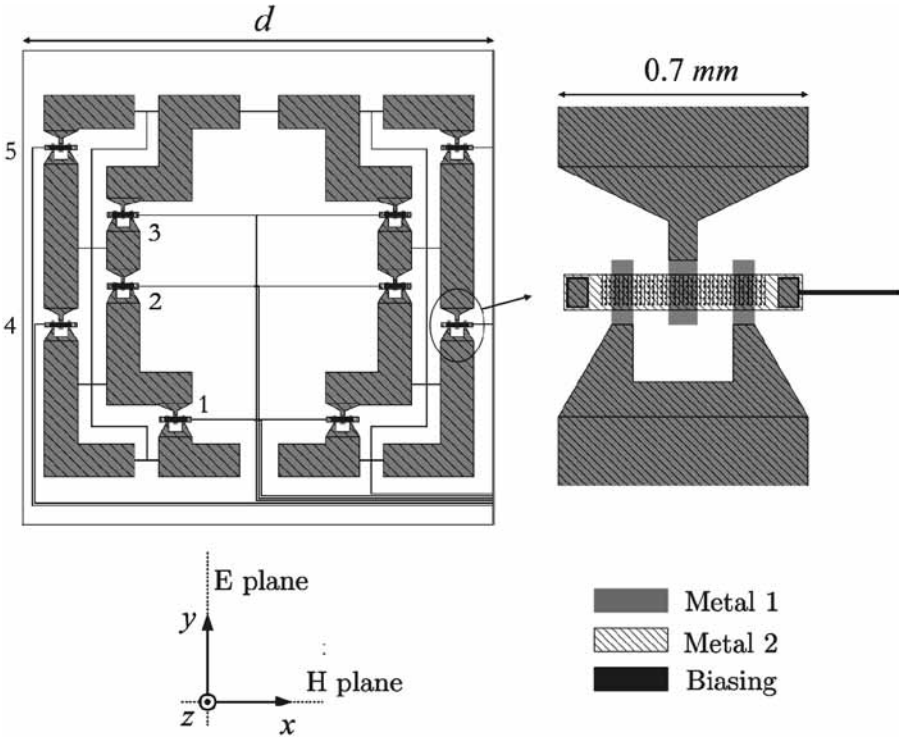

Figure 9.16 Double cross loop reflectarray reconfigurable cell element with MEMS (© 2008 IEEE. *From:* [28]. Reprinted with permission.)

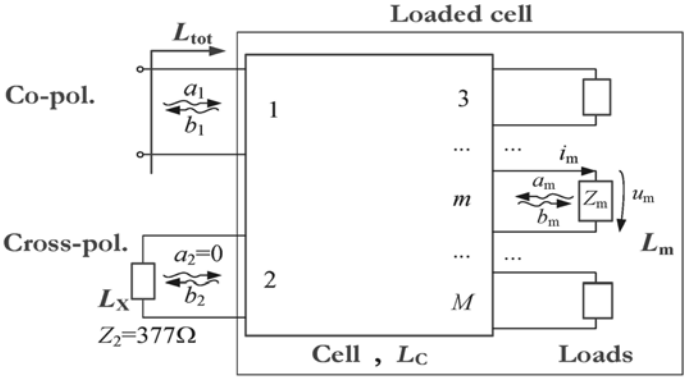

Figure 9.17 Scattering network representing a reflectarray cell loaded by variable MEMS elements. (© 2010 IEEE. *From:* [29]. Reprinted with permission.)

Adding tunability to reflectarray element using varactor diodes is another way of designing reconfigurable reflectarray elements [31]. A tunable reflectarray with patch as radiator element was introduced in [32]. In this method the radiating edge of the patch was loaded with a varactor diode as shown in Figure 9.19 to change its electrical length. In this technique continuous phase variation can be achieved by varying the dc bias of the varactor diode.

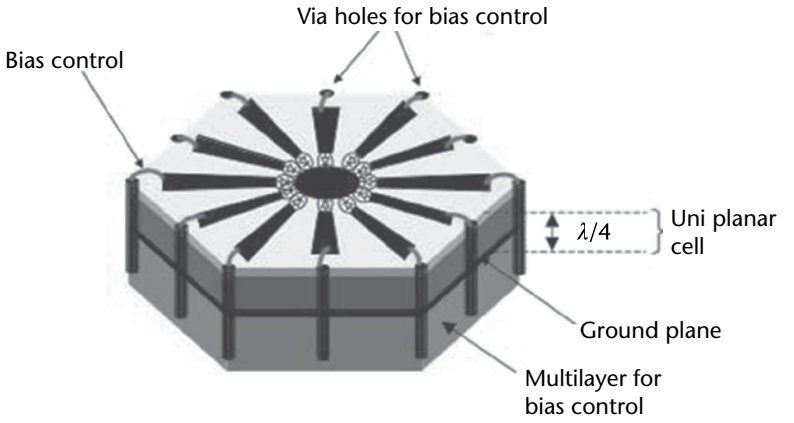

Figure 9.18 Reconfigurable reflectarray cell element using MEMS with CP excitation. (© 2003 IEEE. *From:* [30]. Reprinted with permission.)

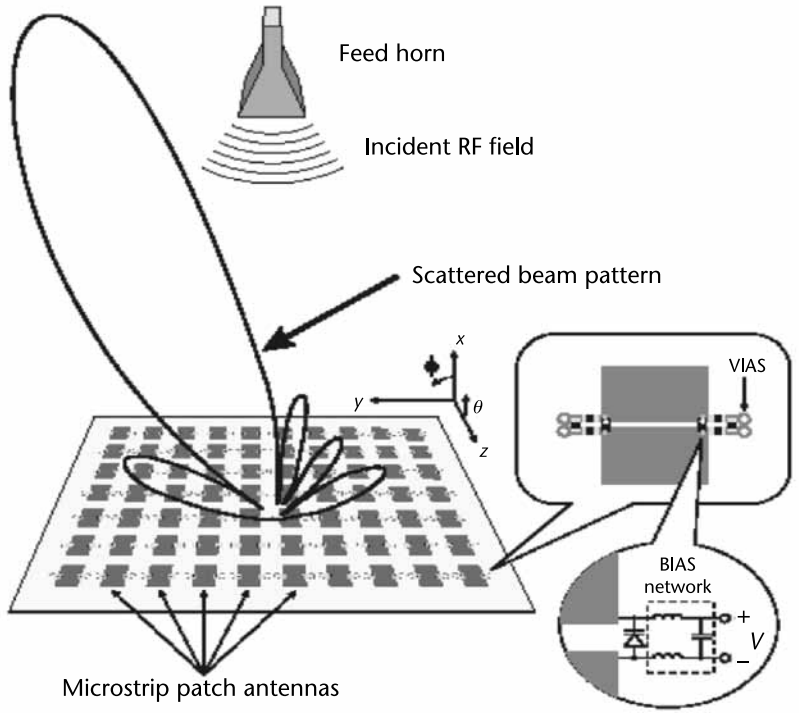

Figure 9.19 Electrically tunable reflectarray elements using varactor diodes. (© 2005 IEEE. *From:* [32]. Reprinted with permission.)

Varactor diodes can also be used as a load to a delay line of patches that were aperture-coupled to a microstrip delay line as explained in [33] and shown in Figure 9.20. However, a combination of PIN and varactor diodes was used in a single cross-loop element [34] to enhance the phase variation of the tunable element. Loss is the main issue in tunable reflectarray elements with varactor diodes. Recently, MEMS elements have been developed to design a variable capacitor which can be used as an alternative for varactor diodes [35]. The loss of the MEMS is much

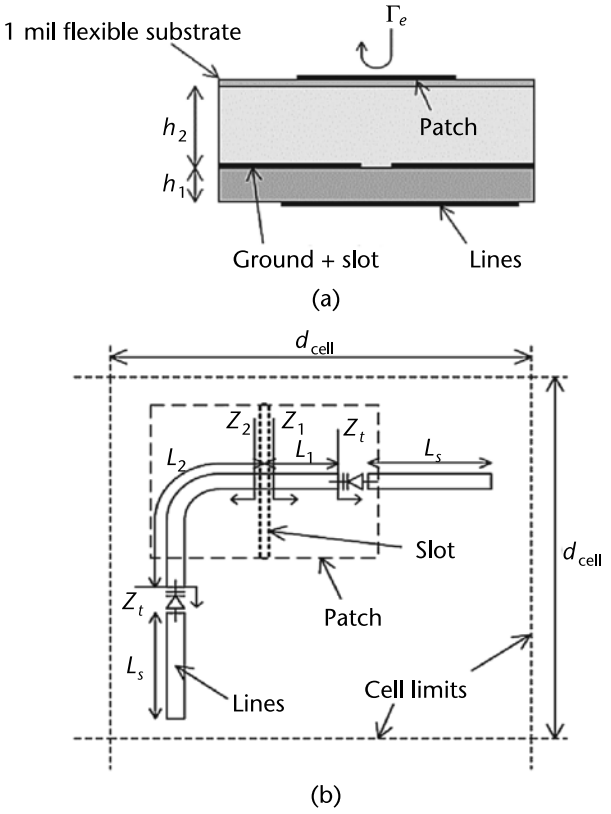

Figure 9.20 Tunable reflectarray element using varactor diode: (a) side view and (b) bottom view. (© 2007 IEEE. *From:* [33]. Reprinted with permission.)

lower than varactor diode although their reliability is still a major impediment to their further application in scanned/steered beam reflectarray.

9.5 Dual Reflectarray Antenna for Beam-Scanning Application

Dual reflector antenna with reflectarray as subreflector and parabolic dish or reflectarray as main reflector has been used in many papers for beam-scanning applications [36, 37]. The phase on the aperture of reflectarray can be controlled dynamically by using the tunable elements. The reduced size of the subreflector translates in a reduced number of required tunable cells. This configuration can be used when a beam scanning with limited angular range is required.

A dual reflectarray antenna made of a passive main reflectarray and a reconfigurable subreflectarray is introduced in [38].The reconfigurable elements are based on switched delay lines aperture coupled to square patches, that can be implemented by using either pin diodes or MEMS as was explained in the previous sections. The beam scanning can be provided by imposing a phase mask into subreflectarray to emulate the optics corresponding to different virtual foci associated to each beam direction as shown in Figure 9.21. By varying the progressive phase distribution on the subreflectarray, the beam is steered from –8° to 5° with practically no distortion on the radiation patterns, as shown in Figure 9.22.

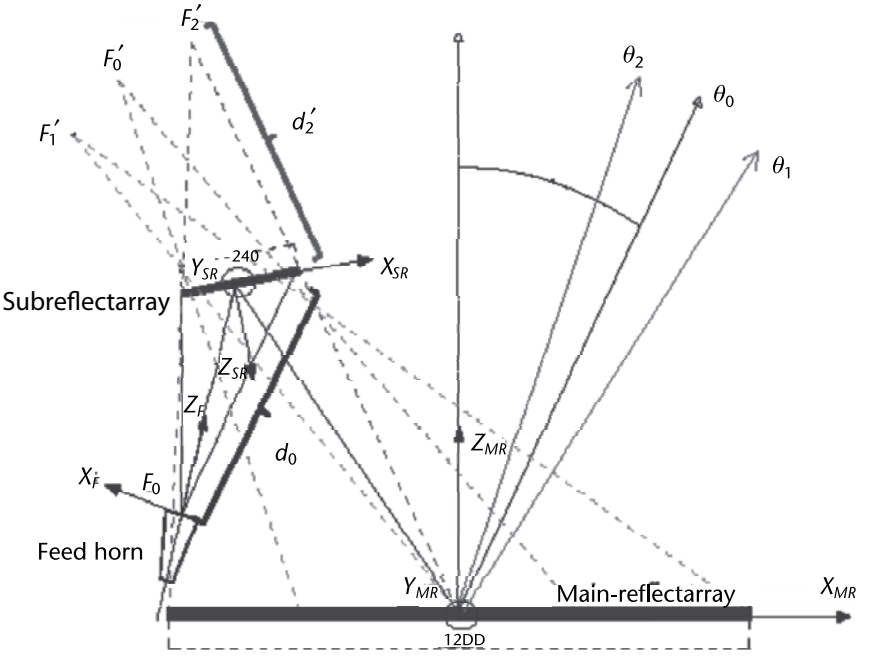

Figure 9.21 A view of a dual reflectarray with beam scanning capability. (© 2012 IEEE. *From:* [38]. Reprinted with permission.)

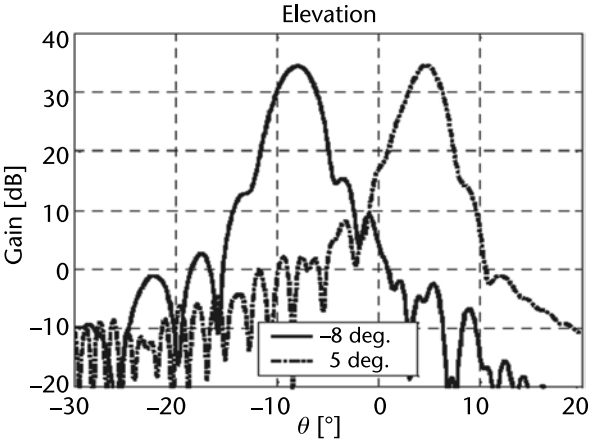

Figure 9.22 Radiation patterns for the ideal phase distribution at 12 GHz (beam scan –8°, 5°) in elevation (XZ plane). (© 2012 IEEE. *From:* [38]. Reprinted with permission.)

References

[1] Nesic, A., et al., "Antenna Solution for Future Communication Devices in mm-Wave Range," *Microwave Review*, December 2001, pp. 9–17.

[2] Mailloux, R. J., *Phased Array Antenna Handbook*, Norwood, MA: Artech House, 1994.

[3] Hum, S. V., M. Okoniewski, and R. J. Davies, "Realizing an Electronically Tunable Reflectarray Using Varactor Diode-Tuned Elements," *IEEE Microwave and Wireless Components Letters*, Vol. 15, No. 6, June 2005, pp. 422–424.

[4] Legay, H., et al., "A Steerable Reflectarray Antenna with MEMS Controls," *IEEE International Symposium on Phased Array Systems and Technology*, 2003, pp. 494–499.

[5] Fusco, V. F., "Mechanical Beam Scanning Reflectarray," *IEEE Transactions on Antennas and Propagation*, Vol. 53, 2005, pp. 3842–3844.

[6] Huang, J., "Beam Scanning Reflectarray with Circular Polarization," U.S. patent 6081234, June 27, 2000.

[7] Gabria, L., et al., "Active Reflectors: Possible Solutions Based on Reflectarrays and Fresnel Reflectors," *International Journal of Antenna and Propagation*, Volume 2009, 2009, Article ID 653952.

[8] J. Gutiérrez-Ríos and J. Vassal'lo, "Fresnel Zone Plate Reflectors Simulation and Radiation Diagram Analysis," *Proceedings of the 3rd COST 284 Workshop on Innovative Antennas*, Budapest, Hungary, April 2003, pp. 1–4.

[9] Chaharmir, M. R., et al., "Mechanically Controlled Reflectarray Antenna for Beam Switching and Beam Shaping in Millimeter Wave Applications," *Electronics Letters,* Vol. 39, No. 7, YEAR??, pp. 591–592.

[10] Chaharmir, M. R., et al., "Cylindrical Multilayer Transmitarray Antenna," *International URSI Commission B, Electromagnetic Theory Symposium (EMTS),* July 2007, Ottawa, ON, Canada.

[11] Webb, G. W., et al., "Optically Controlled Millimeter Wave Antenna," *Microwave Photonics*, 1999, pp. 275–278.

[12] Nishimura, K., and M. Tsutsumi, "Scattering of Millimeter Waves by Metallic Strip Gratings on an Optically Plasma-Induced Semiconductor Slab," *IEEE Transactions on Microwave Theory and Techniques*, Vol. 44, No. 12, December 1996.

[13] Chaharmir, M. R., et al., "Novel Photonically-Controlled Reflectarray Antenna," *IEEE Transactions on Antennas and Propagation*, Vol. 54, No. 4, April 2006, pp. 1134–1141.

[14] Wang, Z. Y., et al., "A New Approach to Highly Electrooptically Active Materials Using Cross-Linkable Hyperbranched Chromophore-Containing Oligomeres as a Macromolecular Dopant," *J. Am. Chem. Soc.*, Vol. 127, 2005, p. 2060.

[15] Chaharmir, M. R., et al., "Application of Waveguide Technology for the Characterization of Photoconductivity of Poly(9-Vinylcarbozole) for Millimeter-Wave Applications," *ANTEM 2005*, Saint-Malo, France, 2005, pp. 232–233.

[16] Weil, C., G. Lussem, and R. Jakoby, "Tunable Invert Microstrip Phase Shifter Device Using Nematic Liquid Crystals," *IEEE MTT-S Intl. Microwave Symposium*, Seattle, WA, June 2002, pp. 367–370.

[17] Hu, W., et al., "Integrated Liquid Crystal Phase Shifter for Reflectarray Antennas," *Loughborough Antennas and Propagation Conference (LAPC)*, Loughborough, United Kingdom, April 2006.

[18] Hu, W., et al., "Design and Measurement of Reconfigurable Millimeter Wave Reflectarray Cells with Nematic Liquid Crystal," *IEEE Transactions on Antennas and Propagation*, Vol. 56, No. 10, October 2008, pp. 3112–3117.

[19] Sievenpiper, D. F., et al., "Two-Dimensional Beam Steering Using an Electrically Tunable Impedance Surface," *IEEE Transactions on Antennas and Propagation*, Vol. 51, No. 10, Part 1, October 2003 pp. 2713–2722

[20] Sorrentino, R., "Recent Advances on Millimetre Wave Reconfigurable Reflectarrays," *EUCAP 2009*, 2009, pp. 2527–2531.

[21] Kamoda, H., et al., "60-GHz Electrically Reconfigurable Reflectarray Using p-i-n Diode," *International Microwave Symposium,* 2009, pp. 1177–1180.

[22] Carrasco, E., M. Barba, and J. A. Encinar, "Electronically Switchable-Beam Reflectarray Antenna," *EUCAP 2010*, Barcelona, Spain, 2010.

[23] Sorrentino, R., "MEMS-Based Reconfigurable Reflectarrays," *EUCAP 2007*, , Edinburgh, UK, November 2007.

[24] Carrasco, E., M. Barba, and J. A. Encinar, "Switchable-Beam Reflectarray with Aperiodic-Gathered Elements Based on PIN Diodes," *Proceeding of Antennas and Propagation Conference (LAPC)*, 2010 Loughborough.

[25] Legay, H., et al., "MEMS Controlled Phase Shift Elements for a Linear Polarized Reflectarray," *28th ESA Antenna Workshop on Satellite Antenna Technology, ESTEC*, Noordwijk, the Netherlands, May 31–June 3, 2005.

[26] Moghadas, H., et al., "Dual-Band MEMS-Tunable Slotted-Cross Reflective Unit Cell with Orthogonal Polarization," *Proceedings of International IEEE Symposium on Antennas and Propagation,* 2012.

[27] Legay, H., et al., "MEMS Controlled Phase-Shift Elements for a Linear Polarised Reflectarray," *28th ESA Antenna Technol. Space Antenna Syst. Technol. Workshop*, Noordwijk, the Netherlands, June 3, 2005, pp. 449–454.

[28] Perruisseau-Carrier, J., and A. Skrivervik, "Monolithic MEMS-Based Reflectarray Cell Digitally Reconfigurable over a 360° Phase Range," *IEEE Antennas and Wireless Propagation Letters,* Vol. 7, 2008, pp. 138–141.

[29] Perruisseau-Carrier, J., E. Girard, and H. Legay, "Analysis of a Reconfigurable Reflectarray Cell Comprising a Multitude of MEMS Control Elements," *EUCAP 2010*, Barcelona, Spain, 2010.

[30] Legay, H., et al., "A Steerable Reflectarray Antenna with MEMS Controls," *IEEE International Symposium on Phased Array Systems and Technology*, 2003, pp. 494–499.

[31] Hum, S. V., M. Okoniewski, and R. J. Davies, "Realizing an Electronically Tunable Reflectarray Using Varactor Diode-Tuned Elements," *IEEE Microwave and Wireless Components Letters*, Vol. 15, No. 6, June 2005, pp. 422–424.

[32] Hum, S. V., M. Okoniewski, and R. J. Davies, "An Evolvable Antenna Platform Based on Reconfigurable Reflectarrays," *NASA/DoD Conference on Evolvable Hardware Proceedings*, June 29–July 1, 2005, pp. 139–146.

[33] Riel, M., and J. J. Laurin, "Design of an Electronically Beam Scanning Reflectarray Using Aperture-Coupled Elements," *IEEE Transactions on Antennas and Propagation*, Vol. 55, No. 5, May 2007, pp. 1260–1266.

[34] Perruisseau-Carrier, J., "Dual-Polarized and Polarization-Flexible Reflective Cells with Dynamic Phase Control," *IEEE Transactions on Antennas and Propagation*, Vol. 58, No. 5, May 2010, pp. 1494–1502.

[35] Rajagopalan, H., Y. Rahmat-Samii, and W. A. Imbriale, "RF MEMS Actuated Reconfigurable Reflectarray Patch-Slot Element," *IEEE Transactions on Antennas and Propagation*, Vol. 56, No. 12, December 2010, pp. 3689–3698.

[36] Arrebola, M., et al., "94 GHZ Beam Scanning Dual-Reflector Antenna with a Sub-Reflectarray," *30th ESA Antenna Workshop*, May 2008.

[37] Rodriguez-Alvarez, J., et al., "Bifocal Antenna Based on Dual-Reflectarray Dual-Offset Configuration," *EUCAP 2012*, 2012, pp. 2348–2352.

[38] Tiendal, C., et al., "Design of Dual-Reflectarray Antenna for Beam Scanning," *Journal of Wireless Networking and Communications*, 2012, pp. 9–14.

CHAPTER 10

Fabrication Technologies

10.1 Outline of Reflectarray Fabrication Technologies

One of the greatest advantages of reflectarray technology resides in the use of straightforward fabrication techniques such as chemical etching [1]. The ubiquitous use of chemical etching for PCB manufacturing allows reflectarray fabrication to exploit an already well establish and very mature manufacturing process. That being said, PCBs most often operate in the subgigahertz frequency regime where etching tolerances and features sizes are appreciably large. Chemically etched reflectarrays are naturally suited for operating frequencies such as X-band (8–12 GHz), Ku-band (12–18 GHz), and Ka-band (26.5–40 GHz). Additionally, emerging bands such as V-bands (50–75 GHz) can exploit reflectarray technology as well. At these higher frequencies, the wavelength is short and hence the reflectarray elements are necessarily physically small. The consequence is that the required feature sizes (e.g., dimensions of patch elements, width of loops, and so on) become quite small so as to flirt with the limitations of chemical etching. Typical minimum feature sizes of chemical etching reside around 0.2 mm, while more accurate (and substantially more costly) techniques can manage 0.1-mm and even 0.05-mm feature sizes. Ultimately, it will be determined by the accuracy of the photomask and hence the resource providing the printing service.

An emerging fabrication technique includes routing (or milling). The approach can be summarized as simply removing the unwanted copper using a very high-speed drill. The accuracies are determined by both the speed (revolutions per minute, RPM) of the drill, the size of the drill bit, and the rigidity of the substrate involved. Slower drills (at a much lower cost) can be used effectively on firmer substrates such as FR4 while softer microwave-friendly substrates, such as those that are Teflon-based, require faster RPMs to successfully remove copper and not substrate. Feature sizes as small as 0.1 mm can be obtained, as discussed in [2].

Another fabrication technique that is subtractive (along with chemical and milling) is laser etching [3]. A laser is used to vaporize the unwanted copper cladding from the surface of the substrate. Once again, care must be taken to ensure the substrate is not removed as well, nor damaged during manufacturing. Laser etching offers minimum feature sizes as low as 0.025 mm, exceeding the performance of

the chemical and milling approaches. That being said, as the technology matures, finer feature sizes are expected.

Lastly, another emerging fabrication technique that is additive rather than subtractive involves inkjet printing [4]. As the name would suggest, inkjet printing involves the use of a printer and nozzle whereby metallic (or possibly dielectric) inks are deposited and patterned on a substrate. This technique offers possible cost savings, especially for large-volume fabrication, but also opens up many interesting possibilities involving the mixing of dielectric and metal inks and possibly the in situ printing of active devices. The minimum feature sizes using inkjet printing is variably dependent on the printer, ink, and substrate used, but generally speaking feature sizes of 0.050 mm are consistently possible with 0.010 mm a reality as the technology matures.

10.2 Element Performance and Minimum Feature Size

10.2.1 Traditional Resonant Elements

In this section, we consider the traditional self-resonant reflectarray element: the patch. By varying the size of the patch, the required reflection phase can be obtained for the reflectarray design. However, the question of whether the physical sizes of the elements and the smallest required feature size remains unaddressed. As discussed in previous chapters, the majority of the patch element's valuable behavior occurs for medium sizes of the patch relative to the element lattice. At the very smallest physical size, the patch offer negligible phase variation, and as such is not required to operate in these regimes. The consequence is that the feature size of the patch element is only limiting in terms of the lattice size of the element. The resonant patch typically uses a half-wavelength lattice size so the minimum feature size is a small fraction of the aforesaid lattice size (e.g., 25% of the lattice size, or $\lambda/8$). In such a scenario, the minimum feature sizes of 0.2 mm, 0.1 mm, and 0.05 mm correspond to feasible reflectarray operating frequencies of 187.5, 375, and 750 GHz, respectively. This does not take into account the etching tolerances of the fabrication process, which will be discussed in the Section 10.3. Nevertheless, it strongly supports the notion that reflectarrays can be fabricated using conventional chemical etching techniques into the subterahertz regime. Note that if laser etching or very fine printed electronics technology is used, one should be capable of pushing the reflectarray operation into the terahertz regime [5].

10.2.2 Subwavelength Elements

Subwavelength elements offer numerous advantages as discussed in previous chapters. One possible disadvantage of subwavelength elements can be the physically smaller size of the elements and hence the physically smaller minimum feature sizes. A reflectarray design consisting of subwavelength patch elements residing within a $\lambda/6$ lattice requires a minimum patch size of $\lambda/24$ (the smallest patch size to obtain a full phase range). Moreover, as evidenced from [6], the gap width between adjacent patches must be as small as $\lambda/700$ in order to generate sufficient capacitance between patches. For such small gap sizes, the highest operating frequencies for

0.2 mm, 0.1 mm, 0.05 mm, and 0.025 mm are 2.15, 4.30, 8.57, and 17.14 GHz. This immediately suggests the need for a larger lattice size (which runs contrary to the goal of subwavelength elements) should one wish to operate at much higher frequencies. This assumes one remains with a patch as the element of choice for subwavelength behavior.

However, it was shown [7] that subwavelength loops offered superior performance over that of the subwavelength patches, requiring gap sizes and loop widths as small as $\lambda/100$ for lattice sizes of $\lambda/6$. For feature sizes of 0.2 mm, 0.1 mm, 0.05 mm, and 0.025 mm, this corresponds to substantially higher operating frequencies of 15, 30, 60, and 120 GHz, respectively. Through the use of novel elements beyond that of the subwavelength loop, it is estimated that subwavelength reflectarrays operating at 300 GHz are feasible using fabrication techniques that have the smallest minimum feature sizes. If 10-μm feature sizes become a reality using inkjet printing (i.e., printed electronics), then even basic subwavelength loops can be used up to 300 GHz. Judicious selection of reflectarray elements can mitigate the high-frequency restrictions imposed by electromagnetics.

10.3 The Impact of Etching Tolerance on Reflectarray Performance

Etching tolerance and fabrication repeatability are also important aspects for reflectarray fabrication. In particular, we consider the ability of the manufacturing process to maintain a particular consistent feature size from prototype to prototype. For example, a loop element with a line width of 0.2 mm can readily be fabricated using any modern technology, but will it consistently remain 0.2 mm for all fabricated designs? Naturally, no design process produces identical designs in every fabrication run and hence it is worthwhile identifying reflectarray elements that are immune to small changes in feature sizes.

10.3.1 Narrowband Resonant Elements

In this example, we consider a reflectarray design with configuration identical to that of Section 7.5. The design consists of resonant patch elements in a 12-mm lattice. The lengths are selected based on the phase of the ubiquitous S-curve. This particular patch element has a phase range of 300°, leading to at most 30° of phase error in particular regions of the reflectarray. The phase error over the aperture of the reflectarray is shown in Figure 10.1. We then introduce random errors in patch length on the order of 0.02 mm, which represents an excellent etching technology with very low etching tolerance and a high degree of repeatability. The resulting phase error is shown in Figure 10.2 where the majority of discernible phase error due to etching errors is found around the center of the reflectarray. The peak phase error amounts to 10° in a very small region, leading to a meager gain drop of 0.025 dB, which is likely inconsequential in most antenna applications. Running thousands of simulated reflectarray designs, each with randomly introduced etching errors of at most 0.02 mm (with variation being uniformly distributed between –0.02 mm and +0.02 mm), a maximum gain drop of 0.035 dB was obtained, indicating that in the worst case, the majority of fabrication processes will lead to negligible gain drops due to etching errors for elements types such as patches in the Ku-band.

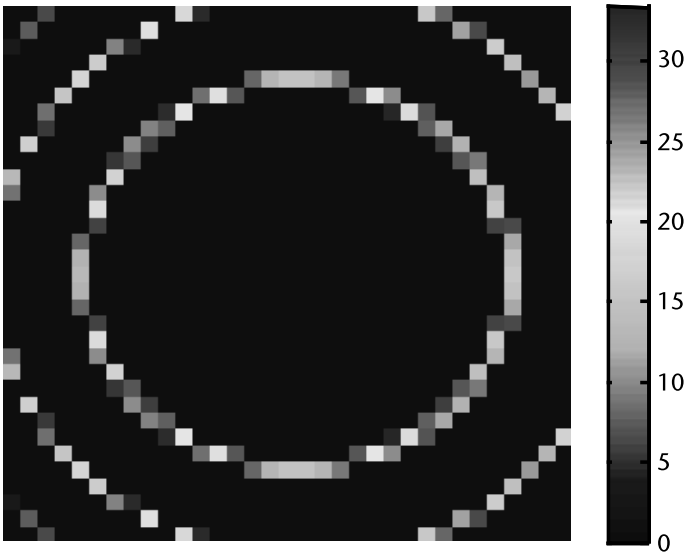

Figure 10.1 Phase error for reflectarray using patch element.

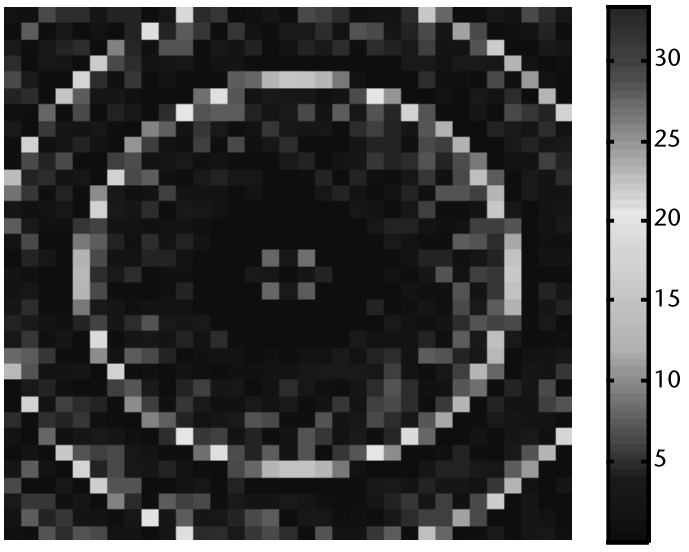

Figure 10.2 Phase error for reflectarray using patch element with uniform random variations in element length introduced, post design to simulate fabrication errors (0.02-mm etching variation).

Lower frequencies will therefore be less susceptible to etching errors, while higher frequencies will be more susceptible, though the maximum gain drop remains quite low, even into the subterahertz regime, assuming that similar etching tolerances are considered.

If a very low-cost fabrication technique were required, the reflectarray gain would suffer as a consequence. Consider a fabrication technique that would allow up to 0.2 mm of etching variation. This is, of course, an outlying scenario as most

fabrication techniques have minimum feature sizes on this order and hence the tolerance must necessarily be smaller than 0.2 mm. Nevertheless, it is worthwhile investigating the consequences of a fabrication process with very low repeatability. For such a scenario, the same reflectarray exhibits an average gain drop of 3.8 dB and a peak gain drop of 4.3 dB. This is an unacceptable gain drop in mostly any antenna design. An example of the phase error associated with a 3.8-dB gain drop is shown in Figure 10.3.

10.3.2 Wideband Resonant Elements

If we now consider a wideband element such as the double cross loop (discussed throughout the text, such as in Chapter 6), we expect a design resilient to unexpected small variations in length. First, the reflectarray has no phase error if etched properly because the element provides a full 360° of phase range. Wideband behavior tends to translate into insensitivity in varying element dimensions. For the double cross loop, an etching variation of 0.02 mm leads to less than a maximum of 2° phase error throughout the reflectarray surface (compare this to 10° phase error for the patch element). If the length variation were increased to 0.2 mm, the resulting average gain drop is approximately 0.3 dB, substantially better than the equivalently error-prone patch reflectarray. Examples of the reflection phase error on the reflectarray surface comprised of double cross loops for 0.02-mm and 0.2-mm etching variation are shown in Figures 10.4 and 10.5, respectively. For identical etching tolerance, a wideband reflectarray appears to provide resilience in terms of electrical performance over that of a narrowband reflectarray. Even in scenarios where narrowband behavior offers sufficient performance, the wideband structure will provide some measure of additional margin in fabrication tolerance.

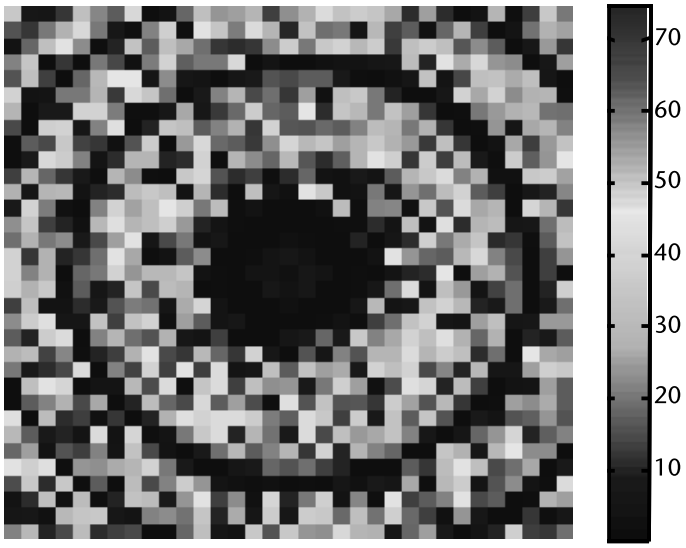

Figure 10.3 Phase error for reflectarray using patch element with uniform random variations in element length introduced, post design to simulate fabrication errors (0.2-mm etching variation).

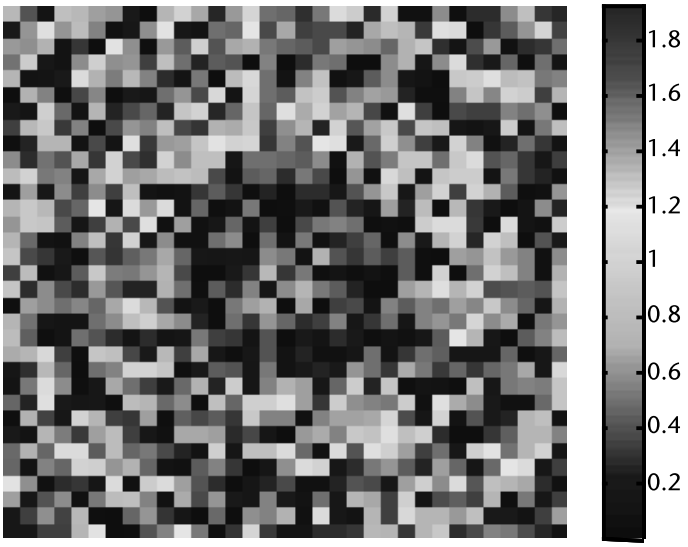

Figure 10.4 Phase error for reflectarray using a double cross-loop element with uniform random variations in element length introduced, post-design, to simulate fabrication errors (0.02-mm etching variation).

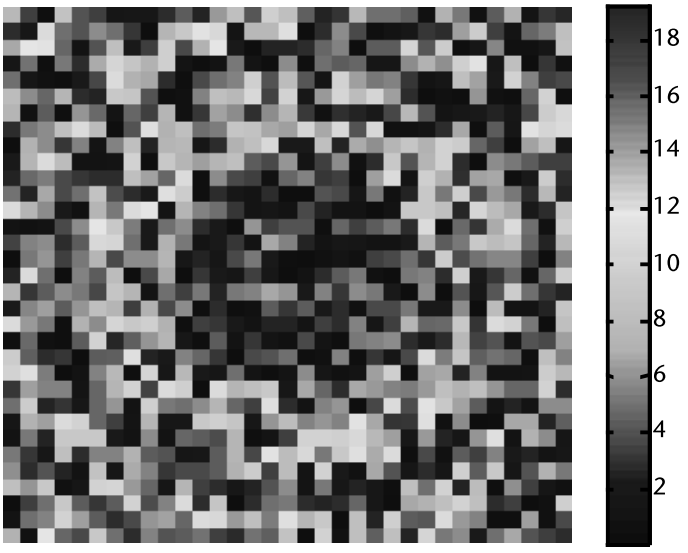

Figure 10.5 Phase error for reflectarray using double cross-loop element with uniform random variations in element length introduced, post-design, to simulate fabrication errors (0.2-mm etching variation).

10.3.3 Subwavelength Elements

Lastly, we consider a recently introduced cell element topology for reflectarrays, that of the subwavelength element. Generally speaking, subwavelength elements provide wideband behavior and should therefore provide improved immunity to electrical performance variation due to etching errors. However, it should be noted that subwavelength elements reside within a physically smaller lattice as compared to their resonant element counterparts. The consequence is that smaller variations

in physical size lead to similar phase variation as larger lattice elements. This implies that subwavelength elements should be more sensitive to etching variation despite having wideband performance. In other words, frequency insensitivity does not always equate to insensitivity to physical change. In particular, if etching tolerances of 0.02 mm and 0.2 mm were considered one would expect maximum phase errors of 4 and 35, corresponding to gain drops of 0.065 dB and 0.95 dB, with their phase errors shown in Figures 10.6 and 10.7, respectively. The impact on

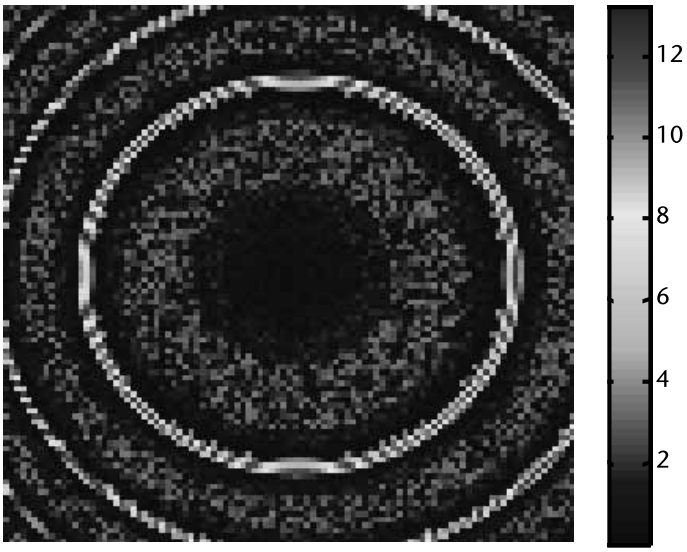

Figure 10.6 Phase error for reflectarray using subwavelength loop element with uniform random variations in element length introduced, post-design, to simulate fabrication errors (0.02-mm etching variation).

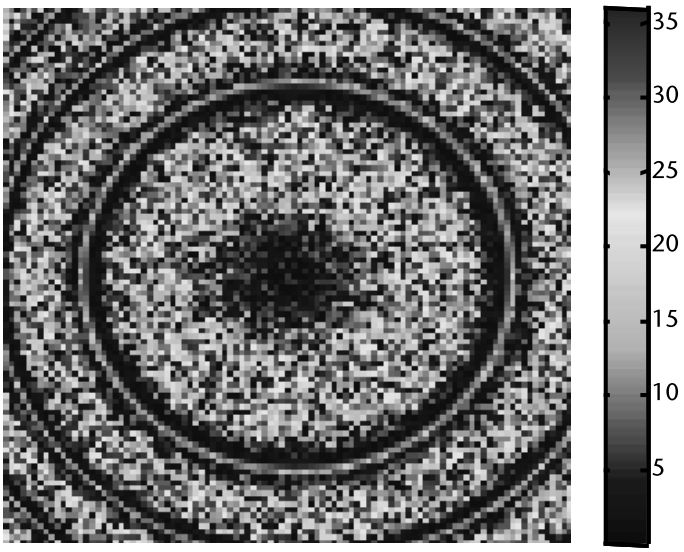

Figure 10.7 Phase error for reflectarray using subwavelength loop element with uniform random variations in element length introduced, post-design, to simulate fabrication errors (0.2-mm etching variation).

gain is substantially less than the narrowband patch element, but greater than the wideband loop element.

More detailed studies can be performed that include variation of other details such as the loop line widths and lattice sizes, all of which will obviously impact performance as etching errors are introduced. Nevertheless, it is a sound design approach to utilize wideband elements in any scenario where etching errors are expected to be considerable.

10.4 Novel Designs Employing the Sole Use of Material Routing

The most common reflectarray consists of printed elements such as patches and loops, fabricated using chemical etching. Such a design consists of a mix of materials from the metal ground plane, to the dielectric supporting substrate and finally the metal elements that have been etched on the surface of the substrate. However, reflectarray designs that consist of dielectrics-only (save for the ground plane) are possible. Additionally, it is feasible to design a reflectarray consisting only of metal with absolutely no dielectric present in the design. These design approaches can exploit milling techniques and hence do not require chemical etching nor microwave substrates. Consequently, these designs can offer advantageous cost reductions and a high degree of environmental ruggedization.

10.4.1 Dielectric-Only Reflectarrays

It should be stated from the onset that a dielectric-only reflectarray is somewhat of a misnomer in that a ground plane must be present to ensure 100% of the incident power is reflected. However, given that a ground plane can consist of a simple sheet of low-cost aluminum, with the remainder of the reflectarray consisting of dielectric, we feel that dielectric-only is a sufficient description, especially considering all of the phase correction is accomplished strictly via dielectric variations. Two major types of dielectric-only reflectarrays are possible: (1) consisting of a ground plane and bare substrate with dielectric resonator antennas (DRAs) acting as the phasing elements [8], and (2) a shaped dielectric surface that is ground plane backed [9].

The DRA-based reflectarray [8] is shown in Figure 10.8(a) while the schematic view is shown in Figure 10.8(b). The physical details of the DRA reflectarray element are shown in Figure 10.8(c) and the phase versus length curve is shown in Figure 10.8(d). The DRA reflectarray in [8] achieved a respectable 12% 1-dB gain bandwidth. Future work using LTCC as a fabrication technique would prove useful in extending this design beyond the 30-GHz operation. It is also possible to design such an antenna in the reverse using dielectric holes (that still act as resonant elements) rather than dielectric blocks [9]. This has the advantage of being fabricated using a milling technique rather than pick and place as is the case of the DRA reflectarray (though milling can be used to design the DRA reflectarray as well).

The second class of dielectric-only reflectarrays consists of what is effectively a Fresnel zone reflector, or a ground plane-backed Fresnel lens. This concept is hundreds of years old, but was recently viewed from the reflectarray perspective in [10]. A typical layout of such a reflectarray is shown in Figure 10.9. Generally speaking, such a reflectarray is more difficult to fabricate and have a larger profile

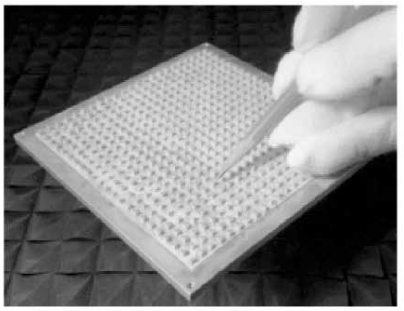

(a)

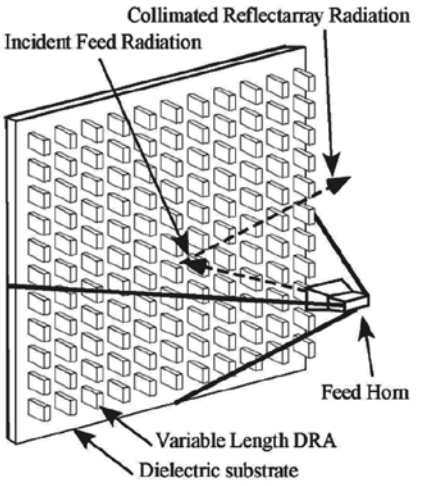

(b)

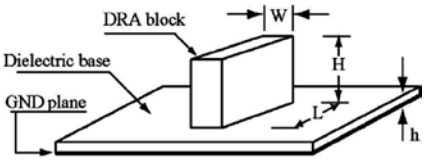

(c)

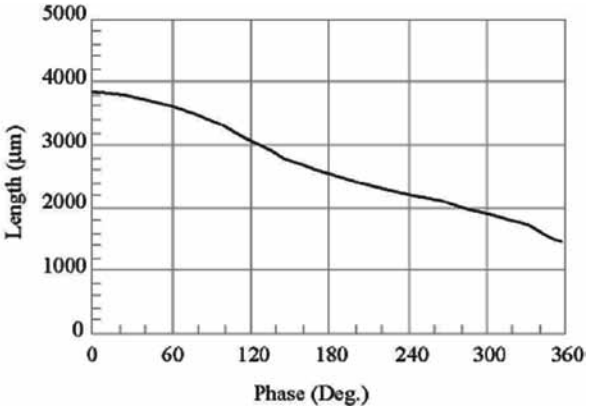

(d)

Figure 10.8 Dielectric resonator antenna (DRA) based reflectarray (a) photograph, (b) reflectarray schematic view, (c) DRA physical details, and (d) reflection phase versus length of DRA reflectarray element. (© 2000 IEEE. *From:* [8].)

than the block or cavity method described previously, although the proposed design in [10] can be synthesized using transmission line theory (simulations of the reflection properties of the dielectric are in fact unnecessary).

10.4.2 Metal-Only Reflectarrays

In a metal-only reflectarray, the entire antenna structure is constructed using metal, with the only dielectric being the surrounding media. Two such designs are possible, one consisting of a perforated metal plate, with the perforations (grooves, holes, or cavities) acting as tunable resonant cavity elements [11] and alternatively a metal surface with varying heights to act as a Fresnel reflector (which is to a solid reflector what a Fresnel lens is to a solid dielectric lens).

The metal-only reflectarray discussed in [11] consisted of a collection of metal rectangular grooves whose dimensions were varied to provide variable reflection phase, as shown in Figure 10.10(a). A fairly unique property of this design technique was the fact that the reflection phase of the variable dimension groove was

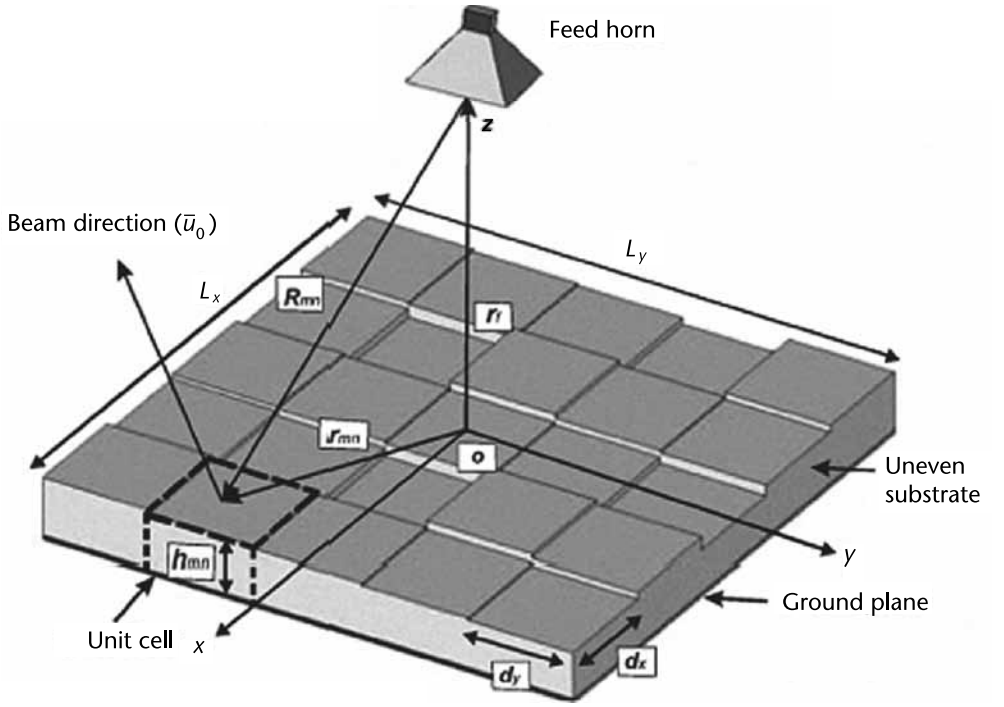

Figure 10.9 Example of an uneven dielectric-only reflectarray (fundamentally a Fresnel zone reflector, or ground plane-backed Fresnel lens). (© 2010 IEEE. *From:* [10].)

derived in a closed form. That is to say, the reflection was determined exactly rather than through electromagnetic simulation. The authors further used computational techniques to better account for the presence of nonuniform collections of elements, which differs from the assumed uniform infinite periodicity. Assuming the minimum feature sizes can be milled into the solid piece of metal, this form of metal-only reflectarray offers an ideal candidate for high aperture efficiency reflectarrays in the subterahertz frequency range. The resulting reflectarray, designed for operation at a fairly high frequency of 90 GHz, is shown in Figure 10.10(b).

It is also possible to design a metal-only reflectarray that is the reflecting analog to the Fresnel lens. One simply implements a solid reflector, which has a constant curvature to its reflecting surface, that has its curvature sectioned every 360°, just like the ubiquitous Fresnel lens. While it remains metal-only and very simplistic in its design, it is likely more complicated in terms of fabrication and is far more bulky than the metal-only design consisting of metal holes from [11].

10.5 Inkjet-Printed Reflectarrays

In this section we discuss the fabrication of a reflectarray using printed electronics. Printed electronics hold promise for cost reduction as well as minimum feature sizes well below that of conventional chemical etching techniques.

In our example of a reflectarray design, a single-clad substrate is used as a support and a very thin bare substrate is printed on and directly bonded to the supporting substrate [12]. A reflectarray comprised of subwavelength loops is then

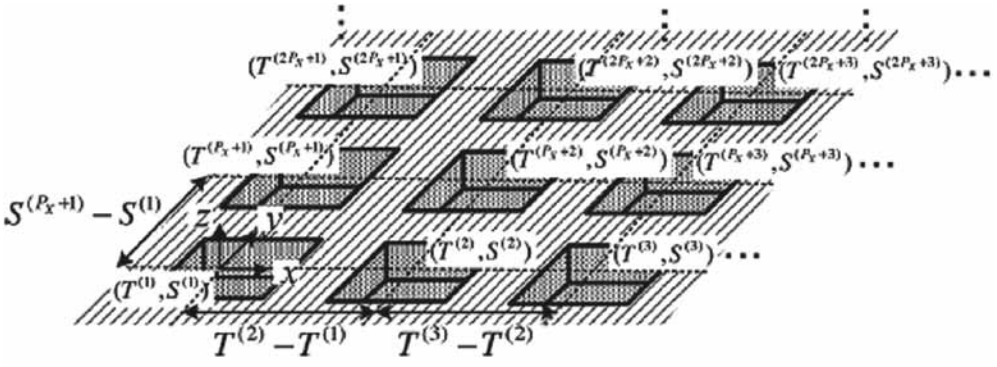

(a)

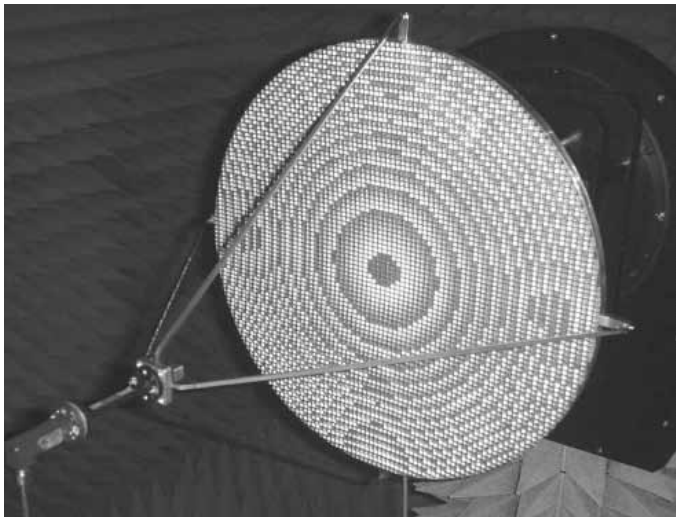

(b)

Figure 10.10 Example of a metal-only reflectarray with the (a) metal grooves (or cavities) and (b) a photograph of the metal-only reflectarray. (© 2011 IEEE. *From:* [11].)

designed, with the layout shown in Figure 10.11(a) and a photograph of the fabricated array shown in Figure 10.11(b). The reflectarray pattern was printed using a Fujifilm Dimatrix DMP-2831 printer using Novacentrix JS-B25HV silver ink. The simulated reflection phase and amplitude are shown in Figures 10.11(c) and 10.11(d) for the cases of PEC and silver ink loops, respectively. All designs were intended for operation at 30 GHz (Ka-band), with measured performance of the reflectarray nearing 55% aperture efficiency at center frequency.

What is of particular importance in this discourse is the fact that all loops in the array had line thicknesses of 0.1 mm, nearing the limits of minimum feature size when using chemical etching. It is expected that inkjet printing accuracies will continue to improve and allow for finer features, allowing one to extend well beyond the 30-GHz operation into the subterahertz regime. There is also significant promise for integrating dielectric and semiconductor inks, leading to the fabrication of active reflectarrays using a single self-contained fabrication process.

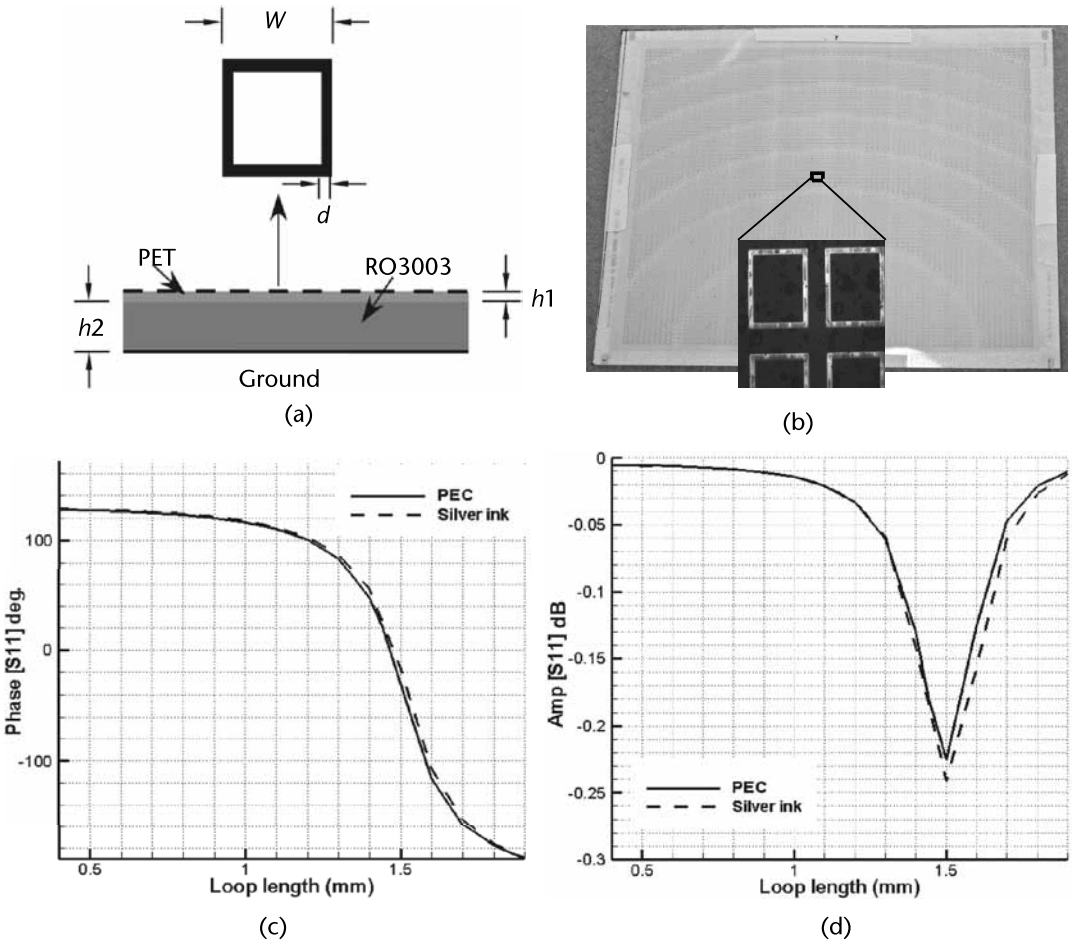

Figure 10.11 Printed electronics subwavelength loop-based reflectarray with (a) layout with h1 = 0.14 mm, h2 = 0.51 mm, (b) photograph of reflectarray, (c) reflection phase curve, and (d) reflection amplitude curves of loop elements, for both PEC and silver ink metallization.

References

[1] Harper, C. A., *Electronic Assembly Fabrication*, New York: McGraw-Hill, 2002.

[2] Nayeri, P., F. Yang, and A. Z. Elsherbeni, "Broadband Reflectarray Antennas Using Double-Layer Subwavelength Patch Elements," *IEEE Antennas and Wireless Propagation Letters*, Vol. 9, 2010, pp. 1139–1142.

[3] Schaeffer, R. D., *Fundamentals of Laser Micromachining*, Boca Raton, FL: CRC Press, 2012.

[4] Cantatore, E., *Applications of Organic and Printed Electronics: A Technology-Enabled Revolution*, New York: Springer, 2013.

[5] Tiaoming, N., et al., "Design and Implementation of Terahertz Reflectarray," *37th International Conference on Infrared, Millimeter and Terahertz Waves (IRMMW-THz)*, September 23–28, 2012.

[6] Pozar, D. M., "Wideband Reflectarrays Using Artificial Impedance Surfaces," *Electronics Letters*, Vol. 43, No. 3, February 1, 2007, pp. 148–149.

[7] Ethier, J., M. R. Chaharmir and J. Shaker, "Reflectarray Design Comprised of Sub-Wavelength Coupled-Resonant Square Loop Elements," *Electronics Letters*, Vol. 47, No. 22, October 2011, pp. 1215–1217.

[8] Keller, M., et al., "A Ka-Band Dielectric Resonator Antenna Reflectarray," *30th European Microwave Conference*, October 2000.

[9] Abd-Elhady, M., W. Hong, and Y. Zhang, "A Ka-Band Reflectarray Implemented with a Single-Layer Perforated Dielectric Substrate," *IEEE Antennas and Wireless Propagation Letters,* Vol. 11, June 2012 pp. 600–603.

[10] Moeini-Fard, M., and M. Khalaj-Amirhosseini, "Uneven Dielectric Reflect-Array Antennas," *5th International Symposium on Telecommunications (IST),* 2010, pp. 82–86.

[11] Cho, Y. H., W. J. Byun, and M. S. Song, "High Gain Metal-Only Reflectarray Antenna Composed of Multiple Rectangular Grooves," *IEEE Transactions on Antennas and Propagation*, Vol. 59, No. 12, December 2011, pp. 4559–4568.

[12] Chaharmir, M. R., et al., "Reflectarray Design Using Printed Electronics Technology," *Electronics Letters*, Vol. 48, No. 22, Nov. 2012, pp. 1388–1389.

CHAPTER 11

Conclusion and Future Directions

Printed reflectarray has its roots in exploratory attempts to utilize a nonuniform planar array of microstrip patches to emulate a conventional reflector antenna. The technology was initially plagued by the relatively high cost of low-loss substrate and narrow bandwidth. However, significant strides were taken to overcome these shortcomings, as pointed throughout this book. At a deeper level, reflectarray is a confluence of phased array and conventional reflector technology. Its similarity to phased array arises from low gain radiators that collectively act together to synthesize a given radiation pattern while utilization of free space rather than lossy feed network distinguishes it from phased array.

As pointed out in Chapter 2, phase transformation between the phase front of the feed radiation and the desired phase front of the synthesized beam can be used to determine the phase response of reflectarray cell elements. A look-up table is used to map the required phase to some geometrical feature of the cell element. An analogous set of concepts and mathematical expressions as developed for the calculation of different efficiency figures of a conventional reflector antenna can be used to gauge the performance of a reflectarray antenna. However, care should be taken to include some additional efficiency figures that are special to a reflectarray antenna such as terms that account for dielectric or conductor loss. The possibility of achieving a wide range phase response from the reflectarray cell elements is essential for its efficient performance. General trends were mentioned in Chapter 2 in terms of the feasibility of realizing the phase range by changing the substrate thickness and permittivity.

Considering reflectarray as a quasiperiodic arrangement of a specific cell element opens up avenues for the advancement of analysis and design of such structures. New developments in the field of periodic structures (frequency selective surfaces, artificial dielectrics, and so forth) and also novel radiating elements can potentially inspire designer to contrive innovative reflectarray cell elements. For instance, general knowledge on factors that influence the bandwidth of a microstrip patch element can be used to improve the bandwidth of a reflectarray comprised of such cell elements. Similar conclusion can be drawn by focusing on FSS comprised of rectangular patches. Reduced angular sensitivity and wideband behavior of an FSS composed of loops can be specifically instructive when considering loop as a potential reflectarray cell element. Background knowledge on cell elements, periodic structures, and single radiating elements has led to a wide variety of geometries of reflectarray cell elements, as pointed out in Chapter 3. Different types

of resonant cell elements such as patch, stacked patch, slot-coupled patch, stub loaded patch, and different types of loops were introduced and techniques were presented to synthesize a given phase characteristic. Nonplanar three-dimensional reflectarray should not be skipped from such a list and a brief account of using a dielectric resonator and shorted waveguide were briefly presented as alternative cell elements. Future research on resonant elements should focus on multiresonant elements and novel methods to engineer frequency dispersion of such elements through judicious control of their resonances. Significant background knowledge in the field of filter synthesis has gone largely unnoticed in the design of reflectarray while this knowledge is instrumental in the synthesis of desired phase response of the cell element.

Subwavelength elements have been shown to be advantageous for a number of reasons, not limited to their reduced angular sensitivity, improved array discretization, low phase dispersion leading to wider bandwidth and reduced losses, array thinning, and facilitating the mosaic reflectarrays. These advantages make subwavelength elements ideal candidates for a number of reflectarray applications. Future research on subwavelength elements can involve exploiting the fact that a wide variety of element shapes have not been fully explored (e.g., the dogbone element), which can be used as dispersive elements should the need arise, while keeping some of the subwavelength elements' advantageous properties (e.g., reduced angular sensitivity). Additionally, it is expected that fragmented subwavelength elements will prove a fruitful area of exploration as they provide a fairly unrestricted look at the geometry of said subwavelength elements.

The freedom to select the cell element can be exploited to realize novel types of reflectarrays. Sensitivity of the cell element to the operating frequency and polarization has been utilized to realize multiband and/or multipolarization operation as thoroughly described in Chapter 4. Intelligent use of these features can bring about significant simplification of the feed structure. Specifically, the reflectarray can be designed so that each operating band and/or polarization corresponds to a given feed structure. Knowledge from the fields of periodic structures and radiating antenna elements were used to establish low cross coupling between elements that correspond to a given frequency band and/or polarization. Design of a reflectarray cell element was presented that simultaneously converted the linear polarization of the feed into circular polarization (CP) and collimated the beam that henceforth relieves the designer from the cumbersome and complicated task of the design and fabrication of a multiband CP feed. Replacement of the ground plane of a reflectarray by FSS was presented as another method to further enhance the flexibility multiband operation. The resulting reflectarray was transparent to out-of-band signals and reflective only in its operating band. Shaped beam reflectarray was also presented in Chapter 4 through the synthesis of the main reflectarray or subreflectarray. Reflectarray was also shown to be particularly amenable to novel applications such as power combining that is achieved by combining incident fields of multiple feeds into a given collimated beam. Reflectarray technology will prove to be specifically superior for shaped beam and special applications in the high-frequency bands that conventional mechanical methods hinder accurate fabrication of shaped reflector antennas. One of the outstanding challenges in multiband reflectarray is realization of reflectarray with dedicated feeds for Tx and Rx bands when these bands are in close proximity to each other (such as X-band).

Development of dispersion engineering technique will be specifically useful in the design of wideband shaped beam structures considering that even the conventional robust reflector technology can be handicapped by this restriction.

In Chapter 5, the presentation of relevant numerical methods for reflectarray analysis was used as an opportunity to gain a better understanding of the underlying physics of reflectarray antenna. Having understood discrete nature of scattering from a periodic structure in the form of Floquet modes raises the possibility of designing reflectarray to collimate a higher-order scattered mode [such as (0, –1) mode] rather than the direct reflection mode as is the case in conventional reflectarray structures. On the other hand, the available knowledge base on equivalent circuit for periodic structures can be used to significantly simplify design and analysis of reflectarray antennas and also inspire such innovative concepts as array thinning in a reflectarray antenna. Methods were also introduced for accurate calculation of the radiation pattern of a reflectarray antenna that were not excessively demanding in terms of CPU and memory requirements. These routines were used to identify the contribution of the each of the constituent components of a reflectarray in the formation of the radiation pattern. The infinite-from-finite numerical technique was discussed showing promise in determining unique properties of periodic structures, namely the electromagnetic differences between infinite and finite arrays. It was shown that characteristic mode theory can be used in the synthesis of reflectarrays by way of defining a computationally efficient means of obtaining reflection phase. Optimization of reflectarrays can be made quite efficient using these objective functions. Further advancement of numerical methods in the design of reflectarrays should focus on exploiting its quasi-periodic feature to obtain a reasonably accurate estimate of its radiation pattern within its operating band through utilization of what is technologically available in terms of CPU and memory. These numerical methods can be further attuned to further our understanding of the underlying physics of reflectarrays and pave the way for innovative implementations of this technology. Currently, the circuit method is specialized to subwavelength lattice reflectarray, whereas the range of this technique can be further extended to cover also resonant lattice structure to significantly reduce the computational requirements of design and analysis.

Limited bandwidth of reflectarray antennas was a major shortcoming that prevented their application when broadband operation is required. However, significant progress has been made in the recent years to circumvent this restriction. As pointed out in Chapter 6, the narrow bandwidth is caused by the element bandwidth for the case of moderate size reflectarrays, whereas spatial dispersion further aggravates this shortcoming in large reflectarrays. Both factors were presented in detail and methods were introduced to overcome these limiting factors. As a result of these efforts, reflectarray technology has been demonstrated to suit the bandwidth requirement of high gain operation at most of the more favorite and widely used bands such as X-, Ku-, and Ka-bands. Future advancement of dispersion engineering should focus on development of theoretical framework for wideband, multiband large reflectarrays by development of techniques that allow fulfillment of multiple constraints at different frequency bands using one and the same set of cell elements.

The concept of losses in reflectarrays was discussed in Chapter 7. The general conclusion was that the majority of losses stem from dielectric losses occur mainly

for elements in the vicinity of resonance. To mitigate these losses, it was shown that elements exhibiting low-frequency dispersion of reflection phase have low losses. Subwavelength elements were identified as a class of very low-dispersion (and hence low-loss) elements. A highly efficient reflectarray was designed, fabricated, and measured combining subwavelength elements and a very low-cost, lossy FR4 substrate indicating that losses can indeed be mitigated. Future work in this regard can focus on determining the theoretical implications of loss being inextricably tied to the frequency dispersion of reflection phase as well as exploring the use of alternative low-cost (but very lossy) materials.

Transmitarray antenna is the dual of a reflectarray antenna in the sense that it is transparent at its operating band and collimates the transmit signal that emanates from the feed. In other words, the phase front transformation is applied to the transmitted signal. As discussed in Chapter 8, this objective can be achieved by a cascade of periodic structures. It is to be noted that all the cell elements with same transverse coordinate on the layers are similar and the phase transformation is achieved by simultaneous variation of the size of geometrical features of these cell elements. Depending on the separation between the layers, different design methodologies were presented for the design of a transmitarray. When interlayer separation is large enough to warrant application of a cascade of S-parameters of layers, full-wave simulations of isolated single layers are used to find complex transmission coefficient of the single layer, which is later cast into a cascade of S-parameter matrices. However, when the layers are too close to each other, full-wave simulation should capture all layers. Similar to the developments in the case of reflectarray, constituent layers of the transmitarray can be populated by cell elements to accommodate multiband/multipolarization operation. The thickness of the transmitarray can be reduced significantly by enhancing the coupling between layers as performed in the case of phase-shifting surfaces. Maintenance of wideband performance in the case of transmitarray is far more complicated than reflectarray because both transmission amplitude and phase should be optimized. New developments in the case of transmitarray should focus on an efficient method to address wideband performance. Intelligent application of filter theory can be quite crucial in handling this challenge.

Reflectarray antenna are particularly amenable to the implementation of new developments in the field of electronic miniaturization and also novel techniques for the adaptive control of circuit components such liquid crystal, laser induced plasma, microelecromechanical embedded elements, and microfludic techniques. Implementation of a number of these methods was presented in Chapter 9 in order to achieve beam steering or beam switching. It was also demonstrated that the same objective can be fulfilled by devising elaborate mechanical movement of reflectarray surface with respect to its ground plane. More advances are expected in this field with the development of new fabrication techniques, materials, and devices.

In Chapter 10, we discussed the various fabrication technologies used for reflectarrays. We showed that traditional chemical etching imposes feature size limitations that push the need for alternative techniques such as laser etching and printed electronics. These alternative fabrication techniques show great promise in pushing the operating regime of reflectarrays into terahertz frequencies.

The strength of reflectarray technology stems from the fact that it can benefit from results of intense research in diverse fields. Advances in our understanding of

periodic structures can potentially inspire novel cell elements and new concepts in the synthesis of reflectarrays. It can also lead to novel applications. At a more practical level, research in the areas of new material such smart materials, ferroelectric, ferrites, and low-loss substrates leads to reflectarrays with higher efficiency and more diverse functionality. Novel fabrication techniques such as printed electronics usher exciting possibilities for low-cost integration of active elements into reflectarrays to further augment its functionality. In summary, the possibilities for reflectarray technology are very exciting from both theoretical and practical perspectives. Future advancements will occur through cross fertilization of research into seemingly unrelated fields.

About the Authors

Jafar Shaker has been with Communications Research Centre Canada since 1996. The focus of his research is periodic structures and also application of optical engineering concepts and design methods in the design of millimeter-wave antennas. He has numerous publications on reflectarray, transmitarray, artificial dielectric, electromagnetic bandgap, and power combining. He has led collaborative activities to design novel reflectarray antennas for a wide variety of bands and applications. Dr. Shaker holds three patents and has coauthored two book chapters on reflectarray antennas. He is an adjunct professor at Carleton University, Ottawa, Canada, and Royal Military College of Canada, Kingston, Canada. Dr. Shaker is a senior member of IEEE.

Mohammad Reza Chaharmir has been with Communication Research Centre Canada as research scientist since 2001 where his research activities involve periodic structures, reflectarray antennas, frequency selective surfaces, photonic bandgap, metamaterials, and antenna beam scanning. He has been published in several journal and conference papers and holds one U.S. patent on reflectarray antennas. Dr. Chaharmir is adjunct professor at Concordia University, Montreal, Canada, since 2005. He has been an IEEE senior member since 2011.

Jonathan Ethier joined the Communications Research Centre (CRC) in Ottawa in 2010, where he is an antenna research engineer. His current research interests include the application of modal theory to microwave antenna analysis and design, reflectarrays, fragmented antennas, electrically small antennas, and optimization using evolutionary algorithms. He has published 15 journal papers and 16 conference papers. Prior to joining the CRC, Dr. Ethier worked in private industry as a military/aerospace design engineer.

Index